THE UNIVERSITY OF CHICAGO

METAL OXIDE GROWTH ON POLYMER SURFACES AND WITHIN POLYMER VOLUMES: APPLICATIONS IN NOVEL MEMBRANE MATERIALS

A DISSERTATION SUBMITTED TO
THE FACULTY OF THE PRITZKER SCHOOL OF MOLECULAR ENGINEERING
IN CANDIDACY FOR THE DEGREE OF
DOCTOR OF PHILOSOPHY

BY
RUBEN ZACHARY WALDMAN

CHICAGO, ILLINOIS
AUGUST 2020

Copyright © 2020 by Ruben Zachary Waldman

All Rights Reserved

Dedicated to my family.

"You write in order to change the world... if you alter, even by a millimeter, the way people look at reality, then you can change it."

— James Baldwin —

TABLE OF CONTENTS

LIST OF FIGURES

LIST OF TABLES

ACKNOWLEDGMENTS

It is impossible to adequately acknowledge all of the people and forces in my life that have enabled me to reach this point. To my parents, Leon and Roberta Waldman, you gave me life and without you I wouldn't be here to do this work. Thank you for giving so much of yourselves to support me to this point, and for your love, care, attention, reassurance, and all that I cannot express in words here. Thank you to my two brothers, Jacob and Jonah, whom I know I can count on for advice and guidance. I acknowledge my grandparents, Fred and Doris Oppenheimer and Naomi Waldman for giving my parents life and for always being a source of inspiration and a wellspring of support. To my grandfather and namesake Rubin Waldman, though we have never met, I dedicate this work to your memory and I am proud to bear your name and legacy. To my ancestors, some of whom in living memory survived unspeakable suffering, I hope this work brings honor.

I have had the privilege to work with many incredibly talented scientists across the University of Chicago and Argonne National Lab. I have grown as a person and as a researcher through these exchanges and collaborations. At the university I'd like to thank all of the members of Paul Nealey's research group for accepting me as a de-facto group member. Thank you to Moshe Dolesji, Elizabeth Ashley, James Dolan, Xiao Li, Hyeong-Min Jin, and Tamar Segal-Peretz in particular for your help in understanding polymer science and troubleshooting self-assembly problems. Thanks to Professor Paul Nealey for your guidance, encouragement, and entertaining group meetings. Thank you to Kimberly McGee for all of your help with paperwork and bureaucracy. I want to thank the staff who make measurements and experiments possible, including Peter Duda, Anna Mukhortova, and Mike Medina at the PNF. I also want to thank Justin Jureller and Qiti Guo at the MRSEC for helping me image the many samples that I've made.

As the first graduate student at the Pritzker School of Molecular Engineering to have worked with an Argonne scientist as their primary advisor, I want to acknowledge the PME administration for making my graduate study between these two institutions possible.

I want to thank the Seth Darling's group, namely Hao-Cheng Yang, Zijing Xia, and visiting students Huiru Zhang, and Xiaobin Yang for productive group meetings and feedback. I want to particularly thank Jeff Elam, Alex Martinson, and all of their group members for giving me access to their ALD labs and trusting me with their equipment. Thanks also to Dave Mandia, the XPS whisperer, for entertaining discussions and productive collaboration. Thank you also to Ed Barry for the rides to and from Argonne in the early years and the fun chats while stuck in traffic. A big thank you to Robin Harris for helping navigate everything that goes along with working for a governmental institution. Finally I would like to acknowledge my advisor Seth Darling for his support in making this PhD possible, both formally as my advisor and as a mentor on how to approach the endeavor of scientific research ethically, professionally, and productively.

Living in Chicago for the past five years has been an absolute joy. Thank you to all of my friends and neighbors for making Hyde Park such a great place to call home. Thank you Lake Michigan for being such a remarkable backdrop to my study of water and the critical issues facing water resources. The moments of contemplation along the lakeshore, especially in the early morning, were so critical to my well-being throughout this time. Thank you also to the community of artists at the Hyde Park Art Center ceramics studio, where I continually relearned that not all knowledge needs to be scientific.

I conclude these acknowledgements with an awareness that the present moment, June 2020, feels as close to a historical crossroads as any I have experienced in my brief life. This dissertation is being published in a country facing significant crises from pandemic to poverty, and to injustices that stem from its original sins of slavery, racism, and colonialism. I hope that through the efforts of all whose who fight for freedom and against hate that the reader picks up this work in a safer world that knows justice and peace.

ABSTRACT

The stresses facing the water-energy nexus in coming decades demand advances in membrane materials research for improved separation performance, energy-efficiency, and new functionality. Water and solute interactions with porous membrane surfaces are complex and are governed by a wide-range of phenomena over length and time scales. Polymers have been used for decades to make membranes relevant to many challenging applications at large production volumes. Inorganic metal oxides have many interesting functional properties, but wholly inorganic membranes are expensive, and integrating them into membranes remains a challenge.

In this dissertation, atomic layer deposition (ALD) and sequential infiltration synthesis (SIS) are explored for their use in the modification of polymeric membranes and in the fabrication of novel isoporous structures. Fundamental insights into the interactions between the metalorganic molecules used in these deposition techniques with the chemical functionalities in polymers are described, yielding first reports of novel metal-oxide/polymer hybrid materials.

This work begins by exploring the ALD of hydrophilic aluminum oxide onto highly porous and tortuous hydrophobic polypropylene ultrafiltration membranes to create dual-faced Janus membranes. The lack of reactive sites for ALD on these hydrophobic polymers yields a gradient deposit of Al_2O_3 through the membrane interior. Controlling the vapor exposure dose enables precision placement of the wetting transition within the membrane, yielding materials suitable for rapid gas bubble aeration.

Next, the dynamics of SIS of aluminum oxide into polyethersulfone is studied using in situ optical techniques. In situ fourier transform infrared spectroscopy (FTIR) and spectroscopic ellipsometry probe the chemical and physical interactions of trimethyl aluminum (TMA) with this polymer which is ubiquitous in ultrafiltration membranes. These analyses reveal the mechanism by which TMA forms reversible associations with functional moieties in the polyethersulfone and compares them to existing studies of other polymer

systems.

In the next chapter, in situ FTIR and density functional theory are used to comprehensively compare the behavior of TMA to its Group 13 analogues trimethyl indium and trimethyl gallium. While the three show qualitatively similar interactions with polymethyl methacrylate (PMMA), the effective diffusivity of TMA is shown to be substantially lower than its heavier counterparts due to the much stronger adduct that it forms with carbonyl. The implications of this finding on processing conditions dictate lower temperatures and purge times to successfully grow conductive indium oxide via SIS for the first time.

These experimental chapters are followed by a computational analysis involving the influence of pore size distribution in membranes along considerations energy efficiency and separation performance. This analysis yields a convenient metric to determine under what conditions pursuing an isoporous material — one with uniform pore size distribution — should be justified.

Lastly, ongoing experimental work in the development of metal oxide isoporous membranes is detailed. Using block copolymer (BCP) self-assembly, a thin film consisting of a PMMA matrix and hexagonally close-packed cylinders of polystyrene is used to template the growth of metal oxides via SIS. The metal oxides directly template the PMMA domain while leaving void polystyrene pores. The processing of these films and their integration into isoporous membranes is discussed, with an outlook to future studies.

CHAPTER 1

INTRODUCTION

1.1 Membranes and the Water Crisis

Water and energy are deeply interconnected sectors of vital importance to society's well-being. Academics and governmental agencies are increasingly considering a unified water-energy nexus to capture the interdependence of these two systems. [2] Both water and energy systems face compounding stresses in many parts of the world at accelerating rates. [3] The feedback between industrialization, economic growth, environmental degradation, and climate change reinforce these negative trends.

As the purchasing power of emerging economies increases, there will be an increase in animal agriculture as the demand for previously inaccessible meat skyrockets. Agriculture worldwide consumes around 70% of annually used water, and raising livestock is significantly more water-intensive than staple crops. [4] Glacial retreat in the Himalayas may render major rivers including Yangtze, Bhramaputra, Ganges, and Mekong rivers intermittent. [5] These waterways support about 1.5 billion people. Reduction in snowmelt due to climate change will further impact South America and the United States, who use the meltwater for agriculture and for power generation. [6]

The shocks facing the water-energy nexus pose grim implications for public health [7] and political stability. [8] There are countless statistics and figures that drive home the seriousness of water access. 3,900 children die every day from waterborne illnesses from unsafe water. [7] The United Nations World Water Development Report projects that by 2050 a quarter of people worldwide will be living without access to safe and adequate drinking water. [9] Responding to climate change demands rapid decarbonization and energy conservation, with significant implications for the water-energy nexus.

A comprehensive strategy to address the issues facing the water-energy nexus must span domains of expertise to mitigate social and environmental disruption. Responses must

be multi-pronged and require both political and technological innovations. [10] If water is to be guaranteed a human right in practice, then integrating the physical science and engineering realities of water system management with social sciences and political frameworks is vital. [11]

Research into materials for water purification will play an integral part of the response. Water purification is a diverse research field unified by the goal to separate polluted mixtures into purified streams with as low an energy input as possible. [1] Importantly, the water crisis is not one of water scarcity — as the amount of water molecules on Earth remains essentially constant. Rather it is a crisis driven by the scarcity of clean water. Mixtures of water and pollutants differ depending on their sources, but in all cases they are thermodynamically favorable; treating water is thus an energy intensive process.

Materials researchers must work toward breakthroughs in water purification and chemical separations that are energy-efficient, that meet challenging separations thresholds, and that can be deployed at massive scale. [12] Membranes are particularly well-poised to meet these demands. A significant portion of the energy expended in chemical separations is in the form of distillation, in which heat is used to drive a *phase change* process to separate materials based on their boiling points. Heat-driven separations are limited by the relatively low thermodynamic efficiencies of heat engines. Membranes, on the other hand, are *mass transfer* processes, which do not suffer from the same thermodynamic limitations. [13] Significantly, while heat-driven processes often require massive plants to realize efficiencies of scale, membrane installations can be more modular and varied in scale. [14–16]

1.1.1 Different Types of mMembranes

According to the IUPAC, a membrane is defined as a, "structure, having lateral dimensions much greater than its thickness, through which transfer may occur under a variety of driving forces." [17] Membranes can be described either by their pore size, or by the size of solutes that they reject to a certain threshold. Figure 1.1, adapted from the following reference, [1]

shows the large range of length-scales over which membrane pores can be designed. This dissertation focuses on membranes in the ultrafiltration to nanofiltration regime, with pores between 2-200 nm in size. The SEM micrographs highlight four typical polymer ultrafiltration membranes. While all are described as having 200 nm pores, they vary significantly in pore structure and tortuosity. In practice, membrane pore size is not often a direct measure of the physical dimensions of the pore, which is difficult in tortuous membranes like those in Figure 1.1. Rather, the membranes are described by the size of particle where rejection is 90%.

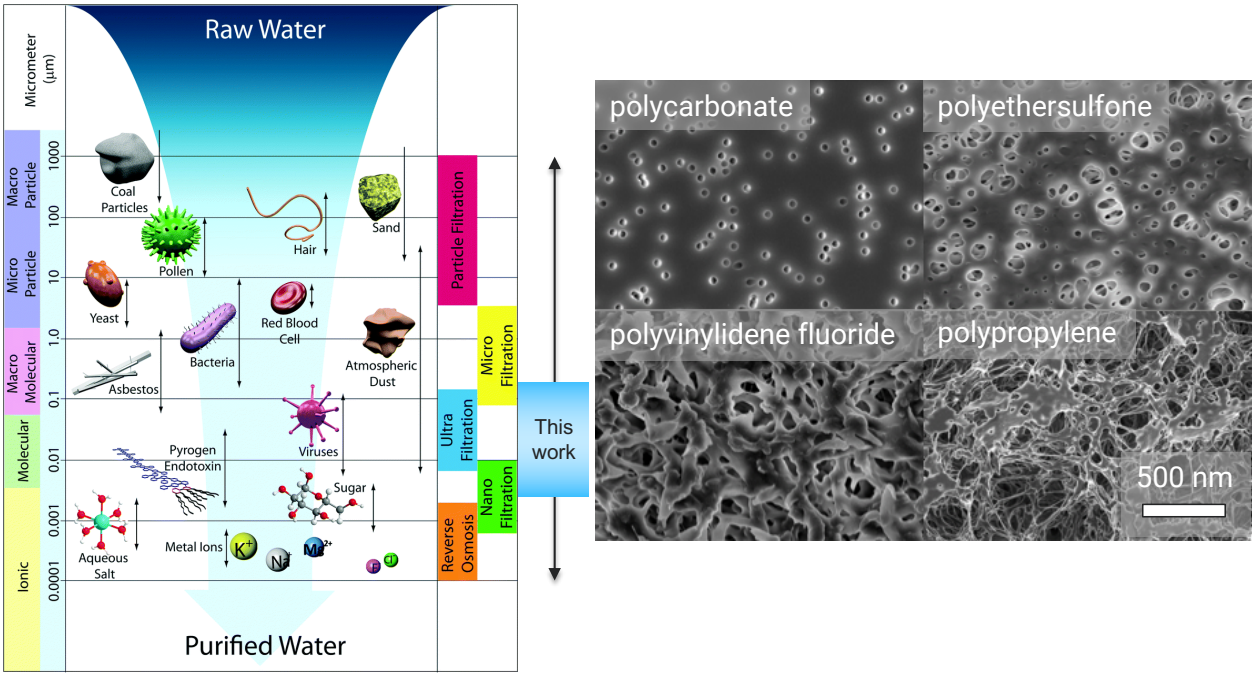

Figure 1.1: Membranes are primarily described by their pore size, leading to different classes for different intended solutes (adapted from [1]). This work focuses on membranes between the ultra/nanofiltration class. The SEM micrographs highlight the pore surfaces of these membranes.

Recovering useable water from contaminated streams requires a process tailored to local geographic and economic conditions. Furthermore, the intended end use of the water should dictate the degree of treatment to be applied. [18] Simply put, designing a solution to scrub all possible pollutants to arbitrarily strict standards would be economically and technologically untenable. A thorough understanding of the input water stream composition

and intended use of the purified product is vital in real-world filtration system design.

1.2 Atomic Layer Deposition and Sequential Infiltration Synthesis

Sequential infiltration synthesis (SIS) has emerged over the past decade [19] as a technique to grow hybrid organic-inorganic materials and rapidly fabricate structured inorganic films. SIS relies upon the diffusion of metal-organic vapor precursors into the bulk volume of polymers. Due to attractive chemical interactions with certain polymer functional groups, precursors can exhibit prolonged residence with the polymer. This enables SIS to realize the entrapment of the inorganic metal oxide reaction products within the polymer. This technique works across multiple length scales — whether transforming the properties of macroscale materials or functionalizing nanoscale devices formed by lithography or polymer self-assembly. [20, 21]

ALD is a technologically mature materials growth technique that is used in semiconductors, solar photovoltaics, and other industries. In ALD, alternating pulses of vapor precursors are used to grow thin conformal layers of inorganic materials on solid substrates. Each precursor irreversibly reacts with the substrate chemically in a self-limiting fashion, presenting alternating surface chemistry appropriate for reaction with the subsequent precursor. As this sequence of alternating surface reactions are cycled repeatedly, the material grows in thickness. In an ideal ALD system, each cycle deposits a uniform layer of material, and the process can be described with a linear growth per cycle. In reality, ALD is complicated by a number of experimental factors. The nucleation of ALD growth is dictated by temperature, chemistry, as well as the presence of suitable reactive groups on the substrate surface. For high surface area substrates, the precursor dose must be sufficient to reach and react with all surfaces to ensure a linear growth rate on the whole sample. Furthermore, co-exposure of the two reactants in the gas phase, known as cross-talk, leads to uncontrolled growth by chemical vapor deposition.

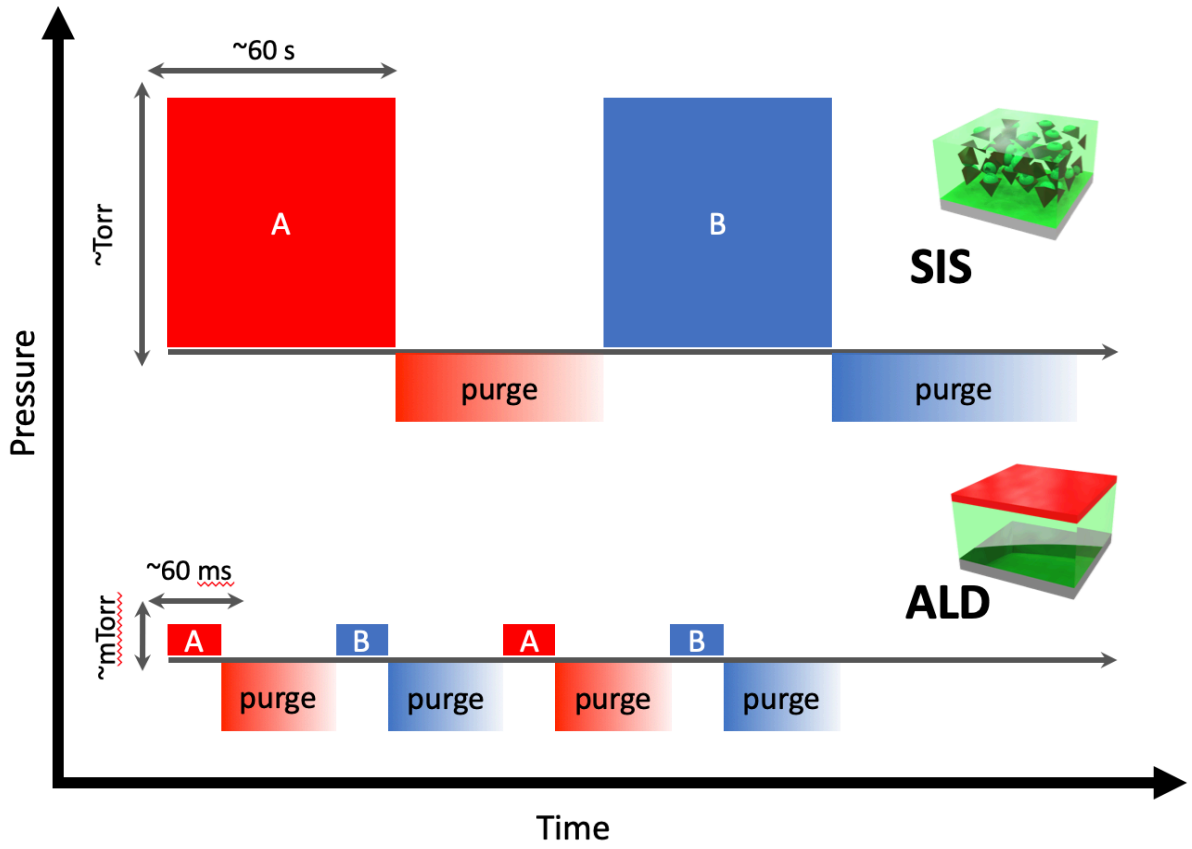

Figure 1.2: Schematic distinguishing SIS and ALD. SIS uses greater vapor pressures and exposure durations to promote precursor diffusion into polymer volumes.

Polymers, composed of entangled molecular chains with associated free volume, are not dense solids, and as a consequence, ALD can diffuse through them substantially. The diffusivity of precursors enables SIS in which the inorganic deposit is distributed within the volume of the polymer and on the surface of the polymer. While SIS often utilizes ALD precursors and is often conducted in the reactors designed for ALD, the processing parameters required for uniformity and reproducibility differ substantially (Figure 1.2). In typical ALD processes, precursor pulses are brief (<2 s) as they are required only to provide sufficient exposure to saturate the surface chemical groups of the growth substrate. In SIS, by contrast, pulse pressures are comparatively larger to provide enough precursors to infiltrate a 3D volume, and exposures are comparatively longer to allow a complete diffusion of the precursors into the polymer phase. The diffusive nature of precursor transport within

polymers, in contrast to simple saturation on solid substrates, means that the distribution of the precursors within the film is sensitive to diffusion time, precursor vapor partial pressure, temperature, interactions between the polymer and precursor, and polymer microstructure.

SIS emerged as a distinct concept as a consequence of attempts to apply ALD to polymeric substrates by the ALD research community. The diffusion of precursors beyond the near surface of polymers was observed as early as 2005, when the George group noted that polymers, including polymethyl methacrylate (PMMA), could uptake trimethyl aluminum (TMA) by absorption within their free volume. [22] However, the crucial role of interactions between precursors and polymer functional groups was not discussed in these early studies. Indeed, the diffusivity of precursors into polymer films was considered a problem in some early studies. In experiments considering PMMA as a masking layer for area-selective ALD for patterned TiO_2 growth, researchers found that titanium tetrachloride ($TiCl_4$) diffused and reacted deeper into PMMA films than titanium isopropoxide (TIP). [23, 24] Unless the PMMA films were of sufficient thickness, precursors would diffuse through the entire film and react with the masked silicon substrate. In these initial studies, the diffusion of ALD precursors into and reaction with polymer films were viewed as challenges to be overcome. In fact — With careful control — restricting growth to very near surfaces of polymers in an ALD-like manner is possible. [25]

In the years since the diffusion of ALD precursors through polymers was observed, SIS has been developed to intentionally enable the direct incorporation of metal oxide or metallic materials within polymers, yielding hybrid materials with novel properties. It should be noted that SIS is distinct from molecular layer deposition (MLD) in which purely organic or organic-inorganic hybrid materials are applied as sequential monolayers using self-limiting surface reactions in which the organic components are incorporated in the vapor phase precursors and are retained in the resulting thin films. [26] SIS-derived hybrid materials may further be subsequently subjected to plasma or thermal annealing treatments to remove the polymer constituents entirely, resulting in purely inorganic metal or metal oxide structures

that retain the form of the original polymer morphology. [27,28] Due to the versatility of SIS, researchers have utilized SIS for a wide host of applications with more on the horizon. The demonstrated application spaces for SIS have been recently reviewed in detail. [20,21,29,30] A survey of SIS literature organized by use inspiration is tabulated in Table 1.1. The first use inspiration category in Table 1.1 lists reports that investigate the fundamental physical chemistry that underpins SIS phenomena or otherwise quantifies processing parameters.

As the application space for SIS widens, the functional implementations of the technique are at risk of outpacing the development of a firm theoretical and experimental physicochemical basis for SIS. Attempts at a complete description of the varied and complex phenomena at play during SIS have only just begun. [21, 31] Complete descriptions are complicated by the disparate length and time scales involved in the SIS process and the wide range of interaction strengths introduced by choice of metal-organic precursor, polymer structure, polymer functional group, temperature, and other experimental design variables. The remainder of this introduction will concisely present the state-of-the-art understanding of SIS.

Table 1.1: Sequential infiltration synthesis research organized by use inspiration.

Use Inspiration	**Material**	**Reactant A**	**Reactant B**	**Polymer**
fundamental physical chemistry	Al_2O_3	TMA	H_2O	PS-*b*-PMMA [32–37]
	-	-	-	spider silk [38]
	-	-	-	PS-*b*-polyepoxyisoprene (PS-*b*-PIO) [39]
	-	-	-	PMMA [31,34,36,40–47]

Continued on next page

Table 1.1 – *Continued from previous page*

	-	-	-	polyethyl-methacrylate (PEMA) [40]
	-	-	-	polypropyl methacrylate (PPMA) [40]
	-	-	-	polybutyl methacrylate (PBMA) [40]
	-	-	-	polyvinyl alcohol (PVA) [41, 42]
	-	-	-	polyvinyl pyridene (PVP) [47]
	-	-	-	polyacrylic acid (PAA) [47]
	-	-	-	PA-6 [41, 42]
	-	-	-	polybutylene terephthalate (PBT) [41, 42]
	-	-	-	polylactic acid (PLA) [41, 42]
	-	-	-	polycarbonate (PC) [41, 42]
	-	-	-	polyethylene oxide (PEO) [41, 42]
	-	-	-	polyethylene terephthalate (PET) [41, 42]
	-	-	-	PS-*b*-P4VP [33]

Continued on next page

Table 1.1 – *Continued from previous page*

	-	-	-	PS-*b*-P2VP [33]
	-	-	-	PS-*random*-PMMA (PS-*r*-PMMA) [48]
	-	-	O_3	PS-*b*-PMMA [49]
	-	-	O_2 plasma	PS-*b*-P4VP [50]
	TiO_2	$TiCl_4$	H_2O	PS-*b*-P4VP [51, 52]
	-	-	-	PS-*b*-PMMA [53]
	-	TIP	-	PS-*b*-PIO [39]
	ZnO	DEZ	H_2O	PS-*b*-PMMA [32, 33, 37]
	-	-	-	PS-*b*-PIO [39]
	-	-	-	PS-*b*-P4VP [33]
	-	-	-	PS-*b*-P2VP [33]
	-	-	-	SU-8 [54]
	W/WO_x[a]	WF_6	Si_2H_6	PS-*b*-PMMA [32, 55]
	SiO_2[a]	TPS	TMA	PS-*b*-PMMA [32]
	VO_x	VOIP	H_2O	PS-*b*-PIO [39]
	In_2O_3	TMIn	H_2O	PMMA [36]
	Ga_2O_3	TMGa	H_2O	-
	SnO_2	TDMASn	H_2O_2	PS-*b*-P2VP [56]
	-	-	-	P2VP [56]
imaging	Al_2O_3	TMA	H_2O	PS-*b*-PMMA [57, 58]
	ZnO	DEZ	H_2O	Poly(3-hexylthiophene -2,5-diyl) P3HT [59]
catalysis	Al_2O_3	TMA	H_2O	PS-*b*-P4VP w. Pd salts [60]

Continued on next page

Table 1.1 – *Continued from previous page*

	TiO_2	$TiCl_4$	H_2O	PEO-*b*-PPO-*b*-PPO [61]
triboelectricity	Al_2O_3	TMA	H_2O	Polydimethylsiloxane (PDMS) [62]
oil sorption	Al_2O_3	TMA	H_2O	Polyurethanes [63, 64]
photodetectors	ZnO	DEZ	H_2O	SU-8 [65]
gas sensors	ZnO	DEZ	H_2O	SU-8 [66]
photoluminesence	Al_2O_3	TMA	H_2O	PET [67]
	ZnO	DEZ	H_2O	PMMA [68]
photovoltaics	Al_2O_3	TMA	H_2O	PS-*b*-PMMA [69]
	ZnO	DEZ	H_2O	P3HT [59, 70–72]
antireflection	Al_2O_3	TMA	H_2O	PS-*b*-P4VP [73]
	-	-	-	PS-*b*-PMMA [73, 74]
porous materials	Al_2O_3	TMA	H_2O	PBT [27]
	ZnO	DEZ	-	-
	TiO_2	$TiCl_4$	-	-
	ZnO	DEZ	H_2O	cellulose acetate [75]
filtration	Al_2O_3	TMA	H_2O	PS-*b*-PMMA [76]
	-	-	-	polyethersulfone (PES) [77]
	-	-	-	polymer of intrinsic microporosity (PIM-1) [78]
	ZnO	DEZ	H_2O	-
	TiO_2	$TiCl_4$	H_2O	-
UV/thermal stability	ZnO	DEZ	H_2O	Kevlar [79]

Continued on next page

Table 1.1 – *Continued from previous page*

chemical stability	Al_2O_3	TMA	H_2O	PMMA [80]
electrical properties	Mo^b	$MoCl_5$	×	P3HT [81]
	-	-	-	Polyaniline (PANI) [82]
	Sn^b	$SnCl_5$	-	
	ZnO	DEZ	H_2O	PANI [83]
	-	-	-	SU-8 [28]
	-	-	-	PS-*b*-P2VP [84]
mechanical properties	Al_2O_3	TMA	H_2O	PA-6 [85, 86]
	-	-	-	Polyurethane (P55D) [86]
	-	-	-	SU-8 [87]
	-	-	-	spider silk [88]
	-	-	-	Electronic packaging resin [89]
	TiO_2	TIP	H_2O	spider silk [88]
	-	-	-	collagen [90]
	ZnO	DEZ	H_2O	spider silk [88]
	-	-	-	cellulose [91]
	-	-	-	Polytetrafluoroethylene (PTFE) [92]
lithography	Al_2O_3	TMA	H_2O	PS-*b*-PMMA [93–99]
	-	-	-	PMMA [93, 100–104]
	-	-	-	Poly4-*tert*-butylstyrene-*b*-poly-2vinylpyridine (PtBS-*b*-P2VP) [105]

Continued on next page

Table 1.1 – *Continued from previous page*

	-	-	-	ZEP520A (e-beam resist) [100, 101]
	-	-	-	CSAR62 (e-beam resist) [102]
	-	-	-	SU-8 [106]
	-	-	-	EUV resist [107]
	-	-	-	Polyphthalaldehyde [108]
	-	-	-	P2VP-*b*-PS-*b*-P2VP [109, 110]
	TiO_2	TIP	H_2O	SU-8 [106]

[a] The material was grown on initial Al_2O_3 nuclei grown by TMA/H_2O

[b]The metal complexes directly and irreversibly with the polymer with no 'B reactant'

End of Table

1.3 Theoretical Underpinnings of SIS

Thermodynamics govern the interactions between the chemical precursors and the polymer chains. A clear understanding of the thermodynamics of the system facilitates the rational design of an SIS process. Figure 1.3 illustrates the governing process of SIS.

1.3.1 Precursor Solubility

The first thermodynamic process in SIS is the change of phase that takes place when the precursor vapor molecule leaves the headspace of the reactor chamber and dissolves into the polymer matrix. If the precursor is insoluble in the polymer, SIS cannot occur. If the precursor can dissolve into the polymer, then the solubility will dictate the equilibrium concentration of the precursor in the polymer. The concentration of the precursor in the film can impact the density of the resulting SIS material. The simplest classical thermodynamic

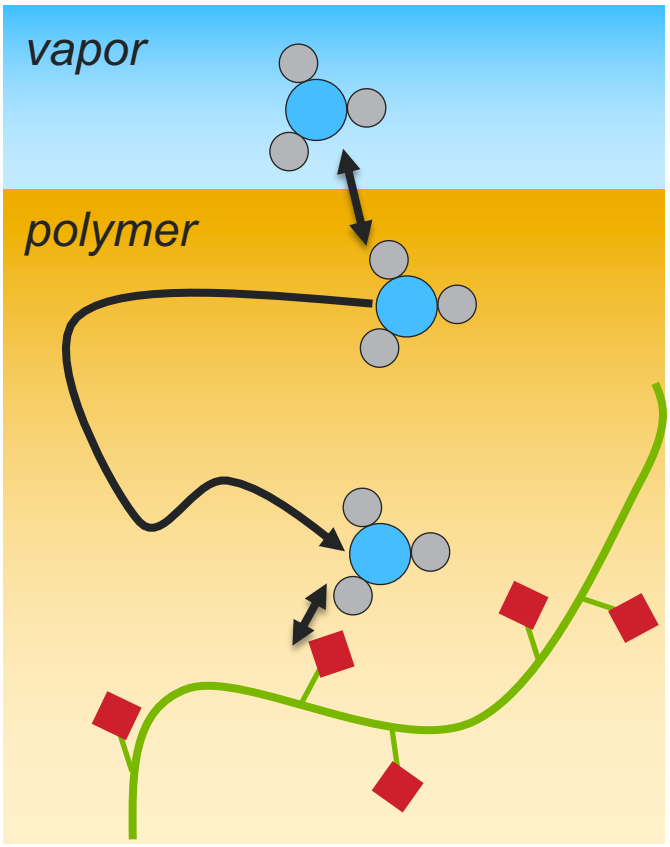

Figure 1.3: Cartoon depicting physical and chemical processes in SIS. Precursor molecules solvate into the polymer, diffuse away from the interfaces, and interact with functional groups along the polymer chains.

model for solubility is Henry's law:

$$C = S * P \tag{1.1}$$

where C is the concentration of the precursor in the polymer, S is the solubility coefficient of the precursor in the polymer, and P is the partial pressure of the precursor in the vapor phase. The van't Hoff equation describes the temperature dependence of the solubility coefficient:

$$S = S_0 e^{-\frac{\Delta H_S}{kT}} \tag{1.2}$$

where k is Boltzmann's contant, T is temperature, S_0 is a material-dependent constant, and ΔH_s is the partial molar enthalpy of dissolution. These basic expressions do not capture the full complexity of the polymer matrix, which consists of free volume elements (also called

microvoids) that contribute to the solubility of infiltrating precursors. These are treated in "dual-sorption theory" or Langmuir models that add contributions from the free volume in addition to the polymer chain volume. [111] These simple expressions provide three possible routes to maximizing the equilibrium solubility of the precursor in the polymer: raising the partial pressure of the precursor vapor, raising the temperature of the system, and choosing precursor/polymer pairs with the smallest ΔH_s. The accessible range of partial pressure for a given precursor is limited to its vapor pressure at the SIS temperature, in order to prevent condensation of the precursor into the liquid phase on the sample and reactor wall surfaces. Engineering of the polymer free volume may also enhance the solubility of precursor molecules within a polymer film. Temperature will have an impact on this parameter beyond that reflected in the solubility enhancement from the van't Hoff equation. This is especially true in the vicinity of phase transition temperatures for the polymer (glass, crystallization, etc.).

The solvation of precursor molecules into a polymer film enables the retention of the precursor within the film during the removal of the partial pressure of the vapor phase by purging via vacuum pumps. These solvated molecules may not be interacting with functional groups along the polymer, but are arrested in their movement by the energetic barriers to site-hopping imposed by their local configurational environment. The molecules must change phase back from their solvated state to the gas phase during this purging process. The transient entrainment of precursor molecules within the polymer network enables material growth in polymers inert to strong interactions with organometallic precursors, for example, polystyrene (PS) [46] and polyethylene (PE) that lack polar groups. [22] If the purge time between metal-organic precursor exposure and oxygen-bearing precursor exposure is sufficiently short, the two reactants can mix and react in the polymer phase at the exclusion of substantial mixing in the vapor phase. In this case, the time allowed for desorption of the precursor from the polymer phase to the vacuum is insufficient to completely remove the molecule from the polymer. In a sense, this can be considered a localized

chemical vapor deposition (CVD) chemistry within the polymer. However, the outgassing of solvated molecules in inert polymers is expected to be rapid, resulting in an extremely low density of the precursor in the film over practical time scales for the introduction of the second precursor without gas-phase mixing occurring. This yields slow growth rates in such processes, leading to studies of polymer modification with oxidative processes such as plasma treatments to modify the polymer prior to SIS and thereby introduce favorable precursor-polymer interactions. [112–115]

1.3.2 Precursor-Polymer interactions

With precursor molecules solvated within the polymer film, the next thermodynamic consideration is the interaction between the precursor and the chemical moieties built into the polymer chain. There are a number of possible interactions that a precursor molecule may have with the polymer. These interactions may lead to the formation of a reversible complex between the precursor and polymer functional group or lead to complete electron transfer yielding a covalent bond between the precursor and polymer functional group. Depending on the interactions of the precursor molecule, the resulting SIS product may be covalently linked to the polymer back- bone in a hybrid material or may exist as a nanocomposite without chemical bonds between the polymer and nucleated metal or metal oxide.

a. Reversible Complex: Research into SIS has provided ample evidence for the existence of a noncovalent attractive interaction between the aluminum atom of TMA and the C==O bond of the ester carbonyl in PMMA. [34, 41, 42, 44, 47] The aluminum in the TMA monomer is sp^2 hybridized with the three methyl groups bound by the hybrid orbitals formed from the 3s and two 3p orbitals. The remaining empty 3p orbital results in a strong Lewis acid, [116, 117] which is capable of accepting the lone pairs of the Lewis basic C==O to form a Lewis adduct. The vapor-phase TMA molecules can be present in equilibrium with a dimer form, where each Al is bound to four methyl groups, at the temperatures and pressures used in SIS, though the stability and interactions of this dimer within polymers

are unkown. [31] Density functional theory (DFT) has been used to estimate the energy of this TMA-PMMA Lewis adduct—the energy of the complex formed between the TMA molecule and a PMMA monomer was calculated to be -0.477 eV at 300 K. [36] The Lewis adduct is reversible, which enables the interaction to be broken and reformed as the precursor diffuses through the polymer film and encounters multiple adduction sites.When water (or other oxygen sources such as ozone, [49] oxygen plasma [50], or hydrogen peroxide [33] is introduced into a polymer with adducted or trapped organometallic precursors supplied during the first half-cycle of SIS, it encounters a different chemical environment than in the case of ALD. In the SIS case, the water can react directly with molecular TMA that still has all three methyl groups, in contrast to a monomethyl- or dimethyl-aluminum terminated surface as in ALD. The interaction of the organometallic precursor with its environment may also change its reactivity (e.g., by weakening bonds), enabling growth even under conditions that are not amenable to ALD. For example, while the lowest reported temperature for ALD growth of In_2O_3 using trimethyl indium and water is 200 °C, [118] Chapter 4 discusses how SIS using these same precursors occurs at 80 °C in PMMA—conditions under which no ALD was observed. [36]

b. Direct Covalent Bonding: If the organometallic precursor and polymer functional group are sufficiently reactive, a substrate-precursor reaction can occur simultaneously with diffusion that directly covalently links the metal to the polymer. For example, TMA and PMMA form a reversible Lewis adduct at low temperatures, but at temperatures in excess of at least 150 °C, the two are proposed to undergo an irreversible pericyclic reaction to form PMMA-Al acetate and ethane as a byproduct. [45]

The reactivity of the precursor polymer-pair and the reaction temperature both dictate the chemical interactions that occur during SIS. SIS requires a balance between reversible complexes and covalently reacted groups with the polymer. Direct covalent reactions with a particular precursor can be achieved at lower temperatures through selection of a polymer functional group with a lower energy barrier. Polyacrylic acid (PAA) differs

from PMMA in that it has carboxylic acid instead of methyl ester moieties. Recent evidence from the points to the direct covalent incorporation of TMA in PAA at significantly lower temperatures (as low as 60 °C) relative to PMMA. This may be attributed to the presence of an acidic proton, which facilitates the reaction, generating methane as a byproduct. [47] Designing SIS reactions *a priori* requires detailed understanding of the reaction pathways and interaction energies between polymer functional groups and metal-organic precursors.

c. Coreactant dosing and subsequent SIS cycles: The most significant changes to the chemical landscape of the hybrid film occur between the first cycle and subsequent SIS cycles. In the first exposure of a metal-organic precursor, the precursor can only interact with functional groups intrinsic to the polymer itself (or residual contaminants such as H_2O). However, after the first full SIS cycle, which includes exposure to the oxygen source—typically water—the film contains both intrinsic polymer functionalities (which may or may not themselves be chemically changed by the first SIS cycle) and metal oxyhydroxides that are now incorporated. These incipient nuclei are often expected to exhibit hydroxyl terminated surfaces, in analogy to a propagating metal oxide ALD surface after water dosing, which may be highly reactive with the organometallic precursor provided in the second SIS cycle.

1.4 Transport in SIS

1.4.1 Diffusion

Diffusion governs the transport of precursor molecules from the free film surface throughout the polymer volume. The fundamental science of small molecule diffusion through polymeric films has a long history in the context of membranes for gas separations. [119–121] The transport of dissolved small molecules in polymers is called "solution-diffusion" and is driven by the chemical potential gradient imposed by the concentration gradient of penetrant precursor molecules in the film. This chemical potential gradient arises from the energetics

of the various interactions described above. [122]

At the simplest level, the transport of the organometallic vapors through the polymer can be modeled as a purely diffusive process. Fick's second law describes how the concentration of the diffusing species changes in space and time:

$$\frac{\partial n}{\partial t} = D\nabla^2 n \tag{1.3}$$

where n is concentration (volume density of precursor molecules), t is time, and D represents the diffusivity of the precursor molecule in the polymer defined by the following equation:

$$D = D_0 e^{-\frac{\Delta H_{\mathrm{D}}}{kT}} \tag{1.4}$$

where k is Boltzmann's constant and T is temperature. ΔH_D is the energy barrier for the penetrant precursor molecule to hop from one site to another, and D_0 is the frequency of site-hopping attempts of the penetrant molecule. A recent review solves this equation for the most common boundary conditions of a thin film on a gas-impermeable substrate and a fiber, yielding expressions for the spatial and temporal concentration of penetrant molecules. [20]

Introducing reversible complex formation between the penetrant molecules and polymer functional groups brings a second level of complexity to modeling the diffusion in SIS. By approximating the polymer as a region with a volumetric density of reactive sites c_0, transport through the polymer can be described as:

$$\frac{\partial n}{\partial t} - D\frac{\partial^2 n}{\partial z^2} = -k^+ n c_0(1-\Theta) + k^- c_0\Theta \tag{1.5}$$

Here, n is the volume density of precursor molecules, and Θ is the fraction of occupied reactive sites and is governed by the reversible complex rates of formation, k^+, and breaking, k^-:

$$\frac{d\Theta}{dt} = -k^+ n c_0(1-\Theta) + k^- c_0\Theta \tag{1.6}$$

Combining these two equations yields the following expression for transport of dissolved molecules within the polymer:

$$\frac{\partial n}{\partial t} - D\frac{\partial^2 n}{\partial z^2} = \frac{d\Theta}{dt} \tag{1.7}$$

This equation is the diffusive equivalent of transport in a chromatography column, where reversible absorption/desorption slows the transport of molecules through the medium. If the concentration of available sites is in local equilibrium with the local density and the solubility of the penetrant molecule is low, the fraction of occupied sites can be approximated as:

$$\Theta = \frac{k^+}{k^-}n \tag{1.8}$$

so that:

$$\frac{\partial n}{\partial t} - \frac{D}{1 + c_0\frac{k^+}{k^-}}\frac{\partial^2 n}{\partial z^2} = 0 \tag{1.9}$$

In the dilute limit, the transport process can be well-described by conventional diffusion with an effective diffusivity term depending on the ratio of the reversible complex formation/breaking rates. These effects can be captured in a reaction-limited diffusivity D^* defined by the following expression:

$$D^* = \frac{D}{1 + c_0\frac{k^+}{k^-}} \tag{1.10}$$

Beyond the dilute approximation, the quasi-equilibrium approximation leads to a diffusivity that itself depends on the fraction of the occupied reactive sites within the polymer. In each of these cases, the approximations yield identical Fickian diffusion profiles, just with diffusivity values reduced by the strength of reversible interactions. Further extending these concepts to irreversible reactions between precursors and functional groups can begin with approximations such as those developed for reactive transport in porous materials. These ideas are thoroughly developed in the following references. [123, 124]

The influence of complexation energy and formation/breaking rates on diffusivity

is well-illustrated by the case of Al_2O_3 SIS vs Al_2O_3/Ga_2O_3 SIS (Chapter 4). Trimethyl aluminum, trimethyl indium, and trimethyl gallium (TMA, TMIn, TMGa) were used along with water for these three materials respectively, such that the ligands were identical and only the metal varied. These three precursors were found to form isostructural complexes with the carbonyl moiety of PMMA, but the energy of the TMA interaction was calculated to be $\sim$3$\times$ greater than either of the other two materials. As a consequence, the depth of In_2O_3 infiltration in a thick PMMA film under similar conditions is significantly deeper than Al_2O_3, highlighting how the design of precursor/polymer energetics influences SIS.

Finally, the long residence time of precursor molecules within the polymer raises the possibility of accessing a regime where both coreactants do not mix in the gas phase but are simultaneously present within the polymer. Effectively speaking, this describes a chemical vapor deposition (CVD)-like growth within the polymer itself. Being CVD-like, the reaction takes place wholly between the two molecules without the polymer playing a role, other than enabling the mixing to take place within the polymer and not the vapor phase.

The diffusion of small molecules in polymers has been extensively studied in the literature. For instance, Barrer carried out systematic studies on various polymers involving gases such as hydrogen, oxygen, and carbon dioxide, establishing correlations between the size of the molecule and the activation energy of the diffusion process. [125] In the case of water, a more relevant example in the context of SIS, diffusivities of 1.7×10^{-9} cm^2/s at 60 °C and 5×10^{-10} cm^2/s at 45 °C have been reported for Kapton polyimide and polyacrylonitrile (PAN) with a reported activation energy of 5.4 kcal/g mol for the Kapton polyimide case. [126, 127] Beyond water, though, there is a scarcity of data for traditional ALD/SIS precursors. However, if we take a value of 10^{-9} cm^2/s as a reference and we consider a micrometer-thick polymer layer, the resulting characteristic diffusion time (in the absence of strong interactions or reactions with the polymer) is on the order of 10 s. Calculating the diffusivity of SIS precursors in different polymer systems is an extremely useful endeavor. A comprehensive study of the diffusivity of TMA within PMMA was conducted by the Perego

group using in situ spectroscopic ellipsometry (SE).27 At 90 °C for a 14 kg/mol PMMA polymer, the diffusivity of TMA was calculated to be 1.2 × 10^{-12} cm^2/s. The three order of magnitude difference from the case of ∼10^{-9} cm^2/s for water highlights the strong role of noncovalent interactions in SIS precursor transport within polymers.

A number of material parameters affect the diffusivity of SIS precursors within polymers independent of the thermodynamics of a given precursor/polymer interaction, as outlined below. It is important to emphasize that all the models above ignore the impact that inorganic clusters growing inside the polymer as part of the SIS can have on both the solubility and the diffusivity of the polymer. The idea that, after a number of SIS cycles, precursor transport within the polymer is greatly impeded agrees well with the experimental observation of dense crusts forming near the surface of polymers after a sufficiently large number of SIS cycles.

1.4.2 Polymer Free Volume

The polymer free volume arises from entropic interactions in the entangled chains of polymers, which can change with the material's processing history. The polymer chain volume combined with the free volume yields the specific volume (volume/mass), which is the inverse of density. Starting with a glassy polymer in which segmental motion of the polymer chains relative to each other is suppressed, heating causes the volume of the polymer chain to increase due to thermal expansion. The free volume does not increase with temperature until the glass transition temperature (T_g), at which point the free volume fraction v_{f0} (free volume/specific volume) obeys the following equation [128]:

$$v_{f0} = v_{f0,T_g} + \Delta\alpha(T - T_g) \tag{1.11}$$

where $\Delta\alpha$ is the difference in the thermal expansion coefficient above and below T_g. By raising the temperature of the film above T_g and rapidly quenching it, some of the

excess free volume from the rubbery state can be frozen in, such that the polymer is less dense than it would be at slower cooling rates. These thermal treatments can, in principle, enhance the diffusivity of precursors in polymers by increasing the number of hopping pathways along which they have to diffuse. More detailed theory of solvated molecule diffusion as a function of glassy/rubbery state can be found in the following review. [129]

The polymer free volume can be locally perturbed in the interphase regions near the substrate and near the free surface, which can affect the diffusivity of metal-organic compounds in these regions. [130, 131] In many systems, this effect is small. For example, in PMMA, the vacuum-polymer interphase region that deviates from bulk PMMA was measured to be ∼2 nm. [132]

1.4.3 Chain Architecture

Developments in polymer synthesis have opened up a massive field of possibilities in polymer chain architecture. Copolymers, bottlebrush polymers, star polymers, and more are possible. There is also a vast range of monomers available, and modifications to monomer groups accessible, with modifications that may directly alter interactions with SIS precursors. More indirect modifications may perturb the free volume of the polymer with implications for SIS precursor diffusivity.

By controlling the volume fraction of methyl methacrylate (MMA) in a PS-*r*-PMMA random copolymer, the density of reactive sites relative to inert PS sites can be tuned. In a study of such a system, Caligiore *et al.* found that the diffusion coefficient of TMA through this copolymer was modestly increased over that measured for pure PMMA, at MMA fractions exceeding 10%. [48] The SIS deposition rate of Al_2O_3 was linear with the MMA fraction, as expected, and the porosity and domain size of the annealed metal oxide did not apparently differ across this wide range of MMA fractions. This study thus shows that the density of reactive sites in a polymer can modestly impact the diffusivity of SIS precursors.

In another example, the influence of polymer free volume on the kinetics of precursor transport through thin films was concisely studied by comparing poly-n-methacrylate polymers. [40] This series of polymers consists of alkyl chains of increasing length on the ester bond of the molecule. The presence of this alkyl group lowers the glass transition temperature of the molecule by disrupting entanglement of the polymer. [133]Thus, at a given reaction temperature, the longest chain polybutyl methacrylate polymer has the largest free volume of the group. Using quartz crystal microgravimetry (QCM), the Jur group found that polymers with increasing free volume elements (longer pendant chains and lower T_g allow more rapid diffusion of TMA under equivalent SIS conditions. However, sufficiently long pendant alkyl groups can themselves crystallize. Crystallization of polymer components has been observed to change the distribution of metal oxide products during SIS, likely due to changes in the diffusion pathways within the film. [71, 72]Therefore, more studies are needed to generalize trends based on such modifications to chain architecture.

While the poly-n-methyl methacrylate isothermal study provides a clear comparison of analogous polymers with disparate T_g, more care must be taken when ascribing changes in SIS behavior across temperatures to T_g. Infiltrated molecules can plasticize polymers, promote chain motion, and lower the effective Tg from what is measured for the polymer by *ex situ* methods. The degree to which this plasticization affects diffusivity must be considered on a case-by-case and cycle-by-cycle basis. Temperature simultaneously affects functional group reactivity at the same time as it increases chain motion. Since the true glassy/rubbery transition of polymers under infiltration is not generally known, care must be taken in ascribing temperature-dependent trends in SIS studies to particular phenomena.

1.4.4 Polymer Molecular Weight

The molecular weight (M_w) of the polymer will also influence the diffusive environment of vapor precursors due to the variable volume density of polymer chain ends. A polymer with a larger M_w will have fewer chain ends, which have a larger configurational free volume

than monomer units within the chain itself. The glass transition temperature of PMMA, for example, increases as a function of M_w due to the influence of chain-end density. [134] This is true across polymers and is described by Flory-Fox theory. [135] A higher density of chain ends leads to more diffusive pathways for vapor precursors, and therefore, SIS in the low-diffusion time limit is expected to yield metal or metal oxide at greater depths in a lower M_w polymer film. The diffusivity of TMA in homopolymer PMMA at 90 °C was calculated to be 3.75 times greater when the molecular weight was decreased from 14 to 3.9 kg/mol. [46] M_w can also affect the density of the resulting SIS product. Al_2O_3 grown in 200 nm 15 kg/mol PMMA thin films by SIS at 90 °C had an average effective refractive index (neff) of 1.396 (porosity 26%), whereas 350 kg/mol PMMA produced an neff of 1.374 (porosity = 29%). [103] This effect is subtle—an order of magnitude difference in molecular weight yields only a 3% change in porosity of the resulting metal oxide product. Nevertheless, this highlights how engineering of the polymer free volume environment and the resulting diffusivity of the precursor through the polymer can influence the properties of the resulting hybrid material. The M_w of the polymer also dictates the density of chain ends, which can have different chemistries as discussed previously. We note, however, that the interaction between organometallic precursors and polymer functional groups affords tunability that is orders of magnitude larger than the reported polymer molecular weight effects alone.

1.5 Periodic Table of SIS

The range of materials that have been deposited by ALD is vast and spans much of the periodic table. [136–138] ALD processes have been developed for the deposition of pure elements, oxides, nitrides, carbides, sulfides, and more. The library of materials grown by SIS to date is, by contrast, far more limited. The periodic tables for ALD and SIS in Figure 1.4 highlight this disparity. The current published library of SIS materials includes Al_2O_3, ZnO, TiO_2, In_2O_3, Ga_2O_3, VO_x, SnO_x, SiO_2*, W/WO_x*, Sn**, and Mo**, where (*) indicates that the material was grown on initial Al_2O_3 nuclei grown by TMA/H_2O and (**) indicates

that the metal complexes directly and irreversibly binds to the polymer with no "B" reactant. Although some reports describe the SIS oxide with the standard thermodynamically stable chemical formula, in other reports, a general MO_x nomenclature is used, as the oxidation state of the metal may not be definitively known. Here, we use the naming from the original reports. SIS of Al_2O_3 in PMMA from TMA and H_2O is the most well-studied SIS system by far. ZnO and TiO_2 are the two next highest in publication frequency with other SIS material processes restricted to a handful of reports. SIS SiO_2 and W/WO_x have only been achieved with a seed cycle of Al_2O_3, as previously mentioned. [32, 55] While this seeding method is useful in providing reactive nuclei for subsequent cycles, the resulting materials will have some Al_2O_3 content, which may impact functional properties. The development of processes for the direct SIS of functional materials is also desirable. [36] A thorough understanding of the chemical physics involved in the varied aspects of SIS will be required as researchers attempt to fill out more of the periodic table in pursuit of novel functional hybrid materials.

Within a given set of precursors and functional groups, advances in polymer synthesis open a wide variety of structural modifications to the polymer. Active and inactive groups can be combined in copolymers, in blocks, random, or gradient structures, to impose mesostructured or unstructured spacing between interactive groups. Novel polymer architectures may be able to control the mean distance between SIS nuclei in unanticipated ways. The duration of vapor exposure and the length of purge between coreactant exposures offer routes to control the distribution of the inorganic product throughout the sample. The temporal changes to the organic/inorganic film as the SIS process proceeds provides yet another axis upon which SIS can be manipulated. The first cycle introduces inorganic nuclei into the bulk, which present distinct reactive sites for subsequent cycles. The inclusion of this material also changes the free-volume pathways and the diffusivity of subsequent exposures. Thus, changing the first cycle determines how all other cycles progress. By changing the purge time in the first cycle, as an example, the density and depth of infiltration of the seeds can be changed. Finally, the co-reactant compatibility with the polymer template must be

considered as an additional challenge. For example, transient and/or reactive coreactants including ozone and nearly all plasmas may not persist deep into thick polymer films or may alter the polymer backbone and/or functional groups.

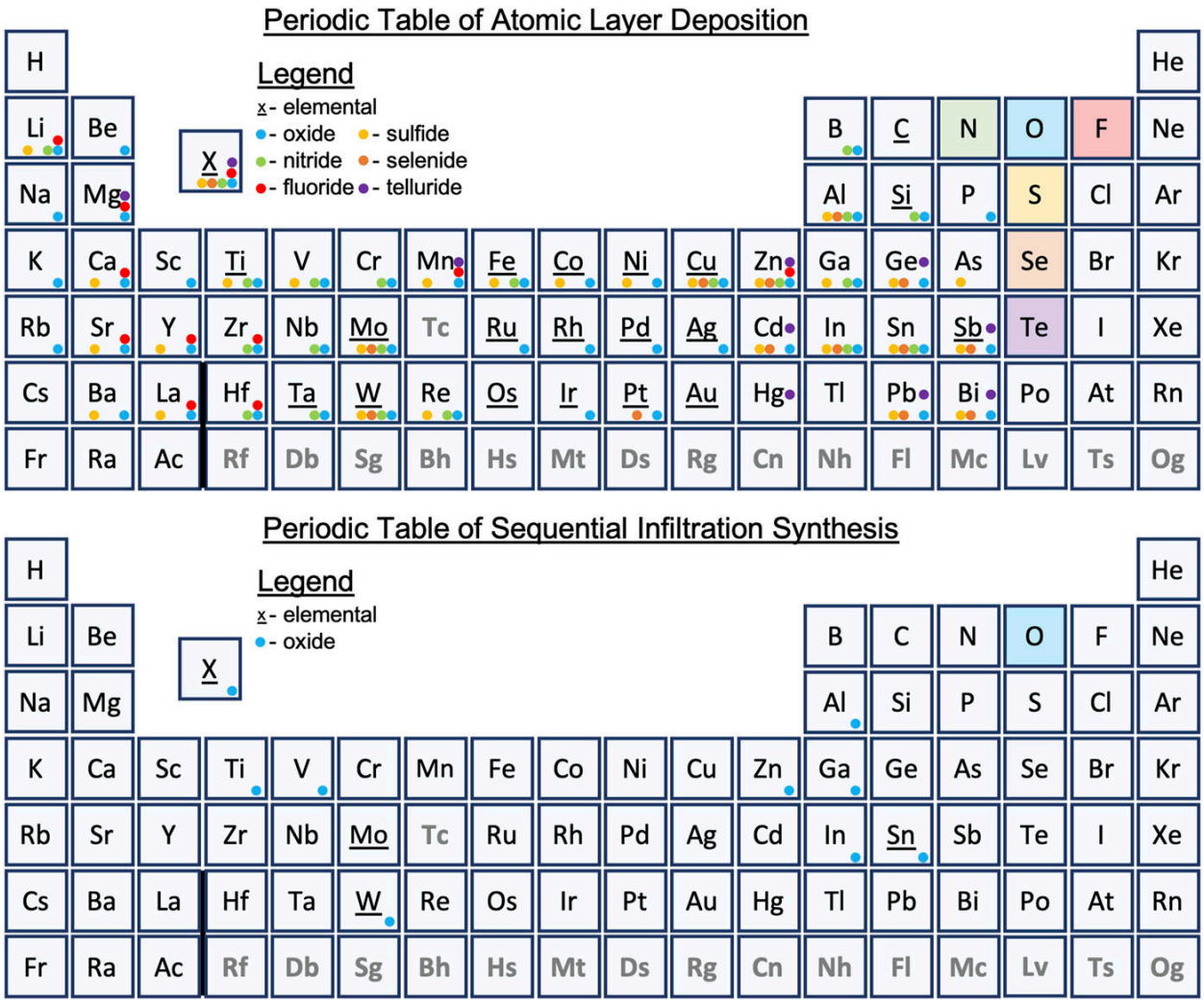

Figure 1.4: The periodic tables of (top) ALD and (bottom) SIS materials. Mo and Sn elemental SIS describe reports of single precursor molecular dopants in polymer films.

CHAPTER 2

JANUS MEMBRANES VIA DIFFUSION-CONTROLLED ATOMIC LAYER DEPOSITION

2.1 Introduction

Janus membranes are an emerging class of membrane materials engineered to have differing properties at their opposite surfaces. These membranes have generated excitement for their potential to manipulate fluid transport properties in powerful new ways. Janus membranes can improve efficiency in conventional applications; they also exhibit entirely novel phenomena useful in unconventional applications. [139] For example, unidirectional diode-like fluid flow across Janus materials has been reported. [140] This behavior is impossible to realize with homogeneous materials. The divergent surface properties of Janus membranes have found applications in a host of challenging fluid manipulations. Recently reported Janus membrane structures demonstrate applications as battery separators, [141, 142] in oil/water emulsification and de-emulsification, [143–146] in fog harvesting, [147,148] in blood plasma separation, [149] in membrane distillation/nanofiltration, [150] and in fine bubble aeration. [151]

The promise of Janus structures has been recognized by the membrane research community, leading to a wide variety of fabrication strategies described in recent reports. These can be broadly classified either as asymmetric fabrication approaches or as asymmetric decoration approaches. Asymmetric fabrication approaches involve directly constructing double layers in a stack. Examples include sequential electrospinning, [152] spray-coating of polymers and nanoparticles, [153] sequential filtration of functional nanomaterials [140, 143, 154] and casting solutions with surface-migrating additives. [155]

Asymmetric decoration approaches, in contrast, rely on the physical/chemical modification of a single side of an extant porous structure. In one class of decoration approaches, a phase interface is introduced at one membrane face, and the decoration is limited

to one side of that interface. The interface can be liquid-gas, such as in the deposition of mussel-inspired polydopamine to membrane surfaces floating in fluids. [156, 157] Alternatively, a solid-gas interface can be introduced in the form of a polymer, which physically blocks part of the membrane from modification and can then be removed by dissolution, etching, or peeling. [158, 159]

Diffusion-limited modifications are another class of asymmetric decoration approaches demonstrated in recent literature. For example, by controlling the time that cotton fabric was exposed to hydrophobic silane vapor, the extent of a hydrophobic modification could be controlled. [160] Similarly, a gradient coverage of hydroxyapatite crystallites were deposited onto PVDF membranes by pre-wetting with one reactant and allowing the second to diffuse in from one side. [149] Recently, oxygen plasma was used to hydrophilize an 18 nm depth of 8 nm diameter silica nanopores made hydrophobic by atomic layer deposition of a trimethyl-silane coating. [161] Such diffusion-mechanism approaches can, in principle, enable control over the thickness the of the Janus modification layer via direct processing conditions.

The thickness of the Janus modification layer, or the through-membrane position of the property gradient, influences the performance of the material across applications and should ideally be controlled with precision. The ratio of the thickness of each layer, along with the sharpness of the transition between the two layers, will have profound effects on fluid transport through the membrane. However, precise control of the transition interface is challenging or impossible for most fabrication approaches. In practice, for example, it can be difficult to reproduce conditions that position the fluid-gas interface adjustably within the membrane. Deposited materials, such as nanoparticles or other functional materials, may inconsistently coat the interior pore surfaces of a membrane. [162] When deposited by filtration or by sol-gel processes, nanomaterials can also constrict the pores of the underlying membrane. Depending on the interactions (e.g. electrostatic, van der Waals) between the decorating material and membrane, along with the intended application of the material,

shedding or delamination of the decoration may occur. Processes yielding well-adhered decorations with tunable extent and coverage would represent a valuable addition to the field, enabling process optimization by control of the spatial extent of the Janus decoration.

This chapter details the development of a diffusion-controlled atomic layer deposition (ALD) approach to impart a hydrophilic/superaerophobic Al_2O_3 layer onto hydrophobic polypropylene membranes. ALD is a technique commonly used in microelectronics and semiconductor fabrication in which alternating vapor pulses react on a surface to enable layer-by-layer conformal growth. [163] In such a conformal regime, ALD allows for membranes to be functionalized with metal oxides without substantially changing the pore geometry. [164,165] Oxides grown on porous materials simply constrict the pore size and introduce a roughness to the pore surfaces associated with the particular metal oxide. [166] Although ALD is typically used to produce uniform, conformal films that coat all surfaces of a substrate, the depth of infiltration into high-aspect-ratio porous materials can be tailored using controlled, sub-saturating precursor exposures. [167, 168] We use sub-saturating exposures as a means to engineer Janus membranes by limiting exposure to precursor flux to one side of the membrane.

The extent of precursor infiltration, and therefore the position of the hydrophilic-hydrophobic interface within the membrane, are tuned using the ALD precursor dose time and partial pressure, the purge time of the vapor reactants, and the number of reaction cycles. The Janus modification process is examined via scanning electron microscopy of the top surface, along with cross-sectional elemental mapping by energy dispersive spectroscopy (EDS). The depth to which dyed water is drawn into the hydrophilized membrane face by capillary rise is shown to depend on the vapor exposure dose, illustrating control of the hydrophilic/hydrophobic interface property. This diffusion-limited ALD approach to Janus membrane decoration brings together the desirable properties of conformal metal oxide coatings and controllable processing kinetics of vapor-phase reactions. The wetting properties of the Janus membranes are investigated using sessile drop contact angle tests which re-

veal a progression from initial hydrophobicity to a decrease in contact angle, followed by the onset of complete wetting and drop imbibition. Captive bubble contact angle measurements demonstrate an analogous transition from aerophilicity to superaerophobicity. We demonstrate the utility of this hydrophilic-hydrophobic Janus membrane in dramatically reducing bubble size in an aeration process relative to pristine polypropylene membranes, which can improve gas delivery in a number of industrial applications. [151] We then discuss the potential for spatially controlled Al_2O_3 surface hydroxyl groups laterally across a substrate's surface to serve as a platform for further functionalization. The introduction of diffusion-controlled ALD for Janus membranes further widens the materials space through which researchers can fabricate porous materials with spatially heterogeneous wetting properties. Beyond small molecule and polymeric modifications, inorganic metal oxides can now be simply and reproducibly integrated into Janus membranes.

2.2 Results and Discussion

2.2.1 Fabrication Process

A schematic describing the fabrication process for Janus membranes is illustrated in Figure 2.1a. Polypropylene membranes are secured in a custom-machined aluminum fixture to limit exposure of the reactant vapors to one face of the membrane (modified surface). This fixture consists of two aluminum plates. The 47 mm diameter membranes are placed between the two plates. The top plate has a machined window of customized size and shape exposing one side of the membrane, referred to as the top or modified surface. The plates are secured together to limit vapor from infiltrating between them and exposing the protected back surface. The polypropylene membranes purchased from Sterlitech Corporation are ∼160 μm-thick discs 47 mm in diameter characterized as having an average pore size of 200 nm based on their separation performance. The SEM micrograph in Figure2.1b of the membrane cross-section reveals a highly polydisperse networked and tortuous pore path morphology.

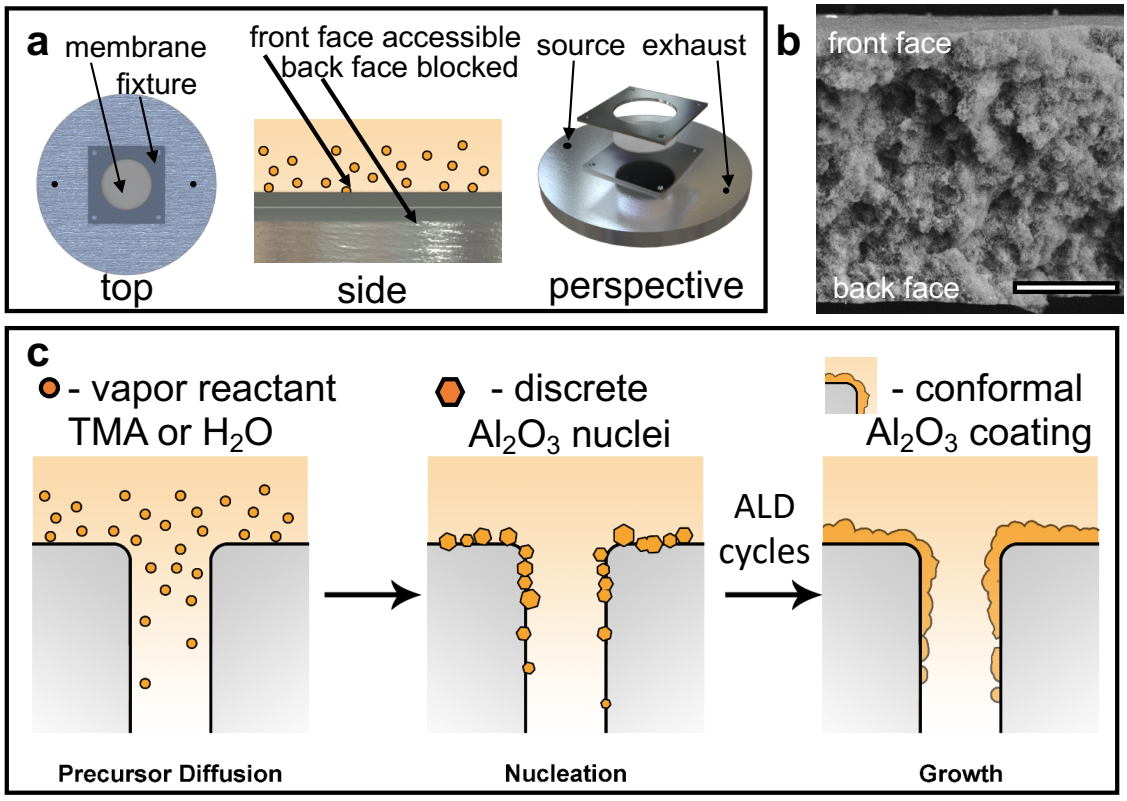

Figure 2.1: a) Schematic of the physical housing of the membrane which isolates the front face for vapor exposure. b) Cross-sectional SEM image of the polypropylene membrane shows the tortuous porous structure leading to diffusion-controlled ALD, scale is 50 μm. c) Vapor diffuses through the pore volume from the front side only. Nucleation occurs more quickly near the surface due to the greater concentration of reactants at the surface. After nucleation, growth proceeds to form a coating with decreasing coverage through the membrane.

The ALD tool is operated in flow mode, where a single cycle is composed of a trimethyl aluminum (TMA) pulse, a purge time where the vapor is exhausted, a water pulse, and a second purge. In all cases, the ALD system was held at 80 °C, and the membrane system was held at vacuum under 100 sccm of nitrogen flow for 30 minutes prior to coating to drive off adsorbed water. The nitrogen flow is then set to a continuous 20 sccm (.25 Torr) for the duration of the deposition process. Janus membranes were fabricated using .015, .06, and .15 second precursor exposures with varying purge time and number of cycles. These pulse durations result in average peak TMA partial pressures of .1, 0.45, and 0.7 Torr, respectively. The chamber is then then purged for ten seconds to remove excess TMA and product gases. The water dosing valve is then opened for the same length of time as TMA,

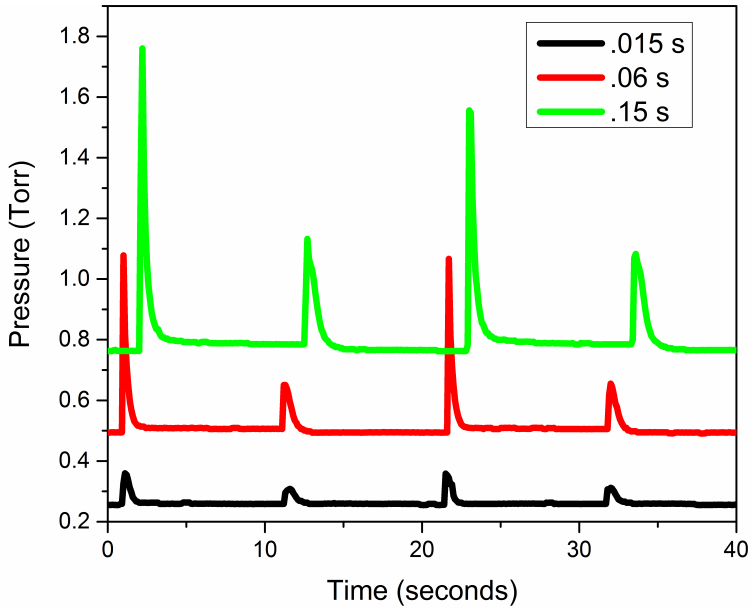

Figure 2.2: Typical ALD pressure traces showing the increased peak vapor pressure with increased dose time

yielding average peak H_2O pressures of 0.05, 0.15, and 0.35 Torr. Representative pressure traces are shown in Figure 2.2. The chamber is then purged again for ten seconds to complete one ALD cycle.

Based on traditional ALD chemistry, one would not expect Al_2O_3 to grow on purely hydrocarbon polymers like polypropylene given the absence of reactive groups. The nucleation of Al_2O_3 on such unreactive polymers has been explained resulting from physisorbed TMA in the near sub-surface of the material, which does not escape during the purge step and consequently reacts with H_2O during the subsequent H_2O exposure. [41] Given a sufficiently low coverage of physisorbed TMA, this mechanism leads to the formation of discrete Al_2O_3 islands. With increasing ALD cycles, more material can grow on these islands in three dimensions to eventually merge and form a continuous film. ALD has further been demonstrated on polypropylene films and fibers in the context of this proposed mechanism [169, 170].

ALD has been used to coat hydrophobic polymeric membranes with thin conformal inorganic metal oxides in an effort to improve their performance For example, researchers

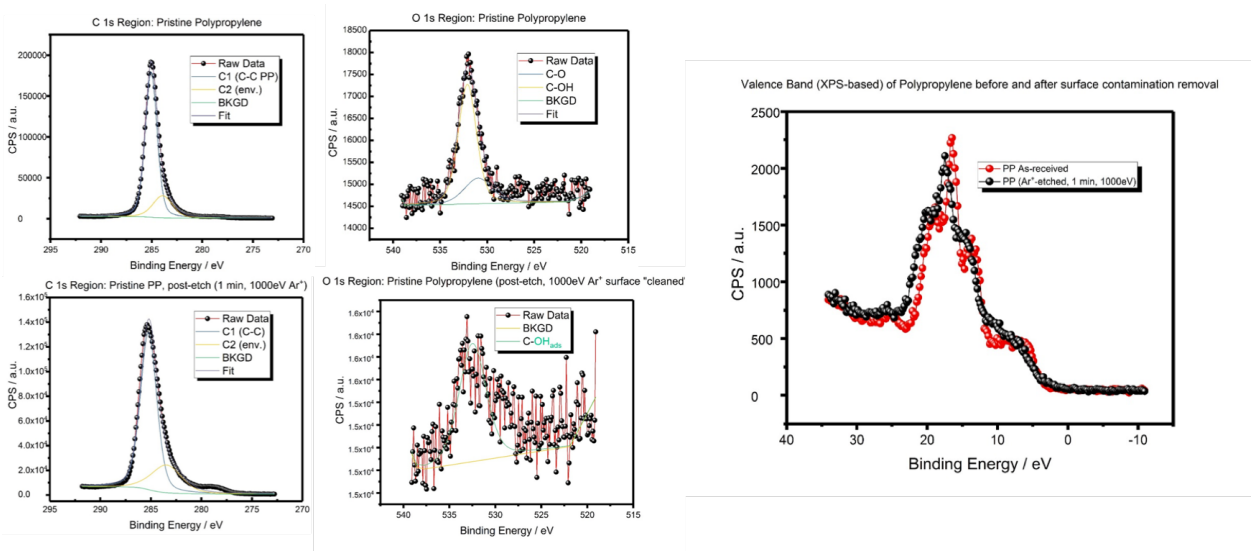

Figure 2.3: XPS data of the pristine polypropylene membranes both before and after Ar+ surface cleaning showing virtually no oxygen content.

coated 25 μm thick polypropylene membranes with conformal Al_2O_3 and TiO_2 by ALD to produce hydrophilic membranes with high flux. [171, 172] Rather than rely on physically trapped residual inorganic precursors, in these studies, reactive surface sites were introduced to the polymer via oxidative damage by submerging in nitric acid or exposing to oxygen plasma. Oxygen plasma has been shown by x-ray photoelectron spectroscopy (XPS) to incorporate oxygen-containing functional groups along polypropylene's hydrocarbon backbone. [173] These pretreatments increase the nucleation rate of Al_2O_3 ALD by creating reactive sites where TMA can chemisorb onto the polymer pore surface. [113]

Though Complete coverage of microporous polypropylene was a design goal in that previous work; here, we have utilized diffusion-limited transport of precursors through high-aspect-ratio and relatively unreactive (and unmodified) polypropylene membranes to enable an inhomogeneous coating through the membrane's thickness in order to impart Janus-like behavior. Figure 2.3 shows ultrahigh-resolution XPS measurements on the as-received pristine polypropylene membranes, which reveal a total oxygen content of 1.10 at.%. After a one minute of 1 KeV Ar+ exposure, the oxygen content is reduced to 0.46 at.%. This reduction in oxygen signal shows that some of the initial oxygen signal is due to

adsorbed species; the remainder suggests some minor C-O content throughout the polymer, presumably the result of impurities or defects in the polymer chains. These sparse moieties present sites by which TMA could potentially directly associate with the polymer to form a covalent linkage, in addition to any non-reacted physisorbed TMA that leads to scattered and slow nucleation.

In order to understand why the processes used in this study does not produce a uniform conformal coating through the entire membrane thickness, one must examine the length scales and morphology of the system. The high aspect ratio, small pore size, and high tortuosity of the polypropylene membranes lead to this asymmetric deposition, with a high density of Al_2O_3 at the exposed surface that decreases through the thickness of the membrane. The mean free path, $\bar{l}$, of the ALD reactant vapors is described by equation 2.1:

$$\bar{l} = \frac{kT}{\sqrt{2}\pi P d_m^2} \tag{2.1}$$

In this expression, P is the precursor partial pressure and d_m is the kinetic diameter of the gas molecule. Under typical ALD conditions the mean free path is generally on the micron scale. For example, the value of TMA at 1 Torr and 450 K is 40 μm. [168] The polypropylene membranes used in these studies have an average pore size of 200 nm, a thickness of ≈160 μm, and a highly tortuous networked pore structure. Ignoring the tortuosity of the porous pathways, the aspect ratio (L/d) of the membrane is ≈800. Since the mean free path far exceeds the average membrane pore diameter ($\bar{l}$/d $\sim 10^3$), the transport of these precursors is described by molecular or Knudsen diffusion. In Knudsen diffusion, the vapor molecules scatter against the pore walls with far greater frequency than with other vapor molecules. Figure 2.1c shows a schematic of how Al_2O_3 nucleates and grows to yield a Janus structure in the Kudsen regime.

2.2.2 Analysis of Janus Fabrication

To demonstrate the Janus character of membranes treated with diffusion-controlled ALD process, drops of water were placed onto both surfaces of a membrane prepared with 350 ALD Al_2O_3 cycles at 0.015 s precursor exposures and 10 s purges. Figure 2.4 shows the hydrophobic character of the unmodified back face of the membrane in contrast with the hydrophilic front surface. SEM images of the two faces reveal that the modified face is conformally coated with a granular deposit whereas the unmodified face shows polymer surfaces which are smooth and featureless. Lastly, elemental analysis by EDS reveals strong aluminum and oxygen peaks on the front surface. The back face of the membrane shows virtually no signal from either aluminum or oxygen, confirming the asymmetry of the ALD growth.

The influence of precursor exposure and cycle number on the resulting Al_2O_3 coating was examined. Figure 2.5 shows top-down SEM images of the Al_2O_3-modified Janus surfaces prepared at various precursor exposures and number of cycles. After 150 cycles, sparse spherical clusters of Al_2O_3 are observed. These clusters appear as bright spheres on the smooth polypropylene membrane surface which has a dark contrast in the SEM images. With increasing reactant exposures, these nuclei grow larger and much more closely spaced. By 200 cycles, the 0.06 s exposure sample is covered with discrete nuclei, whereas the 0.15 s sample has formed a nearly continuous coating. By 300 cycles, ALD Al_2O_3 films appear continuous across exposure times. The thickness of the ALD Al_2O_3 appears to increase with increasing precursor exposure, as evidenced by the polymer ligaments growing in thickness. This behavior results from faster nucleation using larger precursor exposures. Importantly, this functionalization conforms to the membrane pore geometry while introducing a roughness on the scale of the Al_2O_3 nuclei. The average pore size in the Al_2O_3-functionalized region is also constricted to an extent dependent on the processing.

Modeling of diffusion and self-limited reactions in nanoporous substrates has shown that the coverage and transport are strongly influenced by α, a dimensionless parameter rep-

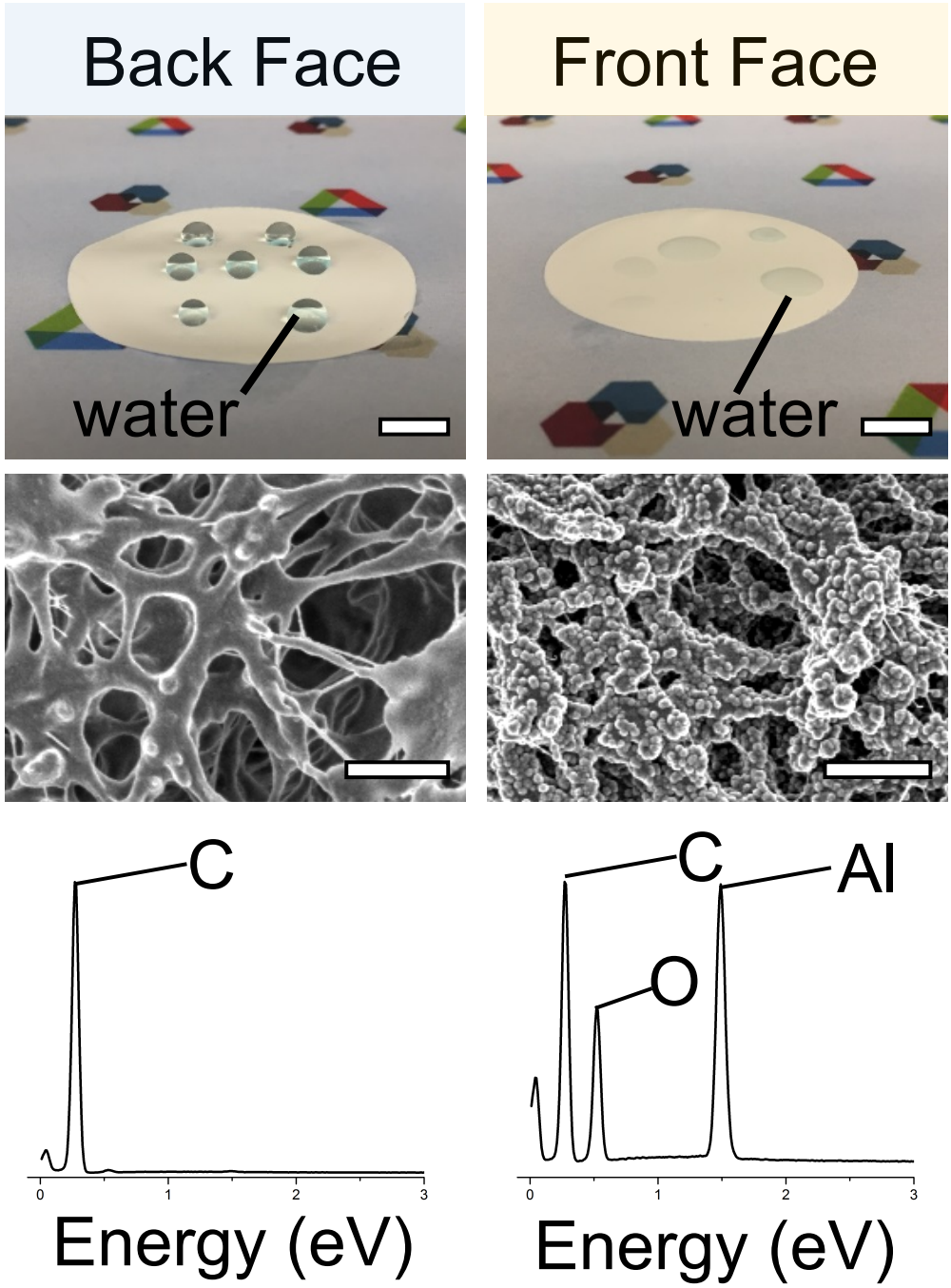

Figure 2.4: Back face and front face of a Janus membrane. The back face is hydrophobic, appears bare in SEM, and shows virtually no EDS signal for oxygen or aluminum. In contrast, water spreads on the hydrophilic front face, the membrane is covered with Al_2O_3 in SEM, and shows substantial oxygen and aluminum in EDS. Scale bars are 5 mm and 200 nm, respectively.

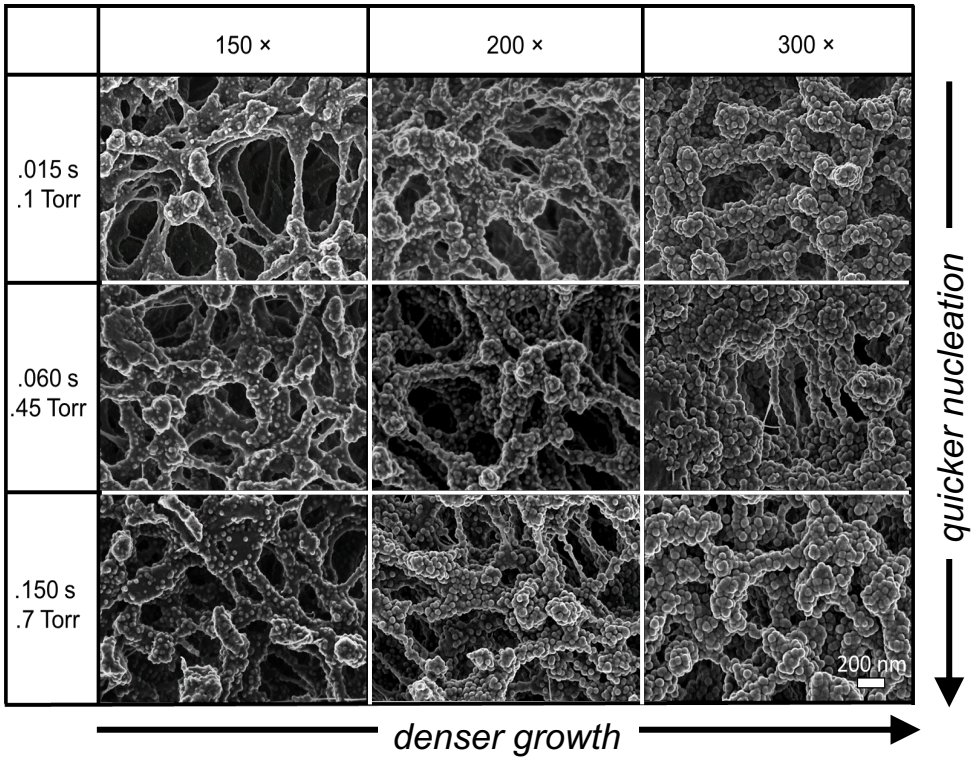

Figure 2.5: Surface SEM images of Janus membrane front faces grown with 150, 200, and 300 cycles at 0.015, 0.06, and 0.15 s exposures, respectively. A general trend of quicker nucleation and following onset of conformal growth is observed at higher exposure doses and more cycles.

resenting the ratio of reaction rate to diffusion rate inside the nanopores. [123] In cases where the ALD precursors are supplied from one side of a porous substrate, and the exposures are insufficient to coat all of the available sites, then values of $\alpha \gtrsim 100$ yield stepped coverage profiles where the outer regions become saturated and the inner regions remain bare. In contrast, $\alpha \lesssim 10$ produces uniform, low coverage throughout the pores. Under the assumptions of Knudsen diffusion and circular pores, $\alpha = 3/2AR^2\beta_0$ where AR is the aspect ratio (pore length/pore diameter) and β_0 is the initial sticking coefficient of the precursor molecule on the pore surface. For a given geometry, the value of α, and hence the shape of the resultant coverage profile, will vary depending on the reactive sticking coefficient on the porous material; a high reaction probability can yield a stepped profile whereas a low reaction probability causes uniform, or gradually sloping low coverage, in otherwise identical porous networks.

With these principles in mind, we performed EDS measurements of the Al signals of Janus membranes to assess the extent of Al_2O_3 penetration through the membranes. Figure 2.6a shows an EDS Al signal map for one of the Janus membranes in cross section superimposed on the corresponding SEM image. It is evident that the Al concentration is higher on the modified surface side of the membrane. Figure 2.6b-d shows depth profiles derived from the EDS Al signal from precursor exposures of 0.015, 0.06, and 0.15 s, respectively, for increasing cycle number. In all cases, the Al concentration is highest at the pore entrance and decreases with depth into the membrane, and the extent of infiltration increases with increasing exposure. Moreover, the magnitude of the Al signals increases with increasing Al_2O_3 ALD cycles.

The EDS line scans in Figure 2.6 exhibit two distinct regimes as a function of ALD cycles. At low cycle numbers (150 cycles), the profiles are fairly flat and show only a small gradual decrease in concentration with depth into the membrane. Above ≈300 cycles, however, the EDS profiles exhibit a step-like profile where the coverage is much higher at the pore entrance than deeper in the pore. Once this transition occurs, the profile shapes do not change much with increasing ALD cycles other than to increase the overall signal intensity.

In addition, all of the profiles at a given exposure converge deep within the membrane, so that all of the curves are essentially superimposed. The data also exhibit a region near the pore entrance where the coverage profile becomes qualitatively linear, as indicated by the shaded bars above Figure 2.6b-d.

These two regimes can be explained by a gradient in TMA reactivity along the pores that sets up in the low cycle limit. The polypropylene membranes have an AR of $\approx$ 800 (neglecting tortuosity), and for the reaction of TMA on Al_2O_3 surfaces, $\beta_0 \approx 10^{-2}$ so $\alpha \approx 10^4$. Consequently, the stepped coverage profiles are expected once the ALD Al_2O_3 nuclei coalesce and form a closed and continuous film on the polypropylene pore surfaces. The gradual coverage profiles for the initial cycles suggest $\alpha < 10$, so that $\beta_0 > 10^{-5}$. This supports the assumption indicative of an extremely sticking coefficient and reaction rate for TMA on pristine polypropylene. Once the Al_2O_3 nuclei grow to sufficient size at the pore entrance, the much higher reaction rate for TMA on Al_2O_3 dominates the slow diffusion into high AR pores, and all of the TMA is consumed at the pore entrance. Thus, the reactivity gradient persists throughout the coating process, and the Al concentration deep in the pores no longer increases.

We performed additional experiments to correlate the depth of the ALD Al_2O_3 deposition into the membranes with the depth to which wetting behavior is modified. We prepared Janus membranes using 350 ALD cycles using precursor exposures of 0.015, 0.03, 0.06, and 0.15 s and 10 s purges. The modified surfaces of these membranes were placed in contact with a solution of blue dye for 1 hr to allow for capillary action to wick the solution into the membrane porosity. The membranes were rinsed and dried thoroughly, prepared in cross section, and examined by optical microscopy as shown in Figure 2.6e. With increasing precursor exposure, the position of the dye interface moved deeper into the membrane. At the lowest exposure of 0.015 s, the solution was imbibed $\sim$4 μm into the membrane. At the highest exposure of 0.15 s, the solution was imbibed $\sim$16 μm into the membrane. The increased depth of the dye front by capillary rise shows that the position of internal Janus

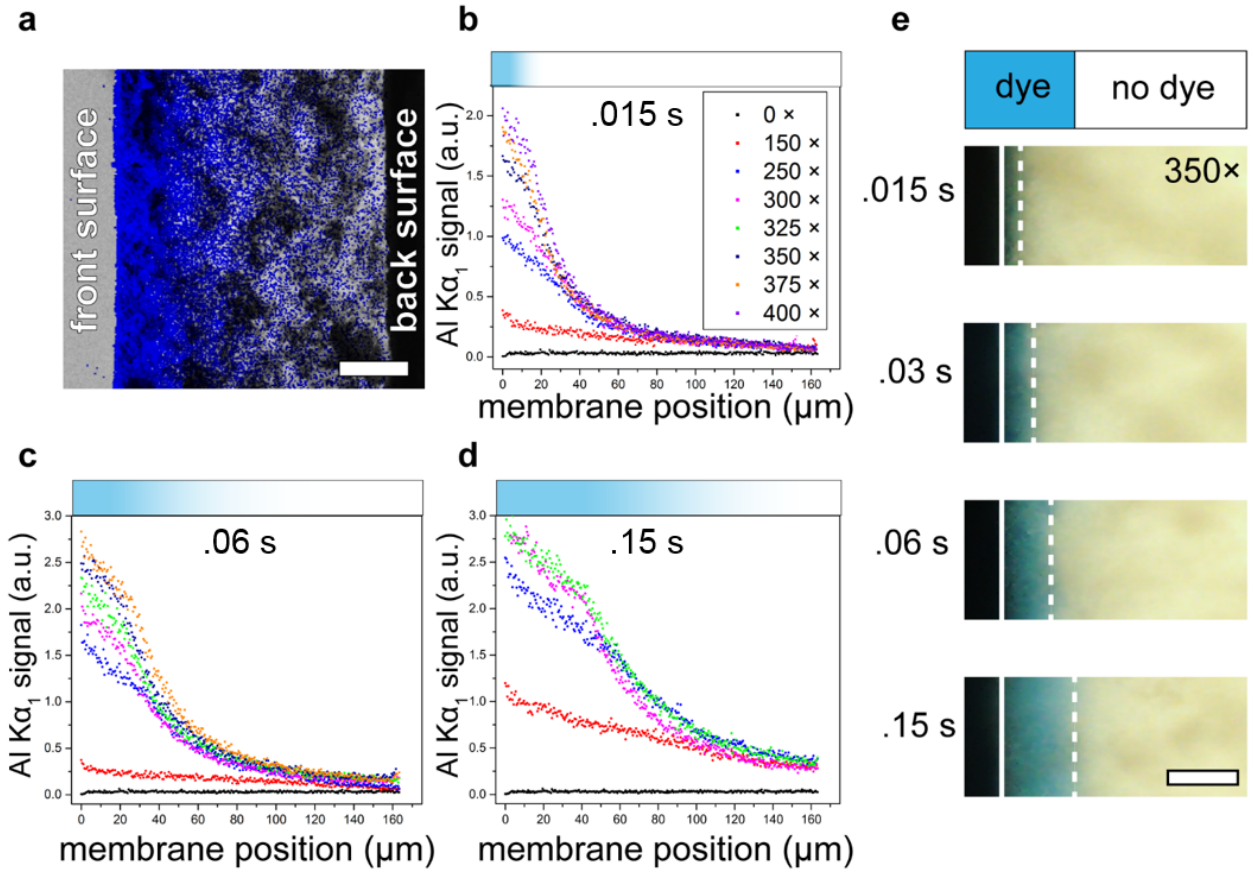

Figure 2.6: a) Cross-sectional SEM image of a Janus-modified PP membrane with overlaid EDS map showing the distribution of aluminum within the membrane. A gradient is apparent. b–d) Cross-sectional EDS measurements (binned parallel to the membrane surface) showing Al_2O_3 distribution as a function of the number of ALD cycles under different precursor exposure times per cycle (0.015, 0.06, and 0.15 s, respectively). Gradient bars above the plots are meant to guide the eye to the two different regimes through the thickness of the membranes, with a denser region near the exposed surface, and a rapid drop off in metal oxide growth further down. e) Dye imbibition into 350 cycle Janus membranes fabricated at different exposure pressures reveals a trend whereby water rises deeper into the membrane porosity with increasing pressure; scale bar is 15 μm.

interface can be tuned. We note that this capillary height represents an indirect measure of the position of the internal Janus interface. Capillary height as probed in this experiment is a function of both the changing geometry of the pore volume, which shrinks at the surface due to pore constriction, and the heterogeneous surface energy of the pore walls as the material transitions from hydrophilic oxide to hydrophobic polypropylene with depth.

2.2.3 Water Contact Angle Measurements

To study the evolution of the modified membrane surface wetting properties, contact angle measurements were conducted at different ALD cycle numbers and precursor exposures. These measurements were conducted as soon as possible after removal from the ALD chamber, to limit the influence of environmental residue adsorption. Contact angles were recorded as the first stable frame after bringing a 1.0 μL drop into contact with the membrane surface. The plotted contact angle values are the average of at least seven drops per membrane, and there was no significant variation observed in any direction along the exposed, functionalized face. Figure 2.7 shows that by increasing the number of ALD cycles, the apparent contact angle of the functionalized surface decreases gradually over the initial 250 cycles, and then drops rapidly with increasing cycles. The onset of hydrophilicity occurs at a lower number of cycles as the exposure dose is increased. This follows from the more rapid onset of nucleation and growth with higher exposure dose observed in surface SEM. The back side of the membrane exhibited a contact angle of over 130° on all membranes, demonstrating a marked Janus property.

The wetting behavior on these porous substrates is an indirect measure of the surface energy due to the porosity and roughness of the membranes. Though the initial contact angle decreased with total cycle number for each of the tested precursor exposure levels in a similar fashion, drop imbibition into the porosity of the membrane differed. At 0.015 s, no complete imbibition was observed even at the highest cycle number tested. At 0.06 s, complete imbibition began at 375 cycles, and at 0.15 s complete imbibition began at 325 cycles.

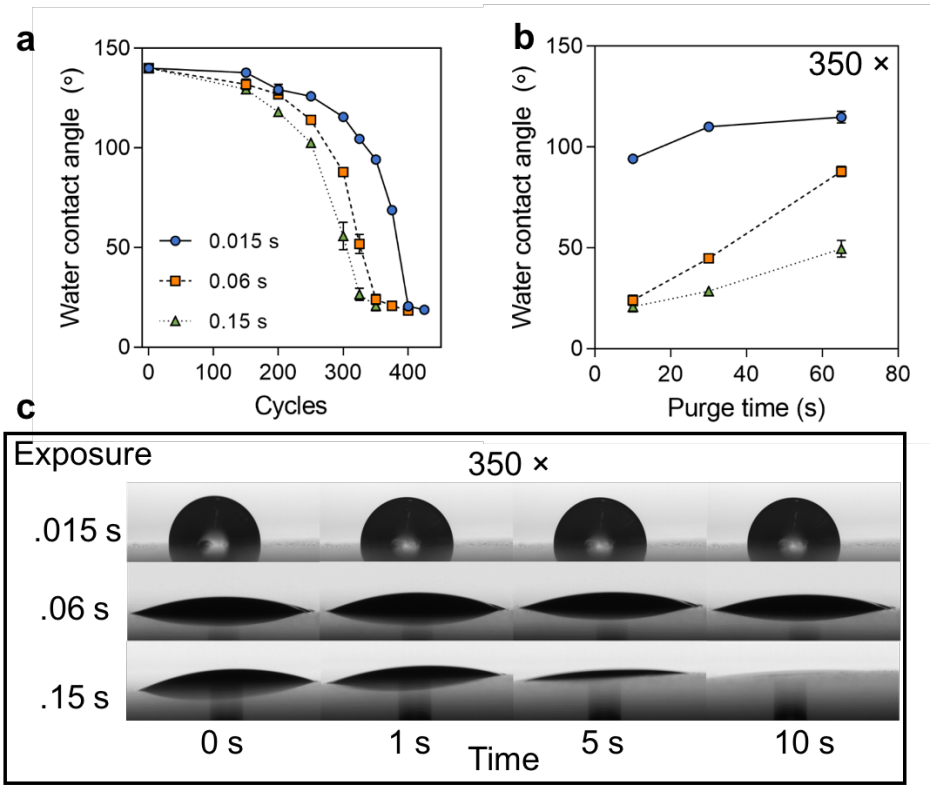

Figure 2.7: a) Contant angle as a function of vapor exposure duration and number of ALD cycles. Hydrophilicity onset after ∼200 cycles occurs sooner at higher exposure doses. b) Contact angle as a function of purge time for 350 cycle membranes across vapor exposures. A decrease in hydrophilicity gain per cycle with greater purge time is observed across vapor exposures. c) Drop imbibition across vapor pressures at 350 cycles as a function of time. Significant drop wicking is observed at 350 cycles only at the longest 0.15 s vapor exposure

The transition from drop spreading on the hydrophilized surface to significant imbibition by the functionalized surface may be thought of as a transition between a Cassie–Baxter state to a Wenzel state. [174] In the Cassie–Baxter state, the rough pore surface stabilizes a suspended air–water interface. As the number of cycles is increased, the surface area fraction of Al_2O_3 increases, along with the roughness and extent of Al_2O_3 coverage. This has the effect of slightly shrinking the pore size as well. A convolution of all of these chemical and structural factors destabilizes the air–water interface at the pore surface, and the water begins to preferentially wick into the pore interior.

To probe the influence of purge time on wettability, Janus membranes were fabricated using 350 ALD Al_2O_3 cycles with precursor exposures of 0.015, 0.06, 0.15 s and purge

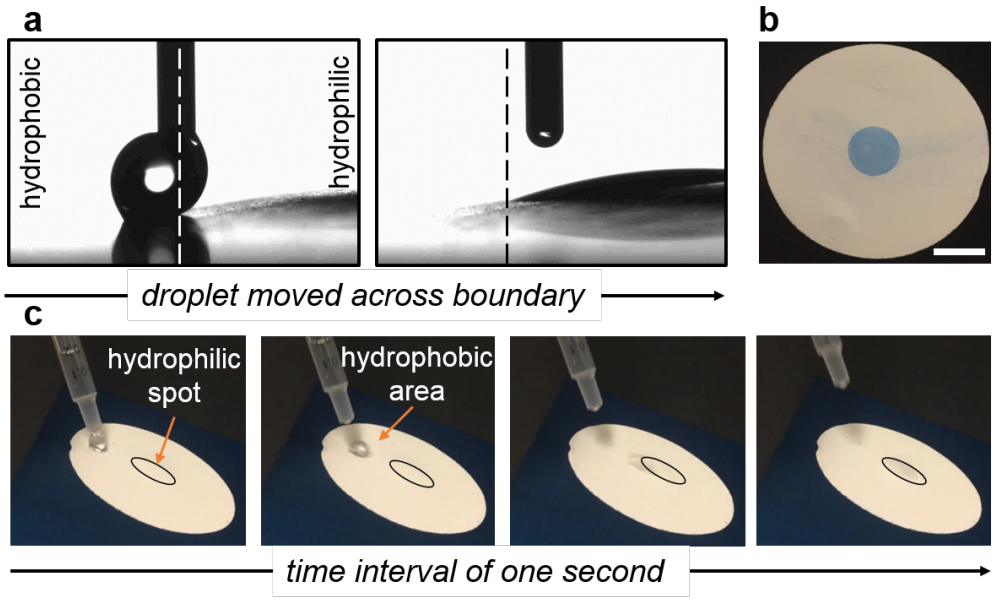

Figure 2.8: a) Water drop brought into contact with the unmodified hydrophobic membrane surface is manipulated laterally with the needle to the ALD-modified region, at which point the water droplet rapidly spreads and is imbibed by the hydrophilized membrane. b) Staining with blue dye reveals the boundary of the Janus modification, scale bar is 10 mm. c) A water droplet deposited on an inclined patterned Janus membrane rolls on the unmodified hydrophobic region only to be immobilized on the 10 mm Janus-modified region.

times of 10, 30, and 65 s. As shown in Figure 2.7b, the average contact angles measured for these membranes increased with increasing purge time, indicating a decrease in wettability. We hypothesize that the longer purge times allow the TMA physisorbed into the polypropylene surface to desorb, which reduces the rate of Al_2O_3 nucleation.

2.2.4 Lateral Patterning of Janus Membranes

Physical masking of the membrane via a fixture can be used to limit vapor exposure and create spatially patterned hydrophilic/hydrophobic regions on the front face of a membrane. Figure 2.8a shows a water droplet deposited on the shielded hydrophobic region of the front face of a Janus membrane (400 cycles, 0.015 s exposures, 10 s purges) and dragged onto the hydrophilic region. The drop abruptly spread and was imbibed as soon as the leading edge came into contact with the Al_2O_3-functionalized surface. The ability to laterally

pattern the modification is further demonstrated in Figure 2.8b, in which the membrane was submerged in a blue dye solution. In this instance, the membrane was set in a fixture that only exposed a central 10 mm diameter region of the membrane to the precursor flux. This mask faithfully templated a hydrophilic region of the membrane to the exposed area only. Lastly, in Figure 2.8c, another Janus membrane with the same 10 mm modified spot was placed on a 30° inclined plane and water was dropped onto the surface Water droplets rolled down the unmodified, hydrophobic polypropylene but were abruptly stopped and imbibed by the hydrophilized spot.

Beyond the direct utility of the functionalized Al_2O_3 surface for its wetting properties, the spatially modified Al_2O_3 surface can be used as a platform to further modify one side of the membrane with molecules that preferentially graft onto the Al-OH hydroxyl groups created by the Al_2O_3 ALD. For example, porous polyurethane foams were modified with sequential infiltration synthesis of Al_2O_3, which served to activate the surface for the subsequent grafting of superoleophilic molecules to enable high-capacity, reusable crude oil sorbents. [63] The processes described in this paper can therefore introduce spatially resolved reactive surface sites on otherwise unreactive polymer membranes for further functionalization.

These spatially resolved hydrophilic zones imply possible paper microfluidic applications for ALD-derived Janus membranes. Paper microfluidics are an expansive research area in which fluids are passively transported through hydrophilic porous materials such as cellulose through channels defined by hydrophobic modifications. [175] These hydrophobic modifications are applied by direct printing techniques, and recently by masked vapor deposition of hydrophobic silanes. [176] The hydrophilic cellulose hydroxyl groups can serve as binding sites for a host of functional molecules that react with species in fluids of interest for applications in sensing and diagnostics. In the ALD-derived Janus membranes described here, the tone of the modification is inverted, such that exposed areas become the hydrophilic zones for fluid manipulations with the hydrophobic membrane forming channel walls.

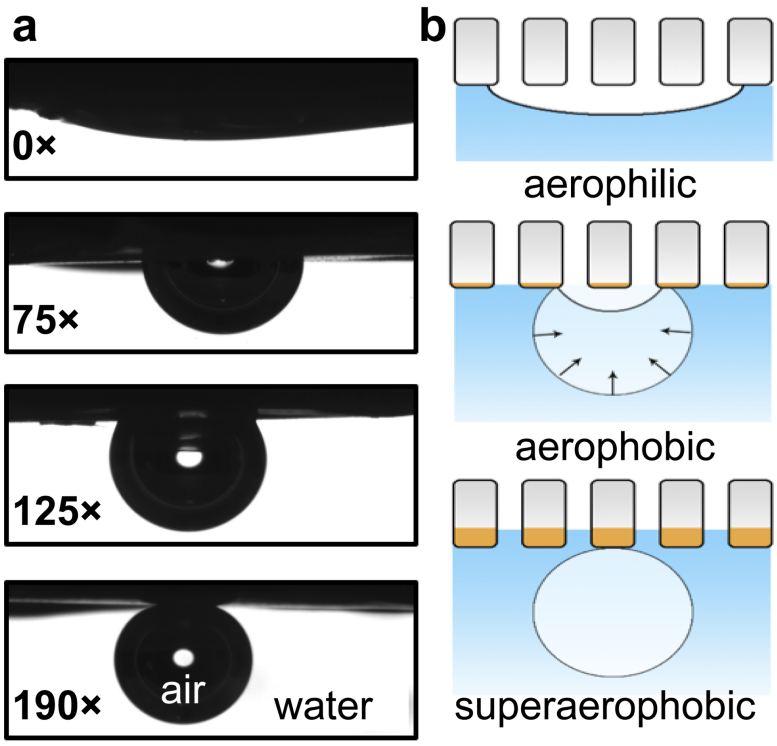

Figure 2.9: a) Captive bubble measurements on Janus membranes fabricated with an increasing number of cycles at 0.015 s vapor exposure. With increasing cycles, the membranes become more aerophobic. The membrane transitions to superaerophobicity in the vicinity of 190 cycles. b) Representations of the membrane/water/air interface. The pristine polypropylene is aerophilic and the air bubble spreads with very low contact angle. At more moderate cycle numbers the membrane is aerophobic; the bubble adheres to the membrane surface. Once the membrane is superaerophobic, the bubble does not adhere to the surface.

2.2.5 Underwater Air Contact Angle Measurements

The gas contact angle of the membranes was next measured to assess air adhesion as a function of the Janus modification. Distilled water was used as the fluid medium, and air bubbles were brought into contact with the modified surface, which was affixed to a glass slide to ensure complete submersion. The membranes were prewetted with ethanol to mitigate the impact of air trapped in aerophilic/hydrophobic samples.

Figure 2.9a shows the underwater–air contact angle of membranes modified with 0–190 ALD Al_2O_3 cycles using 0.015 s precursor exposures. The pristine membrane shows complete spreading of the air bubble. Much as in the case of the water contact angle

measurements, the membrane became more aerophobic with increasing numbers of ALD cycles. The air bubble contact angle reached ≈90° with only 75 ALD cycles and 120° with 125 ALD cycles. A high contact angle exceeding 140° was observed beyond 175 ALD cycles. An apparent transition in air adhesion was observed in the vicinity of 190 ALD cycles. Below this threshold, the bubble exhibited an extremely high contact angle but was pinned in place at its contact line. An air bubble pinned to the syringe tip used to deliver the air could be coaxed onto the membrane by making contact. This immobilized air bubble gradually shrinks as it is imbibed into the membrane.

Above this threshold, the bubble was extremely mobile on the surface. An air bubble pinned to the syringe tip could not be coaxed onto the membrane surface, even when pushed against the modified surface. The bubble had to be released from the syringe to observe the mobile sliding behavior. The membrane surface is described as transitioning from aerophobic to superaerophobic in nature. The superaerophobic phenomena emerge from the hydrophilicity of the Al_2O_3 in combination with the hierarchical roughness of the polypropylene's tortuous porosity and the roughness of the deposited Al_2O_3. [177] This is illustrated in Figure 2.9b. We hypothesize that the aerophobic condition observed below 190 cycles occurs when the air interface encounters a heterogeneous membrane surface composed of discrete Al_2O_3 nuclei and some remaining polypropylene. The presence of the hydrophilic nuclei gives rise to the apparent aerophobic contact angles. The pinning behavior emerges as a combination of the heterogeneous surface energy of the hybrid polymer/metal oxide surface and the roughness at the length scale of membrane pore features and Al_2O_3 roughness. Above the threshold of superaerophobicity, the air bubble contacts a sufficiently conformal Al_2O_3 surface with sufficient coverage that it cannot pin on the surface, and instead slides easily. Below the superaerophobic threshold, there is a net Laplace pressure pointing upward on the droplet due to the contact line. [140] This forces the bubble through the aerophobic Al_2O_3 into the hydrophobic/aerophilic bulk of the membrane. However, once the surface becomes superaerophobic to the point where the air bubble interface does not form a contact

line with the membrane surface, there is no net pressure to drive this air transport.

2.2.6 Fine Bubble Aeration

As a demonstration of the utility of the ALD-derived Janus membranes, aeration experiments were conducted on a pristine polypropylene membrane and a Janus membrane (300 cycles, 0.015 s exposures, and 10 s purges). The experiment utilized a custom bubbler (Figure 2.10b) in which gas flowed through the membrane into a water column. Aeration is a critical dispersion process for the transfer of gases to dissolve into liquids and is widely used in industrial chemical synthesis, aquaculture, CO_2 capture, [178] and wastewater treatment. [179] The dissolution rate of gases into the liquid is enhanced by shrinking the size of the bubbles - a fact based on surface area–volume scaling. At the same flow rate, there is far more surface area for gas diffusion if the gas volume is distributed over many bubbles. As an ancillary effect, the duration of the bubble residence in the liquid increases as the bubble shrinks. [180] The rate of the bubble's rise through a liquid due to buoyancy can be given by Stokes' equation in Equation 2.2

$$\nu = \frac{\Delta\rho_{lg}}{18\mu} g d^2 \tag{2.2}$$

Here ν is the velocity of the bubble upward, $\Delta\rho_l g$ is the density difference between the liquid and gas, μ is the viscosity of the liquid, g is the acceleration of gravity, and d is the diameter of the bubble.

In an aeration process, gas is forced through the membrane and gathers in bubbles, which eventually release from the surface. Bubble release occurs when the buoyant force of the forming air bubble exceeds the adhesion force between the bubble and membrane surface. Minimizing the adhesion will therefore lower the minimum bubble size that can be released. Though hydrophilic surfaces may seem ideal in this sense, a completely wetting membrane will require a significant pressure to displace the water from the pore

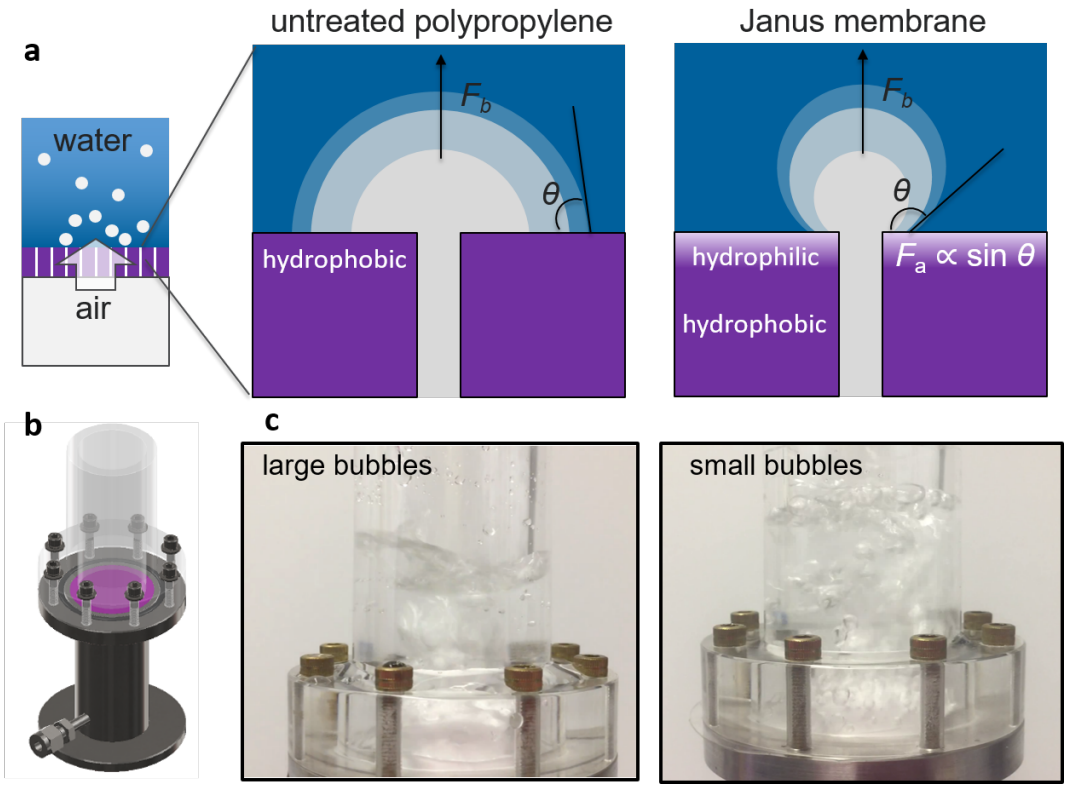

Figure 2.10: a) Graphical representation of the aeration process. In the hydrophobic, untreated membrane, the bubble spreads as a film on the surface leading to large bubbles. The Janus membrane has a superaerophobic surface, which minimizes the adhesion between the membrane surface and the bubble, leading to fine-bubble aeration. b) Design image of the custom-built aeration apparatus. c) Still images extracted from videos of aeration using a pristine polypropylene membrane and a Janus membrane prepared with 300 cycles at 0.015 s vapor exposure. The large bubbles emerging from the unmodified surface contrast dramatically with the millimeter-scale bubbles that release from the Janus surface.

interiors. A Janus membrane with a thin hydrophilic skin layer is therefore ideal, as the site of poor gas adhesion is limited to the near-immediate surface and the pressure loss across the thickness of the membrane is minimized. The adhesion can be further minimized by superaerophobicity deriving from the structural roughness of the material. [181] The illustration in Figure 2.10b demonstrates the difference between the hydrophobic unmodified membrane and the modified Janus membrane. In the case of the unmodified membrane, the air spreads over the polypropylene surface as a film and is released in large bubbles. In the case of the superaerophobic membrane, the bubbles are much smaller and release individually. The adhesion force of the bubble to the membrane surface is related to the area in contact with the membrane and is therefore proportional to $\sin(\theta)$. Aeration performed at a pressure of 1 psi on the pristine membrane and a Janus membrane prepared with 300 cycles of ALD at 0.015 s vapor exposure show the drastic difference in aeration, Figure 2.10c.

2.3 Conclusion

In summary, we have demonstrated the first asymmetric decoration technique to form Janus membranes via atomic layer deposition. A hydrophilic Al_2O_3 wetting layer is grown on hydrophobic porous polypropylene to form Janus membranes. ALD processing parameters were shown to precisely control the density and depth of coverage of the covalent and conformal Al_2O_3 functionalization. This depth-controlled modification is a result of the sub-saturating precursor exposure confined to only one side of the membrane, and diffusion-limited transport of ALD vapors through the high-aspect-ratio pores. Using precise control of precursor exposure, purge time, and number of ALD cycles, contact angle measurements demonstrated an onset of wetting and hydrophilicity of the exposed surface across a range of conditions. Physical masking also enables sharp "lateral" hydrophilic/hydrophobic interfaces along the membrane face. We have used cross-sectional EDS mapping to show that the extent of the Al_2O_3 pushes deeper into the membrane with increasing vapor pressures. We propose a mechanism by which after relatively slow nucleation of Al_2O_3 islands over the first 150-200

cycles, growth proceeds rapidly on nucleated Al_2O_3 leading to a rapid onset of hydrophilicity and a hydrophilic/hydrophobic interface within the membrane interior.

To show the utility of this asymmetric ALD technique in controlling the interfacial properties of microporous membranes, we demonstrate that these Janus membranes can dramatically reduce the size of pressurized air bubbles released into a column of water in an aeration experiment. Thus, this ALD approach offers the ability to make a controlled hydrophilic/hydrophobic interface within microporous membrane materials. The convenient surface-terminated hydroxyl groups that make Al_2O_3 hydrophilic also present a convenient linkage site for macromolecular grafting or subsequent ALD with other functional oxides. Future researchers can employ this diffusion-limited ALD technique to facilitate both in-plane and depth control of functionalizations in porous materials across many applications.

2.4 Materials and Methods

Atomic Layer Deposition: Polypropylene membranes were purchased from Sterlitech Corporation. The purchased membranes were 47 mm in diameter and rated as having a 200 nm pore size and a thickness of ≈160 μm. These were stored in a vacuum desiccator to limit adsorbed contaminants. The Janus modification to these membranes was conducted in an Ultratech Savannah Atomic Layer Deposition Chamber. To ensure isolation of the reactant gases to one surface of the membrane, the polypropylene material was placed between two aluminum plates, with the top plate having holes of varying sizes bored through it. All ALD treatments were conducted at 80 °C.

Contact Angle Measurements: Contact angle measurements were performed on a dataphysics OCA 25 Contact Angle Measurement system. Distilled water was used as the drop fluid, and a 1.0 μL drop size was used in all experiments. Contact angle images were processed and analyzed using dataphysics SCA20 software module. Contact angle was measured from the first stable frame with a stationary contact line as drops spread and were partially imbibed. Captive bubble measurements were conducted in a glass cuvette filled with

distilled water using a J-shaped syringe to deliver air. A 0.05 wt.% solution of Coomassie Blue dye purchased from Sigma Aldrich used for visualizing membrane hydrophilization.

Scanning Electron Microscopy: The surfaces of the Janus membranes were imaged using Carl Zeiss Merlin field-emission scanning electronic microscopy with an acceleration voltage of 1 keV and a typical working distance of 2 mm. Samples were affixed to stubs using copper tape and sputter-coated with 6 nm of carbon to mitigate charging.

Energy Dispersive Spectroscopy: Samples were prepared in cross section by submersion into liquid nitrogen for 1 min and then cracking along a notch prepared by a razor blade. The cleaved edge of the broken membrane was adhered to the vertical edge of a SEM sample stub using copper tape such that the Janus-modified side faced away from the sample stub. The membrane's broken edge was aligned to be flush with the lip of the stub wall. The sample was coated with 12 nm of carbon to mitigate charging. EDS measurements were conducted on a TESCAN LYRA3 field-emission scanning electron microscope with an accelerating voltage of 10 keV and a working distance of 9 mm. EDS map spectra were collected using two Oxford Instruments X-Max^{N} detectors and analyzed using the AZtec software package. The EDS X-ray signal centered at 1.486 keV corresponding to the aluminum Kα_1 peak was mapped across the membrane cross section to generate a bit-map image of the signal intensity. Mapping scans were taken at an image magnification of 1000$\times$ and at a 512 pixel resolution. The energy range and channel number were set to auto, and a process time of 4 μs and a pixel dwell of 50 μs were used. The mapping scan data were binned along the axis parallel to the membrane to generate 2D plots of Al density vs. position in the membrane.

X-Ray Photoelectron Spectroscopy: XPS measurements were carried out on a Thermo Scientific K-Alpha+ spectrometer using a microfocused monochromatic Al Kα (1487 eV) X-ray source with a spot size of 400 μm. Samples were mounted on the instrument's standard stage and affixed to copper tape to help dissipate charging from the insulating (polymeric) samples. Additionally, a dual-beam electron flood gun (ultralow energy coaxial

electron and Ar+ ion beam) was used for charge compensation during all surface analysis. The instrument uses a 128-channel 180° double-focusing analyzer and energy ranges of 0-1350 eV were swept for low-resolution surveys. High-resolution regions of interest (C1s, O1s) were windowed off at the relevant binding energy range for the acquisitions. Mounted samples were evacuated on the sample stage mount in an isolated load-lock chamber until a base pressure of 3×10^{-7} Torr or lower was achieved and were then transferred via a pneumatic transfer manipulator arm to the analysis chamber. Operational pressures in the analysis chamber prior to analysis were typically (1-4) $\times 10^{-9}$ Torr and (2-4) $\times 10^{-7}$ Torr with the e-flood gun on during surface analysis. Autofiring titanium sublimation pump (TSP) filaments and e-flood gun filaments were degassed prior to analysis. Processing of the spectra was performed in Thermo Avantage (v. 5.977, Build 06436) postprocessing software and, if necessary, charge correction of each spectrum was applied by referencing to the adventitious C1s peak arising at 284.8 eV. Peak deconvolution of the high-resolution spectra (C1s, O1s) was performed using the Powell fitting algorithm with mixed Gaussian–Lorentzian (≈30% L/G) line shapes and a Shirley/Smart background.

Aeration Apparatus: Aeration was conducted using a custom-designed apparatus constructed from a stainless steel body and an acrylic top-plate and tube. Screws provide tension to seal the membrane between the acrylic and a Viton o-ring to deliver compressed air through the membrane porosity into a 25 mL water column.

CHAPTER 3

SEQUENTIAL INFILTRATION SYNTHESIS OF ALUMINUM OXIDE IN POLYETHERSULFONE MEMBRANES

3.1 Introduction

Sequential infiltration synthesis (SIS) is a materials synthesis technique by which polymers are infused with inorganic materials using alternating exposures to two chemical vapors. [19, 32, 49] SIS bears similarities to atomic layer deposition (ALD) in terms of requisite equipment and available chemistries, but is qualitatively different. In SIS, the first reactant pulse diffuses into the polymer film and interacts with functional groups along the polymer chains, which are distributed throughout the polymer bulk. The initial nucleation in SIS therefore only takes place in systems where association occurs between the vapor precursor species and a moiety within the polymer. For instance, during Al_2O_3 SIS in poly(methyl methacrylate) (PMMA), trimethylaluminum (TMA) interacts with the carbonyl (C=O) groups in PMMA via an intermediate complex to form a non-covalent adduct. [42–44] Subsequent H_2O exposure converts this species to Al_2O_3. The associations between polymer functional groups and organometallic vapors and the resulting kinetics of the SIS process are sensitive to temperature. [45, 47] Polymer free volume, glassiness, and crystallinity are also understood to play a role in the diffusion–reaction kinetics of SIS. [20, 182] SIS will not take place in non-polar polymers such as polystyrene (PS), which lack functional groups that can associate with the precursor species. [41] In subsequent cycles, SIS takes place on the already nucleated inorganic materials (e.g., Al_2O_3) in addition to any remaining amenable functional groups on the polymer backbone. The inorganic material loading within the polymer can be tuned by parameters including precursor dosage, purge time, temperature, and number of SIS cycles.

Polymers infiltrated with inorganic materials via SIS have found a number of applications in recent reports, as highlighted in Table 1.1. Two major categories of SIS

implementation have been realized. In the first category, the polymer serves as a spatial template for nanoscale oxide feature synthesis, and the polymer template is subsequently removed by plasma etching or burn-out at high temperature. In the second category, the polymer is retained and the resultant hybrid polymer-oxide nanocomposite is utilized.

In the first category, polymer resists such as SU-8 can be patterned via conventional lithographic techniques to define features for oxide infiltration. [28, 106] Ultrathin arrays of ZnO nanowires fabricated in this way have been used as photodetectors. [65] Lithographic limits can be overcome by using block copolymers (BCPs), which self-assemble into nanoscale patterns (spheres, lamellae, cylinders, etc.) with dimensions dictated by molecular weight and penalty of mixing between blocks. [183] The chemical incompatibility between the two blocks enables selective SIS in BCPs. In BCPs, one block, such as PS, does not associate with the precursor species, whereas the other block, such as PMMA or poly(vinyl pyridine) (PVP), [52] does associate. After reaction of the associated precursor, and after all organics are subsequently removed, nanostructured oxides replicating the SIS-active block morphologies remain. BCP-derived oxide nanostructures fabricated via SIS have found utility as lithographic hard masks, [95] anti-reflective coatings, [73,74] and isoporous membranes for protein separations. [76]

In the second category, SIS has been used to form polymer-oxide nanocomposites for enhanced lithographic applications. Al_2O_3 and ZnO have been used to enhance the etch resistance of electron beam lithography resists for high-aspect-ratio pattern transfer. [93,100] Such nanocomposites have interesting mechanical properties—incorporation of ZnO by SIS into lithographically defined polymer pillars yielded nanocomposites with ultra-high modulus of resilience. [87] SIS of Al_2O_3 into polyethylene terephthalate fibers has also been demonstrated to improve mechanical properties and introduce photoluminescent functionality. [182,184] SIS has been used to introduce hydroxyl groups to serve as linkages for grafting chemistry in porous polymeric materials. This functionalization scheme was recently used to convert conventional polyurethane sponges into selective and reusable oil adsorbents. [63,64]

SIS has also found use in the otherwise challenging three-dimensional characterization of BCPs. To achieve this, SIS is used as a contrast stain for the PMMA blocks in PS-*b*-PMMA to generate tomographic transmission electron microscopy maps. [57]

The work in this chapter details the expansion of the expansion of the library of SIS-modified polymer nanocomposites to a previously undescribed polymer system — polyethersulfone (PES). [77] . The chemical formula of PES and the microporous structure of a typical ultrafiltration membrane formed via phase inversion from PES are displayed in Figure 3.1. PES is a hydrophilic polymer extensively used in ultrafiltration; it is desirable for its high-temperature stability and mechanical strength imbued by its aromatic sulfone linkage. [185] There exists a wide literature of modifications to PES membranes to improve performance and lifetime, well-reviewed in the following references. [186, 187] Inorganic materials such as Al_2O_3 have been introduced into PES membranes by a number of techniques. The simplest of these is adding oxide nanoparticles to the polymer solution that is then cast to form a membrane. [188–190] Inorganic oxides can also be added to pre-cast extant membranes, for example, by hydrothermal sol–gel methods. [191] In these processes, the resulting coverage over the pore surface is inconsistent, and pores can be blocked by the post-deposition of materials.

Vapor phase processes, such as ALD, provide the possibility for a conformal coating of inorganic oxides on the complex and tortuous pore surfaces of polymeric membranes, thus limiting pore blockage. [112, 171, 192] ALD was first demonstrated on flat PES films via a plasma-enhanced Al_2O_3 process. [193] ALD TiO_2 coating of porous PES membranes has been demonstrated using various precursors. [194, 195] In the context of these reports, we have explored the interactions between TMA and the PES functional groups in the first PES SIS process. Whereas ALD-treated membranes have conformal metal oxide coatings that begin in the near-surface of the polymer, SIS-treated membranes are a hybrid nanocomposite directly templated by the initial PES template. SIS has been performed on a polycarbonate membrane that was then simply calcined to demonstrate the penetration depth of the process.

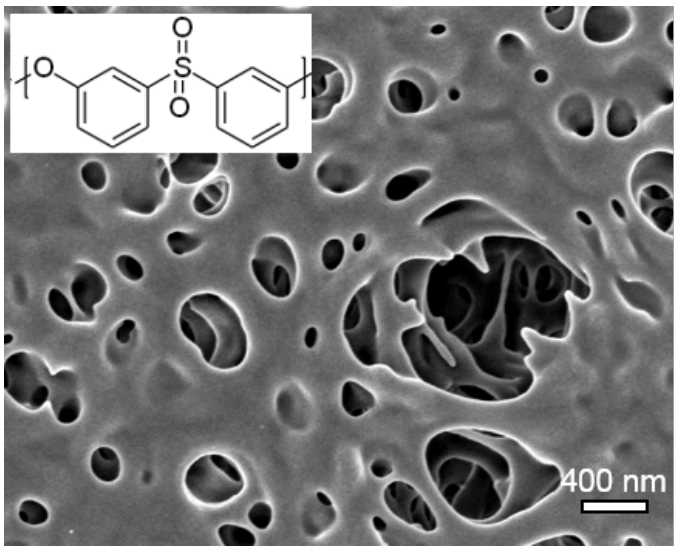

Figure 3.1: The chemical structure of PES is shown over an SEM image of the surface of a typical PES membrane formed via phase inversion with a 200-nm average pore size.

[42] In the work presented in this chapter, SIS is intentionally applied to membranes to explore how hybrid nanomaterial phase-inversion membranes can be achieved.

We use in situ Fourier-transform infrared (FTIR) absorption spectroscopy to elucidate the mechanism by which TMA interacts with PES. In situ FTIR enables detailed study of the interaction chemistry by measuring the distinct vibrational frequencies absorbed by the SIS precursor vapors, the polymer functional groups, and the solid-phase products of their interactions. [41] These measurements provide evidence for the complexation of TMA with the S=O sulfonyl groups in the PES. The conclusions drawn from FTIR are supported by density functional theory (DFT) calculations. We also use in situ spectroscopic ellipsometry to track changes in the optical properties of the PES film *during the SIS process*, from which we infer changes in thickness and refractive index. The effects of SIS processing on the resulting nanocomposite film are further studied by depth-profiled x-ray photoelectron spectroscopy (XPS) to show how the Al_2O_3 loading in the polymer can be controlled by the choice of purge time.

Following these mechanistic studies, we performed Al_2O_3 SIS on commercial PES membranes formed via phase inversion. Pure water flux measurements reveal a modest re-

duction in flux in both SIS- and ALD-modified membranes, which can be attributed to pore constriction. In ALD, pore constriction occurs by the deposition of material on the pore surface, while in SIS the pore itself shrinks as the polymer is swelled by the infiltrated oxide. These findings demonstrate that SIS modifies the polymer bulk, whereas ALD only affects the near-surface of the polymer material. Plane-view and cross-sectional energy dispersive spectroscopy (EDS) measurements were performed on the SIS- and ALD- modified PES membranes. Notably, membranes treated with three SIS cycles and 50 ALD cycles have a similar Al_2O_3 loading. Moreover, cross-sectional EDS measurements of the SIS-treated membrane showed uniform Al concentrations throughout the entire PES membrane thickness, while similar measurements of the ALD-treated samples showed high Al concentrations near the surface but virtually no Al in the middle. These differences stem from the different timescales of vapor exposures between the two methods, [167, 196] and highlight the sensitivity of polymeric substrates to vapor modification conditions.

3.2 Results and Discussion

3.2.1 In situ FTIR spectroscopy

The absorption of TMA in a PES film was first studied by recording FTIR spectra after sequential 10 s pulses of TMA. To avoid growing Al_2O_3 on the IR-transparent KBr windows, gate valves between the SIS and chamber were closed during the 10 s SIS precursor exposures and the 30 s purges. Including the time needed to record the spectra, $\sim$ 110 s of TMA purge and out-diffusion occurred between each TMA dose. The PES absorption spectrum shown in black at the bottom of Figure 3.2a has been reduced in scale relative to the other spectra for clarity. The main peaks in the PES absorption spectrum are listed in Table 3.1, and the assignments are based on previous infrared studies of PES and related compounds. [197–199]

Figure 3.2a displays the difference spectra between sequential doses that have

Table 3.1: PES vibrational features and assignments

Peak Position (cm^{-1})	PeakAssignment [197–199]
1483	Aromatic C=C stretch
1322	Asym O=S=O stretch
1297	Asym O=S=O stretch
1241	C-O-C stretch
1149	Sym O=S=O
1105	Aromatic ring vibration
1071	Aromatic ring vibration
1011	Aromatic ring vibration

been offset vertically for clarity. The spectra are referenced to the initial PES absorption spectrum in bold at the bottom of the figure. Consequently, positive-going peaks indicate newly created species, while negative-going peaks indicate species consumed during the TMA exposure. The blue-shaded regions highlight the C–H stretching region for Al-CH_3 at 2923 cm^{-1} and the C–H rocking features for Al-CH_3 at 700 cm^{-1}. [43, 44, 200, 201]

These features are consistent with TMA absorbed within the PES film. Relatively large increases in the intensity of C–H stretching and rocking regions appear during the first TMA exposure, but these changes diminish with additional TMA exposure and saturate after ∼60 s. Figure 2b shows the normalized integrated intensities of these spectral regions versus TMA exposure time, and demonstrates that the C–H stretching and rocking features follow the same absorption kinetics, as expected for features deriving from the same chemical species. The other features in the spectra will be discussed later in the context of the TMA + PES interaction mechanism.

Following this cumulative 90 s TMA exposure, spectra were collected every 5 min during a continuous TMA purge period to observe any changes in the concentration or bonding of the absorbed TMA. Difference spectra for this sequence are plotted in Figure 3.3 and show the gradual reduction in intensity for the C–H stretching and rocking features. Integration and normalization of these peaks (Figure 3.2c) reveals that TMA is slowly released from the PES on a timescale ∼100× slower compared to the uptake of TMA. After 40 min

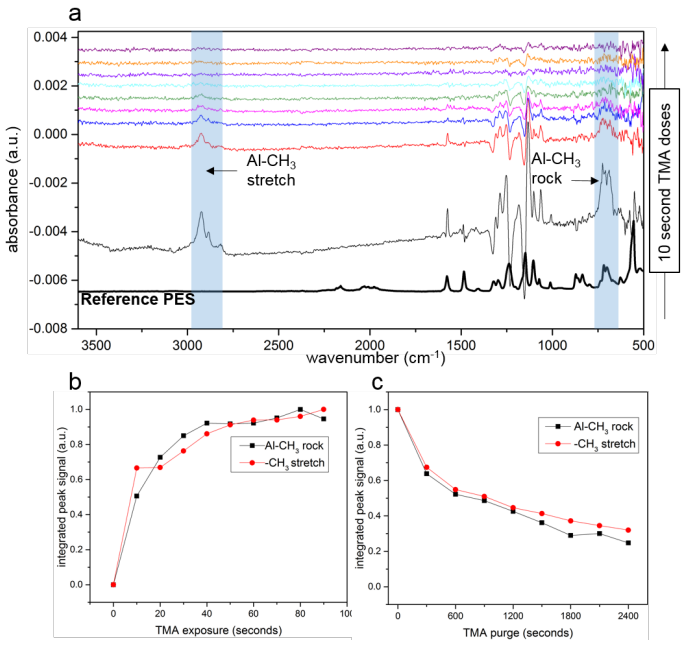

Figure 3.2: (a) Difference spectra of PES films after successive 10 s doses of TMA show the gradual saturation of the TMA signal as measured by the Al-CH_3 stretch and rock vibrations. (b) Integration of these two modes reveals the kinetics of the saturation of TMA within the film. (c) Integration of the Al-CH_3 modes upon purging at 5 min intervals reveals slow kinetics of out-diffusion.

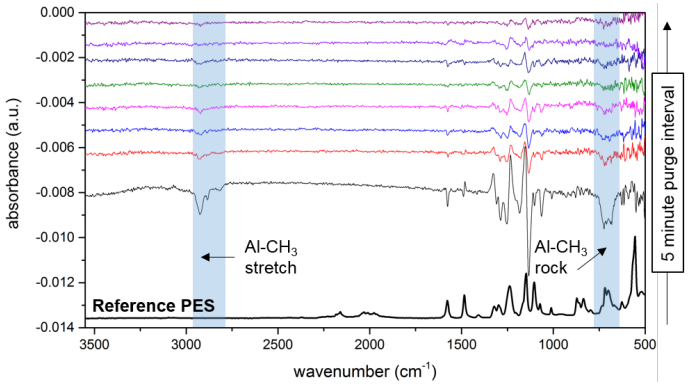

Figure 3.3: FTIR difference spectra versus TMA purge time recorded at 5 min intervals. The first spectrum is referenced to the 90 s cumulative TMA exposure spectrum.

of purging, ∼70% of the integrated absorption intensity is lost, corresponding to ∼30% of the initial saturated TMA retained in the film. The film was then quenched with a water pulse to complete one SIS cycle, the spectral features of which are discussed later.

Following this initial Al_2O_3 SIS cycle in the PES film, four additional TMA/H_2O SIS cycles were performed. Each SIS cycle consisted of a 60 s TMA exposure, 60 s purge, 60 s H_2O pulse, and another 60 s purge. FTIR spectra were recorded after each TMA and H_2O purge. Figure 3.4a shows difference spectra in the high-frequency region after each exposure referenced to the initial PES film. The C–H stretching peaks at 2923 cm^{-1} appear with each TMA exposure and are extinguished with each water exposure. Presumably, H_2O reacts with the infiltrated TMA species and generates methane, which diffuses out of the polymer. This spectral change diminishes with additional SIS cycles so that after four SIS cycles the spectrum no longer appreciably changes. This most likely results from a constriction of the PES free volume diffusive pathways required for TMA and H_2O to reach reactive sites. Figure 3.4b shows difference spectra in the low frequency region of successive H_2O exposures referenced to the initial PES film. The feature centered at 800 cm^{-1} is the broad Al-O phonon mode of Al_2O_3. [202] This peak continues to increase over the first three SIS cycles, but flattens as less new Al_2O_3 is grown with each cycle. This supports the hypothesis that SIS continues for approximately three SIS cycles and then slows drastically as nucleation is replaced by ALD-like growth on metal oxide surfaces.

While the preceding discussion focused primarily on the TMA Al-CH_3 peaks in order to understand the kinetics for TMA absorption and desorption and the effects of multiple cycles, a close examination of the changes in the PES vibrational features upon TMA absorption can yield additional insights into the mechanism of the TMA-PES interaction. Figure 3.2a shows significant changes in the 1000 and 1500 cm^{-1} regions upon TMA exposure. These changes are highlighted in Figure 3.5. The reference PES spectrum at the bottom of Figure 3.5 shows peaks at 1483 cm^{-1} (aromatic C=C stretch), 1322 and 1297 (asymmetric S=O stretch), 1241 (asymmetric C–O–C stretch), 1149 (symmetric S=O stretch), and at

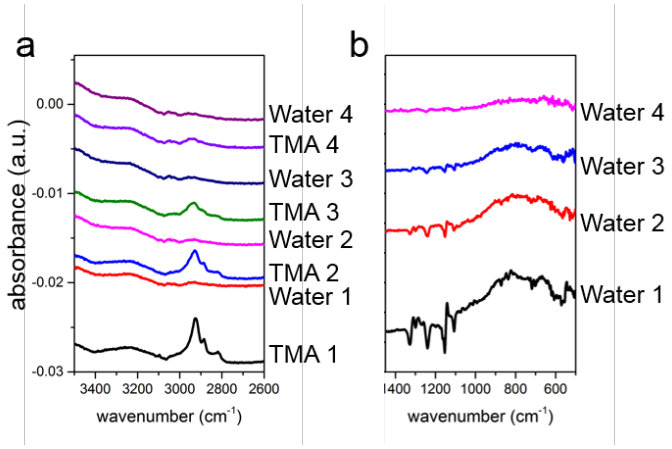

Figure 3.4: FTIR difference spectra versus TMA purge time recorded at 5 min intervals. The first spectrum is referenced to the 90 s cumulative TMA exposure spectrum.

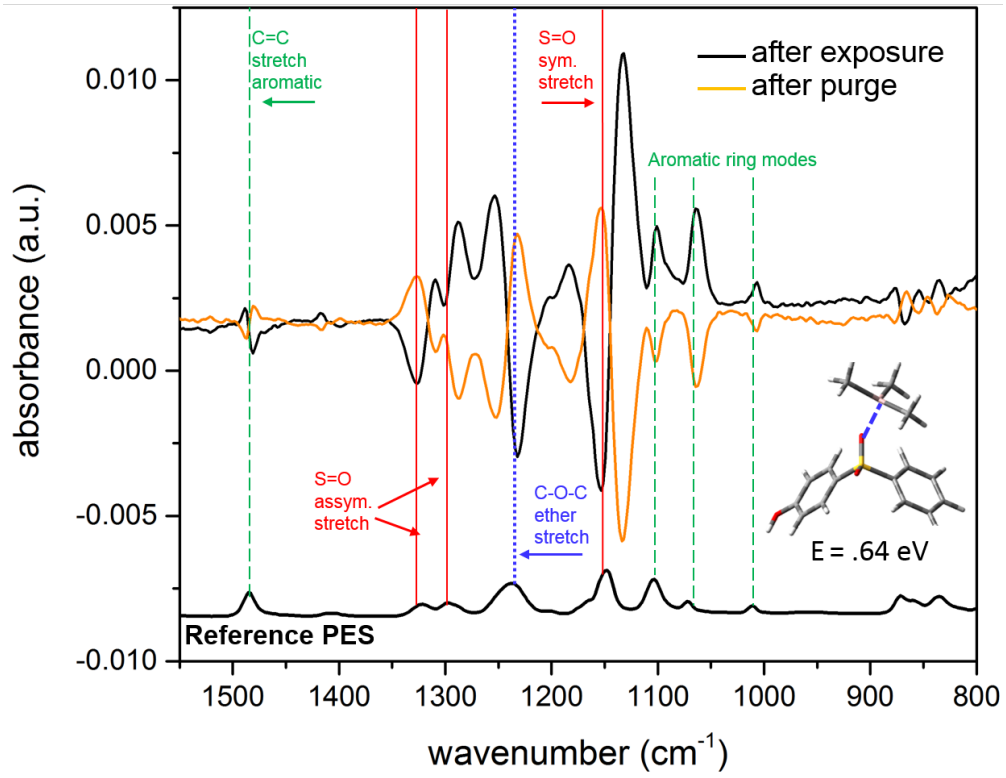

Figure 3.5: Difference spectra between PES and 90 s of cumulative TMA exposure (black) and 40 min of TMA purging (orange) reveal the reversibility of the spectral shifts caused by association between TMA and PES. C–C modes (green), S=O modes (red), and C–O modes (blue) that undergo changes due to TMA complexation are indicated. The inset shows a DFT calculation for the equilibrated structure between TMA and the sulfonyl group of the PES monomer.

1105, 1071, and 1011 cm^{-1} (aromatic ring modes). These peaks have been color-coded in Figure 3.5 to highlight the C–C (green), S=O (red), and C–O (blue) modes.

Following 90 s of TMA exposure (black spectrum), both positive- and negative-going features emerge corresponding to the creation and consumption of IR-absorbing species, respectively. The largest of these changes corresponds to an intensity loss of $\sim 4\%$, suggesting that TMA occupies 4% of the available sites. In the case of the lower frequency aromatic ring modes, only positive peaks are seen. For the S=O modes (red), we see negative peaks indicating a loss of absorbance at this frequency, accompanied by a positive peak at ~ 25 cm^{-1} lower frequency, which indicates the S=O modes lose electron density by forming an adduct (i.e., red-shifted) with the TMA. Conversely, for the C–O peak at 1241 cm^{-1} (blue) and the 1483 cm^{-1} aromatic stretch, there is a negative feature accompanied by a positive peak at 10–30 cm^{-1} higher frequency (blue-shifted). We note that all of these changes are reversible upon prolonged purge as evidenced by the orange trace in Figure 3.5 recorded following 40 min of purging. This spectrum is referenced to the spectrum recorded after TMA exposure (black spectrum), and is essentially a mirror image indicating that all the changes are full reversed under sufficiently long purging. Based on previous in situ FTIR studies of the interaction between TMA and PMMA, [43, 44] we attribute the spectral changes to the S=O peaks to the formation of a weakly bound intermediate complex that weakens the S=O bond thereby shifting it to lower frequency:

$$Al(CH_3)_3 + S = O \longleftrightarrow S = O \cdots Al(CH_3)_3 \tag{3.1}$$

Similarly, the blue-shifted C–O peaks result from TMA physisorbed to the oxygen atoms on the ester groups, and the blue shift is a consequence of a resonance effect. [203] As indicated in Equation 3.1, the physisorbtion is reversible, and this results in TMA desorption to reform the S=O species so that the spectral changes reverse. It is not as clear why the low-frequency ring modes increase upon TMA exposure, but these changes are also reversed

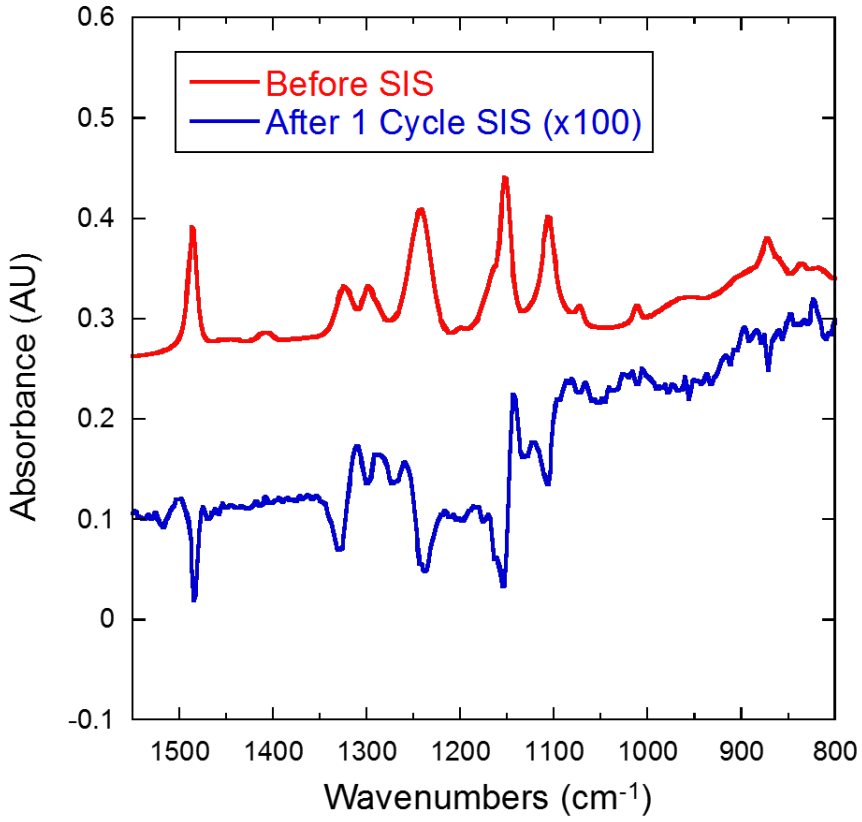

Figure 3.6: FTIR spectrum prior to SIS (red) showing the PES peaks, and following a complete Al_2O_3 SIS cycle (blue) referenced to the red spectrum. The blue spectrum has been scaled by 100×, and the negative going peaks represent functional groups in the PES film that were consumed during the Al_2O_3 SIS process

during the purge step.

A DFT simulation of an isolated PES monomer and TMA molecule was performed to see if the proposed weakly bound intermediate proposed in Equation 3.1 is energetically plausible. These simulations show that there is indeed an attractive association related to the sulfone groups of the polymer. The inset in 3.5 shows the equilibrated configuration with a calculated binding free energy of 0.64 eV. This simulation supports our hypothesis that one SIS interaction pathwas between TMA and PES is qualitatively similar to that between TMA and the carbonyl PMMA, albeit with a different binding strength. [36, 43, 44]

Figure 3.6 shows an FTIR spectrum of the PES before SIS (red) and following the H_2O exposure of the first SIS cycle (blue, scaled by 100×) referenced to the PES spectrum.

We note that there is a net decrease in the intensity of all the peaks described above in the context of the weakly bound intermediate. The magnitude of these changes is $\sim 1\%$ of the initial spectral intensity, indicating that $\sim 1\%$ of the S=O bonds are permanently broken because of the SIS. We attribute this behavior to the formation of Al_2O_3 in the bulk of the PES, where some of the methyl groups from the TMA remain bound to the S or to the aromatic ring. Residual methyl groups bound to carbon atoms in the aromatic rings would account for the net loss in intensity of the aromatic ring vibrational features following SIS.

Another significant feature in Figure 3.6 is the loss of signal at 1231 cm^{-1}, representing the C–O–C aryl ether stretch. In a study of TMA and polyethylene oxide (PEO), which is composed of C–O–C bonds, a loss of absorption at 1100 cm^{-1} was ascribed to TMA cutting ether bonds at that position. [42] Although much of the intensity drop at 1231 cm^{-1} during the TMA exposure is recovered during the subsequent purge, we do observe a net decrease following the H_2O exposure in Figure 3.6. This indicates that C–O-c serve as nucleation sites for the Al_2O_3 SIS in PES in addition to the S=O sites.

These FTIR measurements confirm that TMA associates with the sulfonyl and aryl ether groups of the PES polymer in a qualitatively similar way to the association with the carbonyl and ester groups of PMMA. These data enable mechanistic comparisons between SIS in PES and PMMA, though comparisons of the binding strength and extent of reaction are complicated by the different glass transition temperature, polymer free volume, and TMA solubility and diffusivity in different polymers. [20, 21] The saturation/purge study presented shows an equal rate of association/dissociation between the proposed interactions, as the peak shifts recover identically. Further temperature studies of this process could reveal whether these different sites of association along the PES backbone have different energetics. Studying longer purge times could also provide evidence for the direct conversion of PES-TMA complexes into covalent bonds.

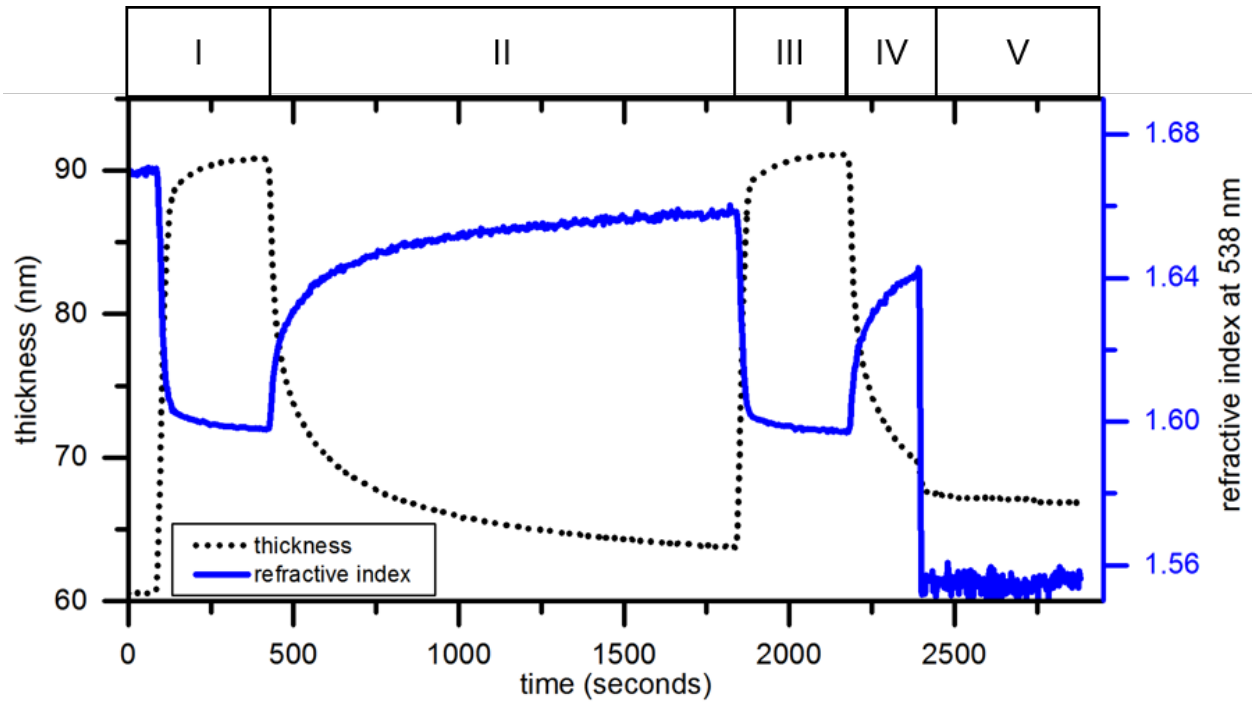

Figure 3.7: In situ spectroscopic ellipsometry data fit to a Cauchy model yields a dynamic view of film thickness and refractive index throughout TMA exposure, purging, and H_2O exposure in a SIS process. The plotted sequence tracks a first 5 min TMA exposure (I) followed by a 25 min purge (II), followed by a second 5 min TMA pulse (III), a 3 min purge (IV), and a 5 min quenching water exposure (V)

3.2.2 In situ spectroscopic ellipsometry and depth-profiled XPS measurements

A challenge inherent to kinetically controlled SIS process design is that any of a number of environmental factors can influence the extent of precursor infiltration and partially reversible removal, which alter the hybrid material product. In order to gain insight into this complexity, dynamic in situ measurements of the film must be made during the SIS process.

Figure 3.7 shows in situ ellipsometry data tracking the thickness and refractive index over a 5 min TMA exposure, followed by a 25 min purge. This sequence reveals an initial film thickness of $\sim$ 60.5 nm with an index of refraction at 538 nm of 1.67. As TMA is introduced into the chamber, the film undergoes rapid swelling over the first $\sim$ 40

s followed by much slower saturation. This is similar to the saturation time observed via FTIR measurements, though differences in the chamber set-up and exposure sequence limit the value of direct comparison of the respective rates. The refractive index was observed to decrease in tandem with the film thickness increase. This suggests that TMA absorbed by the film swells the material much like a typical organic solvent and reduces the film density. At the end of the 5 min exposure, the film thickness increased by 50.0% to 90.8 nm, and the index of refraction decreased by 4.2% to 1.59. As the TMA is purged, the thickness and refractive index partially recover as TMA diffuses out of the polymer film. After 25 min of purging the film, thickness decreased from the saturated thickness of 90.8 nm by 29.7% to 63.8 nm. At an equivalent point of purging in the FTIR measurements, the film had lost $\sim$ 40% of the absorbed TMA as measured by C–H peak intensity. Study of extended purge times using this technique and in situ FTIR may reveal irreversible association of TMA with PES. The precise relationship between the degree of TMA association with polymer functional groups and the swelling of the film is unclear and also merits further study.

Following the 25 min purge, the PES film was exposed to another 5 min of TMA vapor to saturate it once again. In this second exposure, the film reached a slightly higher maximum of thickness of 91.1 nm with a corresponding refractive index of 1.60. The slightly higher refractive index of the film upon a second saturation suggests a denser film, but the thickness is incrementally higher. This shows how sensitive polymer films are to precursors such as TMA and how important sample history is in the SIS process. Changes in chain conformation and polymer free volume that may occur during the first TMA infiltration can be retained even after TMA leaves, as the polymer is well below its glass transition temperature. These effects may change how TMA can infiltrate into the polymer in subsequent exposures. As Figure 3.7 shows, the sample was then purged for 3 minutes. The thickness decreases, and the refractive index increases, as the film densifies in the same way as during the first purge. The film is quenched with a 15 s water pulse held in exposure mode for 5 minutes. An abrupt change in the ellipsometry data is observed, the refractive index drops

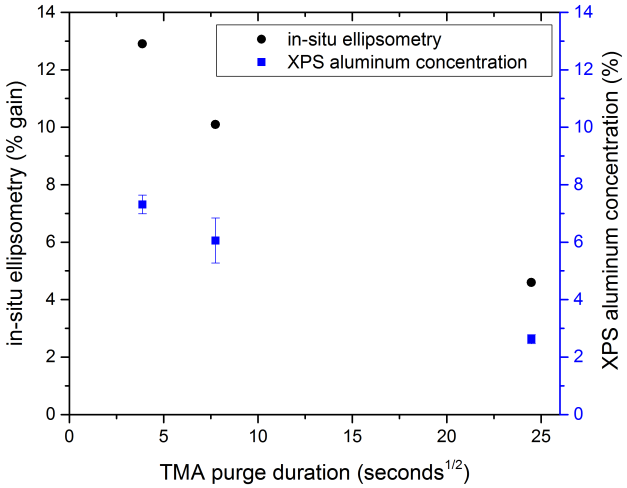

Figure 3.8: Percentage increase in PES film thickness as measured by in situ spectroscopic ellipsometry (black) and averaged aluminum concentration as measured by depth-profiled XPS (blue) versus TMA purge time following 6 min TMA exposure.

to 1.56, and the thickness drops to 67.2 nm. The thickness decrease with water exposure is not instantaneous, but is rather a very rapid decay over several seconds. This may be attributed to the simultaneous infiltration and reaction of the water, as well as the liberation of gas-phase products such as methane that diffuse out of the film. The rapid change in refractive index occurs with the formation of solid-phase Al_2O_3. Future studies employing more sophisticated models than a single Cauchy layer may reveal further insights into how the polymer-inorganic nanocomposites evolve throughout the SIS process.

Figure 3.8 shows the different percentage gains in thickness for equivalent 60 nm thick PES films that were exposed to TMA for 5 min and then quenched with water after 15 s, 1 min, and 10 min purges. Figure 3.8 shows the resulting average aluminum content in the three films as measured by depth-profiled XPS measurements. These data were constructed by averaging the aluminum content measured after each incremental etch. Elemental distributions of these films are included in Figure 3.9. An unprocessed PES film was found to have a uniform distribution of 0.7% Al composition, which was attributed to aluminum contamination of the XPS tool. The uniformity of the aluminum and oxygen features observed across 60 nm demonstrates that the TMA dose and exposure used in the experiment was

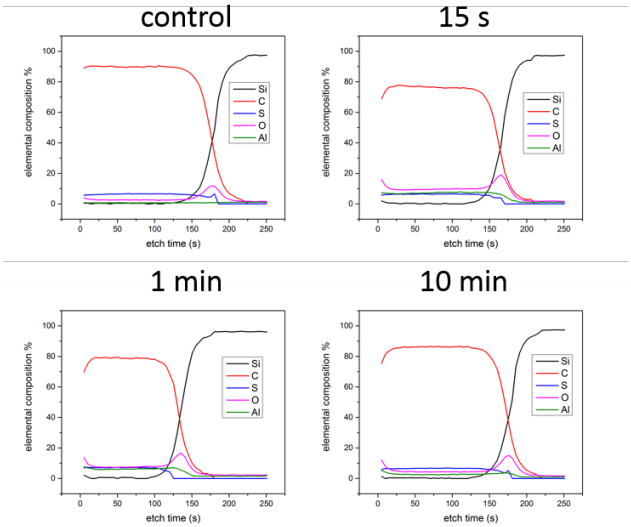

Figure 3.9: Depth-profiled elemental composition of hybrid PES-Al_2O_3 films generated via XPS measurements vs. etch time.

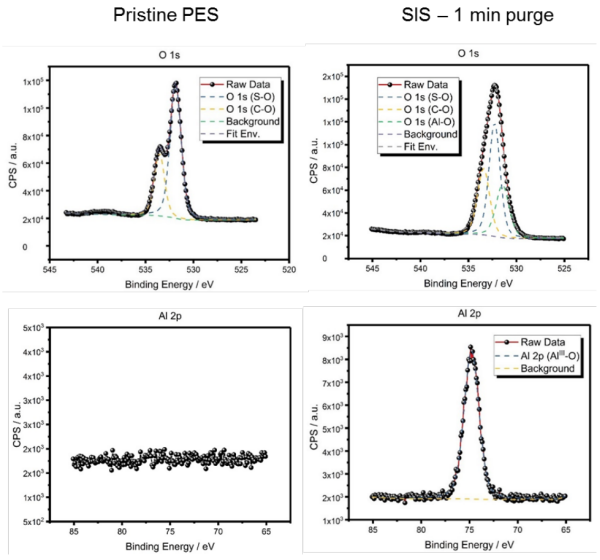

Figure 3.10: O 1s and Al 2p peaks of pristine PES and SIS-modified PES film (one minute purge) surfaces. The introduction of signal at the Al 2p region and of the O 1s Al-O confirms the presence of Al_2O_3.

sufficient for the TMA vapor to diffuse fully into the film to result in a nearly uniform distribution. The 60 nm thickness of the initial PES film is significantly shorter than the diffusion depth of TMA under the selected processes conditions. In the limit of a bulk polymer film, one would expect the infiltrated oxide to have a decreasing concentration profile deeper in the film as a consequence of diffusion limitation. Figure 3.10 compares the oxygen 1s peaks from 530 to 535 eV and the aluminum 2p peak at 74.7 eV, showing the control PES film and the 1 min purge SIS sample. The introduction of a peak at 531.45 eV represents the inclusion of contributions from the Al-O bonding environment. Likewise, the Al 2p peak is completely absent in the unmodified PES film.

3.2.3 SIS in Porous PES Ultrafiltration Membranes

In order to demonstrate the implementation of SIS into membranes, a commercially available UF product was used. Figure 3.11 shows pure water flux data of membranes prepared by a typical SIS recipe and a typical ALD recipe normalized to the flux through an unmodified control membrane. Even over the short timescales of the ALD recipe, TMA will infiltrate into the PES. In amenable polymers, ALD recipes may be thought of as extremely brief SIS recipes. At ALD timescales, the infiltrated depth is limited to the immediate subsurface of the polymer. All the treated membranes show a decrease in flux relative to the as-received PES membranes, which were measured to have a pressure-normalized flux of 1458 $L\text{-}h^{-1}\text{-}m^{-2}\text{-}bar^{-1}$. Notably, a similar reduction in flux was observed between 50 ALD cycles and 3 SIS cycles. More ALD cycles caused a more precipitous decline in flux than increased SIS cycles as described below.

Moderate ALD loading of membranes with metal oxides has been reported to increase their pure water flux. [112] In that example, a hydrophobic polypropylene membrane was treated, and the hydrophilic oxide surface lent a significant flux increase. Such conformal treatments lead to a balance between pore size reduction and enhanced fluid flow. For example, in the treatment of ceramic membranes with ALD N-doped TiO_2, which is

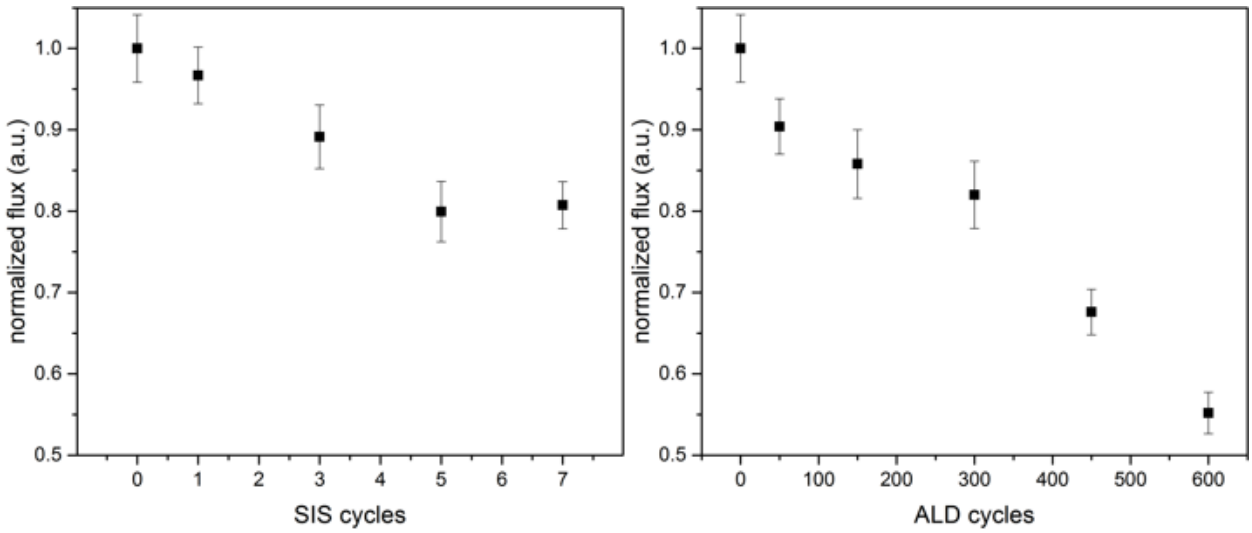

Figure 3.11: Pure water flux measurements of both ALD- (right plot) and SIS-modified (left plot) membranes reveal the continuous decline of flux with increasing ALD cycles and the stabilization of flux decline once five SIS cycles are reached.

extremely hydrophilic under light exposure, an initial flux increase is observed at low cycle numbers because the surface enhancement outweighs pore constriction. [164] However, with more cycles, pore constriction will ultimately outweigh the enhanced surface. [192] The PES membranes in this study are initially hydrophilic — PES is generally considered a high-flux membrane material. Therefore, Al_2O_3 is not intended nor expected to impart a significant hydrophilicity improvement to the membrane.

The flux decline in the modified membranes is attributed to the constriction of the pore volume due to the introduction of Al_2O_3. The fact that many ALD cycles are required to achieve similar flux declines to only a few cycles of SIS highlights the subsurface-limited reactions that take place with ALD recipes compared to the bulk infiltration of polymer that is possible with SIS processing. This phenomenon explains the sensitivity of flux to the first five SIS cycles. The polymer continues to swell as active sites are consumed, which constricts the membrane pore volume significantly. After five cycles, the membrane is sufficiently swollen with Al_2O_3 that infiltration ceases, either because sites within the polymer are consumed or are inaccessible due to the oxide formed in previous cycles. Al_2O_3 deposited in SIS cycles after this occurs may be limited to the surface or interfaces of the

already infiltrated oxide, leading to a significantly reduced material gain per cycle. The ALD-processed membranes show a roughly linear flux decline with number of cycles, consistent with minimal infiltration into the polymer. We therefore infer from the flux decline that pores are gradually shrunk by Al_2O_3 surface growth layer-by-layer outward from the pore wall.

Elemental analysis by EDS was conducted to probe the incorporation of Al_2O_3 into the membrane. Figure 3.12a shows EDS spectra of the top surface of pristine membrane, 7 SIS cycles, and 600 ALD cycles. Notably, the Al peak at 1.486 eV is absent in the pristine polymer and emerges in the processed polymer. Figure 3.12b shows a close-up of the Al peak. The peaks of 3 SIS cycles and 50 ALD cycles are similar, much like how they exhibit similar levels of flux decline. EDS maps of the cross-sectional distribution of Al_2O_3 in pristine, 3 SIS, and 50 ALD cycles are shown in Figure 3.12c. The distribution of the SIS samples is uniform throughout the membrane thickness, whereas the 50 ALD cycle membrane shows a slight decrease in signal at the center of the membrane. This asymmetry is a function of the short exposure doses conducted in the ALD process. The highly tortuous and high-aspect-ratio pore paths in UF membranes can lead to diffusion-limited deposition. [123, 167, 172] This asymmetric deposition may be a desirable feature in certain applications, such as in the formation of Janus membranes described in the previous chapter. [196] Such asymmetry may be avoided by lengthening the timescales of vapor exposure within the ALD regime.

3.3 Conclusion

This chapter explores the sequential infiltration synthesis of trimethylaluminum into a previously undescribed polymer system, polyethersulfone, which is widely used in membrane filtration. In situ FTIR of TMA in-diffusion and out-diffusion of this system identified the nature and kinetics of an attractive interaction between the TMA and the PES moieties, which leads to slow out-diffusion via reversible complex breaking as observed in other successful SIS-polymer systems. Investigations of the spectral shifts caused by TMA confirm

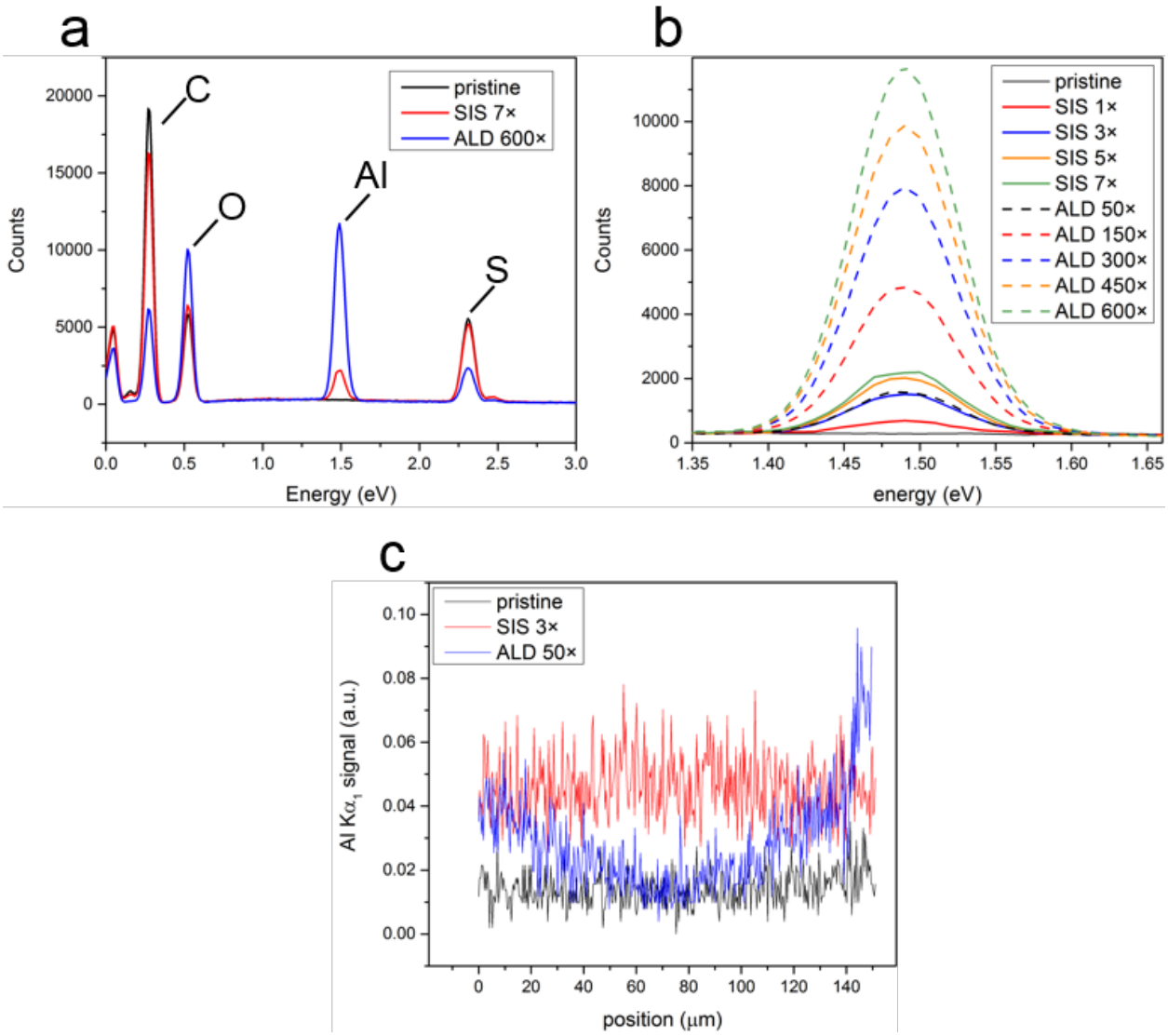

Figure 3.12: EDS spectra of the top surfaces of PES membranes: (a) pristine, seven cycles SIS, and 600 cycles ALD demonstrate the appearance of an aluminum peak at 1.486 eV; (b) the Al EDS peak increases continuously with ALD cycles but saturates after five SIS cycles. Three SIS cycles and 50 ALD cycles yield similar intensities. (c) Cross-sectional EDS line scans reveal a uniform aluminum signal following three SIS cycles. In contrast, 50 ALD cycles show high Al EDS signals at the edges but no change from the uncoated membrane signal at the center, consistent with diffusion-limited coating.

that the sulfonyl moiety in PES behaves similarly to the carbonyl in PMMA. Both act as Lewis basic sites that can complex with the Lewis acidic TMA. These insights into the chemical interactions between vapor precursors and PES are supported by in situ ellipsometry measurements that reveal the kinetics of infiltration, saturation, and out-diffusion on the seconds time-scale. The thickness change of PES films, along with the aluminum content of these films as measured by depth-profiled XPS, confirm the strong role that purge time plays in the resulting polymer-metal oxide hybrid nanocomposite, especially in the short-purge time limit. Insights gained from this characterization are applied to PES ultrafiltration membranes to demonstrate SIS in a highly tortuous networked system. The loading of oxide per cycle is inferred to be much higher over the first five cycles of SIS than in subsequent cycles, as the pure water flux through the modified membrane declines and then stabilizes due to pore constriction. A similar intensity in EDS signal between 3 SIS cycles and 50 ALD cycles highlights the efficient bulk infiltration of SIS in contrast to the surface-limited nature of ALD. PES membranes infiltrated with metal oxides by SIS can enable the stable grafting of other molecules throughout the pore volume of the membrane, introducing new functionalities for advanced filtration applications.

3.4 Materials and Methods

Sample Preparation: PES polymer pellets (M_w = 58 kg/mol) were purchased from Goodfellow Cambridge, dissolved in dimethyl formamide (DMF) at a 4 wt.% solution and spin-coated at 3000 rpm to achieve a $\sim$ 150 nm film. The polymer was spun onto double-sided polished undoped intrinsic silicon wafers to minimize IR absorption by the substrate. The samples were prepared in an argon-filled glovebox, as spin-coating in air was found to yield rough and inconsistent films due to non-solvent-induced phase separation via ambient humidity.

In situ FTIR spectroscopy: In situ FTIR measurements were performed using a Nicolet 6700 FTIR spectrometer (Thermo Scientific) interfaced to a custom ALD reactor. [204] Each FTIR spectrum represents an average of 64 scans taken at 4 cm^{-1} resolution over

the 400–4000 cm^{-1} spectral range, and the signal intensity was calculated as an absorbance. FTIR measurements were conducted at a constant temperature of 110 °C. The PES-coated substrates were allowed to equilibrate in flowing, ultrahigh-purity (99.999%) N_2 using a 300 sccm flow rate at 3.5 Torr pressure within the heated reactor for 2 hr before the beginning of the experiment. A long bake in the chamber was used to drive off solvent, as residual Lewis-basic solvents such as DMF have been shown to play a potential role in SIS nucleation. [54]

Density functional theory: DFT calculations were performed using Gaussian 09 software. [205] Isolated polymer fragments and TMA precursor were first geometrically optimized at the B3LYP/6-31G(d,p) level to ascertain their equilibrium free energies. The two species were then optimized in proximity to search for potential weak-binding interactions. Energy differential between any such bound species and the isolated fragments provides an approximation for the potential energy well of the complex.

In situ spectroscopic ellipsometry: PES films with a thickness of 60 nm were spin-coated onto silicon wafer pieces from a solution of 2.5 wt.% polymer in DMF in a glovebox. In situ spectroscopic ellipsometry was performed using a J. A. Woollam M-2000 V with spectral range of 380-1000 nm at a fixed angle of 70° interfaced to an Ultratech Fiji ALD Chamber. Ellipsometric spectra were collected through Ar-purged windows every 2.5 s. PES samples were introduced into the chamber and held at the process temperature of 110 °C for 45 min prior to beginning the SIS process to remove any residual water or other solvents. A 15 s TMA pulse followed by 5 min of exposure (valve to exhaust pump closed) was performed to saturate the film with TMA. After this exposure, the pump valve was opened to purge the chamber for a controlled duration. Following this purge step, an identical water pulse, exposure, and purge were conducted, completing the SIS cycle.

X-ray photoelectron spectroscopy: XPS surface analysis measurements were carriedout on a Thermo Scientific K-Alpha+ using a micro-focused monochromatic Al Kα (1487 eV) x-ray source with a spot size of 400 μm. Samples were affixed to the transfer stage mount using Cu clips, and depth profiling measurements were performed with an Ar^+ bombard-

ment voltage of 3 keV (low-current) with 5 s per sputter cycle and corresponding effective etch rate of ~ 0.25 nm/s. Raster area of the depth profiles was $2 \times 2\text{mm}^2$ (effectively $5\times$ the x-ray spot size) wide-scan surveys, and high-resolution XPS snapshots for the Al 2p, O 1s, C 1s, Si 2p, and S 2p regions were collected after each sputter cycle, and 100 sputter cycles (500 s total sputtering time) were performed on each sample. Batch fitting and processing of the HR-XPS snap- shots were performed in Thermo Advantage 5.977 software, and mixed Gaussian–Lorentzian peak shapes were used in all fitting routines in the aforementioned regions of interest. Due to overlap of the S 2p region with the Si 2s plasmon loss peak at the interface ($\sim$ 162–165 eV) and closer to the substrate, the S 2p signal was normalized to the depletion rate of the O 1s signal at the interfacial regions of each sample ($\sim$ 130–150 s). Because of this overlap, the S 2p region could not be con- strained to a particular binding energy value in the batch-fitting process without also including the Si 2s signal.

Membrane Fabrication: Both SIS and ALD of the PES membranes were performed on a Veeco/Cambridge Nanotech Savannah ALD Chamber held at 110 °C. Membranes were held at the process temperature for at least 20 min to drive off moisture. ALD processes were conducted in flow mode with a single cycle consisting of a .015 s TMA pulse, a 10 s purge, a .015 s H_2O pulse, and a 10 s purge. The number of cycles performed ranged from 50 to 600. SIS processes were conducted in exposure mode, using a stop valve to keep the reactants in the chamber. A 1 s dose of TMA was held in the chamber with a closed stop valve for 5 min, followed by opening the stop valve for a 30 s purge and a 4 s water pulse with 5 min exposure with close stop valve. Membranes were prepared with 1, 3, 5, and 7 SIS cycles. The membranes were suspended above the base of the ALD chamber by securing them between glass slides at both edges. This allowed for unhindered vapor flow on both faces of the membranes.

Dead end filtration: Flux measurements were taken using an Amicon Stirred Cell Model 8010 using nitrogen gas at a pressure of 10 psi using reverse osmosis-treated water. Permeate was collected in a beaker on a balance, and a Labview program collected the mass

of permeate over time. Three samples at each condition were measured a total of three times, and the average flux normalized by pressure was calculated according to the following equation:

$$\frac{F}{P} = \frac{\Delta V}{\Delta t A P} \tag{3.2}$$

F is flux, V is volume of permeate, t is time, P is the transmembrane pressure, and A is membrane area. An effective membrane diameter of 25 mm was used in this calculation, and the results were converted to L-h^{-1}-m^{-2}-bar^{-1}.

Energy Dispersive Spectroscopy: Membrane samples for elemental analysis were prepared in cross-section by submersion into liquid nitrogen for 1 min and then cracking along a notch prepared by a razor blade. The cleaved edge of the broken membrane was adhered to the vertical edge of a SEM sample stub using copper tape such that the top face of the membrane in the ALD chamber side faced away from the sample stub. The membrane's broken edge was aligned to be flush with the lip of the stub wall. The sample was coated with 4 nm of carbon to mitigate charging. EDS measurements were conducted on a TESCAN LYRA3 field-emission scanning electron microscope with an accelerating voltage of 10 keV and a working distance of 9 mm. EDS map spectra were collected using two Oxford Instruments X-MaxN detectors and analyzed using the AZtec software package. The EDS x-ray signal centered at 1.486 keV corresponding to the aluminum Ka_1 peak was mapped across the membrane cross-section to generate a bit-map image of the signal intensity. Mapping scans were taken at an image magnification of 95000× and at a 512-pixel resolution. The energy range and channel number were set to auto, and a process time of 4 μs and a pixel dwell of 50 μs were used. The mapping scan data were binned along the axis parallel to the membrane to generate 2D plots of Al concentration versus depth.

CHAPTER 4

SEQUENTIAL INFILTRATION SYNTHESIS OF ELECTRONIC MATERIALS: GROUP 13 OXIDES VIA METAL ALKYL PRECURSORS

4.1 Introduction

Sequential infiltration synthesis (SIS) enables inorganic hard or hybrid hard/soft materials to be rapidly fabricated from polymer templates with exquisite microstructural organization and complexity. [29, 206] SIS enables the selective synthesis of robust metal oxides within polymers based on the association of volatile metal-organic precursors with Lewis basic functional groups found within select polymer classes. This distinguishes SIS from traditional atomic layer deposition (ALD) processes applied to polymeric substrates. [207–209] While precursor vapors react on the surface of polymers in ALD, in SIS, the exposure times are much longer to enable diffusion into the polymer free volume, where vapor residence is often further promoted by adduction to polymer functional groups. [21, 30, 31]

However, the state of the art in SIS has demonstrated only a small subset of the library of materials that have been synthesized via ALD, from which SIS is derived. Aluminum oxide (Al_2O_3) formed by trimethylaluminum (TMA) and water is by far the most studied SIS system and has already been applied to important applications in lithography, [19, 93, 95, 101] oil sorption, [63, 64] protein separations, [76] and optical coatings. [73, 74] Nanostructured metal oxides can be fabricated via SIS using BCPs as templates, [32] where one block (commonly polystyrene) is inert to SIS. SIS-derived nanostructures have been fabricated using both self-assembled block BCP thin films and, recently, nanospray-dried powders. [33] The SIS approach has been extended to a sparse selection of other oxides including TiO_2, [34, 51, 52, 106] ZnO, [28, 65] and VO_x [39]; however, the growth of other materials (e.g., W/WO_x [32,55] and SiO_2 [32]) within polymers requires an SIS Al_2O_3 seeding

cycle and therefore constitutes a separate class of reactions that only inherit selectivity from the primary (SIS) process. These secondary SIS reactions leverage irreversible reactions with hydroxyl groups present on primary Al_2O_3 seeds, in contrast to the (generally) reversible complexation of metal precursors with select polymer functionalities. Materials grown by the seeding method are therefore inherently a mixture of Al_2O_3 and the material of interest, which may compromise desired functional properties.

Expanding the library of materials accessible via primary SIS processes will require novel combinations of polymer chemistry, metal precursors, and process conditions. Extending the library to include electrically conductive materials further requires an improved mechanistic understanding of diffusion, adduct formation, metal-organic chemistry, condensation, and crystallization that occurs within the soft templates. While the structural integrity of insulating oxides (e.g., Al_2O_3) may be relatively forgiving of these complexities, a more precise synthesis will likely be required to enable SIS of functional electronic and photoactive materials in which the functional properties depend on well-defined stoichiometry, morphology, connectivity, carrier mobility, carrier concentration, and defect density. [210,211]

In this chapter, we establish primary SIS processes for In_2O_3 and Ga_2O_3, two semiconducting oxides for which neither primary nor secondary SIS has previously been reported, via group 13 metal alkyl precursors analogous to TMA: trimethylindium (TMIn) and trimethylgallium (TMGa), respectively. We experimentally explore and computationally validate the chemical mechanism and exceptional kinetics that control the selective association of these metal-organic precursors with the ester in poly(methyl methacrylate) (PMMA). The physical and electronic properties of the oxide formed with TMIn are investigated for the as-grown PMMA oxide hybrid material and after polymer removal. Intriguingly, this SIS method allows for the growth of indium oxide (In_2O_3) films above 150 nm in thickness, at a remarkably linear rate of $\sim$12 nm per 100 nm of initial PMMA for each SIS cycle. Lastly, Hall probe measurements verify that ample electrical conductivity can be achieved in In_2O_3 films grown by SIS, establishing SIS as a viable synthetic method for transparent conduc-

tive metal oxides. The experimental/computational approach taken in this work can help enable the design of a wider range of primary SIS processes to further expand the functional material SIS library.

4.2 Results and Discussion

4.2.1 In Situ Fourier transform infrared (FTIR) Spectroscopy

Thin films of PMMA with 138 nm thickness were spin-coated from toluene onto 60 nm of an electron-beam-evaporated Au on a Si wafer substrate to enable infrared absorption spectroscopy in reflection mode. Toluene was chosen as an inactive solvent to SIS, as residual solvents that are Lewis basic can act as SIS sites in otherwise SIS-inert polymers. [54] A thick undoped Si window that is o-ring-sealed to a cutout in the flat growth chamber lid allows infrared probe beam access into and out of the ALD reaction chamber. In this configuration, and without any shutters, the probe may interact with the Si/Au/polymer thin-film substrates, as well as any vapor-phase precursors or byproducts present during extended static exposures. The temperature of the ALD chamber was held at 80 °C for all experiments in this work. The infrared absorption spectrum of a PMMA thin film referenced to a bare gold substrate, Figure 4.1a, reveals anticipated features near the characteristic functional group frequencies of PMMA, including 1738 cm^{-1} (C=O stretch) and 1152 cm^{-1} (C-O-C stretch). [212] The calculated vibrations (Perdew-Burke-Ernzerhof (PBE)) of the methyl methacrylate (MMA) monomer, plotted as red lines with chemical assignments, resemble the experimental spectrum for PMMA. In the absence of a polymer film, the gas-phase infrared absorption spectra of the metal-organic precursors in the ALD tool were also acquired and resemble the vibrational frequencies predicted from density functional theory (DFT) calculations of gas-phase monomers, Figure 4.2. Though an equilibrium between monomeric and dimeric TMA is present in the gas phase, we omit modeling the dimeric form for simplicity, as it may not solvate into the polymer film. [20, 213]

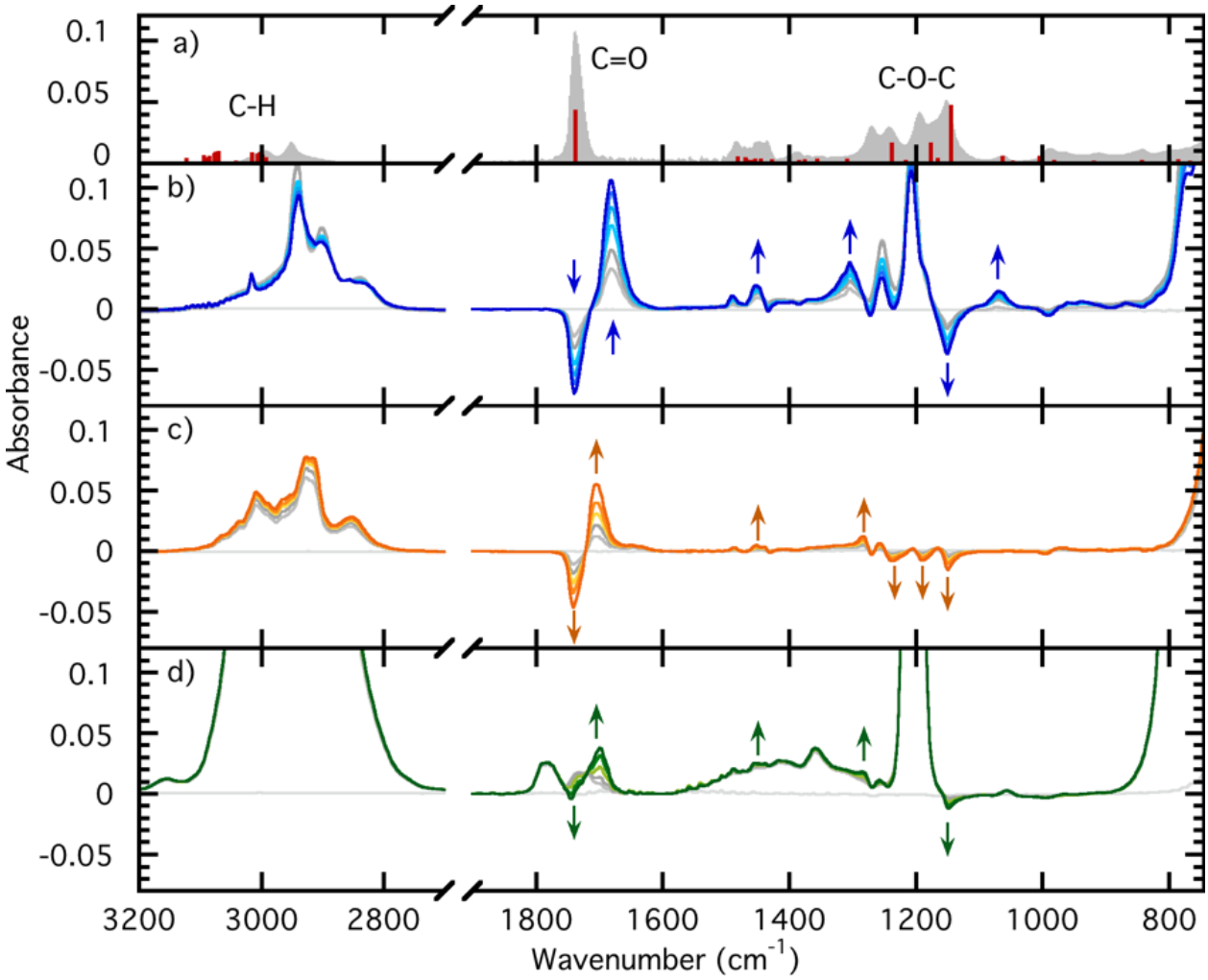

Figure 4.1: (a) Infrared spectra of a 138 nm PMMA thin film (gray regions) with vibrations of an isolated MMA fragment predicted from first-principles computation (red lines). Time-lapsed infrared difference spectra of PMMA thin film upon exposure to (b) TMA for 0, 47, 93, 186, 279, 372, 465 s; (c) TMIn for 0, 4, 5, 6, 7, 9 s; and (d) TMGa for 0, 3, 4, 6, 7, 9 s. Y-axis scaling is equivalent for all panels; however, times selected for TMIn and TMGa are at least 1 order of magnitude smaller than that for TMA.

In SIS, the static exposure of the polymer film to metal precursor vapor results in infiltration of the latter into the free volume of the former. The reversible association or irreversible reaction of the metal-organic molecules with the polymer film can perturb the vibrational frequencies of polymer functional groups and/or the metal-organic complex. Figure 1b depicts time-lapsed spectra, referenced to the pre-exposure PMMA film spectrum (Figure 4.1a), following the introduction of vapor-phase TMA into the chamber. The spectra include potential contributions from gas-phase TMA, infiltrated TMA, reversible TMA-PMMA adducts, irreversible TMA-PMMA species, and irreversible TMA-PMMA reaction byproducts. The signal attributed to TMA vapor is readily deconvoluted through comparison to gas-phase-only spectra, see Figure 4.2, and by noting that these peaks quickly saturate as the equilibrium pressure of TMA vapor in the reaction chamber is achieved within just a few seconds. In contrast, several peaks evolve over minutes timescale (labeled with arrows in Figure 4.1), which have previously been assigned as the signature of largely reversible TMA-PMMA adduct formation. [41, 43–45, 47]

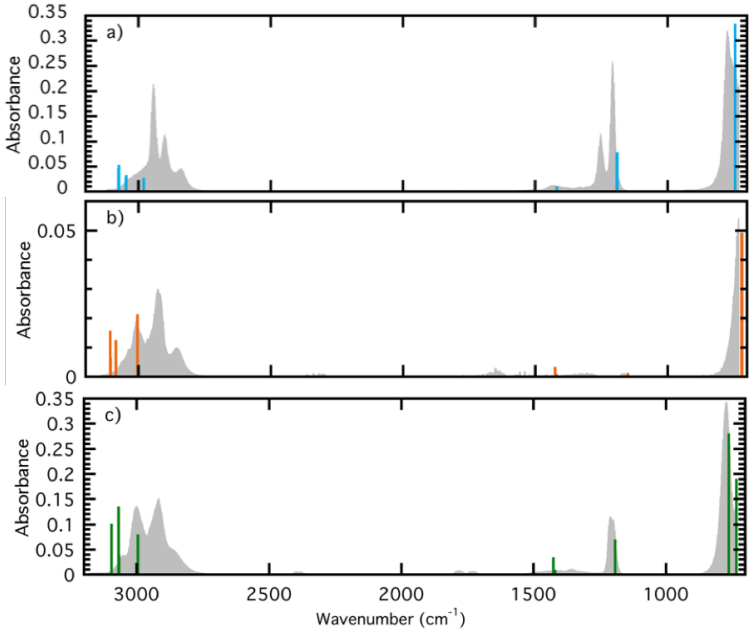

Figure 4.2: Infrared spectra of a gas phase a) TMA b) TMIn c) TMGa only (no polymer) overlaid with calculated vibrations of each precursor derived from first-principles computation (PBE).

Table 4.1: Vapor pressures of TMX compounds

Compound	Precursor Vessel Temp [°C]	Predicted Vapor Pressure [Torr]
TMA	25 (no heating)	11.5
TMIn	50	11.5
TMGa	25 (no heating)	227

For example, the carbonyl stretch of pristine PMMA at 1738 cm^{-1} is slowly bleached, while a new peak assigned to a C=O-Al$(CH_3)_3$ adduct grows in at significantly lower wavenumber, ∼1675 cm^{-1}. SIS with analogous group 13 metal alkyls, TMIn and TMGa, which have not been previously considered, results in qualitatively similar spectra. However, these grow in at a rate of at least 10× faster than the TMA case, Figure 4.1c,d. The timescale (seconds) of TMIn-PMMA and TMGa-PMMA associations would be surprising if purely diffusive transport of TMX precursors through PMMA was taking place, given their comparable size but significantly larger molecular weight relative to TMA. Instead, the more rapid bleach of the carbonyl stretch of PMMA supports a previously advanced hypothesis that diffusion through the PMMA is further controlled by the association/dissociation kinetics of the TMX-PMMA adduct. [44] A more detailed analysis of the association/dissociation kinetics is considered below.

The infrared spectra of the three TMX-PMMA adducts share many spectral features but also differ in significant ways. First, the C=O-In$(CH_3)_3$ and C=O-Ga$(CH_3)_3$ features are significantly less red-shifted ($\Delta\nu$ = 37 and 44 cm^{-1}) from the pristine PMMA C=O peak relative to C=O-Al$(CH_3)_3$ ($\Delta\nu$ = 66 cm^{-1}), which suggests that TMA forms the most tightly bound adduct. Second, the share of carbonyls participating in adduct formation varies significantly among the group 13 metals selected. The fraction of carbonyl groups associated with the metal alkyl precursors can be monitored through the absolute magnitude of the PMMA C=O bleach. The absolute value of the bleach in all cases is less than that of the pristine PMMA C=O absorption, which indicates that some population of carbonyls in the PMMA does not associate with TMX. A larger partial pressure of TMX was observed to increase the concentration of TMX dissolved in the polymer, which, in turn, increased

the equilibrium concentration of adducts. However, the energy of the PMMA-TMX adduct plays a role independent of the vapor pressure. For example, although much greater TMGa vapor pressures are achievable (Table 4.1), as is clear from the much larger alkyl stretching intensity of the vapor in the 2900 cm^{-1} region (Figure 14.1), the absolute magnitude of the equilibrium C=O bleach follows TMA > TMIn > TMGa.

Upon subsequent pumping of the SIS reaction chamber to rough vacuum, any noninfiltrated TMX vapor is quickly pumped away (<1 s). Therefore, shortly after pumping, the remaining vibrational features (still referenced to a pristine PMMA film) correspond exclusively to differences in the PMMA film (negative features/bleaches) or to the presence of a PMMA-TMX adduct (positive features/absorption), Figure 4.3. Time-lapsed spectra clearly reveal adduct dissociation (i.e., reversibility) in the case of all metal alkyls; however, the dissociation of C=O-Al$(CH_3)_3$ occurs on a timescale of at least 10× longer than for either TMIn or TMGa.

4.2.2 Density Functional Theory

First-principles DFT calculations were performed to identify the minimum energy conformations of three potential alkyl metal-MMA adducts, shown in Figure S3. The energies for each adduct for each TMX are tabulated in Table 4.2. The lowest-energy adduct for each of the three compounds was identified as the conformation in which the group 13 metal is proximal and roughly in line with the C=O bond. This lowest-energy adduct is nearly isostructural across each TMX molecule; therefore, only MMA-TMIn is shown in Figure 4.4. Though the same binding geometry is calculated to be the lowest-energy complex for each TMX (X = Al, In, Ga), the change in C=O stretching frequency ($\Delta\nu$) and Helmholtz free energy change (ΔF) upon complexation differs appreciably across the metals, Table 4.3. The vibrational frequencies of eigenmodes calculated for the minimum energy conformations are included for comparison to experimental spectra in Figure 4.3. This experimental shift in C=O stretching frequency upon MMA-TMX association, which is notably larger for MMA-TMA, is observed

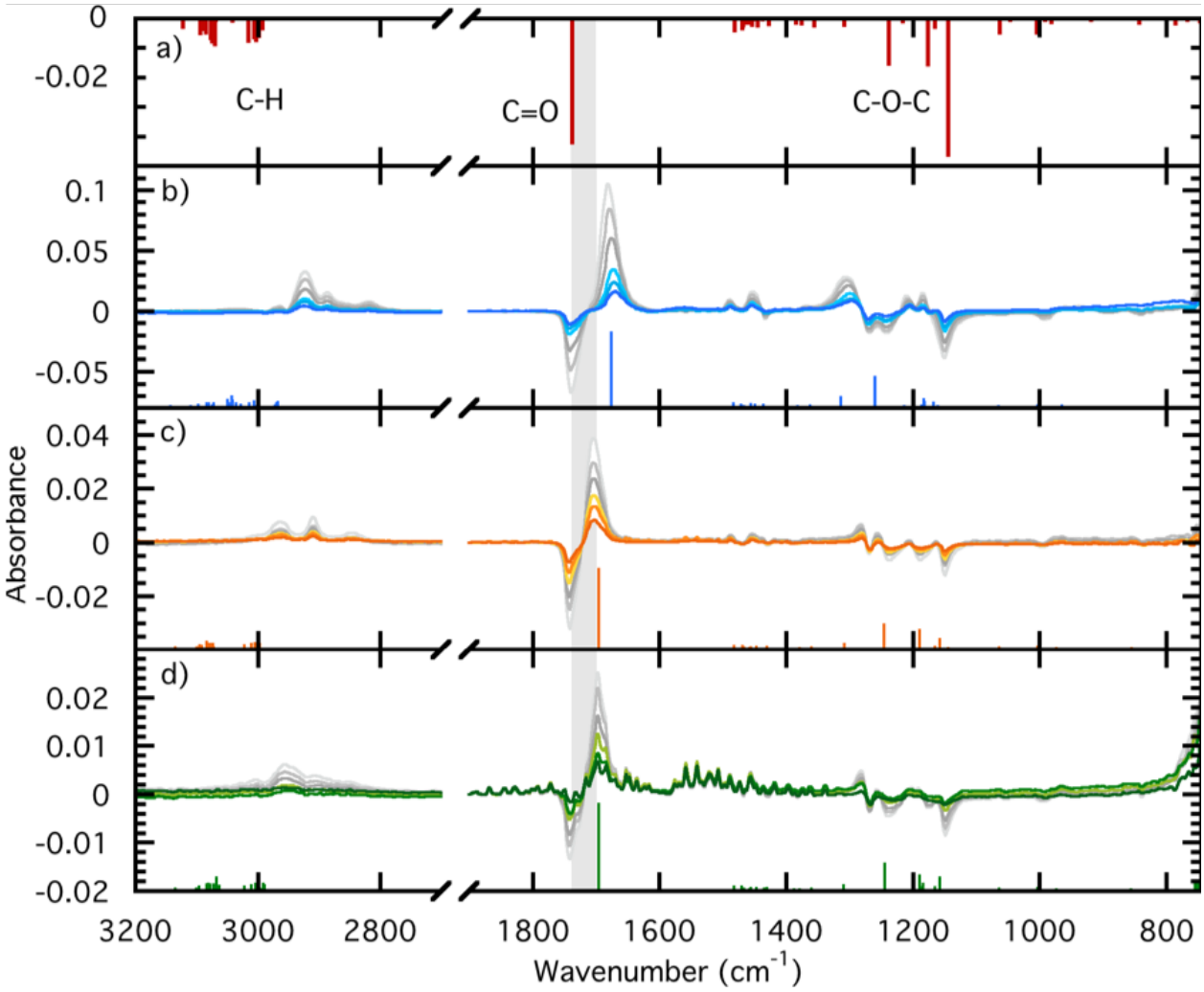

Figure 4.3: (a) Vibrations of an isolated MMA fragment predicted from first-principles computation (red lines) inverted to predict PMMA bleach signal. Time-lapsed infrared difference spectra of PMMA film thin after pumping; (b) TMA after 100, 300, 500, 700, 1000 s; (c) TMIn after 1, 4, 10, 30, 210 s; and (d) TMGa after 1, 4, 10, 30, 70, 210 s. The primary bleach and absorption peak after TMIn and TMGa exposures are highlighted for comparison to TMA. The vibrational frequency of computationally predicted modes of the lowest-energy TMX-PMMA complexes is also included below each experimental spectrum. The spectral time slices selected for TMIn and TMGa are at least $\sim$10 $\times$ shorter than that for TMA.

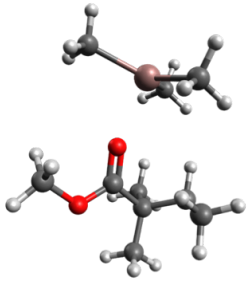

Figure 4.4: Lowest-energy configuration of the MMA-TMX adduct (X = Al, In, Ga). The atom coordinates of energy-minimized structures for each metal are similar, as reported in column b) of Table 4.2.

to be in good agreement with first-principles calculation. It is notable that the predicted infrared spectra for all of the other low-energy conformations do not share this excellent agreement with the experiment.

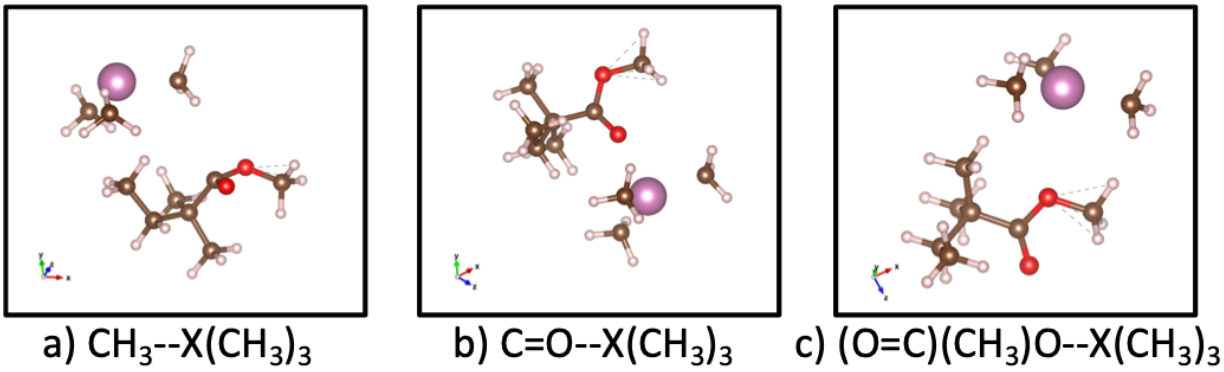

Figure 4.5: Energy minimized conformations of three low energy TMX-MMA adducts exhibited by each of three metals (X=Al, In, Ga). a) Interaction between the alkane chains of MMA and TMX is not a likely candidate shows shallow minimum in Table 4.2. b) Lowest energy configuration, where metal interacts with theoxygen of the carbonyl group, further supported by FTIR. c) Interaction between the metal and the C-O-C ester oxygen

Several other spectral features predicted for MMA-TMX association are also resolved experimentally and are agreement with computation. These include subtle changes to C-O-C vibrational modes near 1200 cm^{-1}, which show both a bleach of the pristine PMMA modes and new absorption features that are assigned to the adducts.

Table 4.2: Helmholtz free energies for the three TMX-MMA adducts for Al, In, Ga.

Compound	a) CH_3–X$(CH_3)_3$	b) C=O–X$(CH_3)_3$	c) (O=C)(CH_3)O–X$(CH_3)_3$
TMA	-0.000654 eV	-0.447eV	-0.0471eV
TMIn	-0.0875 eV	-0.165 eV	-0.0341 eV
TMGa	-0.0793 eV	-0.131 eV	-0.0768 eV

Table 4.3: Experimental and first-principles calculations of C=O frequency change, O-X distance, and calculated Helmholtz free energy change for MMA associations with TMX.

precursor	ν(cm^{-1}) [exp]	$\Delta\nu$(cm^{-1}) [exp]	$\Delta\nu$(cm^{-1}) [DFT]	distance (Å) [DFT]	ΔF@300K(eV) [DFT]
TMA	1675±6	66	60.2	1.974	-0.447
TMIn	1704±1	37	41.1	2.466	-0.165
TMGa	1697±1	44	40.8	2.277	-0.131

4.2.3 Kinetics

The more detailed kinetics of PMMA-TMX association and disassociation may be resolved through the analysis of the time-dependent intensity of distinct spectral features with fast (∼1 spectrum/second) in situ FTIR spectroscopy during and after TMX exposure. As previously noted, the first features to rise and saturate in each case are those assigned to gas-phase TMX, which saturates the reactor headspace within seconds of the ALD valve-opening. Next, as Figure 4.6 shows, the spectral features characteristic of the MMA-TMX association grow in and saturate on the timescale of seconds for TMIn and TMGa, while those of TMA saturate on the timescale of minutes. The minute-scale kinetics for association saturation of TMA ($\tau \sim 200$ s) into a 138 nm thick PMMA film corroborates previous reports. [43, 44] However, the rapid association saturation of TMIn and TMGa with PMMA ($\tau < 10$ s) is a striking departure that highlights the strong effect of adduct association strength on diffusion. The strong association of TMA with PMMA, as deduced from the first-principles calculation, may result in the rapid association of TMA to PMMA in the near surface. However, the strongly bound MMA-TMA adduct is expected to be slow to dissociate, which appears to block additional TMA from diffusing deeper into the film for further association. We posit that the lower affinity of TMIn and TMGa for PMMA relative to TMA allows

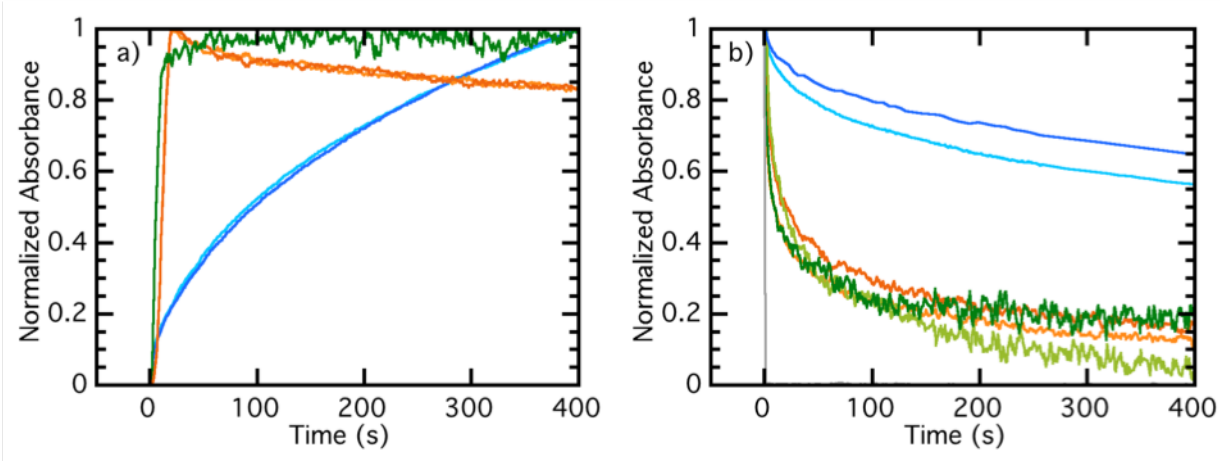

Figure 4.6: Infrared absorption kinetics of TMX (a) association and (b) dissociation with PMMA, where X = Al (blue), In (orange), and Ga (green). Normalized PMMA C=O bleach (lighter color, 1741 cm^{-1}) and C=O-X$(CH_3)_3$ adduct (darker color, see Table 4.3 for wavenumber) upon exposure to TMX. For comparison, the rapid rate of TMX precursor pumping of TMGa (gray, 1208 cm^{-1}), for example, is also shown in (b). The data in (a) are normalized to their maximum absorbance in the first 400 s of exposure. In (b), the absorbance is normalized to its value immediately preceding exposure to vacuum.

for much greater reversibility of association and therefore faster activated hopping diffusion deeper into the PMMA film. The minor intensity decay of the C=O-In$(CH_3)_3$ signal during long exposure follows the slow loss of TMIn gas from the SIS reaction chamber due to imperfect gate valve seal performance. This dynamic equilibration of PMMA-TMIn complex with variable gas-phase TMIn concentration is further evidence for the rapid association-dissociation of this adduct.

Upon pumping the SIS reaction chamber, the features assigned to gas-phase TMX in the headspace are, as expected, the first to be removed, Figure 4.6b. The rate of PMMA-TMX dissociation (and concurrent pumping of desorbed TMX as it is released) is again similar between TMIn and TMGa, but which is in stark contrast to TMA. The kinetics of TMA release fits a biexponential decay in which an initial faster component ($\tau \sim 85$ s, 25%) contributes less than a slower component ($\tau \sim 2000$ s, 75%). Both lifetimes are similar to those previously published for TMA SIS. [43,44] In contrast, the decay of vibrational signatures of TMIn and TMGa adducts with PMMA is significantly faster. The kinetics of TMIn

and TMGa dissociations also fits a biexponential decay; however, the faster ($11 < \tau < 23$ s) component accounts for the majority of the contribution (56-64%). The smaller contribution of the decay fits to a slower and more variable lifetime ($170 < \tau < 1400$ s). The difference in the kinetics of dissociation further suggests that the MMA-TMA is more strongly bound relative to the MMA-TMIn and MMA-TMGa complexes, in qualitative agreement with DFT simulations. However, a quantitative analysis of the biexponential decay kinetics is beyond the scope of this initial report. The temperature of the polymer film is an important parameter to approach in future quantitative kinetic studies, as temperature drastically affects the infiltration rate of TMX into PMMA, in terms of both the stability of the TMX-MMA adduct and the diffusivity of TMX in the film. [44, 45, 170] Likewise, fully irreversible reactions between TMA and PMMA to form PMMA-Al acetate have been recently observed at higher temperatures. [47] While the adducts described herein appear to be reversible within the timescales explored experimentally, the evidence of irreversible reactions between TMA and carbonyls has been reported for extended (hours) vapor exposures even at lower temperatures. [43, 44] Irreversible reactions between TMA and other Lewis basic functional groups on substituted phenyls have been observed, suggesting that single-component irreversible reactions between TMA and organic molecules can be designed across a wide temperature range. [214]

The significantly faster infiltration rates of TMIn/TMGa observed by FTIR suggest that these weakly complexing precursors would diffuse deeper into thick films than TMA would in the same exposure time. Thus, engineering weaker interactions between vapor precursors and polymer functional groups may be a route to overcome diffusion-limited deposition profiles for SIS in macroscopic polymer structures over practical timescales.

To successfully template the growth of metal oxides within PMMA via SIS, the TMX-PMMA complex must be quenched with a reactive oxygen source prior to complete dissociation and out-diffusion. For example, if we aim to utilize at least 70% of the adducts present under equilibrium with TMX gas, the oxygen source ("B half-cycle") must be sup-

plied within roughly 5 s of purging TMIn or TMGa. In contrast, more than 120 s of purging may be tolerated to capture at least 70% of the TMA-PMMA complexes present in a 140 nm PMMA film at 80 °C.

These differences present a fundamental experimental trade-off between compounds that are strongly bound to polymer functional groups (e.g., TMA and PMMA) and more weakly bound adducts (e.g., TMIn/TMGa and PMMA). TMA requires a much longer time to diffuse into and out of films relative to TMIn/TMGa; however, the long timescale offers a convenient experimental variable, purge time, to tune the deposition rate/cycle of the SIS process. [44,76] In the case of TMIn/TMGa under the same process conditions, the timescale for adduct dissociation and the diffusion of TMX out of thin films are comparable to the purge times necessary to prevent gas-phase mixing of reactants (chemical vapor deposition (CVD)) and therefore offer less fine-tuned control over growth rate. However, the rapid adduct formation rate suggests that In_2O_3 and Ga_2O_3 may be deposited much deeper into polymer thick films over experimentally convenient times, whereas Al_2O_3 may not.

4.2.4 Indium Oxide Film Growth

While the diffusion and association of TMA with PMMA have previously been investigated via FTIR, the time-resolved chemical effect of H_2O quenching (ALD analogous "B" cycle) has not. The first four full cycles of TMIn SIS (a 5 s TMIn pulse, a 400 s TMIn exposure, a 5 s purge, a 400 s H_2O exposure, and a 240 s purge) were probed with in situ FTIR to examine the involvement of PMMA in the chemical reactions that occur upon water exposure/quenching. The baseline and bleach of the C=O feature of pristine PMMA at 1741 cm^{-1} are roughly equal for each of the first four SIS cycles as shown in Figure 4.7. This suggests that the ester functionality is not consumed upon quenching of the PMMA-TMIn adduct with H_2O, but is instead released for future adduction with TMIn in subsequent SIS cycles. This is distinct from other reports with TMA, in which peaks associated with adduct-forming polymer groups are lost, indicating direct incorporation of the metal oxide or

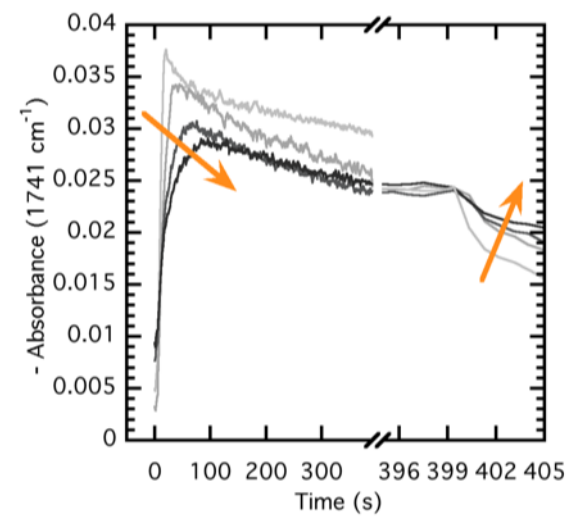

Figure 4.7: Absolute value of absorbance at 1741 cm^{-1} during SIS cycles 1-4 (from lighter to darker gray). The absorbance during cycle 1 (lightest gray) has been normalized after the x-axis break for better visualization of dissociation kinetics. The kinetics of association during absorption and dissociation during desorption are both measurably slower in successive cycles.

polymer chain scission. [41, 42, 47] The role that polymer functionalities play in subsequent secondary SIS cycles, which contain metal oxide surfaces in the film for the metal-bearing precursor chemisorption, is still an open question. Figure 4.7 suggests that the rate at which the adduct signature saturates systematically decreases with cycle number, which suggests a reduction in the diffusion rate as the PMMA is "filled" with $InO_x(OH)_y$. The changing diffusive landscape in the film is presumably affected by both physical and chemical changes as SIS proceeds. The physical presence of metal oxyhydroxide nuclei within the polymer free volume may block pathways previously accessible for adsorption and diffusion. Similarly, the rate of TMIn-PMMA dissociation also appears slowed, at least over the 5 s window allowed for TMIn gas purge before the introduction of H_2O.

With this mechanistic understanding of the rate of adduction and diffusion in the TMIn systems, the SIS-processing conditions for the growth of In_2O_3 in PMMA were explored. A series of samples were prepared with a total of 1, 2, 3, 5, 7, and 9 SIS cycles, where each SIS cycle consists of a (5-30-5-2-60-120) process sequence. This nomenclature refers to a 5 s pulse of TMIn vapor, 30 s of exposure to TMIn with a sealed vacuum valve,

followed by 5 s of pump and purge to vacuum, followed by a 2 s water pulse and 60 s of water exposure, and followed by a 120 s pump and purge. Reference silicon wafer samples included in this study showed no deposition of material by ellipsometry, which suggests that CVD-like reactions due to cross talk of vapor-phase precursors did not take place, despite the relatively brief (5 s) purge after TMIn exposure. In a second control experiment with a Si wafer, 200 cycles of a short (0.015 s, ALD-like) dose of TMIn followed by a very large water exposure (5 s dose + 60 s exposure, SIS-like) also showed no growth. Longer water purges are important to minimize the amount of water retained in the film for the next cycle of TMIn, which could otherwise provide a direct reaction pathway outside of primary or secondary SIS. In fact, water can be intentionally dosed before the metal-organic precursor to grow the material in polymers. [68] The PMMA was spin-coated to an initial film thickness of 148 $\pm$ 0.7 nm as measured by variable angle spectroscopic ellipsometry. The hybrid PMMA/(EMA) model fits two Cauchy-parameterized components of constant refractive index equal to the pristine PMMA thin film (A = 1.49, B = 0.00125, C = 0) and literature values for In_2O_3 (A = 1.9503, B = 0.036512, C = 0). [215] The total thickness of the as-grown film swells roughly linearly at a rate of 20.6 nm/SIS cycle, while the volume fraction of In_2O_3 begins to saturate over five SIS cycles, as Figure 4.8a demonstrates. Hybrid PMMA/Ga_2O_3 films that result from SIS were not systematically studied as a function of cycle number but also show a $\sim$2$\times$ increase in hybrid film thickness over four cycles, clearly indicating that Ga_2O_3 SIS takes place in a similar fashion.

Cross sections of these hybrid PMMA/In_2O_3 films were imaged by scanning electron microscopy (SEM) to assess the distribution of the inorganic deposit through the thickness of the film. Figure 4.9 shows the evolution of the film as a function of the number of SIS cycles. The left column shows standard SEM images of the film cross section, whereas the right column shows images collected using a detector that filters out secondary electrons and only collects backscattered electrons. While secondary electrons are generated from the sample itself as the beam electrons are decelerated and contain topographic information

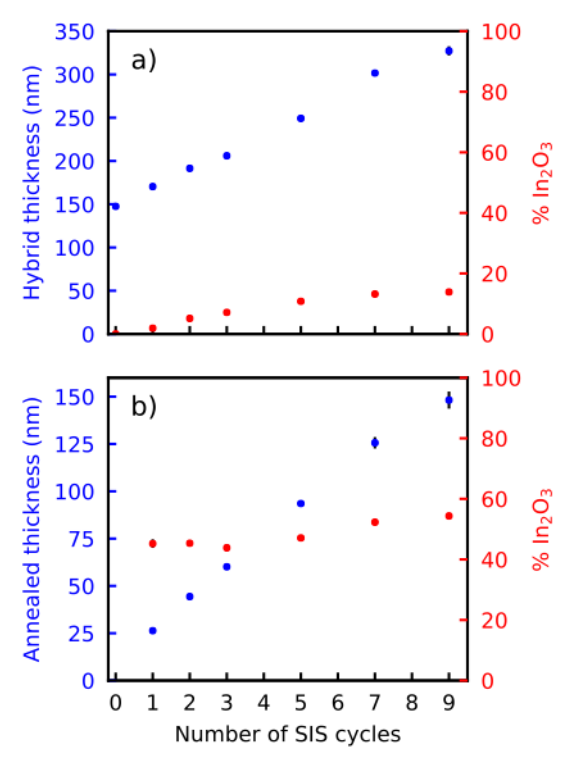

Figure 4.8: Spectroscopic ellipsometry-modeled thickness and composition of In_2O_3 SIS film growth for (a) as-grown composite of PMMA and In_2O_3 and (b) In_2O_3 films following polymer removal.

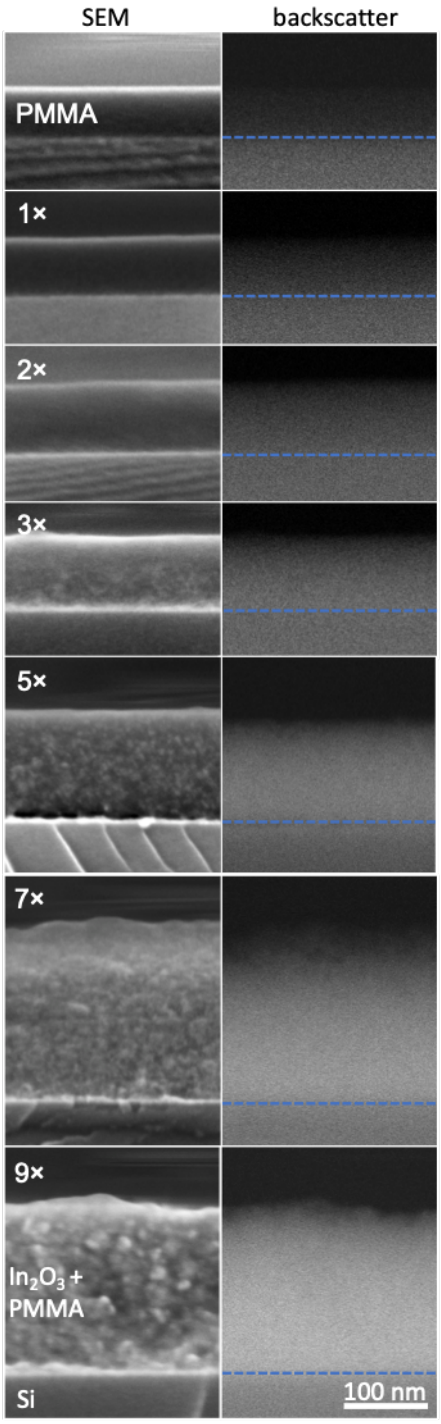

Figure 4.9: Cross-sectional SEM images of In_2O_3 SIS in PMMA thin films for increasing cycle numbers. The left-hand column shows SEM images that reveal topographic information, while the right-hand column displays only the higher-energy backscattered electron signal, in which brightness is indicative of high-Z elements. The blue dotted line is included as a visual cue of the film/substrate boundary.

about the surface, backscattered electrons are generated by the elastic collisions between the source beam and the sample. These backscattered electrons are typically of much higher energy and probe deeper into the sample. These backscattered electrons are more likely to be derived from high atomic number elements due to the elastic nature of the collisions by which they arise. Since In (Z = 49) is significantly heavier than the C, O, H, which constitute the initial PMMA film, the brightness of the backscattered signal can aid in determining the In_2O_3 distribution. For example, while the standard SEM image of the PMMA and the 1× SIS sample appear quite similar, the backscattered image for the SIS sample is considerably brighter, which indicates the incorporation of In_2O_3. Furthermore, the thickness of the 1× sample is increased relative to the pristine PMMA film. With increasing SIS cycles, the film continues to swell and some contrast or roughness becomes apparent in the topographic images, with apparent grains that increase in size with additional SIS cycles. The backscattered signal also increases with cycle number, though the intensity from the film surface to the substrate is relatively constant. This suggests that the 148 nm thick PMMA films are well within the diffusion length of the TMIn SIS process.

The maximum intensity of the backscattered signal is observed slightly below the film surface for each case, suggesting that the inorganic deposit at the film surface is of lower density than deeper into the film. This decrease in inorganic deposit density at the near surface has been observed in reports of SIS TMA using both time-of-flight secondary ion mass spectroscopy [31, 46] and cross-sectional energy dispersive spectroscopy. [100–102] This effect was proposed to emerge as a consequence of the local decrease of glass transition temperature and the increase of free volume in the near surface of polymer thin films. [131]

To assess the impact of diffusion-limited transport of TMIn on the through-film distribution of the resulting In_2O_3, a thick (> 500 nm) PMMA thin film was prepared with three SIS cycles. A cross section of this film was also imaged by SEM, Figure 4.10. The cross section of this thicker film reveals a clear transition from the hybrid material from the top ∼400 nm to the bottom ∼250 nm of the material. The top section reveals the

roughness/contrast that was observed across the entirety of the thin films in Figure 4.9. The lower section lacks this contrast and appears to have fractured with plastic deformation. Likewise, there is a clear decrease in the backscatter intensity at the bottom of the film, suggesting a significant drop in InO_x content. The bands in the backscattered intensity at the bottom of the film are likely an artifact of the nonplanar fractured surface. As anticipated from the kinetic studies, longer exposures would be required to achieve a saturated indium product profile in thicker films.

The as-grown films measured in Figure 4.8a were subsequently annealed at 400 °C in air for 3 hr to remove the polymeric content by pyrolysis. The ellipsometric response of the resulting films was fit to an EMA model with variable total thickness and fraction of In_2O_3 and void (air). The post-annealed oxide films, which range from 44 to 54% In_2O_3, exhibit a linear increase in thickness for each SIS cycle performed (∼17 nm/SIS cycle), Figure 4.8b. Therefore, the total swelling rate of the as-grown hybrid films slightly exceeds the final In_2O_3 growth rate of the annealed films. This lower rate is attributed to dehydration and densification of the as-deposited $InO_x(OH)_y$, while the polymer is simultaneously removed by pyrolysis at high temperature. Furthermore, changes in polymer free volume and chain conformation during SIS are not well understood and could impact the density of each component. The mesoporous nature of the annealed films was confirmed by top-down SEM images; however, the marginally increased density with cycle number as derived from ellipsometry fitting is difficult to corroborate, Figure 4.11. Figure 4.12 shows cross-sectional SEM images of the annealed films that further confirm their mesoporous nature and the approximately linear growth rate modeled through ellipsometry. The range of porosity and pore sizes possible is the subject of future investigations. Under these processing conditions, In_2O_3 is deposited at a rate of 12 nm per SIS cycle for every 100 nm of initial PMMA thickness.

X-ray photoelectron spectroscopy (XPS) surface analysis of the PMMA/In_2O_3 composite (as-grown), as well as annealed films, was performed on the samples described in

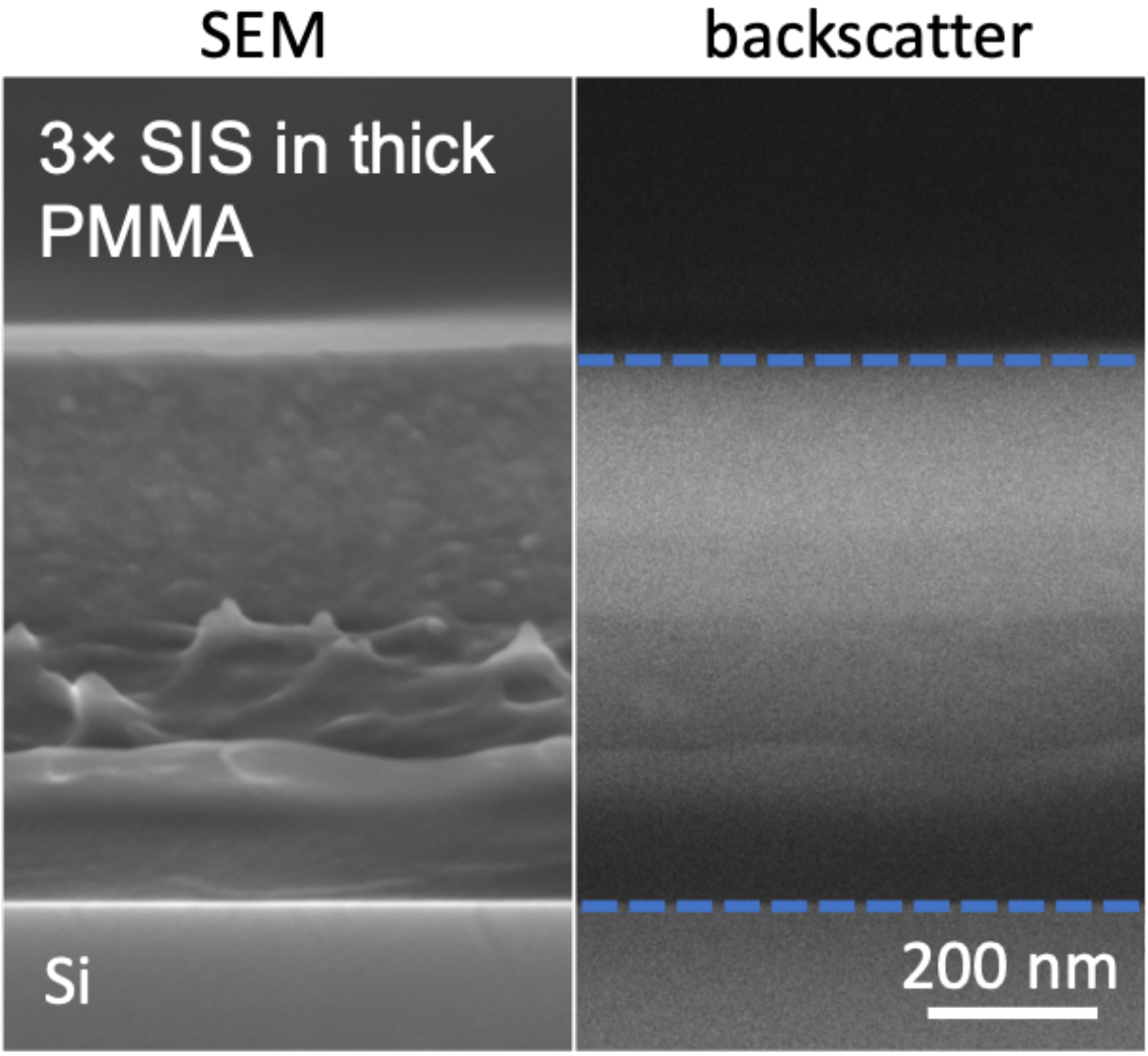

Figure 4.10: Cross-sectional SEM image of a thick (>500 nm) PMMA film after three cycles of In_2O_3 SIS. Morphologically, a clear transition between an In_2O_3-rich top layer and a plastic-deformed PMMA-rich bottom layer. The backscattered signal supports a diffusion-limited In_2O_3 gradient with a decreasing signal deeper into the film. Blue dotted lines at the film interfaces are included as a visual cue.

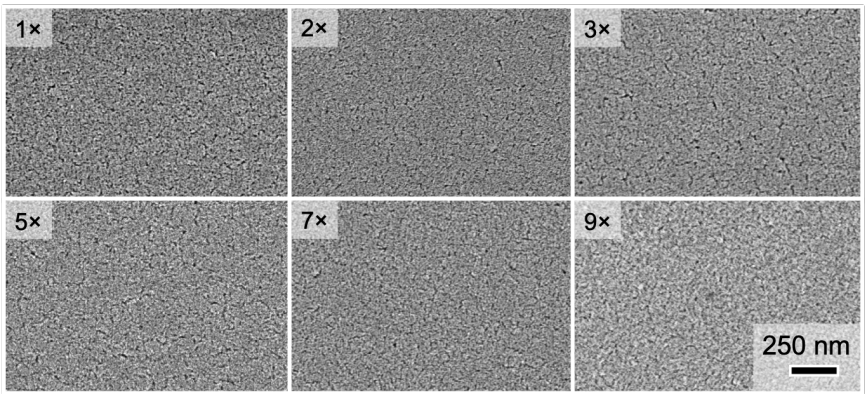

Figure 4.11: SEM images of the top surface of annealed In_2O_3 films grown in PMMA by SIS with increasing cycle number. The resultant films have an apparent porosity.

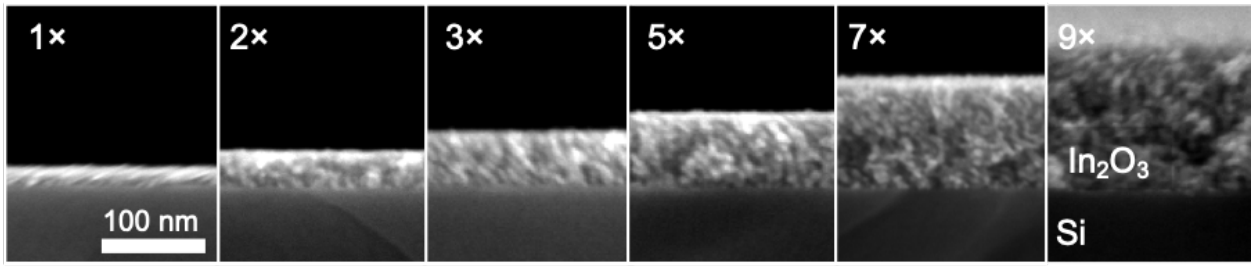

Figure 4.12: Cross-sectional SEM images of annealed In_2O_3 films for increasing SIS cycle numbers. A mesoporous morphology with increasing thickness is observed.

Figure 4.8 to assess the bonding environments of the SIS-grown In_2O_3 surfaces. The In 3d and O 1s regions for these materials are shown in Figure 4.13. The as-grown composite of PMMA and In_2O_3 has two distinct chemical environments as shown in the high-resolution In 3d and O 1s spectra where the dominant bulk oxide (In_2O_3) peaks (shaded blue) arise at binding energies of 444.6 and 530.9 eV for the In $3d_{5/2}$ and O 1s subshells, respectively. These peaks are shifted ∼0.5 eV higher than expected, [216] which may be due to PMMA-induced partial charging that may not be completely compensated by the electron flood gun. Both the In 3d and O 1s regions also have shoulder peaks (shaded green) of ∼533.4 eV that are attributed to the presence of surface OH groups associated with the In_2O_3, namely, $In(OH)_3$, as well as overlap with the O 1s contribution of the O-C=O moiety of the PMMA. [217, 218] Using the two-cycle case as an example, the relative concentration of $In(OH)_3$ and In_2O_3 in the as-grown $In2O_x(OH)_y$ and PMMA composite is 21%. After the removal of the PMMA by annealing in air, the relative amount of hydroxylated $In(OH)_3$ is also observed to decrease significantly to ∼3%. Similar trends are observed for other samples (1, 3, 5, 7, and 9 SIS cycles).

4.2.5 Water Exposure Effects

Irreversible reactions in the the SIS process may also be monitored through in situ FTIR of the reaction product gases evolved during exposure mode (closed-gate valve). The ALD growth of In_2O_3 thin films has previously been reported to occur with alternating exposures of TMIn and O_3; however, growth with H_2O at low temperature is surprising. [215] While ALD growth at much higher temperatures (250 °C) has been reported for TMIn and H_2O, the growth rate is quite slow. [219, 220] Still, in analogy to TMA and H_2O surface reactions, the most likely irreversible reaction byproduct during the low-temperature growth of TMIn and H_2O is methane. Methane may evolve upon the reaction of PMMA-TMIn with H_2O to form $InO_x(OH)_y$, as well as during TMIn reaction with $InO_x(OH)_y$ if available. The $InO_x(OH)_y$ produced during the first SIS cycle provides functional groups not present in

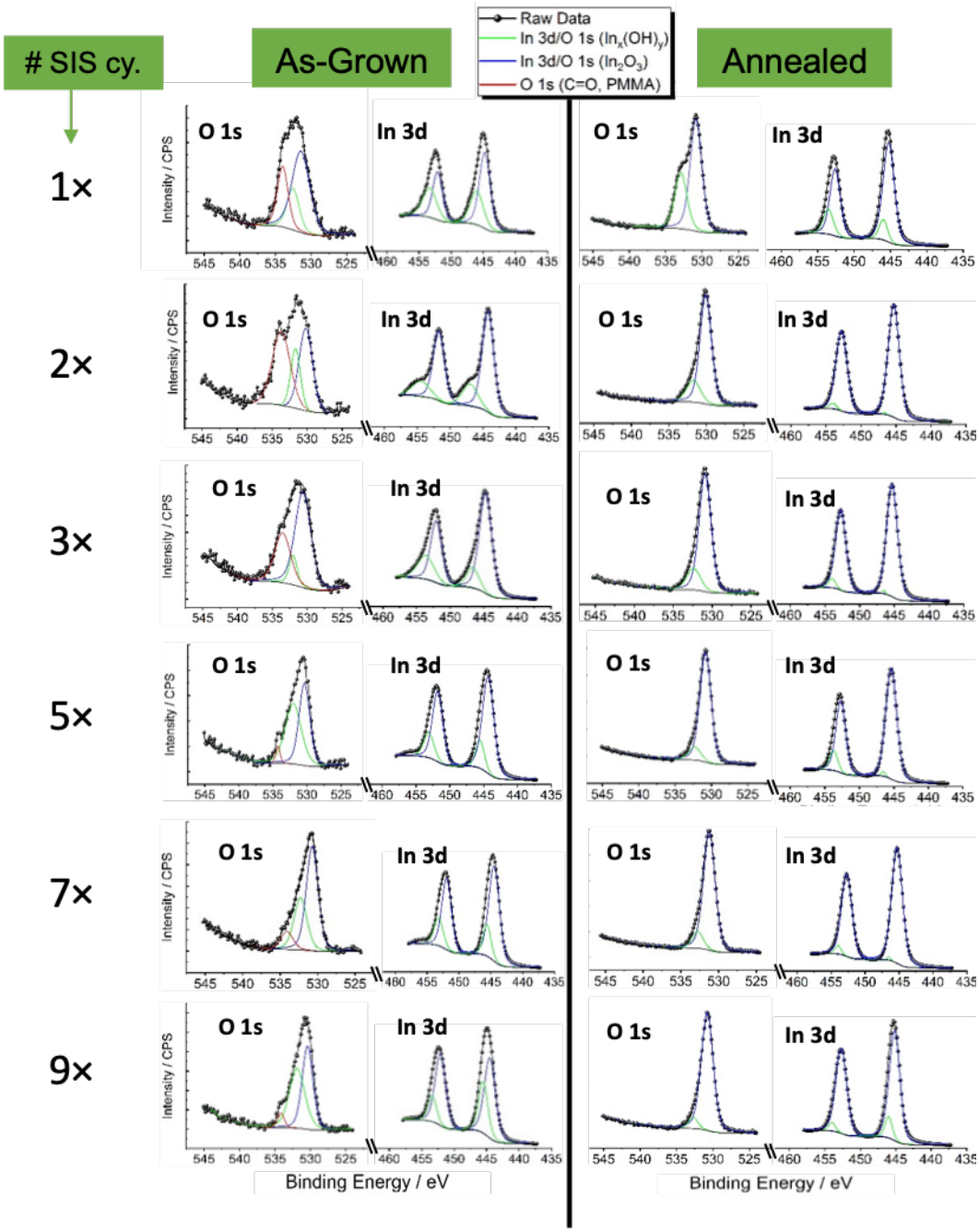

Figure 4.13: High-resolution XPS (HR-XPS) spectra of the O 1s and In 3d regions corresponding to the number of SIS cycles for as-grown In_2O_3-PMMA composite (left panel) and In_2O_3 films after PMMA removal (right panel).

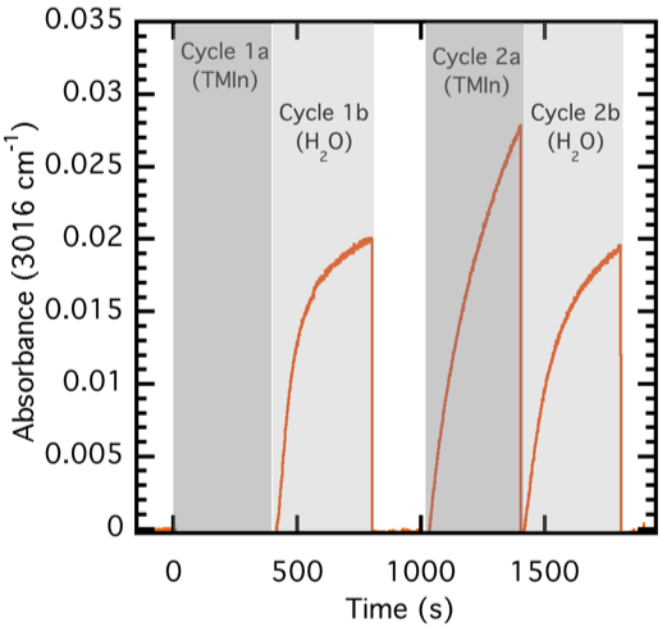

Figure 4.14: Absorbance at 3016 cm^{-1} after baseline subtraction, assigned to methane gas, reveals the irreversible reaction byproduct released during water exposure, as well as during the second, but not first, TMIn exposure.

pristine PMMA films. Therefore, as expected, the evolution of methane is not observed during the first SIS half-cycle (during TMIn exposure) as there are no hydroxyls with which to react, Figure 4.14. However, methane is clearly observed upon water exposure to the adduct in the first SIS cycle. Methane is also produced, as expected, during both the TMIn and water dose in the second cycle, as shown by the signature of methane gas as monitored at 3016 cm^{-1}.

The slow generation of the methane signal over hundreds of seconds of water exposure in the TMIn case is quite different from the case of TMA in which the "B" reaction is very rapid. In situ ellipsometry studies suggest that water diffuses through PMMA at an order-of-magnitude higher rate than TMA. [46] Unlike a TMIn-exposed surface, a TMA-exposed surface is also sufficiently reactive with water to enable ALD at low temperatures, even room temperature. [221] To assess the influence of water exposure time on the In_2O_3 SIS process, a series of samples were prepared in which the water exposure was varied between 5 and 240 s. Each experiment was performed for five total SIS cycles on PMMA spin-coated

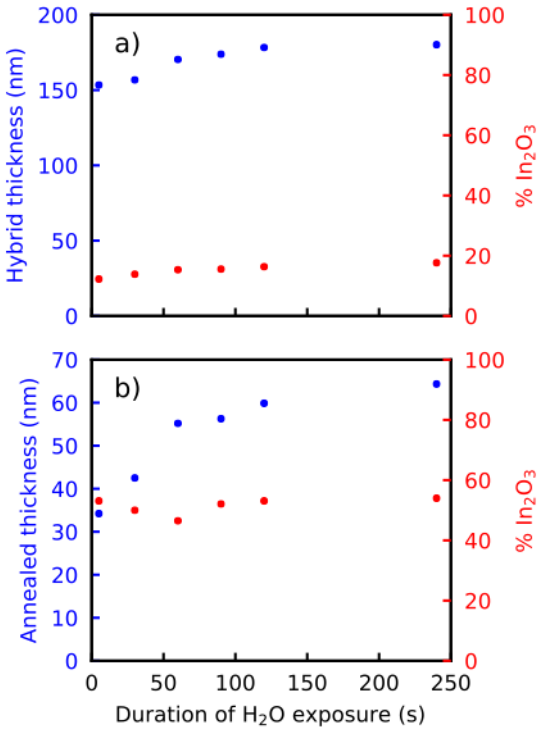

Figure 4.15: Thickness and composition of In_2O_3 SIS film growth for (a) as-deposited film after five SIS cycles and (b) films post-annealed in air as a function of water exposure, as determined by spectroscopic ellipsometry.

to a thickness of 146 nm on Si wafers. The thicknesses of the as-grown films and annealed In_2O_3 films were measured and modeled as previously.

Figure 4.15 reveals that the as-grown hybrid film thickness begins to saturate at water exposures of >120 s and that the In_2O_3 fraction saturates even more slowly. While the porosity of the annealed In_2O_3 films is relatively constant, the total annealed In_2O_3 film thickness begins to saturate for water exposures of >120 s. A far lower reactivity for hydrolysis of the second and third alkyl groups of TMX has also been reported in solution systems. [222,223] Taken together, the notably slow reaction kinetics of adducted TMIn with H_2O implies that the duration of water exposure is an important variable in In_2O_3 SIS.

4.2.6 Polymer Selectivity

SIS is particularly well suited to transform self-assembly materials like block copolymers into hybrid inorganic nanostructures. [32, 39, 52, 76, 84] SIS works in this context due to the selectivity of the deposition between polymers. For example, in the ubiquitous PS-*b*-PMMA BCP, polystyrene (PS) is inert to the metal precursor adduction, whereas PMMA, with its Lewis basic ester groups, will adduct some metal precursors, thereby retaining them for much longer. Figure 4.16 shows a ∼30 nm thick symmetric vertical-lamella-forming PS-*b*-PMMA BCP thin film. A neutral surface energy copolymer mat was used to promote the vertical morphology. [224] The inset of this image shows the phase-separated BCP film before SIS. Five cycles of In_2O_3 SIS, followed by the thermal removal of polymer, reveal In_2O_3 nanowires that have directly templated the PMMA domains. This experiment demonstrates that the TMIn SIS process shows selectivity analogous to TMA in PS-*b*-PMMA BCPs.

4.2.7 Electronic Property Characterization

In_2O_3, particularly when doped with Sn/Zn, is of technological interest for its good optical transparency combined with low electronic resistivity. [225] In_2O_3 has been extensively studied and grown by various methods including magnetron sputtering, [226] pulsed laser

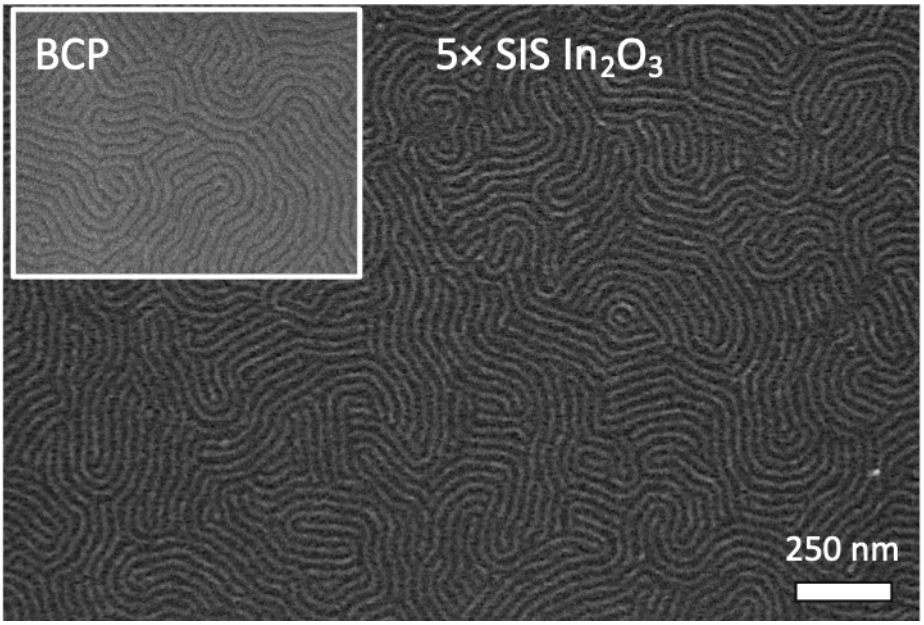

Figure 4.16: SEM image of SIS of In_2O_3 in vertical-lamella-forming PS-*b*-PMMA BCP followed by thermal annealing for polymer removal. Indium oxide deposition is restricted to the PMMA and not in the PS. The inset of the BCP film before processing shows that the original phase-separated morphology is retained after SIS processing.

deposition, [227] and electron beam evaporation. [228] We briefly examine the electrical properties of SIS-grown In_2O_3 thin films grown on Si substrates with a 1 μm insulating thermal SiO_2. After SIS, PMMA was removed via exposure to UV-ozone and subsequently annealed at 400 °C in a reducing environment (3% H_2 in N_2) to promote oxygen vacancies that provide charge carriers in undoped In_2O_3. [211, 229, 230]All films, including those that received only a single SIS cycle, exhibit electrical properties characteristic of undoped In_2O_3 thin films, Figure 4.17. Effective carrier concentrations are -1 $\times$ 10^{20} cm^{-3} and mobilities are in the range of $\sim$10 cm^2 $V^{-1}s^{-1}$, as may be expected for the annealed samples, which show crystallinity by X-ray diffraction (XRD) (see Figure 4.18). Using the Scherrer formula for spherical nanocrystallites, the domain size of 10 cycles of annealed In_2O_3 was estimated to be 27 nm. No clear diffraction peaks were observed in XRD measurements of hybrid PMMA/In_2O_3 films prior to annealing. Resistivities of these annealed films, were of the order of 10^{-3} Ω-cm, independent of the number of SIS cycles, which is comparable to the values reported for other ALD-grown In_2O_3 films. [220, 231, 232] Future studies will be required to

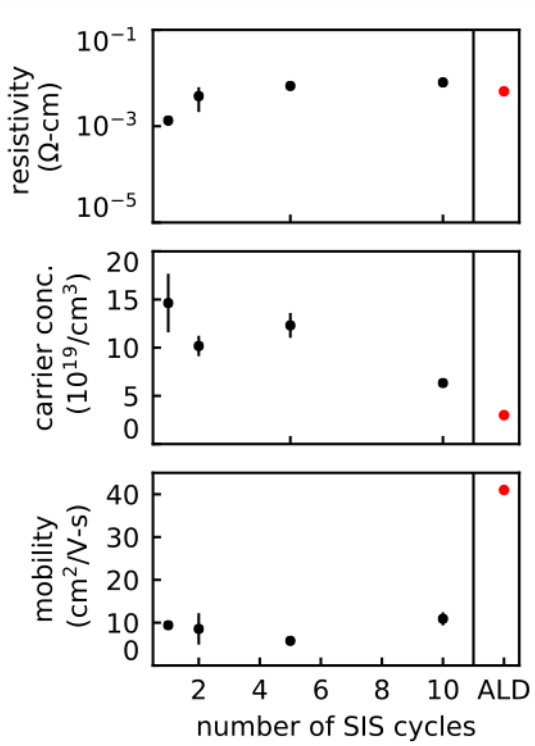

Figure 4.17: Conductivity, carrier concentration, and mobility of SIS-derived In_2O_3 thin films as a function of SIS cycle number after annealing in a reducing environment.

correlate more detailed effects of atomic connectivity, porosity, and oxygen vacancies on the carrier concentration and Hall mobility of conductive metal oxide films grown by SIS.

4.3 Conclusion

We demonstrate a rational expansion of the primary SIS material library to include two electronically functional materials, In_2O_3 and Ga_2O_3. Infrared spectroscopy of metal-organic infiltration and association kinetics, supplemented by DFT calculations of TMX-MMA configuration and binding energies, inform SIS-processing conditions, which yield ample deposition of In_2O_3. A comparison of TMIn and TMGa to the canonical example of TMA reveals that the latter reversibly binds more strongly to the carbonyl functional group in PMMA. Though FTIR evidence suggests that slightly more TMA associates are within a given volume of PMMA for an equal partial pressure in the long-time limit, a much lower barrier to

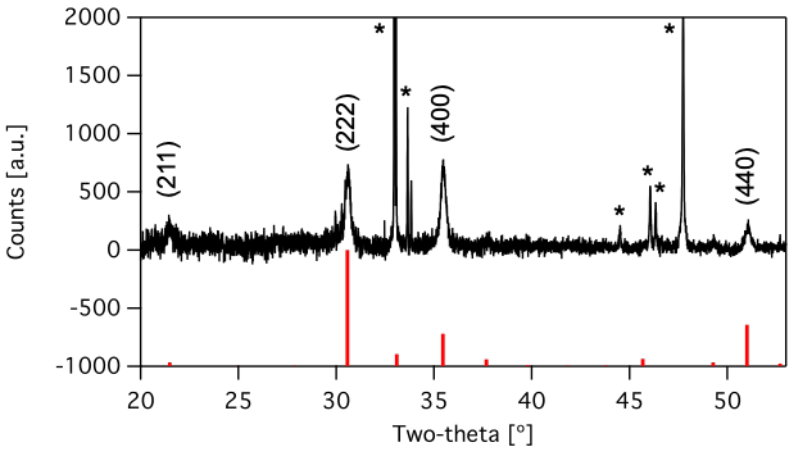

Figure 4.18: XRD spectrum of 10 cycle SIS-derived In_2O_3 thin films after polymer removal and post-annealing. Reference peaks (red vertical lines) are from JCPDF In_2O_3 (01-073-6440). Sharp peaks marked by asterisk (*) originate from 1 μm-thick SiO_2 coated Si substrate.

activated diffusion for TMGa and TMIn enables more complete saturation of adduct formation in many short times. Surprisingly, TMIn SIS at a low temperature and with H_2O enables tens-of-nanometers thick In_2O_3 film growth under conditions that would produce no ALD deposition on flat inorganic substrates after hundreds of cycles. The effects of polymer conformation and composition, along with alternative oxygen sources, [49] may enable further tunability of the structural and electronic properties of SIS derived materials.

4.4 Materials and Methods

Density functional theory: First-principle density functional theory calculations were performed using the FHI-aims code (fhi-aims.171221_1). [233] We used the "tight" default settings for basis functions, mesh, and angular momentum decomposition. A molecular fragment consisting of five carbon, two oxygen, and eight hydrogen atoms was used for the methyl methacrylate model. Initial configurations of the MMA-TMX complexes were explored using rapid minimization in the JMOL package. [234] These configurations were subsequently used as input for the FHI-aims structural optimizations with the PBE0 exchange-correlation (xc) functional [235] and with maximum forces of 0.001 eV $Å^{-1}$. Analogous structural optimiza-

tions were performed for the TMA, TMIn, and TMGa molecules. Vibrational spectra were calculated using the aims.vibration wrapper with the PBE xc-functional. Structures were first optimized with PBE xc-functional [236] until maximum forces were less than 0.0004 eV $Å^{-1}$. The dynamical matrix was subsequently calculated by displacing the atoms ±0.001 to 0.0025 Åalong the Cartesian directions and calculating the concomitant change in potential energy and then diagonalizing the dynamical matrix. We checked that the six null-space modes had frequencies close to zero and were well below the frequencies of the physical vibrational modes. We did a few vibrational calculations using the PBE0 xc-functional and observed no significant differences in vibrational spectra. Energy differences between the bound MMA-TMX compounds and the free MMA fragment/TMX components were calculated using the PBE0 electronic energies, and rotational and vibrational free energies at 300 K from PBE vibrational and rotational spectra. The vibrational frequency (in cm^{-1}) of all computed eigenmodes was uniformly increased by 1.2% to match the major feature (C=O stretch) of the PMMA experiment to theory.

Sequential infiltration synthesis: SIS experiments were conducted on a Veeco/ Cambridge Savannah ALD with lid modified to allow the entry and exit of an infrared beam at an angle of approximately 30° after reflection off an IR-reflective sample. In all experiments, the temperature of the growth chamber was held at 80 °C. The TMIn precursor was heated at 50 °C to boost its vapor pressure, while the TMA and TMGa precursors were unheated. All processes utilized a constant N_2 flow of 5 sccm. PMMA films were held in the chamber under a N_2 flow and rough vacuum for at least 10 min before beginning SIS to drive off water. SIS sequences consist of dose, exposure, and pump/purge steps for both the TMX precursor and water. The dose time describes the duration over which the ALD valve is opened to allow the desired precursor to fill the growth chamber. Prior to the dose, the stop valve is closed, isolating the reactor from the vacuum pump. The total exposure time is the sum of the dose time and exposure wait time, during which the precursor is held in the sample chamber and N_2 continues to flow. Finally, the stop valve is opened end to

the precursor exposure and begin the pump/purge. After the TMX purge time has elapsed, the stop valve is again closed, water is dosed, a wait period controls the exposure time, and finally, the growth chamber is pumped/purged to complete a single SIS cycle. Typical SIS film growth is performed with a (5-30-5 — 2-60-120) cycle sequence. This nomenclature refers to a 5 s pulse of TMIn vapor, 30 s of exposure to TMIn with a sealed vacuum valve, followed by 5 s of pump and purge to vacuum, followed by a 2 s water pulse and 60 s of water exposure, and followed by a 120 s pump and purge.

Fourier transform infrared (FTIR) spectroscopy: FTIR spectroscopy was performed using the external beam from a Bruker Vertex 70 that was focused by the off-axis parabolic gold-coated mirror and directed through a thick undoped Si wafer that served as an infrared window to the growth chamber. After reflection off of the gold-coated sample, the infrared beam exits through the same long Si window before being focused by a second off-axis parabolic goal-coated mirror and finally detected with an external LN_2-cooled MCT A detector. Typical acquisition parameters averaged 4 scans at 4 cm^{-1} resolution with a scanner velocity of 40 kHz, resulting in a $\sim$1 spectrum/sec. As the FTIR studies focus on TMX precursor dynamics, a purge time after the completion of exposure (>400 s), which is much longer than that used for SIS (5 s), was used to study the kinetics of TMX dissociation.

X-ray photoelectron spectroscopy: XPS experiments werecarried out using a Thermo ScientificK-α+ spectrometer with a microfocused monochromatic Al Kα (1487 eV) X-ray source with a spot size of 400 μm for the surface analysis. Operational pressures were $\sim$7 $\times$ 10^{-9} Torr with a dual-beam electron flood gun charge compensation used for all measurements. Regions of interest for In 3d, O 1s, and C 1s HR-XPS measurements were scanned with a pass energy of 50 eV. HR-XPS spectra shown herein are after a 5 s low-energy Ar+ sputtering (1 kV) treatment to remove surface-bound contaminants, and due to the presence of the PMMA polymer, HR-XPS spectra were not charge-corrected relative to the C 1s peak for adventitious carbon at 284.8 eV. Spectral postprocessing and fitting were performed in Thermo Avantage (version 5.977, Build 06436) software using 30% Lorentz-mixed Gaussian

line shapes and Smart backgrounds in all cases.

Spectroscopic ellipsometry: Ellipsometric spectra were acquired on a J.A. Woollam α-SE tool over the 380-900 nm band at 65, 70, and 75° using 10 s normal acquisitions. Data were acquired and fit using CompleteEase software.

Scanning electroscope microscopy: SEM images were taken on a Carl Zeiss Merlin microscope at an accelerating voltage of 5.52 kV and a working distance of 3 mm. Cross-sectional samples were cracked under liquid nitrogen to preserve morphology and mounted on 90° vertical stubs. Standard images were collected using the InLens electron detector, while backscattered electron images were collected using the energy-selective backscattered electron detector with the filtering grid set to 500 V to deflect topographic secondary electrons.

Atomic force microscopy Noncontact (intermittent) mode AFM images were acquired in ambient conditions using the Asylum Research MFP-3D microscope and Nanosensors PPP-NCH AFM probes (204-497 kHz resonance frequency range). AFM images were processed using Gwyddion software.

X-ray diffraction XRD spectra were collected using a Bruker Diffractometer D8 Advance. Cu Kα radiation: 40 mA, 40 kV, Kλ = 0.154 nm; a scan step size = 0.006° (1 s per step)

Hall effect measurements The carrier concentration and mobility of In_2O_3 films deposited on Si wafers with thick thermal oxide were evaluated using a Hall effect measurement system (Ecopia HMS-3000) with a 0.57 T permanent magnet.

CHAPTER 5

THE CASE FOR ISOPOROUS MEMBRANES: NUMERICAL ANALYSIS OF SELECTIVITY AND ENERGY EFFICIENCY

5.1 Introduction

Researchers aim to improve membrane performance along two metrics: selectivity and permeability. Though the precise definition of these terms is context-specific, in general, selectivity refers to how well a membrane performs at separating components and permeability refers to the throughput of fluid the membrane can process. Membranes are generally recognized to be limited by a selectivity-permeability tradeoff; the better a membrane is at separating similar components, the lower its permeance will be. This principle is most commonly discussed in the context of diffusion-driven membranes for gas separations and desalination/reverse osmosis. [237,238] This chapter, in contrast, focuses on the analogous tradeoff in the context of convection-driven ultrafiltration/nanofiltration membranes used in water purification.

The primary energy expenditure in the context of convection-driven membrane operation is the supplied transmembrane pressure. To reduce the costs associated with supplying pressure, the membrane permeance should be maximized. At the same time, significant research effort has been devoted to highly selective separations in this pore size regime (10-100 nm), particularly toward the goal of isoporous membranes in which all of the pores are the same size. In light of the attention in the community to isoporous structures, in this paper we discuss the relationships between membrane pore-size distribution, membrane selectivity, and membrane permeance, along with the methods researchers have employed to achieve isoporosity. We introduce a numerical model that weighs pore-size distribution and projects under which regimes of fluid flux and size-selectivity it would be appropriate to pursue extremely narrow pore-size distributions and, conversely, when the costs of these effort outweigh potential improvements.

5.1.1 Membranes and Energy

The relationship between a pressure-driven membrane and the energy it takes to operate is dictated by its permeance — the flux achieved for a given applied transmembrane pressure. [1] The simplest expression for this relationship is based on the Hagen-Poiseuille (H-P) equation, which describes laminar flow through a pipe:

$$v = \frac{\pi r^4 \Delta P}{8\eta L} \tag{5.1}$$

This equation is valid when$L$, the length of the pipe, far exceeds$r$, the radius of the pipe. ΔP is the pressure difference across the pipe, η is the kinematic viscosity of the fluid, v is the flow rate of the fluid through the pipe in units m^3s^{-1}. Corrections to the H-P equation in thin and low aspect-ratio membrane selective layers, known as orifice effects, have lower order dependencies on r, and are thus safely ignored. [239] The H-P equation can be generalized to a non-tortuous membrane of contstant thickness L consisting of N pores:

$$v_{\text{total}} = \sum_{i=1}^{N} \frac{\pi r_{\text{i}}^4 \Delta P}{8\eta L} \tag{5.2}$$

The isoporous membrane is the limiting case in which each pore is identical in radius. In such a membrane, there is no need to index r in 5.2, and the total flow rate can be just multiplied through by N. Converting this total flow rate into a flux requires knowledge of the membrane porosity ε, which is the area ratio of pores to total membrane surface. Considering N pores the flux would be:

$$F = \frac{\varepsilon * v_{total}}{A_p} \tag{5.3}$$

where A_p is the total pore area for N pores. ε varies widely across the various types of membranes, because it maximizes the density of pathways for fluid flow per area of membranes. Polymeric membranes formed by phase inversion processes exhibit a wide range of ε values,

from as low as 0.4 to 0.9, as a consequence of particular processing details. [240] In such highly tortuous membranes composed of networks of polymer ligatures, ε is often calculated as the ratio of pore volume to total membrane volume. In track-etched membranes like polycarbonate, ε can range between 5 and 15%. [241] Isoporous membranes, such as those under development in academic research, have been fabricated with high porosities.

The H-P equation predicts a linear relationship between the applied pressure across a membrane and the resulting flux. This relationship is usually observed across the normal operating conditions of the membrane at steady-state, though phenomena such as initial compaction of the membrane, cake formation, and fouling, lead to a decline in flux over time. [242, 243]

Since the applied transmembrane pressure is the primary recurring energy cost in membrane operation, it is vital to maximize the permeance of the membrane while still meeting separations goals. The transmembrane pressure is supplied by pumps, which must be powered by the operator. Since pressure is the energy density of the fluid, the power required for a pressure-driven membrane process is inversely proportional to its flux. Given that the volume flow rate scales by r^4, using the membrane with the biggest possible pores while still achieving one's target rejection should be the most energy-efficient approach.

Fluid transport through porous membranes is governed by both convection and diffusion. The Peclet number is the ratio of these two transport modes, and in under the pore dimensions considered here, this number is much greater than one, meaning convection (specifically bulk flow in response to the applied pressure) dominates. [244] When the hydraulic radius of the solute is on the order of the pore dimension, convection of solutes through the pore is hindered relative to solvent. Counterintuitively, then, solutes smaller than pores can be separated by those pores, [245] which can be accounted for by rejection models. [246] Pore rejection models can also take electrostatics, solute/pore and solute/solute interactions, and other hydrodynamic effects into account. [247–249]

The distribution of different pore sizes in a membrane thus affects both permeance

and overall rejection and is a consequence of the membrane fabrication process. Polymeric membranes formed by phase inversion processes are well described by log-normal distributions of pore radii. [250–252] This characterization is based on direct imaging of the pore surface, rejection of standard solutes, [253] and various porosimetry methods. [254–257] Multiple experimental methods are used in these characterizations as polymeric membranes vary in pore size, porosity, and tortuosity throughout their thickness. [258]

The log-normal distribution describes a distribution where the logarithm of the values fall on a normal distribution, such that:

$$X = e^{\mu+\sigma Z} \tag{5.4}$$

Here μ and σ are the mean and variance of the underlying normal variable Z. Typical phase-inversion ultrafiltration membranes have mean-pore normalized variances of 0.2, when experimental particle rejection data are fit to the log-normal distribution. [244] The morphology and characteristics of such membranes are detailed in Figure 5.1a. There are other types of membranes whose pore dimensions are normally distributed (Figure 5.1b). The most common types are track-etched polymer membranes [259] and anodized aluminium oxide membranes. [260] The rejection profiles of these types of membranes are generally sharper than membranes with broader log-normally distributed pores.

5.1.2 Isoporous Membrane Fabrication

Isoporous membranes are those with pore size and shape distributions approaching a delta function — an idealized scenario in which each pore has an identical rejection profile. In this idealized scenario, the isoporous rejection would resemble a step function, with perfect rejection above some critical solute size, and complete permission below this solute size (Figure 5.1c). (This idealized scenario assumes convective hindrance can be ignored.) Motivated by the sharp rejection profiles expected from such membranes, [261] researchers have

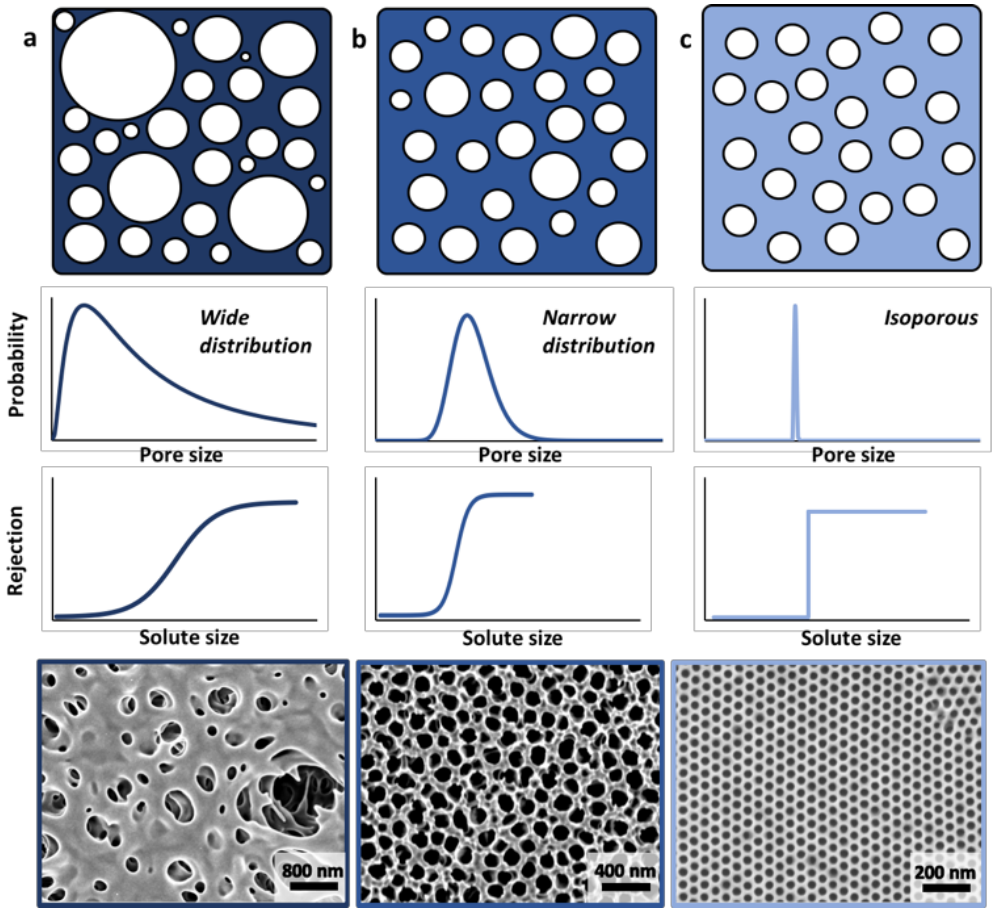

Figure 5.1: Characterizing model membrane pore size distributions. The first row is a cartoon illustrating the pore surface view of a) log-normal pore distribution, b) a normal pore distribution, and c) an isoporous distribution. The second row shows the shapes of continuous pore size probability functions for the three membrane types. In the limiting isoporous case, the probability density function is a delta function. The third row is the rejection of the various membranes. The transition from solutes passing to being rejected sharpens as the pore distribution shrinks. In the idealized isoporous case, rejection would approach a step function, with the caveat that convective hindrance effects are neglected. In the last row, SEM micrographs show real-world examples of the three distribution classes. A phase-inversion polyethersulfone membrane, an anodized aluminium oxide membrane, and a BCP-derived aluminum oxide membrane.

developed many techniques to achieve membranes approaching isoporosity across a range of pore scales, each with their own advantages and disadvantages. [262] With few exceptions, isoporous membrane fabrication techniques suffer from limitations of scalability.

Like many other nanotechnologies, isoporous membrane fabrication strategies can be characterized as either top-down or bottom-up. Top-down approaches to isoporous membrane fabrication rely on lithographic techniques such as photolithography, electron-beam lithography, and nanoimprint lithography. [263] Individual nanopores of tunable dimension have been drilled through ultrathin inorganic materials with techniques such as focused ion milling, [264] high intensity electron beams, [265] and ion track etching. [266] Hot-embossed polymer resist layers have been used as masks for the transfer of pores into Si_3N_4. [267] Larger millimeter-scale arrays of sub-micron pores in ultra-thin ceramics have been demonstrated via several lithographic techniques. [268, 269] Furthermore, pores can be etched directly into polymer layers via ion beam exposure through lithographically-defined stencils in a process termed aperture array lithography. [270] Many of these techniques involve expensive and energy-intensive cleanroom microfabrication processes, which limit their commercial applicability. While these devices may find niche applications in microfluidic biomedical contexts where minute fluid volumes are processed, [271–273] they lack the mechanical durability [274] and scalability to address global water challenges.

Bottom-up approaches to isoporous membrane fabrication rely on controlled self-assembly phenomena to arrange micron or sub-micron features in materials that are either pore-forming or can be converted into porous materials. Such phenomena rely on engineered intermolecular interactions to enable high-throughput pattern-generation on the micro- and nano-scale. Self-assembly for isoporous membranes can also arise in more simple materials under carefully engineered processing conditions, namely the breath figure method. [275] Using well-controlled condensation/evaporation, micron-scale isopores can be generated in commodity polymer membrane materials [276] like cellulose triacetate [277] and polyethersulfone. [278] Inverse opal structures derived from carefully dried supramolecular packings

of nanoparticles are another intriguing possibility — the pores can be made either at the interstices or at the necks where two removed particles had contacted. [279]

Block copolymers (BCPs) are among the most promising self-assembly systems being studied for isoporous membranes. [280–282] BCPs are linear chains of two blocks of different monomers, which self-assemble into nanoscale patterns (spheres, lamellae, cylinders, etc.) with dimensions dictated by molecular weight and penalty of mixing between blocks. The BCP hexagonally close-packed cylindrical phase is perhaps the most widely studied, due to its similarities to the ideal H-P scenario and due to its high ε. The state of the art in block-copolymer isoporous membrane design is the focus of the next chapter.

The motivation underlying virtually all of these studies on isoporous membranes to date has been the sought-after step function for size selection. However, with the significant attention paid to developing new routes toward isoporous membranes, it is worth viewing separations from the perspective of energy efficiency. This view can offer new insights into when and how isoporosity should be sought as a membrane design goal. Here, we explore this question using a simplified numerical model. With this model, we project under which regimes of flux and size-selectivity it would be appropriate to pursue extremely narrow pore-size distributions and, conversely, when the costs of these effort outweigh potential improvements.

5.2 Methodology

The model employed here begins with several assumptions of the membrane strucutre. The membrane consists of perfectly cylindrical pores all of constant length L. Tortuosity in real systems — to first order — simply scales the H-P equation linearly and is therefore neglected in this case. The membranes consist of N=5E6 pores that are sampled from the log-normal distribution in equation 5.4. In the model a constant mean (μ=0) was used and σ was sampled from 0.001 to 0.6. A constant mean was chosen to enable direct comparisons across values of σ. The mean pore size (mps) of each distribution was calculated using the following

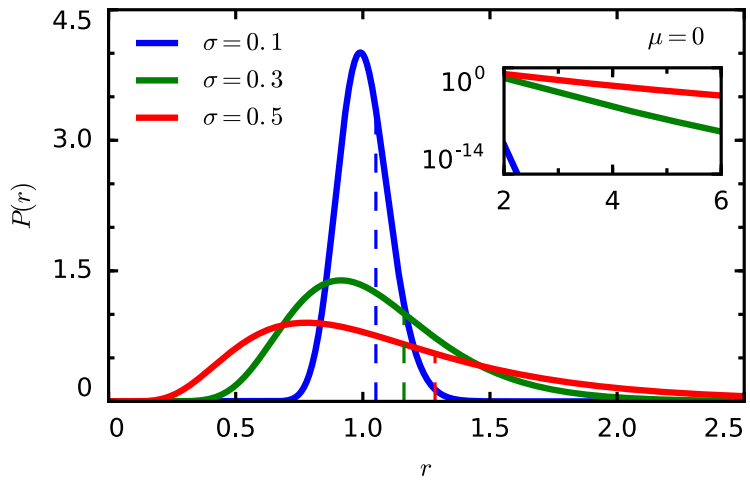

Figure 5.2: Representative log-normal propabability distributions of μ=0. The dashed lines are located at the mean pore size (mps). The inset highlights the diminishing probability of large outlier pores. Small increases in σ lead to order of magnitude increases in *P(r)* at larger r values

expression:

$$mps(\sigma) = e^{\mu + \frac{\sigma}{Z}} \tag{5.5}$$

Note that the mean μ of the log-normal distribution is distinct from the mps. Figure 5.2 shows representative probability density functions of log-normally distributed pore radii, demonstrating the increase of large outliers from the mps with σ. The H-P model predicts a linear relationship between the applied pressure across a membrane and the resulting flux, and this steady-state linear behavior is considered, excluding effects like initial compaction, fouling, and cake formation. Filtration processes can be operated under conditions of constant transmembrane pressure, constant flux, or in semi-constant modes. When a constant pressure mode is employed, flux gradually declines as a cake layer forms and fouling proceeds. We have chosen to analyse membrane pore distributions under a condition of constant flux so that pressure can be directly calculated as a stand-in for energy. Since pressure is the energy density of the fluid, by considering membrane process on a unit volume, we directly relate the pressure to the energy needed to use the membrane for a separation process.

Starting with a condition of constant flux across membranes of varying σ, the

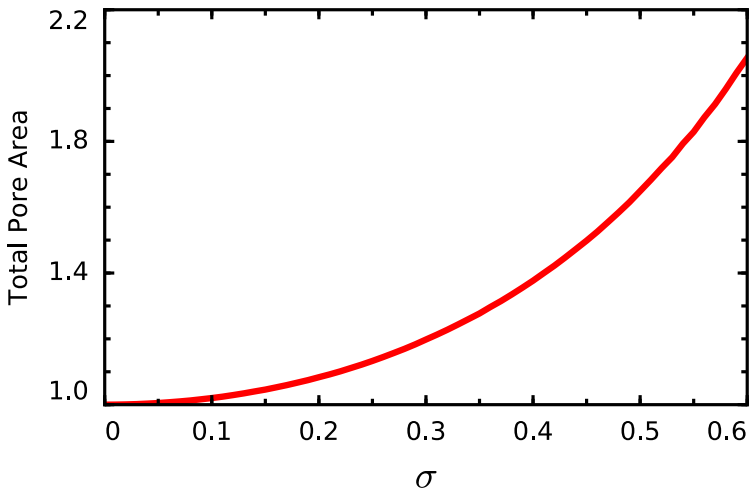

Figure 5.3: Relationship between cumulative pore area normalized by $N\pi$ as a function of σ of log normal distribution with μ=0

total flow rate through each membrane was calculated by assuming a global porosity, εm and using the total pore area, A_p, across all N pores. Figure 5.3 plots A_p/N as a function of σ, showing rapid growth as σ increases. The requisite pressure needed to achieve constant flux across these different distributions was then calculated by combining equations 5.2 and 5.3:

$$\Delta P = \frac{F A_p 8 \eta L}{\varepsilon \pi \sum_{i=1}^{N} r_i^4} \tag{5.6}$$

Figure 5.4 shows how ΔP decreases as a function of σ. Note that ΔP is normalized by its maximum value found solving Equation 5.6. Three representative values of σ from Figure 2 are included for guidance. Using ΔP as a function of σ, the flow rate through each individual pore, v_i, is calculated using equation 5.1.

5.2.1 Membrane Rejection

While the inverse relationship between ΔP and σ shown in Figure 5.4 naively suggests that an isoporous membrane is the least energy-efficient choice, the rejection performance of the membrane pores must be considered. To assess the size-selectivity of the membranes across

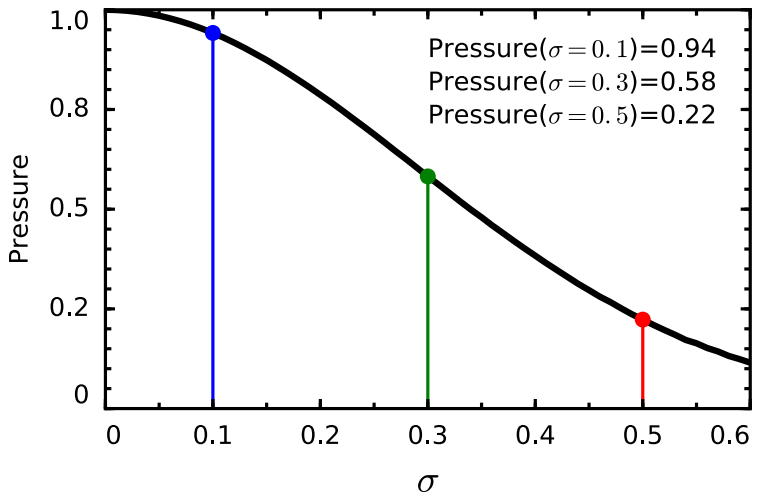

Figure 5.4: Normalized pressure to achieve a unit flux as a function of σ, where the maximum value is in the isoporous case. The permeance of the membrane scales with r^4, and as share of larger outlier pores increases, the pressure decreases.

pore-size distributions, we describe a monodisperse solute with hydraulic radius r_s, which is a multiple of the mps for each distribution. r_s ranges from 1.005 to 6.0 times mps(σ). This range of solute sizes allows for the comparison of membrane rejection under different conditions. The common definition of the rejection coefficient R is:

$$R = 1 - \frac{c_p}{c_f} \tag{5.7}$$

where c_f is the solute concentration in the feed and c_f is the solute concentration in the permeate. In this simplified model for membrane selectivity, we define a binary size-based rejection rule based solely on size exclusion, which can be termed pure mechanical sieving. Note that this rejection model does not incorporate convective hindrance as discussed in the introduction, which is a reasonable simplification in the case of low flow rates. This model also excludes particle/pore and particle/particle interactions, and assumes that there is no retention of solute within the membrane pores. These phenomena are certainly important in membrane separations, but they can be considered separately from the influence of pore-size distribution, which is the focus of the current analysis.

The binary selection rule that is employed dictates that solute particles only pass

through pores where the radius $r_i > r_s$. A logical matrix, M_i is constructed to select pores that meet the condition for solute flow. The cumulative flow rate through each pore that meets this condition is considered flow that transmits solute through the membrane, whereas pores that do not meet this condition are considered to perfectly reject the solute. The rejection coefficient through the membrane is therefore defined as:

$$R = 1 - \frac{\sum_{i=1}^{N} M_i v_i}{v_{total}} \tag{5.8}$$

This expression for membrane rejection coefficient makes the assumption that the solute particle is homogeneously distributed throughout the fluid, which ignores the effects of concentration polarization, solute back diffusion, and cake formation. This expression states that for pores which reject the particles, pure water flows through at the rate dictated by the H-P equation. For pores that do permit the solute particle to pass, the fluid is transported across with solute concentration c_f. Thus, if c_f is normalized to unity, the permeate concentration is simply the fraction of total flow rate through solute-selective pores. Figure 5.5a shows the rejection coefficient R as a function of σ for increasing values of r_s. Figure 5.5b shows an alternate view of R as a function of r_s for increasing σ.

With the requisite ΔP and R computed as a function of σ, the energy expenditure required to meet a target rejection, t_r, can be calculated If $r \geq t_r$ the membrane meets or exceeds the target rejection with one batch process. The energy expenditure in this case is simply proportional to ΔP — the pressure required to process that volume of fluid at a normalized flux. However, if R ¡ t_r, the fluid would require multiple batch processes to be adequately treated. In this scenario, we consider c_p after the filtration to become c_f of a subsequent process. Since each membrane operation reduced the solute concentration by a factor of R, the integer number of passes to reach t_r, n, can be calculated from a geometric series to be:

$$n = \frac{log(1 - t_r)}{log(1 - R)} \tag{5.9}$$

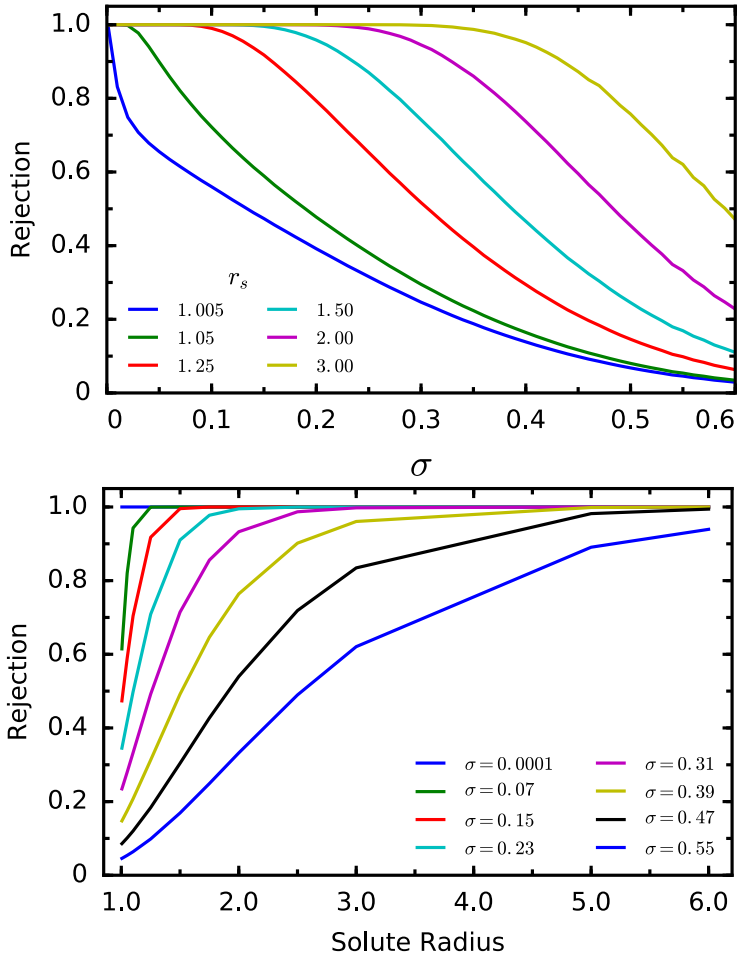

Figure 5.5: a) The rejection coefficient for membranes of increasing variance in pore size distribution for different solute sizes, r_s, relative to the mean pore size. b) The rejection coefficient as a function of r_s for membranes with increasing variance in pore size distribution.

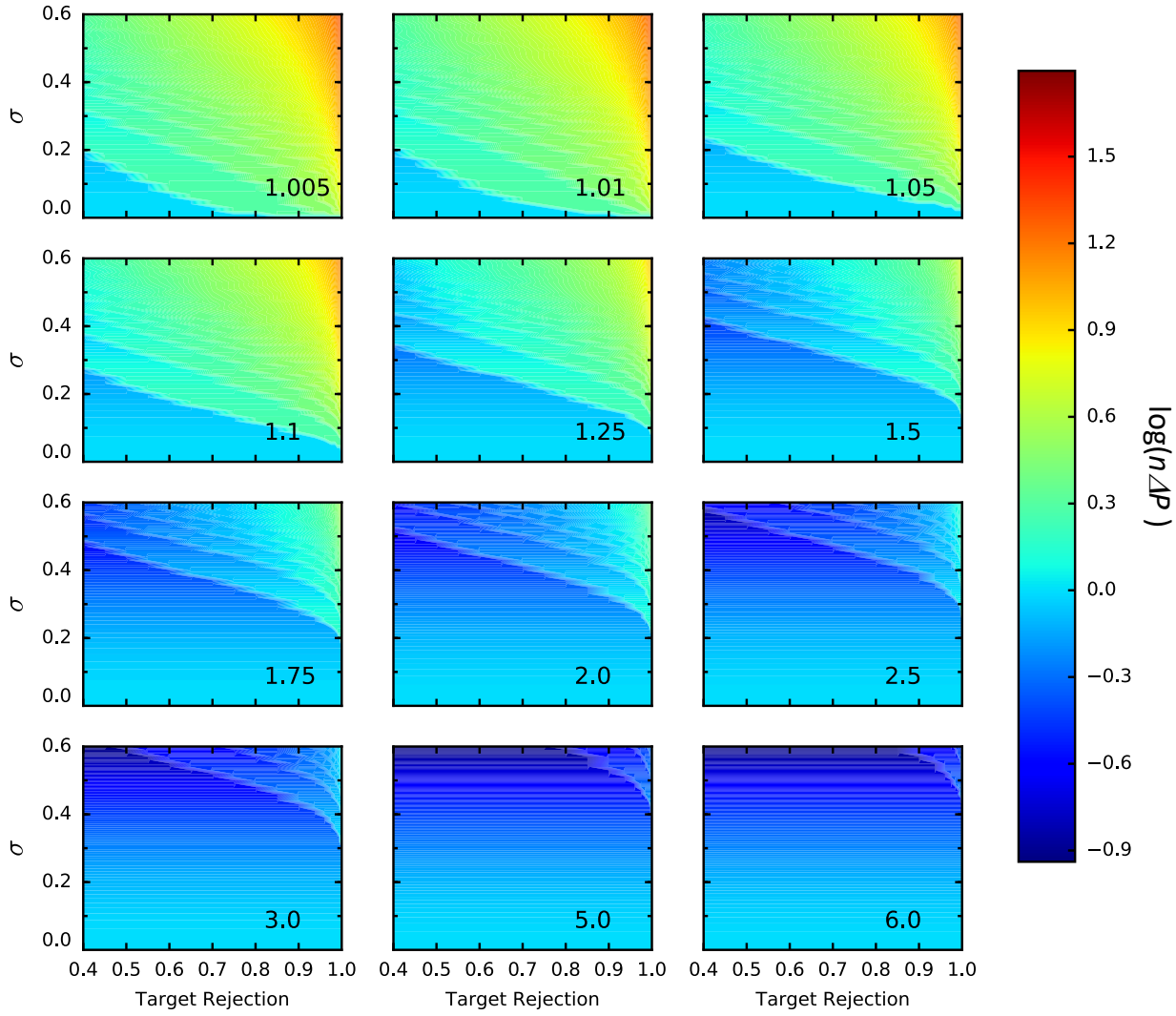

Figure 5.6: Colormaps of energy-expenditure, $n\Delta P$, as a function of σ, the variance of the membrane pore log-normal distribution, and target rejection of a separation process. Each subplot is the data computed for a given rs, solute size relative to the mean pore size. The applied transmembrane pressure ΔP, is normalized to the case of an isoporous membrane. n is the number of sequential membrane passes required to achieve a target rejection. The color map data is plotted logarithmically. The target rejection axis is plotted linearly in order to focus on moderate target rejection thresholds.

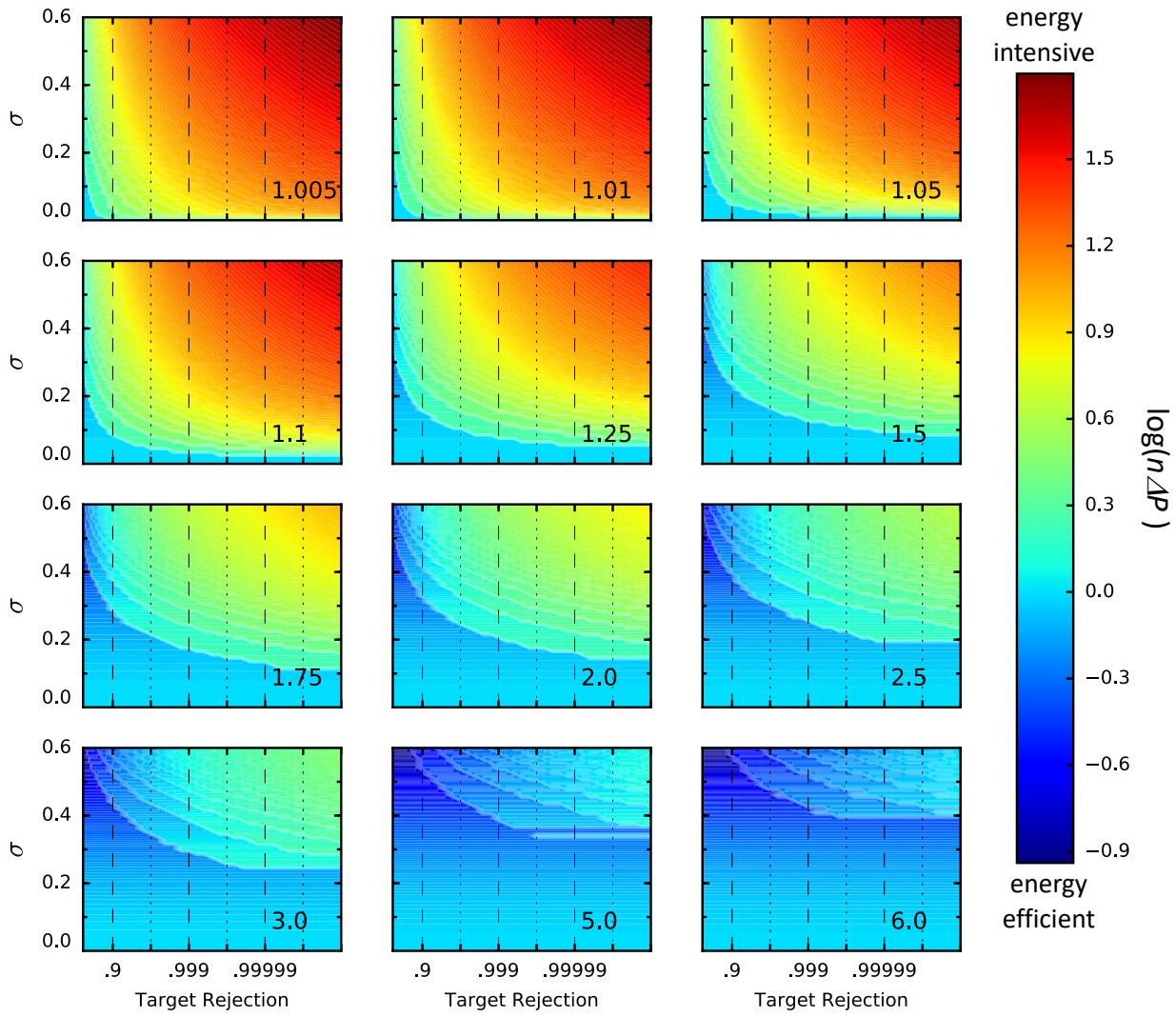

Figure 5.7: Colormaps of energy-expenditure, $n\Delta P$, as a function of σ, the variance of the membrane pore log-normal distribution, and target rejection of a separation process. Each subplot is the data computed for a given rs, solute size relative to the mean pore size. The applied transmembrane pressure ΔP, is normalized to the case of an isoporous membrane. n is the number of sequential membrane passes required to achieve a target rejection. The color map data is plotted logarithmically. The target rejection axis is plotted in increasing nines, to highlight the behavior in the limit of ultrapure target rejection thresholds.

Here n is rounded up to the nearest integer to capture the batch nature of multiple membrane processes. The total energy expended to bring the fluid to a purity set by t_r, is thus proportional to $n\Delta P$.

The base-10 logarithm of $n\Delta P$ is plotted in Figures 5.6 and 5.7 as a function of σ and t_r. The logarithm is taken to improve readability given the range of data. The two figures differ in the scaling of the t_r x-axis. The first has a linear scaling across the range, which emphasizes low target rejections. The second is logarithmically scaled out in increasing nines, represented by vertical lines, revealing the energy consumption landscape of increasingly ultra-pure separations.

5.3 Discussion

When considering the energy consumption of membrane processes, there is a fundamental trade-off between increasing permeance and decreasing size-selectivity. In the constant-flux scenario in this analysis, a decrease in the requisite pressure represents energy savings. Figure 5.4 shows the relationship between this quantity and the σ of the pore distribution, revealing two regimes. There is a gradual decrease in pressure between the isoporous case and σ $\sim$0.1. The curve then becomes linear over most of the σ range, though an inflection to sub-linear decrease is apparent at highσ values. Typical phase-inversion ultrafiltration membranes have been shown to fit a log-normal distribution with σ=0.2. [244] In this picture, such a membrane would therefore require $\sim$20% less energy than an equivalent isoporous membrane — assuming the rejection target is achieved with a single pass. Figure 5.5 reveals how increasing the permeance of the membrane compromises its performance as measured by the rejection coefficient. As the distribution of the membrane's pore increases, the rejection drops. The onset of this drop in rejection is delayed to larger values of σ as the size of the solute relative to the mean pore size increases. Viewed another way, membranes with large values of σ are only highly effective if the solute is much larger than the mean pore size.

The analysis thus far captures a well-recognized fundamental trade-off between

permeability and size-selectivity in membranes. [244] This trade-off in the present case of convective transport is related to the size of the pore that must behave both as a channel for fluid flow and as the mechanism for separation. This phenomenon is fundamentally similar to the upper-limit concept in gas permeation membranes introduced by Robeson. [283] The trade-off is also a feature of other diffusion-based membranes such as reverse osmosis membranes used in desalination. [238]

Introducing the quantity $n\Delta P$ as a figure of merit enables the simultaneous consideration of a membrane's permeability and size-selectivity in overall energy efficiency. In Figure 5.5a, each curve represents the maximum allowable pore distribution to achieve a certain rejection with a certain particle size. At any point on these curves, moving directly left toward isoporosity raises the energy requirement by decreasing the permeability. Consider a given value for rejection in Figure 5.5a as the target rejection for a separation process. If the membrane pore-size distribution is to the right of a curve for a given solute size, the fluid would need two passes through the membrane, which would double the energy expenditure. The solution to equation 5.9 for n thus captures the increase in energy required to use a membrane with a wide pore-size distribution even as the permeability increases.

Figures 5.6 and 5.7 highlight the role increasing n has on the total energy expenditure of membranes with widening distribution in moderate and challenging target purifications. In Figure 5.6, starting from the top right plot where r_s=1.05, there are horizontal bands of uniform at the bottom of the plots. These bands, which span the target rejection range of the figure, increase in height as the solute size increases. These solid regions are those where the rejection coefficient for the membrane exceeds the target rejection, namely where n=1. Moving up vertically in these regions, the quantity $n\Delta P$ decreases solely due to enhanced permeability with higher σ. As σ increases further, a sharp jump in $n\Delta P$ is apparent, occurring when n increases. The first jump occurs at lower values of σ for each solute size sampled. Moving vertically upward still, additional jumps associated with increased n punctuate the underlying trend of decreasing ΔP.

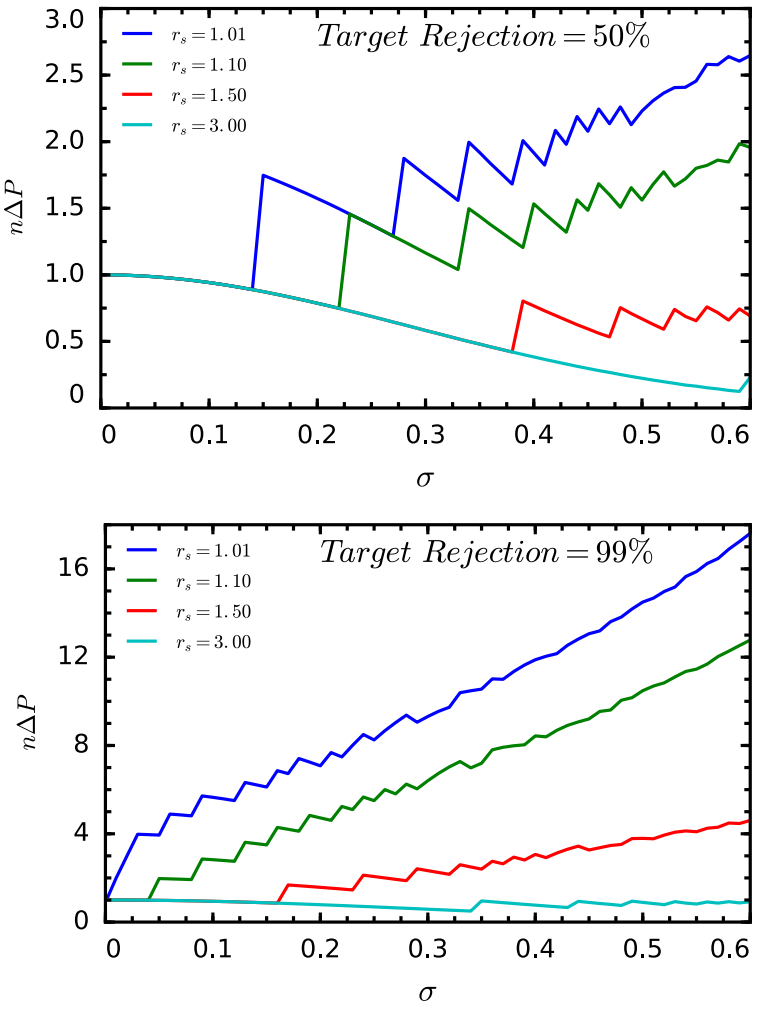

Figure 5.8: Linecuts highlighting the change in behavior of $n\Delta P$ vs. σ as a function of target rejection and solute size. Note that $n\Delta P$ is linearly scaled. a) At low target rejections a substantial drop in pressure with wider pores can be exploited without the influence of n's increase. b) At ultrapure rejections, any decrease in ΔP by moving to wider pores is quickly outweighed by the cost of successive cycling. In such a context, the isoporous membrane can be considered the most energy-efficient.

Figure 5.8a shows a vertical linecut taken from Figure 5.6 at a representative low target rejection of 50%, at several solute sizes. Note that $n\Delta P$ itself and not the logarithm of $n\Delta P$ is plotted here. The minimum value of each line is located at the σ that is most energy-efficient for this separation. These minima are located at pore-size distributions much wider than the isoporous membrane. For applications in which a low target rejection is acceptable, for example, in the clarification of natural products like dairy and juices, an isoporous membrane would impose higher energy costs than a wide pore distribution membrane.

Figure 5.7 expands the same data as Figure 5.6 in the limit of ultra-high target rejections. The leftmost vertical band ranges from 40% to 90%, the second from 90% to 99%, the third from 99% to 99.9%, and so on in increasing nines. In the top row of plots in Figure 5.6, it is clear that the onset of n's growth occurs at values of σ approaching isoporosity. This means that the widest allowable pore size distribution for a membrane before successive purification cycles are needed occurs is quite narrow. A representative line-cut of target rejection 99% is displayed in Figure 5.8b. Here, at low solute sizes, the minimum is extremely close to the isoporous membrane. Due to the shape of the pressure vs. σ curve (Figure 5.4), the difference in energy efficiency between an idealized isoporous membrane and an extremely narrow log-normal membrane is miniscule.

An alternative strategy to achieving high rejection is to select a membrane with a mean pore size substantially smaller than the targeted solute ($r_s \gg 1$) but having a wide pore-size distribution, such that even the small population of larger pores would still be narrow enough to reject the solute. Since the transmembrane pressure scales with the inverse fourth power of the pore radius, such a strategy carries a major energy cost.

This analysis makes clear that the choice of membrane structure along the selectivity-permeability trade-off is highly context-dependent. The relatively slow rate at which permeability increases with the variance of pore distribution is not sufficient to justify the corresponding increase in energy of sequential multiple pass membrane processes. For that

reason, the minimum energy to achieve a target separation is dictated almost entirely by the size-selectivity of the membrane. Membranes that have low permeability but high size-selectivity thus are the most energy-efficient options in achieving high-purity separations.

5.4 Conclusion

The value of isoporous membranes has been a topic of debate in the scientific community for at least 80 years. [245] The present analysis demonstrates conclusively that the high rejection characteristics of membranes approaching isoporosity outweigh the minimized permeance of such membranes when high-purity separations are critical. $n\Delta P$, the number of membrane passes required to meet a selectivity threshold multiplied by the transmembrane pressure, is introduced as a figure of merit in evaluating the total energy expenditure required to process a fluid to a targeted level of purity. By viewing this analysis in light of the challenges facing the water-energy nexus, the potential advantages of isoporous membranes over traditional materials takes on new significance. Researchers should focus on membranes with the ultra-narrow rejection curves for targeted separations, such as those exhibited by isoporous membranes, without concern for the reduced permeance of these devices relative to broader pore distribution materials. This simple model of convective bulk-transport membranes has ramifications for the distinctly different thin-film composite or reverse osmosis membranes [238] in that unrealized gains in size-selectivity can far outweigh permeability costs from an energy perspective.

CHAPTER 6

BLOCK COPOLYMER-DERIVED METAL OXIDE ISOPOROUS MEMBRANES

6.1 Introduction

Block copolymers are increasingly recognized for their potential in creating highly selective isoporous membranes, and several processing/fabrication approaches to acheive this goal have been described in the literature. In BCP membranes, the orientation of the pore-forming phase relative to the membrane surfaces must be controlled to ensure a continuous channel with minimized tortuosity. Controlled solvent annealing [284–287] and substrate surface energy neutralization [76, 288, 289] are two popular strategies to control domain alignment, along with annealing under steep thermal gradients, [290] and electric [291] or magnetic field-driven methods. [292, 293] Copolymers with more than two blocks and other structural complexities also find use in this area. [294]

BCPs have been implemented in isoporous membrane fabrication in two main ways. The first shares many similarities to top-down approaches, but with BCPs acting as a self-assembled template for the transfer of features smaller than what can be accessed by other lithographic means. For example, micelle-forming BCPs were used to transfer pores into Si, Si_3N_4, and metals. [295,296] Porous BCP-derived films have also been integrated into substrates with previous lithographically-dervied pores. [297] In terms of ease of processing and scalability, such approaches share many of the drawbacks of other lithographic top-down methods.

In the second implementation, the self-assembled material itself forms the active layer of the isoporous membrane. Using self-assembly with nonsolvent induced phase separation (SNIPS), isopores are generated directly in the top layer of material in both flat sheet and hollow fiber form factors. [298–302] SNIPS involves involves blade-coating a polymer solution from a water-immiscible solvent onto a glass plate, allowing the solvent to partially

evaporate, followed by submersion into a water bath. The solvent gradient in the film due to partial evaporation, along with the instability of the polymer-solvent-water mixture, yields a thick spongy support layer with BCP-defined isopores forming an active skin layer.

Scaled roll-to-roll fabrication of isoporous BCP membranes using this method has been demonstrated and appears poised to move beyond research settings. [303,304] In these implementations, the polymer forms a selective isoporous skin layer of variable thickness supported by a spongy tortuous layer.

The pore-forming phase of the BCP can be converted into a pore void by several different means. A small molecule with selective solubility in the cylinder-forming block, such as 3-n-pentadecylphenol (PDP) in P4VP, can be incorporated in the polymer solution and then selectively dissolved after the membrane is cast. [286] Oligimers or short homopolymers can likewise be added to the cylinder-forming phase and be removed by after casting by a block-selective solvent. [285, 305, 306] The reduction in volume in the cylinder-phase leads the retained block to collapse and form an open pore volume. Pores can be generated by selectively chemically etching the cylinder-forming block, for example polylactide (PLA) features can be etched in basic solutions to form isopores. [307, 308] Pores can be generated by selective solvent swelling of the cylinder-forming blocks. When the selective solvent is evaporated, the polymer chains forming the cylinder can collapse to yield an open pore volume ringed by an annulus of the cylinder-forming block. [309–312]

BCPs are also useful in that the pore size and surface chemistry can be precisely engineered. By controlling the extent of swelling via duration, temperature, and solvent, the generated pores can be manipulated in size. [309, 313] The molecular weight of the pore-forming block represents a direct route to pore-size control during polymer synthesis. [294] Pore-size tuning can even be achieved after pore formation by direct chemistry on the pore surface. [314] The pore surface chemistry and structure is of key importance in new membrane design, particularly in anti-fouling, catalytic, selective adsorption, and other advanced functions. [315] The pore surface is composed of polymer functional groups, which

can be designed for accessible chemistry for post-pore generation modifications. For example, catechol-lined pores have been biomineralized into zirconia-containing pores to enhance stability and hydrophilicty. [316] Stimuli-responsive pores, such as those with pH-dependent swelling, [317] can enable active membranes for targeted separations. [318] By incorporating sol-gel components into BCP-scaffolds, a variety of inorganic isoporous materials have been demonstrated. [319]

In this chapter, an alternative route combining both top-down and bottom-up nanofabrication approaches is introduced. Sequential infiltration synthesis (SIS) is used with cylinder-forming PS-*b*-PMMA BCP films where the SIS-inert PS domains forms the cylinders. Because PS lacks Lewis-basic functional groups, during vapor purging, SIS metalorganic precursors are retained in the PMMA matrix and not in the cylinders. Upon removal of the polymer, an inorganic metal oxide directly templating the BCP self-assembled structure is retained. These polymer films are transferred to and processed on porous supporting structures to implement them in membrane configurations. This method enables simultaneous control of pore size, thickness, and material surface chemistry. SIS and atomic layer deposition (ALD) are thus poised to offer a wide range of material surfaces with precise pore tailoring to membranes. [320, 321]

6.2 Results and Discussion

6.2.1 Vertical Cylinder Self-Assembly

The metal oxide isoporous membranes fabricated by SIS directly template the continuous PMMA domain in the PS-*b*-PMMA BCP, and any defects in the self-assembly of this polymer film will be reflected in the final structure. The thin film processing of this polymer must therefore ensure that the PS cylinders orient themselves normally to the substrate surface. These PS cylinders, in the ideal case, must exist as monoliths that traverse the free surface of the film (air/BCP interface) to the substrate surface (BCP/substrate interface). Pristine

Si surfaces are preferentially wet by PMMA over PS. The implications of this fact are that cylinder-forming PS-*b*-PMMA BCPs will self-assemble to ensure maximal coverage of the Si surface by PMMA. The result is PS cylinders lying parallel to the substrate. Therefore, a surface-energy neutralizing random copolymer mat is employed to remove the driving force for preferential wetting of the PMMA phase.

A previous study by Zhou *et al.* [76] determined the random copolymer mat composition and thermal annealing conditions for the successful self-assembly of vertically oriented PS cylinders in PS-*b*-PMMA (M_n= 20.2-*b*-50.5 kg/mol, center to center spacing L_0=38.3 nm). Though strategies for vertical assembly of PS-*b*-PMMA cylinder-forming systems where the PMMA forms the cylinder had been studied [288, 289, 322], there had been limited reports for the PS-cylinder system of interest. [323] Zhou *et al.* found that a polystyrene-*random*-methyl methacrylate-*random*-glycidyl methacrylate (P(S-*r*-MMA-*r*-GMMA)) copolymer composed of 4 mol% GMMA and 63 mol% styrene monomers yielded the most optimal vertical assembly. By annealing thin films in a nitrogen glovebox environment at various temperatures, 270 °C for 3 hours was found to be the temperature and time that enabled vertical assembly over the largest range of film thicknesses. At this temperature, the surface energy of PS and PMMA in air are presumed to be equal. In thicker films, the free surface must be truly surface energy neutral as well, otherwise guidance from the substrate surface will be insufficient to orient the cylinders vertically.

The same BCP, random mat composition, and annealing conditions were adapted to this work, and the assembly of the films were verified using scanning electron microscopy. Films were spin-coated to thicknesses not exceeding 140 nm to ensure that the cylinders were continuous and monolithic throughout the film. In thicker films, the self-assembly at either surface is essentially decoupled. While the neutral layer and 270 °C annealing temperature ensure a vertical orientation at either surface, there will be cylindrical alignment defects at a plane within the film due to this decoupling. Both the work by Zhou *et al.* and another study by Segal-Peretz *et al.* [57] use transmission electron microscopy (TEM) tomography to

reconstruct volumes of this BCP system at this thickness and observe no mid-plane defects, enabling confidence in this choice of thickness.

6.2.2 Polymer Film Transfer to Porous Support Layers

In order to utilize block copolymer thin films in membrane applications, the substrate must act as a porous support layer so that fluid can flow through the membrane. The flat, featureless silicon wafers used to spin coat uniform thin films are unsuitable for this purpose. For that reason, the transfer of the film from the spin-coated substrate onto a porous support must be accomplished. This task must be done in a way that does not plastically deform the thin film, as any tears or mechanically-induced defects would limit the ultra-selective performance of the layer. However, the 140 nm polymer film is extremely delicate and prone to wrinkling and folding.

Floating the film onto a liquid bath is one route by which this transfer can be accomplished. The surface tension of the air water interface can keep the film taut. While some studies have used hydrofluoric acid to etch away silicon dioxide to release polymer films, a water soluble undercoat is much safer. An aqueous solution of poly(acrylic acid) sodium salt (PAA) is a preferable alternative, as it can be spin-coated onto the Si wafer to form a flat surface for the spin-coating and cross-linking of the random copolymer mat prior to spin-coating the BCP. PAA does not mix toluene, the solvent used to dissolve the components of the BCP stack, and therefore the films do not mix and are maintained as a stack. Furthermore, PAA does not cross-link or otherwise lose its solubility in water under the conditions of random mat cross-linking or block copolymer annealing. After the film is assembled, the Si wafer can be lowered into a deionized (DI) water bath. The water dissolves the PAA undercoat and releases the film onto the surface of the water. This sequence of operations is detailed in Figure 6.1(1-4).

Once the film is resting on the water surface, it must be transferred onto its final porous substrate (Figure 6.15,6).Though this operation can be done by practiced hand,

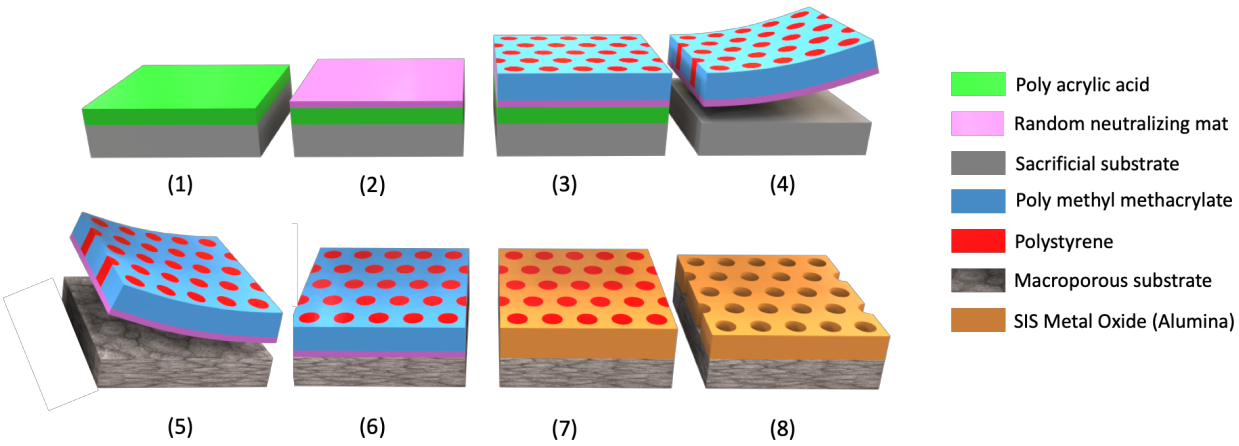

Figure 6.1: Process flow for the fabrication of BCP derived isoporous metal oxide membranes on porous support structures.

inevitably small movements will lead to undue forces on the film and lead to plastic deformation, tearing, and wrinkling of the film as it is lowered into the water bath. It is very difficult to reproducibly introduce the Si wafer at a constant rate and at a constant angle, and to withdraw the porous substrate with the polymer filmed positioned properly on it. To optimize this process and reduce transfer-induced defects, a mechanical means of film release and transfer was designed. [324]

Figure 6.2 shows a schematic of this apparatus. The clamp (1) and loading arm (2) can be fixed to a vertical linear rail which allow the silicon substrate to be lowered into the drain chamber (3) which is filled with water. Once the silicon substrate is submerged into the water and the film is released the loading arm can be withdrawn. The drain chamber is composed of two threaded parts to allow for the porous substrate (5) to be exchanged. An o-ring (4) provides sealing of the top and bottom (6) components of the drain chamber. The bottom part of the drain chamber consists on a support structure for the porous substrate and a channel for suction to be applied by a syringe pump, as show in Figure 6.3.

Once the polymer film is released onto the water surface and the syringe pump is engaged, the water level in the drain chamber gradually lowers. The receding water level forms a meniscus with the hydrophilic walls of the drain chamber that curves upwards.

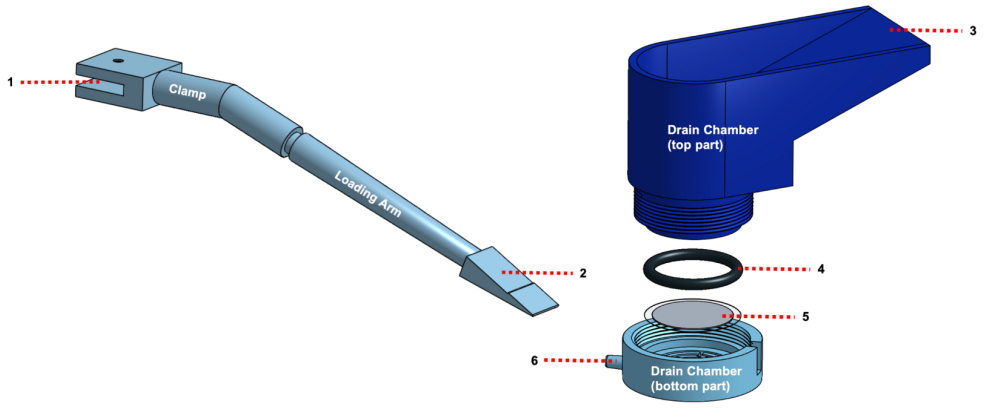

Figure 6.2: Schematic detailing the apparatus for transferring BCP films onto porous support structures in a reproducible manner.

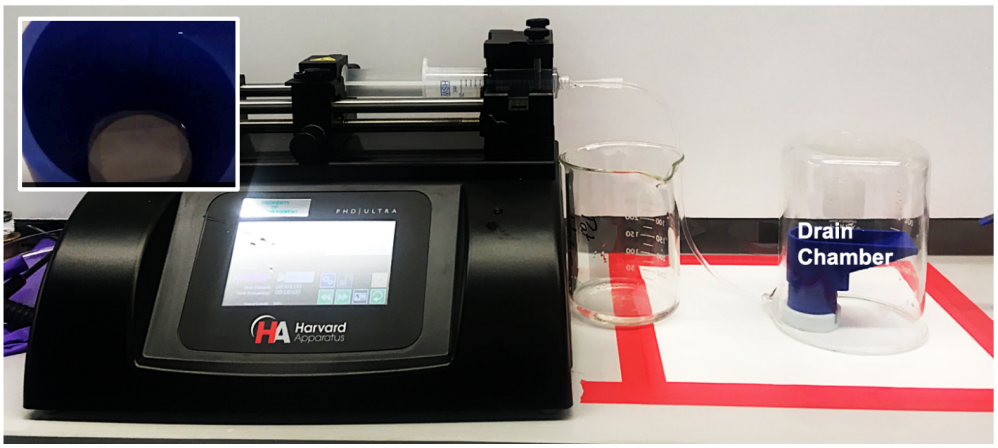

Figure 6.3: Operating the film transfer apparatus with a syringe pump to apply suction. Inset shows meniscus centering of BCP film as water level lowers to bring film into contact with the porous support structure.

This meniscus automatically centers the film in the receding water column, as shown in the inset of Figure 6.3. The water is withdrawn through the porous substrate itself, so that the centered film first touches the porous support at the center. This ensures that the film remains taut throughout. When withdrawing polymer thin films onto porous supports by hand, one common issue is that a thin layer of water is retained on the porous support surface on which the film can slide freely. With the described apparatus, any water between the film and membrane surface is drained away. After the transfer process is completed, the new composite membrane can be removed and allowed to dry in air. Conducting this process under glassware, or ideally in a cleanroom environment, will reduce the likelihood of dust contamination.

While any flat sheet membrane can be used as the porous support layer, there are several properties by which to evaluate the best candidate. One consideration is the local roughness of the membrane surface. If the surface is too rough, asperities in the surface will place stresses on the film that can cause it to mechanically fail. Failure may occur during the film transfer process itself, or may be caused by the stresses induced by the subsequent SIS and etching or annealing processes. For example, PVDF membranes rated as having 200 nm pores were found to yield membranes with significant cracking, as shown in Figure 6.4. However, PES membranes rated as the same size pores did not exhibit cracking. The microstructure of these two membrane types reveal that PES forms a smooth skin which can support the BCP film much more evenly than the rough PVDF features.

Anodized aluminum oxide (AAO) is a superior choice of microporous support because it has a much higher porosity than any common polymeric support. The bottom panel of Figure 6.4 shows that for AAO membranes with the reported same 200 nm pore size, a greater share of the BCP film is suspended over open pores, meaning the flux of the membrane can be greater than in the one suspended on PES. The uniformity of the underlying AAO pores means that each suspended region of BCP film is similar in size.

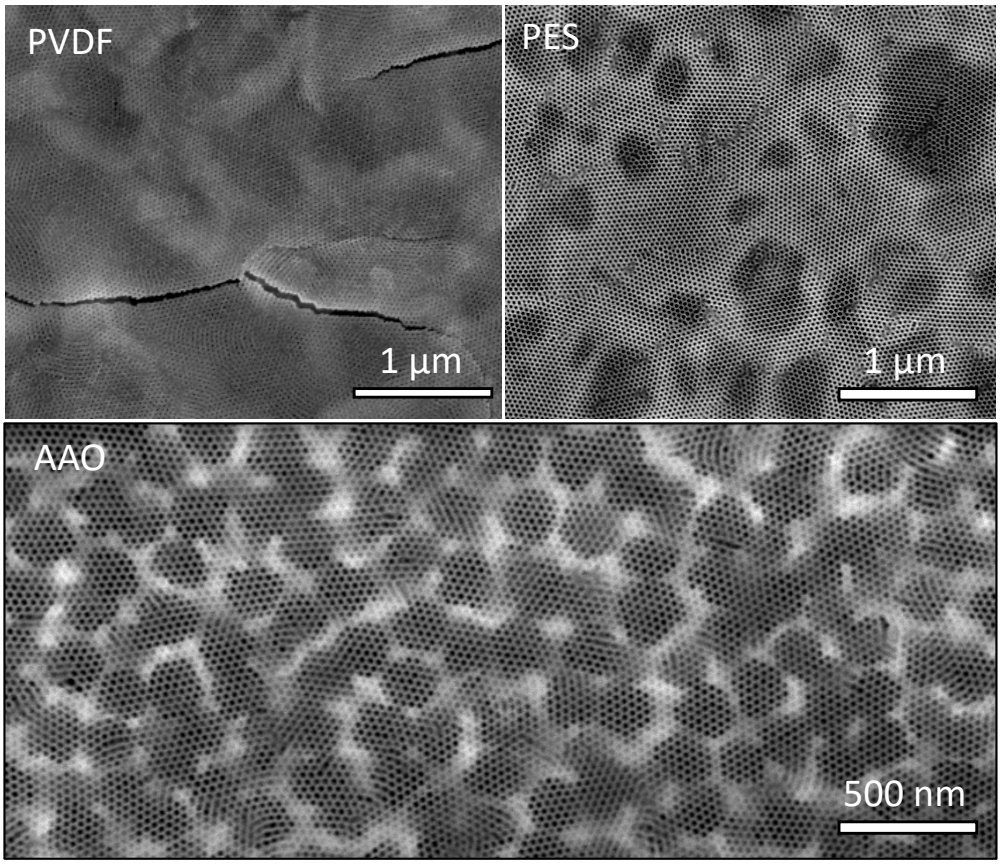

Figure 6.4: Al_2O_3 isoporous layers generated after transfer of BCP films onto PVDF, PES, and AAO substrates.

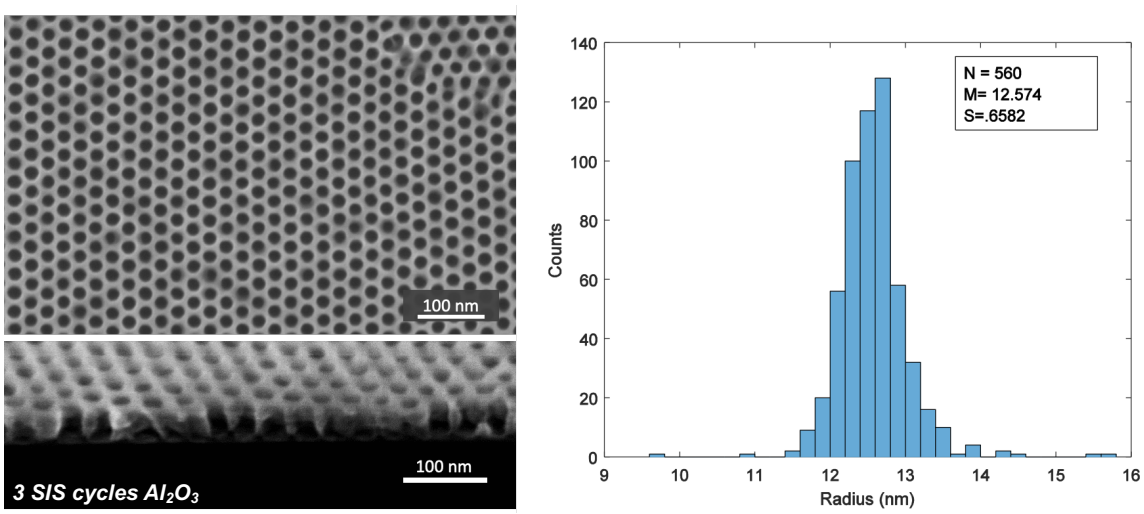

Figure 6.5: Isoporous membrane fabricated by O_2 annealing after 3 SIS cycles of Al_2O_3 on a Si substrate both from top view and in cross section. A histogram of image thresholded SEM images shows the narrow distribution of pores.

6.2.3 Isoporosity in BCP-derived SIS membranes

Once the BCP self-assembled structure is annealed, SIS can be conducted identitcally on either Si substrates or after transferring to AAO. For Al_2O_3 grown by SIS, oxygen plasma etching is a suitable route to remove the BCP template and yield an inorganic system. The resulting structure shown in Figure 6.5 shows typical BCP film of $\sim$ 140 nm initial thickness was subjected to 3 SIS cycles at 95 °C followed by oxygen plasma etching. The cross-section SEM confirms that these cylindrical pores are monolithic, and that the membrane film thickness is much smaller the initial BCP film thickness. Image thresholding was used to calculate the pore size distribution of the top surface, presented in the histogram at the right.

This analysis reveals that the pore radius falls on an extremely tight distribution with an average pore size of 12.5 nm with a variance of 0.65 nm. While some variance may be introduced by the image thresholding process, many of the outliers can be attributed to pores at grain boundaries. Figure 6.6 shows a bigger snapshot of the top surface, showing the prevalence of grain boundaries and the outlier pores at their surfaces. Volumetric

reconstructions of these materials by TEM tomography reveal that grain boundary defects typically resolve into single pores within the film into single cylinders or do not traverse the membrane thickness. [57, 76] Therefore, these grain boundary defects are not expected to substantially effect the filtration performance of the membrane.

Nonetheless, maximizing the grain size in the self-assembly would further reduce the impact of these deviations from isopores. Strategies like directed self-assembly (DSA) could eliminate grain boundaries completely, but at the expense of introducing significant complexity to the fabrication and limiting device areas to the sub-millimeter scale due to limitations in e-beam pattern writing. There are also defects within grains that look like two merged pores. These defects emerge when a PS cylinder lies parallel to the free membrane surface and bridges two adjacent cylinders. These defects can also be discounted, as the defect only exists at the surface, and the two cylinders are separated by a PMMA/Al_2O_3 feature deeper in the membrane.

6.2.4 Dimensional Control of Isopores

The conversion of block copolymer templates into isoporous metal oxide membranes offers precise control of over pore dimensions and pore thickness. The first route to control dimensions is the BCP molecular weight and volume fraction. Assuming the BCP is kept within the cylinder-forming phase, the diameter scales as some sub-linear function of molecular weight of the cylinder-forming block. [294] Thus, changing BCP composition is one route to control the porosity and pore dimension in these materials.

As the number of SIS cycles is increased, the volume of the hybrid film expands to accommodate the introduced volume of metal oxide. This leads to a simultaneous decrease in pore radius and increase in membrane thickness in the final membrane. Figure 6.7 shows In_2O_3 membranes grown with 3 and 10 SIS cycles following the procedure described in chapter 4. The relative roughness of the pore walls relative to the Al_2O_3 case is a consequence of the two materials' microstructures and will be discussed in the following section. The rate

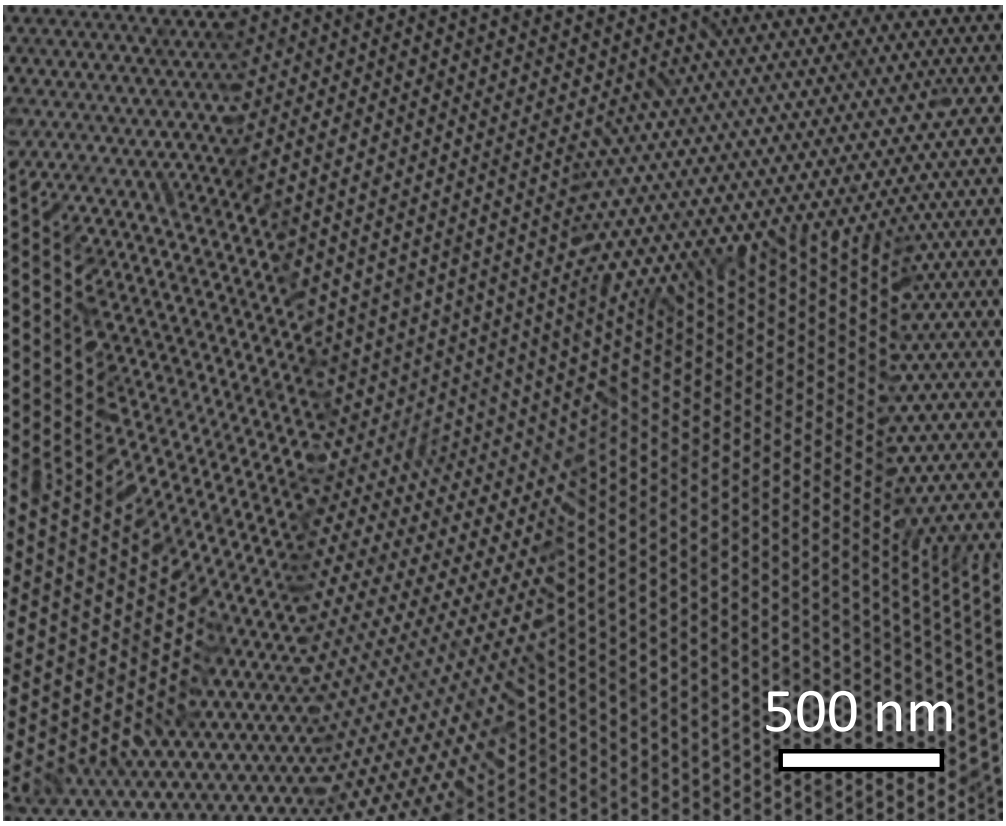

Figure 6.6: Isoporous membrane Al_2O_3 displaying grain boundary defects and in-grain defects.

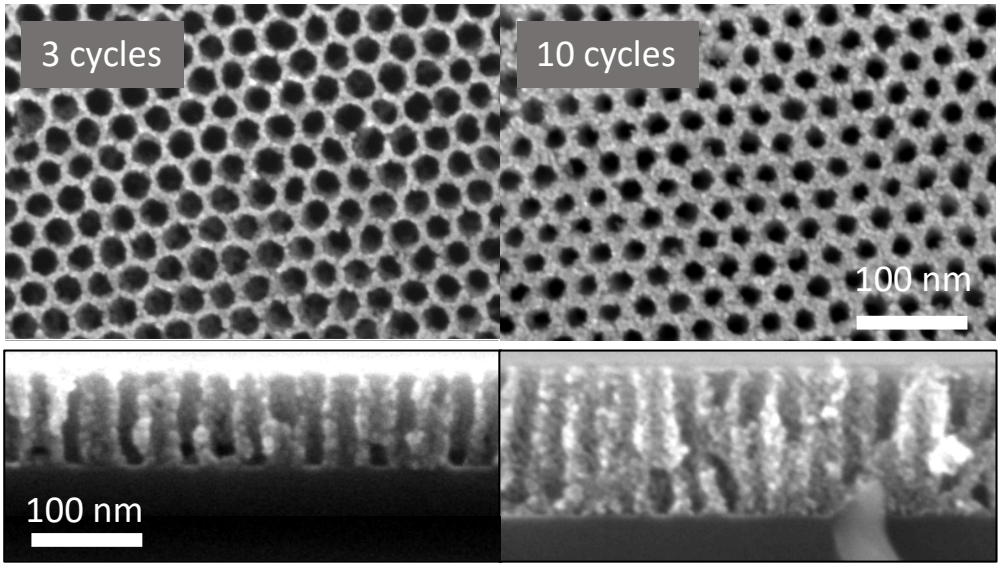

Figure 6.7: Top surface and cross-section SEM images of In_2O_3 isoporous membrane. Increasing the number of SIS cycles decreases the pore size and increases the membrane film thickness.

of pore shrinking and film thickness expansion is sensitive to the SIS processing conditions, and must be calibrated in designing precise pores.

These membranes can be subjected to further ALD growth after removal of the organic components of the hybrid film. This approach enables sensitive dialing-in of the pore size. Since the recovered framework is completely inorganic, ALD growth of new materials on the pore surfaces is not restricted to the narrow library of SIS materials. For example, a membrane derived from an initial template of PS-*b*-PMMA was prepared using 3 cycles of Al_2O_3 SIS. This structure was then overcoated with TiO_2 using alternating pulses of tetrakis(dimethylamido)titanium (TDMAT) and water at 100 °C. Figure 6.8 shows SEM images of the top surface of these membranes, with cross-sectional insets, in 25 cycle increments. Image thresholding of the surface SEM images is used to measure the pore radii. These are plotted below showing the expected linear decrease of pore radius per ALD cycle. The slope of this line implies that each ALD cycle shrinks the pore radius by approximately .043 nm/cycle.

The linear shrink in pore size offered by ALD represents an extremely sensitive

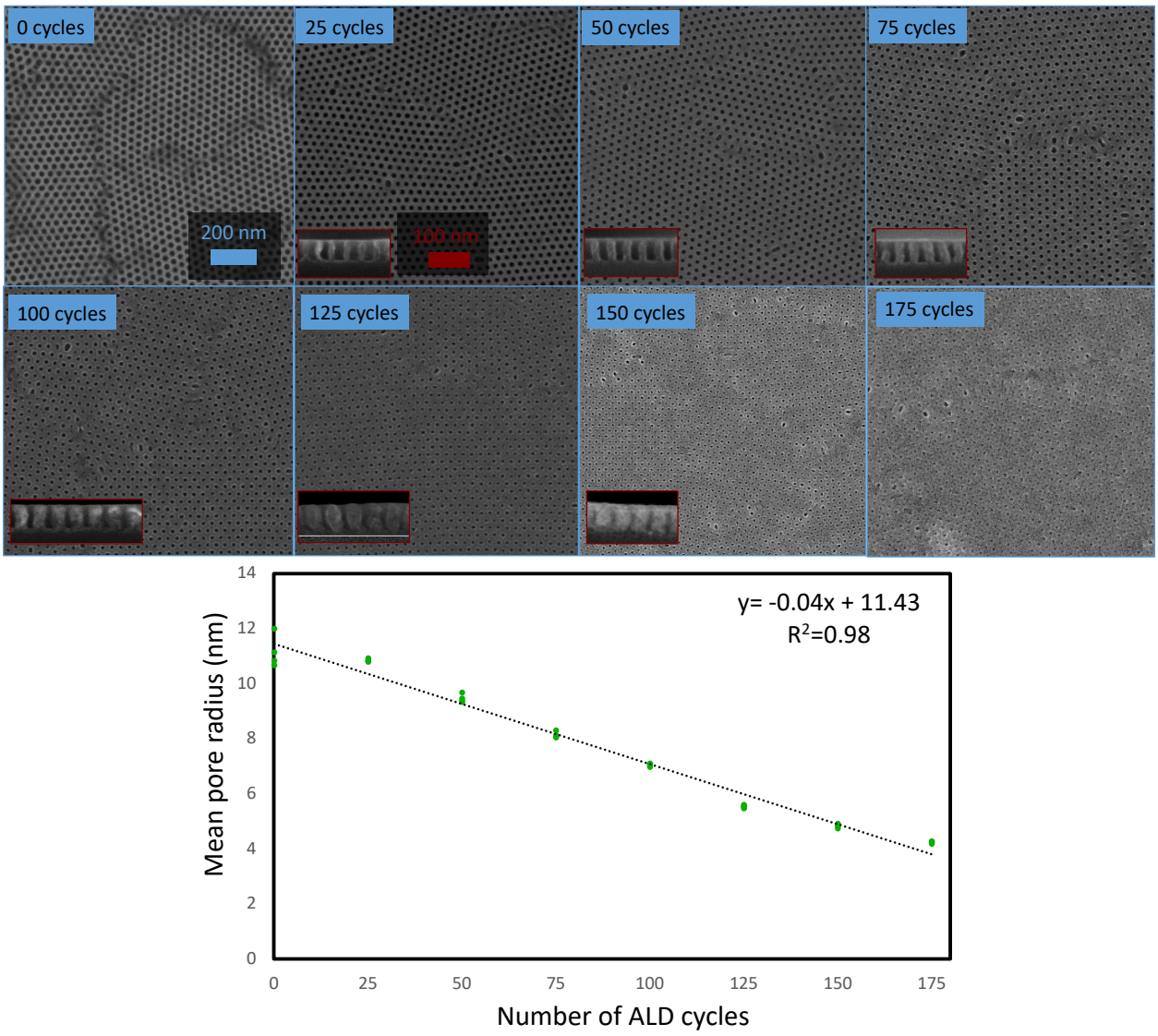

Figure 6.8: ALD overcoating a Al_2O_3 isoporous membrane with TiO_2 in 25 cycle increments. The pore shrinkage is linear, as expected from the conformal nature of ALD.

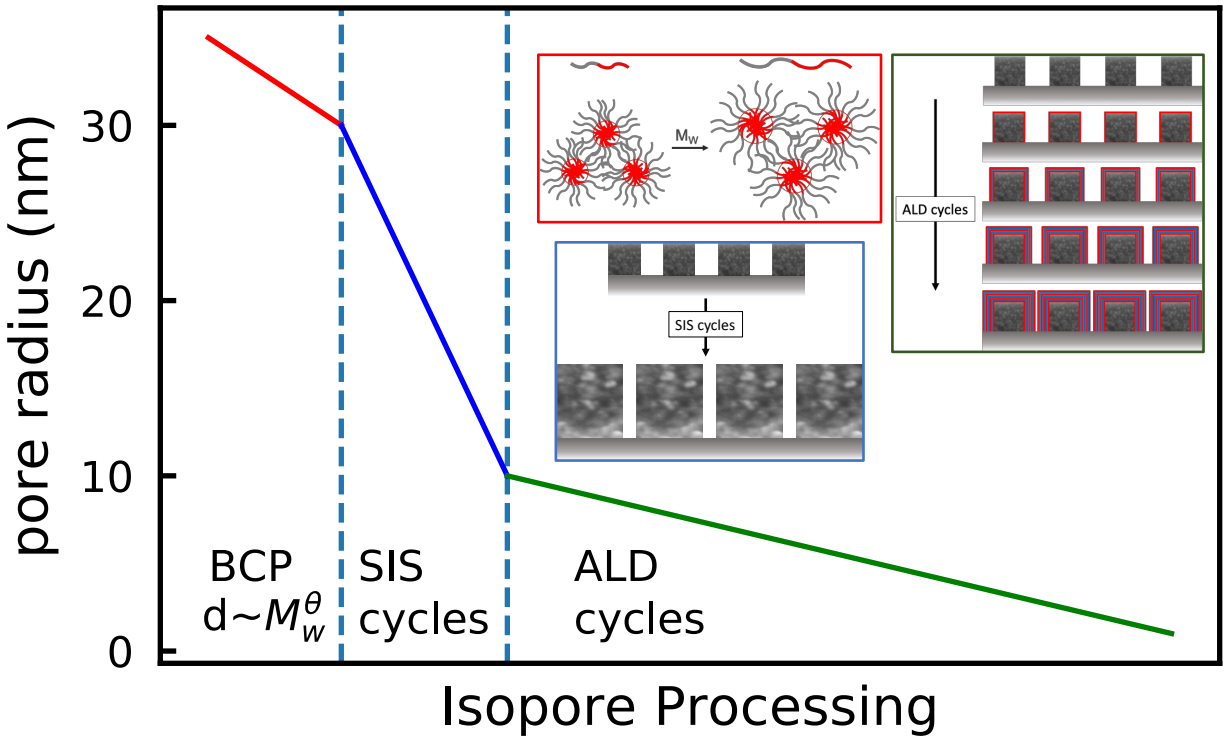

Figure 6.9: Schematic detailing pore dimension control in BCP-derived SIS isoporous membranes.

route to pore size adjustment from the initial SIS-derived pore size. It should be noted that ALD-overcoating also increases the thickness of the membrane by material growth on the top surface. However, there are some limitations to this approach. The conformal nature of ALD growth means that any surface roughness of the SIS framework is preserved and becomes more significant in the high cycle limit. As the pore size is shrunk below ∼5 nm, asperities in the pore walls throughout the membrane thickness may neck and partially or completely seal the pore. As the pores decrease in size, increasingly long vapor exposures are required to ensure a saturated chemisorbed surface within the pore interior. The cross-sections in Figure 6.8 show an increase in pore roughness over time. Roughness inherent to the deposited material also contributes to deviations from the isoporous structure, in addition to non-idealities present in the SIS-derived framework.

Figure 6.9 shows how these three steps can be used together to design isoporous membrane layers of controlled thickness and pore size. The initial polymer cylinder dimen-

sions can be controlled to an extent limited by the phase diagram for a given BCP. Next, the processing conditions of SIS can be tuned to determine the infiltration per SIS cycle. This step impacts both the film thickness and pore size of the inorganic framework. After removal of the polymer matrix, the pores can be shrunk further with ALD overcoating. This strategy offers the most sensitive control over the pore size, and cause a slight increase in the membrane pore thickness. Significantly, ALD overcoating is amenable to a wide range of ALD materials. This fabrication method thus enables a platform for independent control of pore size on the nanometer length-scale and the materials chemistry of isoporous surfaces.

6.2.5 Hierarchical Porosity in SIS materials

SIS-derived Al_2O_3 isoporous membranes appear smooth under SEM microscopy, though TEM tomographic studies reveal a roughness that may be associated with the sharpness of the BCP interface. In_2O_3 differs significantly from Al_2O_3 in this regard, as the polymer removal process causes crystallization and restructuring of the metal oxide. While the BCP framework in Al_2O_3 SIS examples was removed by oxygen plasma etching, indium oxide behaves as a plasma scavanger, and etch rates of the In_2O_3/BCP hybrid films are suprising negligible, even at elevated temperature. For that reason, BCP is removed from In_2O_3 samples by high temperature annealing in air (400 °C, 3 hours). Figure 6.10 shows through plane TEM images of In_2O_3 SIS in the same PS-*b*-PMMA BCP system. Figure 6.10a shows the as-grown hybrid film show the as-grown hybrid system after 3 SIS cycles (3AG). The lighter PS cylinders show no incorporation of indium oxide, whereas the continuous PMMA matrix is decorated with indium oxide clusters. The incorporated metal oxide is amorphous, as evidenced by the TEM diffractogram in the Figure 6.10b. After annealing, Figure 6.10c shows strong evidence of recrystallization. The PS cylinders and PMMA matrix have been removed, and the amorphous clusters have recrystallized into sintered nanoparticles. However, solid-state diffusion appears insufficient to completely destroy the morphology imposed on the initial amorphous sturucture by the BCP, and the hexagonally-closed packed pores

are retained. The inset shows clearly the atomic lattice, and the diffractogram in Figure 6.10d confirms the cubic In_2O_3 morphology of these mesostructured nanoparticles. Figure 6.10e shows the annealed structure of a sample with 10 cycles of In_2O_3 SIS. Here, the pores imposed by the BCP are smaller, and the contrast is much darker. This is a consequence of the thicker film that results from more metal oxide loading at high cycle numbers.

The inset of Figure 6.10c reveals that the crystallization does not yield a fully dense material, and there are apparent pores within the In_2O_3 region that emerge as the volume of the hybrid phase is reduced during annealing. These smaller pores may be considered interstitial volume between pseudo-randomly packed In_2O_3 nanoparticles. The interconnectivty and necking of these In_2O_3 nanoparticles is presently unknown. This material starkly contrasts with the Al_2O_3 material which retains an amorphous structure, and yields a dense material directly templating the BCP.

6.3 Conclusion

Combining SIS with BCP self-assembly enables nanoscale patterned growth of inorganic metal oxide structures. By using BCP systems such as vertically-oriented cylinders, isoporous membranes can be constructed. PS-*b*-PMMA with a continuous PMMA matrix yields metal oxide films hexagonally-close packed pores where the SIS-inert PS cylinders had been before polymer removal. By designing tools to assist in the water-transfer method, membranes can be produced on porous support layers in a reproducible manner that suppresses defects. This approach is a platform for the study of ultra-selective separations phenomena where pore size approaches uniformity and can be tuned with sub-nanometer level control. Molecular engineering of BCP structure and chemistry, the processing parameters of SIS, and post-annealing ALD overcoating present routes to control pore dimension and membrane thickness independently. SIS and ALD material libraries enable these isoporous surfaces to be functionalized with a range of material surfaces, enabling independent control of pore dimensions and surface chemical properties. Furthermore, SIS growth of materials

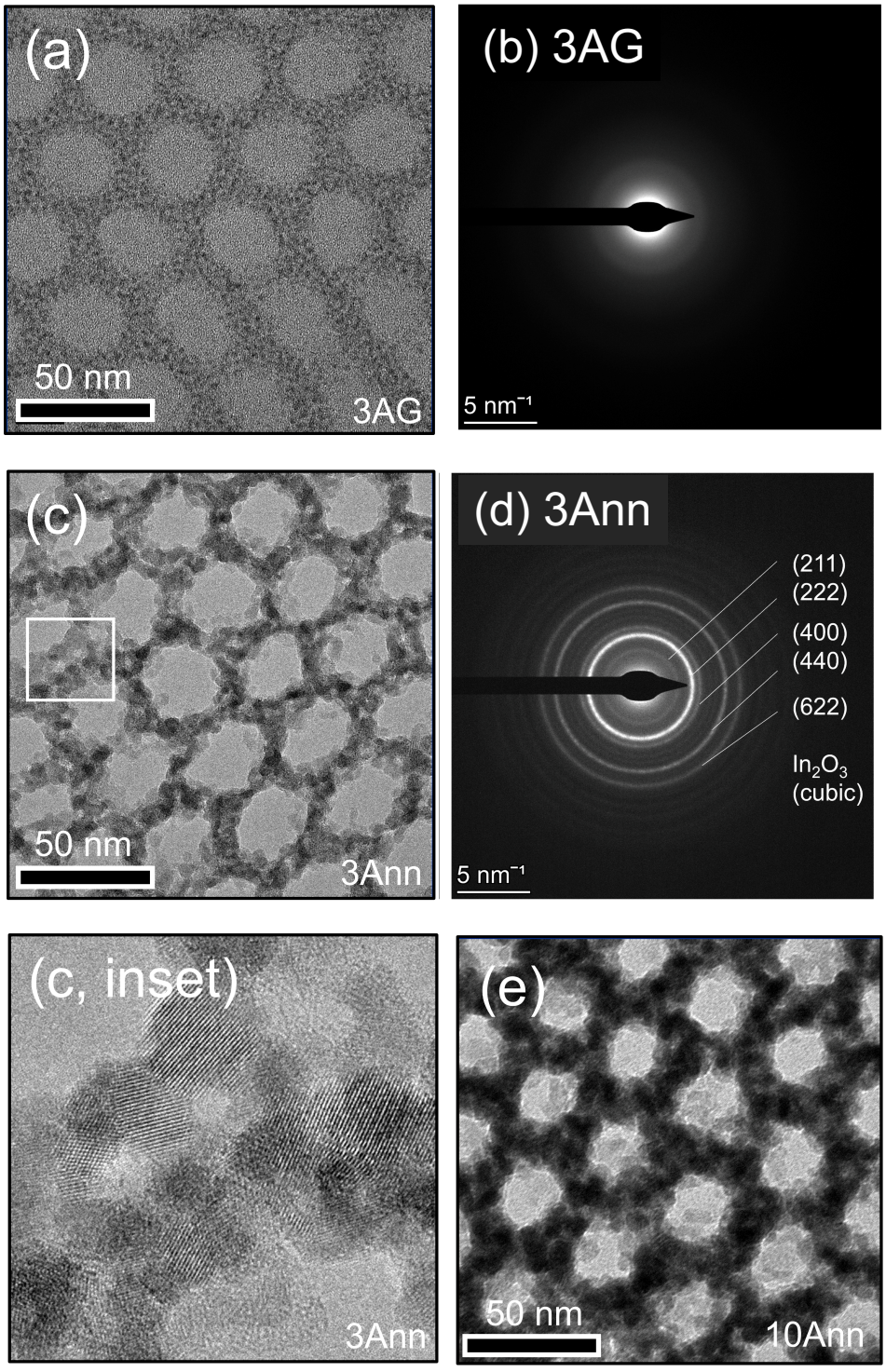

Figure 6.10: a) TEM image of an SIS In_2O_3 in BCP film in the hybrid state. b) Diffractogram of this film reveals amorphous nature of hybrid film. c) TEM image of the same film after annealing showing reconstruction into mesostructured nanoparticles. The inset reveals the atomic lattice spacing consistent with a crystalline material and the development of a smaller pore structure between the nanoparticles. d) TEM image of 10 cycle growth after annealing.

like In_2O_3, which crystallize during polymer removal, permit the formation of heirarchically porous frameworks.

6.4 Materials and Methods

6.4.1 BCP Film Preparation

Silicon wafer substrates were prepared by cleaning in piranha solution (3:7 by volume of concentrated sulfuric acid to 30% H_2O_2 at 130 °C) for twenty minutes followed by thorough rinsing with deionized water. The silicon wafers were optionally coated with ∼100 nm of polyacrylic acid (PAA), by spin-coating a solution of 5 wt% PAA in deionized water at 4000 rpm for two minutes. Next, a ∼10-nm layer of neutralizing random copolymer mat composed of 63% styrene, 33% methyl methacrylate, and 4% glycidyl methacrylate is spin-coated from a 0.5 wt% solution in toluene at 4000 rpm for one minute. These were then cross-linked on a hot-plate in a nitrogen-filled glovebox at 230 °C for 20 minutes. After cross-linking, the samples were sonicated in toluene for 5 minutes to remove any excess un-crosslinked random copolymer. Next, ∼80-140 nm of PS-b-PMMA (20.2-b-50.5 kg/mol) purchased from Polymer Source Inc. was spin-coated from a 2-4 wt%. solution in toluene at 4000 rpm. These samples were finally annealed in a nitrogen-filled glovebox at 270 °C for three hours to promote the self-assembly of the polystyrene cylinders in a PMMA matrix.

6.4.2 TEM Aample Preparation and Measurements

An 80 nm BCP films was prepared using the previous protocol. A diamond scribe was then used to scratch this polymer stack into small squares less than two mm on a side. The silicon substrate was carefully lowered into a DI water bath at a shallow angle, so that the water would gradually dissolve the PAA layer and cause the self-assembled block copolymer layer to release onto the water surface. A thin fiber was used to break the polymer film into small pieces along the scratched lines. These fragments of the film were carefully col-

lected by floatation onto TEM support films and dried at room temperature (Figure 6.11). The support films used were microporous silicon nitride (Si_3N_4) windows purchased from TEMWindows/SimPore Inc. These TEM supports consist of a 100-μm thick Silicon substrate with a 500-μm square 50 nm thick self-supporting Si_3N_4 window in its center. This window itself is patterned with 2-μm circular perforations. Subsequently, these BCP film covered microporous Si_3N_4 support films were placed in the ALD chamber and subjected to the SIS procedures mentioned above. The experimental analytical electron microscopy (AEM) data of these as-prepared products were measured using ThermoFisher Tecnai F20 and Talos F20X Field Emission Transmission and Scanning Transmission Electron Microscopes (TEM/ STEM) operating at 200 kV. All data were recorded at room temperature in low background high visibility Beryllium double tilt specimen holders. TEM image and diffraction data were collected on the Tecani F20 using a Gatan Ultrascan 4kx4k CCD post column camera while STEM images were acquired on both the Tecnai F20 and Talos F20X using bright field (BF) and high angle annular dark field (HAADF) detectors which were integrated into the respective microscopes. As-needed images and diffraction data were calibrated using reference specimens of graphite and gold.

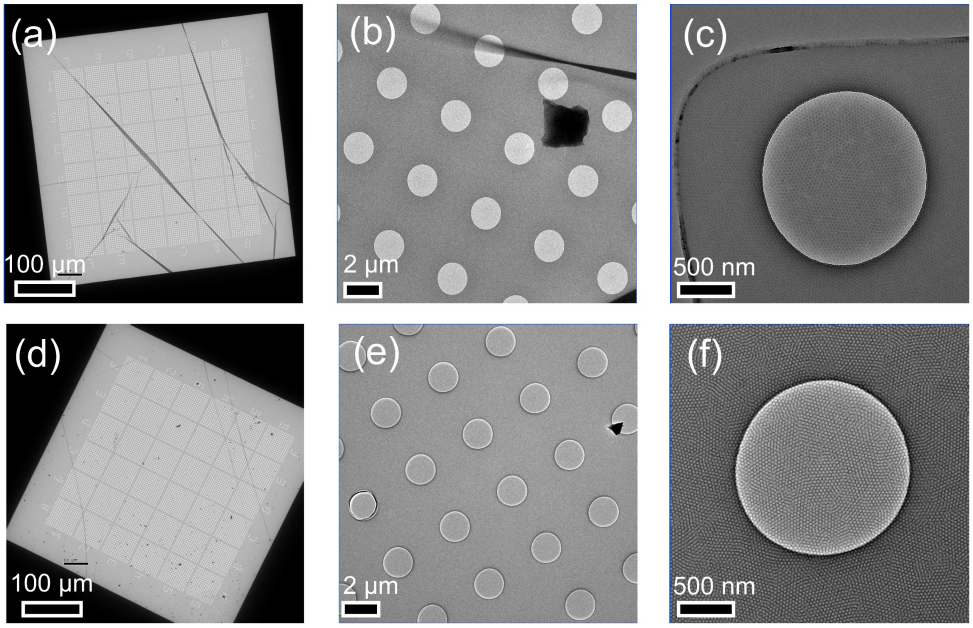

Figure 6.11: TEM images of block copolymer film covered TEM grid before (a, b, c) and after (d, e, f) three cycles of SIS processes.

REFERENCES

[1] Anna Lee, Jeffrey W. Elam, and Seth B. Darling. Membrane Materials for Water Purification: Design, Development, and Application. *Environmental Science Water Research & Technology*, 2:17–42, 2016.

[2] Peter H. Gleick. Water and Energy. *Annual Review of Energy and the Environment*, 19(1):267–299, 1994.

[3] Mark A. Shannon, Paul W. Bohn, Menachem Elimelech, John G. Georgiadis, Benito J. Mariñas, and Anne M. Mayes. Science and Technology for Water Purification in the Coming Decades. *Nature*, 452(7185):301–310, 2008.

[4] United Nations World Water Development Report: Water in A Changing World, 2009.

[5] Pratap Singh and Lars Bengtsson. Impact of Warmer Climate on Melt and Evaporation for the Rainfed, Snowfed and Glacierfed Basins in the Himalayan Region. *Journal of Hydrology*, 300(1-4):140–154, 2005.

[6] Raymond S. Bradley, Mathias Vuille, Henry F. Diaz, and Walter Vergara. Threats to Water Supplies in the Tropical Andes. *Science*, 312:1755–1756, 2006.

[7] Maggie A. Montgomery and Menachem Elimelech. Water And Sanitation in Developing Countries: Including Health in the Equation. *Environmental Science & Technology*, 41(1):17–24, 2007.

[8] Peter H. Gleick. Water and Conflict : Fresh Water Resources and International Security. *International Security*, 18(1):79–112, 1993.

[9] United Nations Department of Economic and Social Affairs. International Decade for Action 'Water for Life', 2010.

[10] Jan Eliasson. The Rising Pressure of Global Water Shortages. *Nature*, 517(7532), 2015.

[11] Jay R. Lund. Integrating Social and Physical sciences in Water Management. *Water Resources Research*, 51:5905–5918, 2015.

[12] David S. Sholl and Ryan P. Lively. Seven Chemical Separations to Change the World. *Nature*, 532(435-437):6–8, 2016.

[13] Yaşar Demirel. Thermodynamic Analysis of Separation Systems. *Separation Science and Technology*, 39(16):3897–942, 2004.

[14] Anthony G. Fane, Rong Wang, and Matthew X. Hu. Synthetic membranes for water purification: Status and future. *Angewandte Chemie International Edition*, 54(11):3368–3386, 2015.

[15] Jay R. Werber, Chinedum O. Osuji, and Menachem Elimelech. Materials for Next-Generation Desalination and Water Purification Membranes. *Nature Reviews Materials*, 1:16018, 2016.

[16] Yizhou Zhang, Noelia E. Almodovar-Arbelo, Jacob L. Weidman, David S. Corti, Bryan W. Boudouris, and William A. Phillip. Fit-for-Purpose Block Polymer Membranes Molecularly Engineered for Water Treatment. *npj Clean Water*, 1(2), 2018.

[17] W. J. Koros, Y. H. Ma, and T. Shimidzu. Terminology for Membranes and Membrane Processes (IUPAC Recommendations 1996). *Pure and Applied Chemistry*, 68(7):1479–1489, 1996.

[18] Anthony Bennett. Membranes in industry: Facilitating reuse of wastewater. *Filtration Separation*, 42(8):28–30, 2005.

[19] Qing Peng, Yu-Chih Tseng, Seth B. Darling, and Jeffrey W. Elam. Nanoscopic patterned materials with tunable dimensions via atomic layer deposition on block copolymers. *Advanced Materials*, 22(45):5129–5133, 2010.

[20] Collen Z. Leng and Mark D. Losego. Vapor phase infiltration (VPI) for transforming polymers into organic-inorganic hybrid materials: A critical review of current progress and future challenges. *Materials Horizons*, 4(5):747–771, 2017.

[21] Ruben Z. Waldman, David J. Mandia, Angel Yanguas-Gil, Alex B. F. Martinson, Jeffrey W. Elam, and Seth B. Darling. The chemical physics of sequential infiltration synthesis — a thermodynamic and kinetic perspective. *The Journal of Chemical Physics*, 151(19):190901, 2019.

[22] C. A. Wilson, R. K. Grubbs, and S. M. George. Nucleation and Growth during Al_2O_3 Atomic Layer Deposition on Polymers. *Chemistry of Materials*, 17(23):5625–5634, 2005.

[23] Ashwini Sinha, Dennis W. Hess, and Clifford L. Henderson. Area Selective Atomic Layer Deposition of Titanium Dioxide: Effect of Precursor Chemistry. *Journal of Vacuum Science & Technology B: Microelectronics and Nanometer Structures Processing, Measurement, and Phenomena*, 24(6):2523–2532, 2006.

[24] Ashwini Sinha, Dennis W. Hess, and Clifford L. Henderson. Transport Behavior of Atomic Layer Deposition Precursors through Polymer Masking Layers: Influence on Area Selective Atomic Layer Deposition. *Journal of Vacuum Science & Technology B: Microelectronics and Nanometer Structures Processing, Measurement, and Phenomena*, 25(5):1721–1728, 2007.

[25] Hong Chen Guo, Enyi Ye, Zibiao Li, Ming-Yong Han, and Xian Jun Loh. Recent Progress of Atomic Layer Deposition on Polymeric Materials. *Materials Science and Engineering: C*, 70:1182–1191, 2017.

[26] Steven M. George, Byunghoon Yoon, Robert A. Hall, Aziz I. Abdulagatov, Zachary M. Gibbs, Younghee Lee, Dragos Seghete, and Byoung H. Lee. *Molecular Layer Deposition of Hybrid Organic-Inorganic Films*, chapter 5, pages 83–107. John Wiley Sons, Ltd, 2012.

[27] Bo Gong, Qing Peng, Jesse S. Jur, Christina K. Devine, Kyoungmi Lee, and Gregory N. Parsons. Sequential Vapor Infiltration of Metal Oxides into Sacrificial Polyester Fibers: Shape Replication and Controlled Porosity of Microporous/Mesoporous Oxide Monoliths. *Chemistry of Materials*, 23(15):3476–3485, 2011.

[28] Chang Yong Nam, Aaron Stein, Kim Kisslinger, and Charles T. Black. Electrical and structural properties of ZnO synthesized via infiltration of lithographically defined polymer templates. *Applied Physics Letters*, 107(20):203106, 2015.

[29] Ashwanth Subramanian, Nikhil Tiwale, and Chang Yong Nam. Review of Recent Advances in Applications of Vapor-Phase Material Infiltration Based on Atomic Layer Deposition. *JOM*, 71(1):185–196, 2019.

[30] Itxasne Azpitarte and Mato Knez. Vapor Phase Infiltration: from a Bioinspired Process to Technologic Application, a Prospective Review. *MRS Communications*, 8(3):727–741, 2018.

[31] Collen Z. Leng and Mark D. Losego. A Physiochemical Processing Kinetics Model for the Vapor Phase Infiltration of Polymers: Measuring the Energetics of Precursor-Polymer Sorption, Diffusion, and Reaction. *Physical Chemistry Chemical Physics*, 20:21506–21514, 2018.

[32] Qing Peng, Yu-Chih Tseng, Seth B. Darling, and Jeffrey W. Elam. A route to nanoscopic materials via sequential infiltration synthesis on block copolymer templates. *ACS Nano*, 5(6):4600–4606, 2011.

[33] Inbal Weisbord, Neta Shomrat, Hen Moshe, Alejandro Sosnik, and Tamar Segal-Peretz. Nano Spray-Dried Block Copolymer Nanoparticles and Their Transformation into Hybrid and Inorganic Nanoparticles. *Advanced Functional Materials*, page 1808932, 2019.

[34] Jeffrey W. Elam, Mahua Biswas, Seth B. Darling, Angel Yanguas-Gil, Jonathan D. Emery, Alex B.F. Martinson, Paul F. Nealey, Tamar Segal-Peretz, Qing Peng, Jonathan Winterstein, J. Alexander Liddle, and Yu-Chih Tseng. New Insights into Sequential Infiltration Synthesis. *ECS Transactions*, 69(7):147–157, 2015.

[35] Matteo Lorenzoni, Laura Evangelio, Marta Fernández-Regúlez, Célia Nicolet, Christophe Navarro, and Francesc Pérez-Murano. Sequential Infiltration of Self-Assembled Block Copolymers: A Study by Atomic Force Microscopy. *The Journal of Physical Chemistry C*, 121(5):3078–3086, 2017.

[36] Ruben Z. Waldman, Nari Jeon, David J. Mandia, Olle Heinonen, Seth B. Darling, and Alex B. F. Martinson. Sequential Infiltration Synthesis of Electronic Materials: Group 13 Oxides via Metal Alkyl Precursors. *Chemistry of Materials*, 31(14):5274–5285, 2019.

[37] Rotem Azoulay, Neta Shomrat, Inbal Weisbord, Galit Atiya, and Tamar Segal-Peretz. Metal Oxide Heterostructure Array via Spatially Controlled-Growth within Block Copolymer Templates. *Small*, 15(51):1904657, 2019.

[38] Seung-Mo Lee, Eckhard Pippel, Oussama Moutanabbir, Jae-Hyun Kim, Hak-Joo Lee, and Mato Knez. In Situ Raman Spectroscopic Study of Al-Infiltrated Spider Dragline Silk under Tensile Deformation. *ACS Applied Materials & Interfaces*, 6(19):16827–16834, 2014.

[39] Daniel H. Yi, Chang-Yong Nam, Gregory Doerk, Charles T. Black, and Robert B. Grubbs. Infiltration Synthesis of Diverse Metal Oxide Nanostructures from Epoxidized Diene-Styrene Block Copolymer Templates. *ACS Applied Polymer Materials*, 1(4):672–683, 2019.

[40] Richard P. Padbury and Jesse S. Jur. Effect of Polymer Microstructure on the Nucleation Behavior of Alumina via Atomic Layer Deposition. *The Journal of Physical Chemistry C*, 118(32):18805–18813, 2014.

[41] Gregory N. Parsons, Sarah E. Atanasov, Erinn C. Dandley, Christina K. Devine, Bo Gong, Jesse S. Jur, Kyoungmi Lee, Christopher J. Oldham, Qing Peng, Joseph C. Spagnola, and Philip S. Williams. Mechanisms and Reactions during Atomic Layer Deposition on Polymers. *Coordination Chemistry Reviews*, 257(23):3323–3331, 2013.

[42] Bo Gong and Gregory N. Parsons. Quantitative in situ infrared analysis of reactions between trimethylaluminum and polymers during Al_2O_3 atomic layer deposition. *Journal of Materials Chemistry*, 22(31):15672–15682, 2012.

[43] Mahua Biswas, Joseph A. Libera, Seth B. Darling, and Jeffrey W. Elam. New insight into the mechanism of sequential infiltration synthesis from infrared spectroscopy. *Chemistry of Materials*, 26:6135–6141, 2014.

[44] Mahua Biswas, Joseph A. Libera, Seth B. Darling, and Jeffrey W. Elam. Kinetics for the sequential infiltration synthesis of alumina in poly(methyl methacrylate): An infrared spectroscopic study. *Journal of Physical Chemistry C*, 119(26):14585–14592, 2015.

[45] Erinn C. Dandley, Craig D. Needham, Philip S. Williams, Alexandra H. Brozena, Christopher J. Oldham, and Gregory N. Parsons. Temperature-dependent reaction between trimethylaluminum and poly(methyl methacrylate) during sequential vapor infiltration: Experimental and ab initio analysis. *Journal of Materials Chemistry C*, 2(44):9416–9424, 2014.

[46] Elena Cianci, Daniele Nazzari, Gabriele Seguini, and Michele Perego. Trimethylaluminum Diffusion in PMMA Thin Films during Sequential Infiltration Synthesis: In Situ Dynamic Spectroscopic Ellipsometric Investigation. *Advanced Materials Interfaces*, 5(20):1801016, 2018.

[47] Grant T. Hill, Dennis T. Lee, Philip S. Williams, Craig D. Needham, Erinn C. Dandley, Christopher J Oldham, and Gregory N. Parsons. Insight on the Sequential Vapor Infiltration Mechanisms of Trimethylaluminum with Poly(methyl methacrylate), Poly(vinylpyrrolidone), and Poly(acrylic acid). *The Journal of Physical Chemistry C*, 123:16146–16152, 2019.

[48] Federica E. Caligiore, Daniele Nazzari, Elena Cianci, Katia Sparnacci, Michele Laus, Michele Perego, and Gabriele Seguini. Effect of the Density of Reactive Sites in P(S-*r*-MMA) Film During Al_2O_3 Growth by Sequential Infiltration Synthesis. *Advanced Materials Interfaces*, 6(12):1900503, 2019.

[49] Jacopo Frascaroli, Elena Cianci, Sabina Spiga, Gabriele Seguini, and Michele Perego. Ozone-Based Sequential Infiltration Synthesis of Al_2O_3 Nanostructures in Symmetric Block Copolymer. *ACS Applied Materials and Interfaces*, 8(49):33933–33942, 2016.

[50] Yunlong She, Jihyung Lee, Benjamin T. Diroll, Byeongdu Lee, Samir Aouadi, Elena V. Shevchenko, and Diana Berman. Rapid Synthesis of Nanoporous Conformal Coatings via Plasma-Enhanced Sequential Infiltration of a Polymer Template. *ACS Omega*, 2(11):7812–7819, 2017.

[51] Olga M. Ishchenko, Sivashankar Krishnamoorthy, Nathalie Valle, Jérôme Guillot, Philippe Turek, Ioana Fechete, and Damien Lenoble. Investigating Sequential Vapor Infiltration Synthesis on Block-Copolymer-Templated Titania Nanoarrays. *The Journal of Physical Chemistry C*, 120(13):7067–7076, 2016.

[52] Jun Yin, Qiang Xu, Zhaogen Wang, Xueping Yao, and Yong Wang. Highly ordered TiO_2 nanostructures by sequential vapour infiltration of block copolymer micellar films in an atomic layer deposition reactor. *Journal of Materials Chemistry C*, 1(5):1029–1036, 2013.

[53] Qing Peng, Yu-Chih Tseng, Yun Long, Anil U. Mane, Shane DiDona, Seth B. Darling, and Jeffrey W. Elam. Effect of Nanostructured Domains in Self-Assembled Block Copolymer Films on Sequential Infiltration Synthesis. *Langmuir*, 33(46):13214–13223, 2017.

[54] Xinyi Ye, John Kestell, Kim Kisslinger, Mingzhao Liu, Robert B. Grubbs, J. Anibal Boscoboinik, and Chang-Yong Nam. Effects of Residual Solvent Molecules Facilitating the Infiltration Synthesis of ZnO in a Nonreactive Polymer. *Chemistry of Materials*, 29(10):4535–4545, 2017.

[55] Jae Jin Kim, Hyo Seon Suh, Chun Zhou, Anil U. Mane, Byeongdu Lee, Soojeong Kim, Jonathan D. Emery, Jeffrey W. Elam, Paul F. Nealey, Paul Fenter, and Timothy T. Fister. Mechanistic Understanding of Tungsten Oxide In-Plane Nanostructure Growth via Sequential Infiltration Synthesis. *Nanoscale*, 10:3469–3479, 2018.

[56] Barun K. Barick, Assaf Simon, Inbal Weisbord, Neta Shomrat, and Tamar Segal-Peretz. Tin Oxide Nanostructure Fabrication via Sequential Infiltration Synthesis in

Block Copolymer Thin Films. *Journal of Colloid and Interface Science*, 557:537–545, 2019.

[57] Tamar Segal-Peretz, Jonathan Winterstein, Manolis Doxastakis, Abelardo Ramirez-Hernandez, Mahua Biswas, Jiaxing Ren, Hyo Seon Suh, Seth B. Darling, J. Alexander Liddle, Jeffrey W. Elam, Juan J. de Pablo, Nestor J. Zaluzec, and Paul F. Nealey. Characterizing the Three-Dimensional Structure of Block Copolymers via Sequential Infiltration Synthesis and Scanning Transmission Electron. *ACS Nano*, 9(5):5333–5347, 2015.

[58] Chun Zhou, Tsuyoshi Kurosawa, Takahiro Dazai, Jan Doise, Jiaxing Ren, Cody Bezik, Tamar Segal-Peretz, Roel Gronheid, Paulina Rincon-Delgadillo, Akiyoshi Yamazaki, Juan de Pablo, and Paul F. Nealey. Studying the Effects of Chemistry and Geometry on DSA Hole-Shrink Process in Three-Dimensions. *Journal of Micro/Nanolithography, MEMS, and MOEMS*, 17(3):1–7, 2018.

[59] Stas Obuchovsky, Matan Levin, Artem Levitsky, and Gitti L. Frey. Morphology Visualization of P3HT:Fullerene Blends by Using Subsurface Atomic Layer Deposition. *Organic Electronics*, 49:234–241, 2017.

[60] Yunlong She, Emmett D. Goodman, Jihyung Lee, Benjamin T. Diroll, Matteo Cargnello, Elena V. Shevchenko, and Diana Berman. Block-Co-polymer-Assisted Synthesis of All Inorganic Highly Porous Heterostructures with Highly Accessible Thermally Stable Functional Centers. *ACS Applied Materials & Interfaces*, 11(33):30154–30162, 2019.

[61] Bo Gong, Do Han Kim, and Gregory N. Parsons. Mesoporous Metal Oxides by Vapor Infiltration and Atomic Layer Deposition on Ordered Surfactant Polymer Films. *Langmuir*, 28(32):11906–11913, 2012.

[62] Yanhao Yu, Zhaodong Li, Yunming Wang, Shaoqin Gong, and Xudong Wang. Sequential Infiltration Synthesis of Doped Polymer Films with Tunable Electrical Properties for Efficient Triboelectric Nanogenerator Development. *Advanced Materials*, 27(33):4938–4944, 2015.

[63] Edward Barry, Anil U. Mane, Joseph A. Libera, Jeffrey W. Elam, and Seth B. Darling. Advanced oil sorbents using sequential infiltration synthesis. *Journal of Materials Chemistry A*, 5:2929–2935, 2017.

[64] Edward Barry, Joseph A. Libera, Anil U. Mane, Jason R. Avila, David DeVitis, Keith Van Dyke, Jeffrey W. Elam, and Seth B. Darling. Mitigating oil spills in the water column. *Environmental Science: Water Research & Technology*, 4(1):40–47, 2018.

[65] Chang Yong Nam and Aaron Stein. Extreme Carrier Depletion and Superlinear Photoconductivity in Ultrathin Parallel-Aligned ZnO Nanowire Array Photodetectors Fabricated by Infiltration Synthesis. *Advanced Optical Materials*, 5(24):1700807, 2017.

[66] Leonidas E. Ocola, Yale Wang, Ralu Divan, and Junhong Chen. Multifunctional UV and Gas Sensors Based on Vertically Nanostructured Zinc Oxide: Volume Versus Surface Effect. *Sensors*, 19(9):2061, 2019.

[67] Halil I. Akyildiz, Kelly L. Stano, Adam T. Roberts, Henry O. Everitt, and Jesse S. Jur. Photoluminescence Mechanism and Photocatalytic Activity of Organic-Inorganic Hybrid Materials Formed by Sequential Vapor Infiltration. *Langmuir*, 32(17):4289–4296, 2016.

[68] Leonidas E. Ocola, Aine Connolly, David J. Gosztola, Richard D. Schaller, and Angel Yanguas-Gil. Infiltrated Zinc Oxide in Poly(methyl methacrylate): An Atomic Cycle Growth Study. *The Journal of Physical Chemistry C*, 121(3):1893–1903, 2017.

[69] Jonathan E. Allen, Biswajit Ray, M. Ryyan Khan, Kevin G. Yager, Muhammad A. Alam, and Charles T. Black. Self-Assembly of Single Dielectric Nanoparticle Layers and Integration in Polymer-Based Solar Cells. *Applied Physics Letters*, 101(6):063105, 2012.

[70] Moshe Moshonov and Gitti L. Frey. Directing Hybrid Structures by Combining Self-Assembly of Functional Block Copolymers and Atomic Layer Deposition: A Demonstration on Hybrid Photovoltaics. *Langmuir*, 31(46):12762–12769, 2015.

[71] Stas Obuchovsky, I. Deckman, M. Moshonov, Tamar Segal-Peretz, G. Ankonina, T. J. Savenije, and Gitti L. Frey. Atomic Layer Deposition of Zinc Oxide Onto and Into P3HT for Hybrid Photovoltaics. *Journal of Materials Chemistry C*, 2(42):8903–8910, 2014.

[72] Stas Obuchovsky, Hadar Frankenstein, Jane Vinokur, Anna K. Hailey, Yueh-Lin Loo, and Gitti L. Frey. Mechanism of Metal Oxide Deposition from Atomic Layer Deposition inside Nonreactive Polymer Matrices: Effects of Polymer Crystallinity and Temperature. *Chemistry of Materials*, 28(8):2668–2676, 2016.

[73] Diana Berman, Supratik Guha, Byeongdu Lee, Jeffrey W. Elam, Seth B. Darling, and Elena V. Shevchenko. Sequential Infiltration Synthesis for the Design of Low Refractive Index Surface Coatings with Controllable Thickness. *ACS Nano*, 11(3):2521–2530, 2017.

[74] Atikur Rahman, Ahsan Ashraf, Huolin Xin, Xiao Tong, Peter Sutter, Matthew D. Eisaman, and Charles T. Black. Sub-50-nm Self-Assembled Nanotextures for Enhanced Broadband Antireflection in Silicon Solar Cells. *Nature Communications*, 6:5963, 2015.

[75] Wenyi Xie, Saad Khan, Orlando J. Rojas, and Gregory N. Parsons. Control of Micro- and Mesopores in Carbon Nanofibers and Hollow Carbon Nanofibers Derived from Cellulose Diacetate via Vapor Phase Infiltration of Diethyl Zinc. *ACS Sustainable Chemistry & Engineering*, 6(11):13844–13853, 2018.

[76] Chun Zhou, Tamar Segal-Peretz, Muhammed Enes Oruc, Hyo Seon Suh, Guangpeng Wu, and Paul F. Nealey. Fabrication of Nanoporous Alumina Ultrafiltration Membrane

with Tunable Pore Size Using Block Copolymer Templates. *Advanced Functional Materials*, 27(34):1701756, 2017.

[77] Ruben Z. Waldman, Devika Choudhury, David J. Mandia, Jeffrey W. Elam, Paul F. Nealey, Alex B.F. Martinson, and Seth B. Darling. Sequential Infiltration Synthesis of Al_2O_3 in Polyethersulfone Membranes. *JOM*, 71(1):212–223, 2019.

[78] Emily K. McGuinness, Fengyi Zhang, Yao Ma, Ryan P. Lively, and Mark D. Losego. Vapor Phase Infiltration of Metal Oxides into Nanoporous Polymers for Organic Solvent Separation Membranes. *Chemistry of Materials*, 31(15):5509–5518, 2019.

[79] Itxasne Azpitarte, Ana Zuzuarregui, Hayrensa Ablat, Leire Ruiz-Rubio, Alberto López-Ortega, Simon D. Elliott, and Mato Knez. Suppressing the Thermal and Ultraviolet Sensitivity of Kevlar by Infiltration and Hybridization with ZnO. *Chemistry of Materials*, 29(23):10068–10074, 2017.

[80] Emily K. McGuinness, Collen Z. Leng, and Mark D. Losego. Increased Chemical Stability of Vapor-Phase Infiltrated AlO_x-Poly(methyl methacrylate) Hybrid Materials. *ACS Applied Polymer Materials*, 2020.

[81] Weike Wang, Chaoqiu Chen, Christopher Tollan, Fan Yang, Mikel Beltrán, Yong Qin, and Mato Knez. Conductive Polymer-Inorganic Hybrid Materials through Synergistic Mutual Doping of the Constituents. *ACS Applied Materials and Interfaces*, 9(33):27964–27971, 2017.

[82] Weike Wang, Fan Yang, Chaoqiu Chen, Lianbing Zhang, Yong Qin, and Mato Knez. Tuning the Conductivity of Polyaniline through Doping by Means of Single Precursor Vapor Phase Infiltration. *Advanced Materials Interfaces*, 4(4):1600806, 2017.

[83] Weike Wang, Chaoqiu Chen, Christopher Tollan, Fan Yang, Mikel Beltrán, Yong Qin, and Mato Knez. Conductive Polymer-Inorganic Hybrid Materials through Synergistic Mutual Doping of the Constituents. *ACS Applied Materials and Interfaces*, 9(33):27964–27971, 2017.

[84] Ashwanth Subramanian, Gregory S Doerk, Kim Kisslinger, Daniel H. Yi, Robert B. Bernard Grubbs, and Chang-Yong Nam. Three-Dimensional Electroactive ZnO Nanomesh Directly Derived from Hierarchically Self-Assembled Block Copolymer Thin Films. *Nanoscale*, 11(19):9533–9546, 2019.

[85] Yujie Sun, Richard P. Padbury, Halil I. Akyildiz, Matthew P. Goertz, Jeremy A. Palmer, and Jesse S. Jur. Influence of Subsurface Hybrid Material Growth on the Mechanical Properties of Atomic Layer Deposited Thin Films on Polymers. *Chemical Vapor Deposition*, 19(46):134–141, 2013.

[86] Christina D. McClure, Christopher J. Oldham, and Gregory N. Parsons. Effect of Al_2O_3 ALD Coating and Vapor Infusion on the Bulk Mechanical Response of Elastic and Viscoelastic Polymers. *Surface and Coatings Technology*, 261:411–417, 2015.

[87] Keith J. Dusoe, Xinyi Ye, Kim Kisslinger, Aaron Stein, Seok Woo Lee, and Chang Yong Nam. Ultrahigh Elastic Strain Energy Storage in Metal-Oxide-Infiltrated Patterned Hybrid Polymer Nanocomposites. *Nano Letters*, 17(12):7416–7423, 2017.

[88] Seung-Mo Lee, Eckhard Pippel, Ulrich Gösele, Christian Dresbach, Yong Qin, C. Vinod Chandran, Thomas Bräuniger, Gerd Hause, and Mato Knez. Greatly Increased Toughness of Infiltrated Spider Silk. *Science*, 324(5926):488–492, 2009.

[89] S. Dwarakanath, P. Raj, C. Z. Leng, V. Smet, M. D. Losego, V. Sundaram, and R. Tummala. Infusing Inorganics into the Subsurface of Polymer Redistribution Layer Dielectrics for Improved Adhesion to Metals Interconnects. In *2017 IEEE 67th Electronic Components and Technology Conference (ECTC)*, pages 150–155. IEEE Computer Society, 2017.

[90] Seung-Mo Lee, Eckhard Pippel, Oussama Moutanabbir, Ilja Gunkel, Thomas Thurn-Albrecht, and Mato Knez. Improved Mechanical Stability of Dried Collagen Membrane after Metal Infiltration. *ACS Applied Materials & Interfaces*, 2(8):2436–2441, 2010.

[91] Keith E. Gregorczyk, David F. Pickup, Miren Garcia Sanz, Itxasne Azpitarte Irakulis, Celia Rogero, and Mato Knez. Tuning the Tensile Strength of Cellulose through Vapor-Phase Metalation. *Chemistry of Materials*, 27(1):181–188, 2015.

[92] Seung-Mo Lee, Vladislav Ischenko, Eckhard Pippel, Admir Masic, Oussama Moutanabbir, Peter Fratzl, and Mato Knez. An Alternative Route Towards Metal-Polymer Hybrid Materials Prepared by Vapor-Phase Processing. *Advanced Functional Materials*, 21(16):3047–3055, 2011.

[93] Yu-Chih Tseng, Anil U. Mane, Jeffrey W. Elam, and Seth B. Darling. Enhanced Lithographic Imaging Layer Meets Semiconductor Manufacturing Specification a Decade Early. *Advanced Materials*, 24:2608–2613, 2012.

[94] Stefanie Greil, Atikur Rahman, Mingzhao Liu, and Charles T. Black. Gas Transport Selectivity of Ultrathin, Nanoporous, Inorganic Membranes Made from Block Copolymer Templates. *Chemistry of Materials*, 29(21):9572–9578, 2017.

[95] Ricardo Ruiz, Lei Wan, Jeffrey Lille, Kanaiyalal C. Patel, Elizabeth Dobisz, Danvers E. Johnston, Kim Kisslinger, and Charles T. Black. Image Quality and Pattern Transfer in Directed Self Assembly with Block-Selective Atomic Layer Deposition. *Journal of Vacuum Science & Technology B, Nanotechnology and Microelectronics: Materials, Processing, Measurement, and Phenomena*, 30(6):06F202, 2012.

[96] Atikur Rahman, Pawel W. Majewski, Gregory Doerk, Charles T. Black, and Kevin G. Yager. Non-Native Three-Dimensional Block Copolymer Morphologies. *Nature Communications*, 7:13988, 2016.

[97] Stefano Dallorto, Daniel Staaks, and Adam Schwartzberg. Atomic Layer Deposition for Spacer Defined Double Patterning of sub-10 nm Titanium Dioxide Features. *Nanotechnology*, 29(40):405302, 2018.

[98] Daniel F. Sunday, Elizabeth Ashley, Lei Wan, Kanaiyalal C. Patel, Ricardo Ruiz, and R. Joseph Kline. Template-Polymer Commensurability and Directed Self-Assembly Block Copolymer Lithography. *Journal of Polymer Science Part B: Polymer Physics*, 53(8):595–603, 2015.

[99] Gregory S. Doerk, He Gao, Lei Wan, Jeff Lille, K. C. Patel, Yves-Andre Chapuis, Ricardo Ruiz, and Thomas R. Albrecht. Transfer of Self-Aligned Spacer Patterns for Single-Digit Nanofabrication. *Nanotechnology*, 26(8):085304, 2015.

[100] Yu-Chih Tseng, Qing Peng, Leonidas E. Ocola, David A. Czaplewski, Jeffrey W. Elam, and Seth B. Darling. Etch properties of resists modified by sequential infiltration synthesis. *Journal of Vacuum Science & Technology B*, 21(32):11653–12152, 2011.

[101] Yu-Chih Tseng, Qing Peng, Leonidas E. Ocola, David A. Czaplewski, Jeffrey W. Elam, and Seth B. Darling. Enhanced Polymeric Lithography Resists via Sequential Infiltration Synthesis. *Joutnal of Materials Chemistry*, 21:11722–11725, 2011.

[102] Yuki Ozaki, Shunya Ito, Nobuya Hiroshiba, Takahiro Nakamura, and Masaru Nakagawa. Elemental Depth Profiles and Plasma Etching Rates of Positive-Tone Electron Beam Resists after Sequential Infiltration Synthesis of Alumina. *Japanese Journal of Applied Physics*, 57(6):06HG01, 2018.

[103] Erinn C. Dandley, Paul C. Lemaire, Zhongwei Zhu, Alex Yoon, Lubab Sheet, and Gregory N. Parsons. Wafer-Scale Selective-Area Deposition of Nanoscale Metal Oxide Features Using Vapor Saturation into Patterned Poly(methyl methacrylate) Templates. *Advanced Materials Interfaces*, 3(2):1500431, 2016.

[104] Nikhil Tiwale, Ashwanth Subramanian, Kim Kisslinger, Ming Lu, Jiyoung Kim, Aaron Stein, and Chang Yong Nam. Advancing Next Generation Nanolithography with Infiltration Synthesis of Hybrid Nanocomposite Resists. *Journal of Materials Chemistry C*, 7:8803–8812, 2019.

[105] Jonathan W. Choi, Zhaodong Li, Charles T. Black, Daniel P. Sweat, Xudong Wang, and Padma Gopalan. Patterning at the 10 Nanometer Length Scale Using a Strongly Segregating Block Copolymer Thin Film and Vapor Phase Infiltration of Inorganic Precursors. *Nanoscale*, 8:11595–11601, 2016.

[106] Chang Yong Nam, Aaron Stein, and Kim Kisslinger. Direct fabrication of high aspect-ratio metal oxide nanopatterns via sequential infiltration synthesis in lithographically defined SU-8 templates. *Journal of Vacuum Science & Technology B, Nanotechnology and Microelectronics: Materials, Processing, Measurement, and Phenomena*, 33(6):06F201, 2015.

[107] Marina Baryshnikova, Danilo De Simone, Werner Knaepen, Krzysztof Kachel, BT Chan, Sara Paolillo, Jan Willem Maes, David De Roest, Paulina Rincon Delgadillo, and Geert Vandenberghe. Sequential Infiltration Synthesis for Line Edge Roughness Mitigation of EUV Resist. *Journal of Photopolymer Science and Technology*, 30(6):667–670, 2017.

[108] Jean-François de Marneffe, Boon Teik Chan, Martin Spieser, Guy Vereecke, Sergej Naumov, Danielle Vanhaeren, Heiko Wolf, and Armin W. Knoll. Conversion of a Patterned Organic Resist into a High Performance Inorganic Hard Mask for High Resolution Pattern Transfer. *ACS Nano*, 12(11):11152–11160, 2018.

[109] Shisheng Xiong, Yves-Andre Chapuis, Lei Wan, He Gao, Xiao Li, Ricardo Ruiz, and Paul F. Nealey. Directed Self-Assembly of High-Chi block Copolymer for Nano Fabrication of Bit Patterned Media via Solvent Annealing. *Nanotechnology*, 27(41):415601, 2016.

[110] Shisheng Xiong, Lei Wan, Yoshihito Ishida, Yves-Andre Chapuis, Gordon S. W. Craig, Ricardo Ruiz, and Paul F. Nealey. Directed Self-Assembly of Triblock Copolymer on Chemical Patterns for Sub-10-nm Nanofabrication via Solvent Annealing. *ACS Nano*, 10(8):7855–7865, 2016.

[111] W.R. Vieth, J.M. Howell, and J.H. Hsieh. Dual Sorption Theory. *Journal of Membrane Science*, 1:177–220, 1976.

[112] Qiang Xu, Jun Yang, Jiawei Dai, Yang Yang, Xiaoqiang Chen, and Yong Wang. Hydrophilization of Porous Polypropylene Membranes by Atomic Layer Deposition of TiO_2 for Simultaneously Improved Permeability and Selectivity. *Journal of Membrane Science*, 448:215–222, 2013.

[113] Maximilian Gebhard, Lukas Mai, Lars Banko, Felix Mitschker, Christian Hoppe, Montgomery Jaritz, Dennis Kirchheim, Christoph Zekorn, Teresa de Los Arcos, Dario Grochla, Rainer Dahlmann, Guido Grundmeier, Peter Awakowicz, Alfred Ludwig, and Anjana Devi. PEALD of SiO_2 and Al_2O_3 Thin Films on Polypropylene: Investigations of the Film Growth at the Interface, Stress and Gas Barrier Properties of Dyads. *ACS Applied Materials & Interfaces*, 10(8):7422–7434, 2018.

[114] Steven E. Brandt and Jeremy M. Grace. Initiation of Atomic Layer Deposition of Metal Oxides on Polymer Substrates by Water Plasma Pretreatment. *Journal of Vacuum Science & Technology A*, 30(1):01A137, 2012.

[115] Jovan Kamcev, David S. Germack, Dmytro Nykypanchuk, Robert B. Grubbs, Chang-Yong Nam, and Charles T. Black. Chemically Enhancing Block Copolymers for Block-Selective Synthesis of Self-Assembled Metal Oxide Nanostructures. *ACS Nano*, 7(1):339–346, 2013.

[116] Simon D. Elliott and James C. Greer. Simulating the Atomic Layer Deposition of Alumina from First Principles. *Journal of Materials Chemistry*, 14:3246–3250, 2004.

[117] Yuniarto Widjaja and Charles B. Musgrave. Quantum Chemical Study of the Mechanism of Aluminum Oxide Atomic Layer Deposition. *Applied Physics Letters*, 80(18):3304–3306, 2002.

[118] Do-Joong Lee, Jang-Yeon Kwon, Jae Il Lee, and Ki-Bum Kim. Self-Limiting Film Growth of Transparent Conducting In_2O3 by Atomic Layer Deposition using Trimethylindium and Water Vapor. *The Journal of Physical Chemistry C*, 115(31):15384–15389, 2011.

[119] Soney C George and Sabu Thomas. Transport Phenomena Through Polymeric Systems. *Progress in Polymer Science*, 26(6):985–1017, 2001.

[120] Tapan Banerjee and G.Glenn Lipscomb. Mixed Gas Sorption in Elastic Solids. *Journal of Membrane Science*, 96(3):241–258, 1994.

[121] A.R. Berens and H.B. Hopfenberg. Diffusion of Organic Vapors at low Concentrations in Glassy PVC, Polystyrene, and PMMA. *Journal of Membrane Science*, 10(2):283–303, 1982.

[122] Pratibha Pandey and R.S. Chauhan. Membranes for Gas Separation. *Progress in Polymer Science*, 26(6):853–893, 2001.

[123] Angel Yanguas-Gil and Jeffrey W. Elam. Self-Limited Reaction-Diffusion in Nanostructured Substrates: Surface Coverage Dynamics and Analytic Approximations to ALD Saturation Times. *Chemical Vapor Deposition*, 18(1-3):46–52, 2012.

[124] Angel Yanguas-Gil. *Growth and Transport in Nanostructured Materials*. Springer, 2017.

[125] R. M. Barrer and Eric K. Rideal. Permeation, Diffusion and Solution of Gases in Organic Polymers. *Trans. Faraday Soc.*, 35:628–643, 1939.

[126] V.T. Stannett, G.R. Ranade, and W.J. Koros. Characterization of Water Vapor Transport in Glassy Polyacrylonitrile by Combined Permeation and Sorption Techniques. *Journal of Membrane Science*, 10(2):219–233, 1982.

[127] D. K. Yang, W. J. Koros, H. B. Hopfenberg, and V. T. Stannett. Sorption and Transport Studies of Water in Kapton Polymide. *Journal of Applied Polymer Science*, 30(3):1035–1047, 1985.

[128] T. A. Barbari. Dual-Mode Free Volume Model for Diffusion of Gas Molecules in Glassy Polymers. *Journal of Polymer Science Part B: Polymer Physics*, 35(11):1737–1746, 1997.

[129] Wen-Yang Wen. Motion of sorbed gases in polymers. *Chemical Society Reviews*, 22:117–126, 1993.

[130] Christian Ohrt, Klaus Rätzke, Nagayasu Oshima, Yoshinori Kobayashi, Brian E. O'Rourke, Ryoichi Suzuki, Akira Uedono, and Franz Faupel. Free Volume Profiles at Polymer-Solid Interfaces Probed by Focused Slow Positron Beam. *Macromolecules*, 48(5):1493–1498, 2015.

[131] Joseph L. Keddie, Richard A. L. Jones, and Rachel A. Cory. Interface and Surface Effects on the Glass-transition Temperature in Thin Polymer Films. *Faraday Discuss.*, 98:219–230, 1994.

[132] John Algers, Ryoichi Suzuki, Toshiyuki Ohdaira, and Frans H. J. Maurer. Free Volume and Density Gradients of Amorphous Polymer Surfaces As Determined by Use of a Pulsed Low-Energy Positron Lifetime Beam and PVT Data. *Macromolecules*, 37(11):4201–4210, 2004.

[133] Senta Rogers and Leo Mandelkern. Glass Transitions of the Poly-(n-Alkyl Methacrylates). *The Journal of Physical Chemistry*, 61(7):985–991, 1957.

[134] Edward V. Thompson. Dependence of the Glass Transition Temperature of Poly(methyl methacrylate) on Tacticity and Molecular Weight. *Journal of Polymer Science Part A-2: Polymer Physics*, 4(2):199–208, 1966.

[135] Thomas G. Fox and Paul J. Flory. Second-Order Transition Temperatures and Related Properties of Polystyrene. I. Influence of Molecular Weight. *Journal of Applied Physics*, 21(6):581–591, 1950.

[136] David J.H. Emslie, Preeti Chadha, and Jeffrey S. Price. Metal ALD and Pulsed CVD: Fundamental Reactions and Links with Solution Chemistry. *Coordination Chemistry Reviews*, 257(23):3282–3296, 2013.

[137] W.M.M. Kessels. Overview of all Materials Prepared by Atomic Layer Deposition (ALD), 2019.

[138] Riikka L. Puurunen. Surface Chemistry of Atomic Layer Deposition: A Case Study for the Trimethylaluminum/Water Process. *Journal of Applied Physics*, 97(12):121301, 2005.

[139] Hao-Cheng Yang, Jingwei Hou, Vicki Chen, and Zhi-Kang Xu. Janus Membranes: Exploring Duality for Advanced Separation. *Angewandte Chemie International Edition*, 55(43):13398–13407, 2016.

[140] Yan Zhao, Hongxia Wang, Hua Zhou, and Tong Lin. Directional Fluid Transport in Thin Porous Materials and its Functional Applications. *Small*, 13(4):1601070, 2017.

[141] Hong-Jie Peng, Dai-Wei Wang, Jia-Qi Huang, Xin-Bing Cheng, Zhe Yuan, Fei Wei, and Qiang Zhang. Janus Separator of Polypropylene-Supported Cellular Graphene Framework for Sulfur Cathodes with High Utilization in Lithium-Sulfur Batteries. *Advanced Science*, 3(1):1500268, 2016.

[142] Yeon-Su Oh, Gwan Yeong Jung, Jeong-Hoon Kim, Jung-Hwan Kim, Su Hwan Kim, Sang Kyu Kwak, and Sang-Young Lee. Janus-Faced, Dual-Conductive/Chemically Active Battery Separator Membranes. *Advanced Functional Materials*, 26(39):7074–7083, 2016.

[143] Ming-Bang Wu, Hao-Cheng Yang, Jing-Jing Wang, Guang-Peng Wu, and Zhi-Kang Xu. Janus Membranes with Opposing Surface Wettability Enabling Oil-to-Water and Water-to-Oil Emulsification. *ACS Applied Materials & Interfaces*, 9(6):5062–5066, 2017.

[144] Liang Hu, Shoujian Gao, Yuzhang Zhu, Feng Zhang, Lei Jiang, and Jian Jin. An Ultrathin Bilayer Membrane with Asymmetric Wettability for Pressure Responsive Oil/Water Emulsion Separation. *Journal of Materials Chemistry A*, 3:23477–23482, 2015.

[145] Zijie Wang, Yu Wang, and Guojun Liu. Rapid and Efficient Separation of Oil from Oil-in-Water Emulsions Using a Janus Cotton Fabric. *Angewandte Chemie International Edition*, 55(4):1291–1294, 2016.

[146] Zijie Wang, Morgan Lehtinen, and Guojun Liu. Universal Janus Filters for the Rapid Separation of Oil from Emulsions Stabilized by Ionic or Nonionic Surfactants. *Angewandte Chemie International Edition*, 56(42):12892–12897, 2017.

[147] Feifei Ren, Guoqiang Li, Zhen Zhang, Xuedong Zhang, Hua Fan, Chen Zhou, Yulong Wang, Yinghui Zhang, Chaowei Wang, Kai Mu, Yahui Su, and Dong Wu. A Single-Layer Janus Membrane with Dual Gradient Conical Micropore Arrays for Self-Driving Fog Collection. *Journal of Materials Chemistry A*, 5:18403–18408, 2017.

[148] Moyuan Cao, Jiasheng Xiao, Cunming Yu, Kan Li, and Lei Jiang. Hydrophobic/Hydrophilic Cooperative Janus System for Enhancement of Fog Collection. *Small*, 11(34):4379–4384, 2015.

[149] Wenbin Zhang, Liang Hu, Hanmei Chen, Shoujian Gao, Xiangcheng Zhang, and Jian Jin. Mineralized Growth of Janus Membrane with Asymmetric Wetting Property for Fast Separation of a Trace of Blood. *Journal of Materials Chemistry B*, 5:4876–4882, 2017.

[150] Yu-Xi Huang, Zhangxin Wang, Jian Jin, and Shihong Lin. Novel Janus Membrane for Membrane Distillation with Simultaneous Fouling and Wetting Resistance. *Environmental Science & Technology*, 51(22):13304–13310, 2017.

[151] Hao-Cheng Yang, Jingwei Hou, Ling-Shu Wan, Vicki Chen, and Zhi-Kang Xu. Janus Membranes with Asymmetric Wettability for Fine Bubble Aeration. *Advanced Materials Interfaces*, 3(9):1500774, 2016.

[152] Jing Wu, Nü Wang, Li Wang, Hua Dong, Yong Zhao, and Lei Jiang. Unidirectional Water-Penetration Composite Fibrous Film via Electrospinning. *Soft Matter*, 8:5996–5999, 2012.

[153] Kaichi Sasaki, Mizuki Tenjimbayashi, Kengo Manabe, and Seimei Shiratori. Asymmetric Superhydrophobic/Superhydrophilic Cotton Fabrics Designed by Spraying Polymer and Nanoparticles. *ACS Applied Materials & Interfaces*, 8(1):651–659, 2016.

[154] Jingchao Zhang, Yong Yang, Zhicheng Zhang, Pengpeng Wang, and Xun Wang. Biomimetic Multifunctional Nanochannels Based on the Asymmetric Wettability of Heterogeneous Nanowire Membranes. *Advanced Materials*, 26(7):1071–1075, 2014.

[155] Yan Zhang and Mihail Barboiu. Dynameric Asymmetric Membranes for Directional Water Transport. *Chemical Communications*, 51:15925–15927, 2015.

[156] Hao-Cheng Yang, Kun-Jian Liao, He Huang, Qing-Yun Wu, Ling-Shu Wan, and Zhi-Kang Xu. Mussel-Inspired Modification of a Polymer Membrane for Ultra-High Water Permeability and Oil-in-Water Emulsion Separation. *Journal of Materials Chemistry A*, 2:10225–10230, 2014.

[157] Hao-Cheng Yang, Wenwei Zhong, Jingwei Hou, Vicki Chen, and Zhi-Kang Xu. Janus Hollow Fiber Membrane with a Mussel-Inspired Coating on the Lumen Surface for Direct Contact Membrane Distillation. *Journal of Membrane Science*, 523:1–7, 2017.

[158] Jongho Lee, Tahar Laoui, and Rohit Karnik. Nanofluidic Transport Governed by the Liquid/Vapour Interface. *Nature Nanotechnology*, 9(4):317–323, 2014.

[159] Zhenxing Wang, Xiaobin Yang, Zhongjun Cheng, Yuyan Liu, Lu Shao, and Lei Jiang. Simply Realizing "Water Diode" Janus Membranes for Multifunctional Smart Applications. *Materials Horizons*, 4, 2017.

[160] Hongxia Wang, Jie Ding, Liming Dai, Xungai Wang, and Tong Lin. Directional Water-Transfer through Fabrics Induced by Asymmetric Wettability. *Journal of Materials Chemistry*, 20:7938–7940, 2010.

[161] Yaqin Fu, Ying-Bing Jiang, Darren Dunphy, Haifeng Xiong, Eric Coker, Stan Chou, Hongxia Zhang, Juan M. Vanegas, Jonas G. Croissant, Joseph L. Cecchi, Susan B. Rempe, and C. Jeffrey Brinker. Ultra-thin Enzymatic Liquid Membrane for CO_2 Separation and Capture. *Nature Communications*, 9(1):990, 2018.

[162] Hongxia Wang, Hua Zhou, Weidong Yang, Yan Zhao, Jian Fang, and Tong Lin. Selective, Spontaneous One-Way Oil-Transport Fabrics and Their Novel Use for Gauging Liquid Surface Tension. *ACS Applied Materials and Interfaces*, 7(41):22874–22880, 2015.

[163] Anne C. Dillon, A. W. Ott, J. D. Way, and S. M. George. Surface Chemistry of Al_2O_3 Deposition Using $Al(CH_3)_3$ and H_2O in a Binary Reaction Sequence. *Surface Science*, 322(1-3):230–242, 1995.

[164] Anna Lee, Joseph A. Libera, Ruben Z. Waldman, Aftab Ahmed, Jason R. Avila, Jeffrey W. Elam, and Seth B. Darling. Conformal Nitrogen-Doped TiO_2 Photocatalytic Coatings for Sunlight-Activated Membranes. *Advanced Sustainable Systems*, page 1600041, 2017.

[165] Fengbin Li, Yang Yang, Yiqun Fan, Weihong Xing, and Yong Wang. Modification of Ceramic Membranes for Pore Structure Tailoring: The Atomic Layer Deposition Route. *Journal of Membrane Science*, 397-398:17–23, 2012.

[166] Fengbin Li, Ling Li, Xingzhi Liao, and Yong Wang. Precise Pore Size Tuning and Surface Modifications of Polymeric Membranes Using the Atomic Layer Deposition Technique. *Journal of Membrane Science*, 385-386(1):1–9, 2011.

[167] Jeffrey W. Elam, Joe A. Libera, M. J. Pellin, and P. C. Stair. Spatially Controlled Atomic Layer Deposition in Porous Materials. *Applied Physics Letters*, 91(24):243105, 2007.

[168] Jeffrey W. Elam, D. Routkevitch, P. P. Mardilovich, and S. M. George. Conformal Coating on Ultrahigh-Aspect-Ratio Nanopores of Anodic Alumina by Atomic Layer Deposition. *Chemistry of Materials*, 15(18):3507–3517, 2003.

[169] Mika Vähä-Nissi, Emilia Kauppi, Khoren Sahagian, Leena-Sisko Johansson, Maria Soledad Peresin, Jenni Sievänen, and Ali Harlin. Growth of Thin Al_2O_3 Films on Biaxially Oriented Polymer Films by Atomic Layer Deposition. *Thin Solid Films*, 522:50–57, 2012.

[170] Jesse S. Jur, Joseph C. Spagnola, Kyoungmi Lee, Bo Gong, Qing Peng, and Gregory N. Parsons. Temperature-dependent subsurface growth during atomic layer deposition on polypropylene and cellulose fibers. *Langmuir*, 26(11):8239–8244, 2010.

[171] He Chen, Liang Kong, and Yong Wang. Enhancing the Hydrophilicity and Water Permeability of Polypropylene Membranes by Nitric Acid Activation and Metal Oxide Deposition. *Journal of Membrane Science*, 487:109–116, 2015.

[172] Qiang Xu, Yang Yang, Jie Yang, Xiaozu Wang, Zhaohui Wang, and Yong Wang. Plasma Activation of Porous Polytetrafluoroethylene Membranes for Superior Hydrophilicity and Separation Performances via Atomic Layer Deposition of TiO_2. *Journal of Membrane Science*, 443:62–68, 2013.

[173] Berkem Ozkaya, Simon Grosse-Kreul, Carles Corbella, Achim Von Keudell, and Guido Grundmeier. Combined In Situ XPS and UHV-Chemical Force Microscopy (CFM) Studies of the Plasma Induced Surface Oxidation of Polypropylene. *Plasma Processes and Polymers*, 11(3):256–262, 2014.

[174] José Bico, Uwe Thiele, and David Quéré. Wetting of Textured Surfaces. *Colloids and Surfaces A: Physicochemical and Engineering Aspects*, 206(1-3):41–46, 2002.

[175] Yuanyuan Yang, Eka Noviana, Michael P. Nguyen, Brian J. Geiss, David S. Dandy, and Charles S. Henry. Paper-Based Microfluidic Devices: Emerging Themes and Applications. *Analytical Chemistry*, 89(1):71–91, 2017.

[176] Trinh Lam, Jasmine P. Devadhasan, Ryan Howse, and Jungkyu Kim. A Chemically Patterned Microfluidic Paper-based Analytical Device (C-μPAD) for Point-of-Care Diagnostics. *Scientific Reports*, 7(1):1–10, 2017.

[177] Christian Dorrer and Jürgen Rühe. Superaerophobicity: Repellence of Air Bubbles from Submerged, Surface-Engineered Silicon Substrates. *Langmuir*, 28(42):14968–14973, 2012.

[178] Jingwei Hou, Chao Ji, Guangxi Dong, Bowen Xiao, Yun Ye, and Vicki Chen. Biocatalytic Janus Membranes for CO_2 Removal Utilizing Carbonic Anhydrase. *Journal of Materials Chemistry A*, 3(33):17032–17041, 2015.

[179] Tatsuki Ueda, Kenji Hata, Yasuto Kikuoka, and Osamu Seino. Effects of Aeration on Suction Pressure in a Submerged Membrane Bioreactor. *Water Research*, 31(3):489–494, 1997.

[180] Li Zheng and Poojitha D. Yapa. Bouyant Velocity of Spherical and Nonspherical Bubbles/Droplets. *Journal of Hydraulic Engineering*, pages 852–854, 2000.

[181] Yingjie Li, Haichuan Zhang, Tianhao Xu, Zhiyi Lu, Xiaochao Wu, Pengbo Wan, Xiaoming Sun, and Lei Jiang. Under-Water Superaerophobic Pine-Shaped Pt Nanoarray Electrode for Ultrahigh-Performance Hydrogen Evolution. *Advanced Functional Materials*, 25(11):1737–1744, 2015.

[182] Richard P. Padbury and Jesse S. Jur. Systematic study of trimethyl aluminum infiltration in polyethylene terephthalate and its effect on the mechanical properties of polyethylene terephthalate fibers. *Journal of Vacuum Science & Technology A: Vacuum, Surfaces, and Films*, 33(1):01A112, 2015.

[183] Guoliang Liu, Mark P. Stoykovich, Shengxiang Ji, Karl O. Stuen, Gordon S. W. Craig, and Paul F. Nealey. Phase Behavior and Dimensional Scaling of Symmetric Block Copolymer-Homopolymer Ternary Blends in Thin Films. *Macromolecules*, 42(8):3063–3072, 2009.

[184] Halil I. Akyildiz, Michael Lo, Eoghan Dillon, Adam T. Roberts, Henry O. Everitt, and Jesse S. Jur. Formation of Novel Photoluminescent Hybrid Materials by Sequential Vapor Infiltration into Polyethylene Terephthalate Fibers. *Journal of Materials Research*, 29(23):2817–2826, 2014.

[185] R.B. Rigby. *Engineering Thermoplastics: Properties and Applications*. Marcel Dekker, New York, 1985.

[186] A. L. Ahmad, A. A. Abdulkarim, B. S. Ooi, and S. Ismail. Recent Development in Additives Modifications of Polyethersulfone Membrane for Flux Enhancement. *Chemical Engineering Journal*, 223:246–267, 2013.

[187] Changsheng Zhao, Jimin Xue, Fen Ran, and Shudong Sun. Modification of Polyethersulfone Membranes — A review of Methods. *Progress in Materials Science*, 58(1):76–150, 2013.

[188] Jing Feng Li, Zhen Liang Xu, Hu Yang, Li Yun Yu, and Min Liu. Effect of TiO_2 Nanoparticles on the Surface Morphology and Performance of Microporous PES Membrane. *Applied Surface Science*, 255(9):4725–4732, 2009.

[189] Nermen Maximous, G. Nakhla, K. Wong, and W. Wan. Optimization of $Al2O_3$/PES Membranes for Wastewater Filtration. *Separation and Purification Technology*, 73(2):294–301, 2010.

[190] Silvia Simone, Francesco Galiano, Mirko Faccini, Marcel Boerrigter, Christiane Chaumette, Enrico Drioli, and Alberto Figoli. Preparation and Characterization of Polymeric-Hybrid PES/TiO_2 Hollow Fiber Membranes for Potential Applications in Water Treatment. *Fibers*, 5(2):14, 2017.

[191] Amir Razmjou, Jaleh Mansouri, Vicki Chen, May Lim, and Rose Amal. Titania Nanocomposite Polyethersulfone Ultrafiltration Membranes Fabricated Using a Low Temperature Hydrothermal Coating Process. *Journal of Membrane Science*, 380(1-2):98–113, 2011.

[192] Qianqian Wang, Xiaoting Wang, Zhaohui Wang, Jun Huang, and Yong Wang. PVDF Membranes with Simultaneously Enhanced Permeability and Selectivity by Breaking the Tradeoff Effect via Atomic Layer Deposition of TiO_2. *Journal of Membrane Science*, 442:57–64, 2013.

[193] Sun Jin Yun, Jung Wook Lim, and Jin-Ho Lee. Low-Temperature Deposition of Aluminum Oxide on Polyethersulfone Substrate Using Plasma-Enhanced Atomic Layer Deposition. *Electrochemical and Solid-State Letters*, 7(1):C13, 2004.

[194] Peter E. Petrochenko, Giovanna Scarel, G. Kevin Hyde, Gregory N. Parsons, Shelby A. Skoog, Qin Zhang, Peter L. Goering, and Roger J. Narayan. Prevention of Ultraviolet (UV)-Induced Surface Damage and Cytotoxicity of Polyethersulfone Using Atomic Layer Deposition (ALD) Titanium Dioxide. *JOM*, 65(4):550–556, 2013.

[195] Ting Sheng, He Chen, Sen Xiong, Xiaoqiang Chen, and Yong Wang. Atomic Layer Deposition of Polyimide on Microporous Polyethersulfone Membranes for Enhanced and Tunable Performances. *AIChE Journal*, 60(10):3614–3622, 2014.

[196] Ruben Z. Waldman, Hao-Cheng Yang, David J. Mandia, Paul F. Nealey, Jeffrey W. Elam, and Seth B. Darling. Janus Membranes via Diffusion-Controlled Atomic Layer Deposition. *Advanced Materials Interfaces*, 1800658:1–11, 2018.

[197] M. Fontyn, K. van 't Riet, and B. H. Bijsterbosch. Surface Spectroscopic Studies of Pristine and Fouled Membranes Part I . Method Development Characterization and Pristine Membrane. *Colloids and Surfaces*, 54:331–347, 1991.

[198] Mercedes L. Mendez, Analia I. Romero, Veronica B. Rajal, Jose I. Castro, Laura Palacio, and Antonio Hernandez. Properties of Polyethersulfone Ultrafiltration Membranes Modified with Polyethylene Glycols. *Polymer Engineering and Science*, 54(5):1211–1221, 2014.

[199] Jae Hyun Choi, Jonggeon Jegal, and Woo Nyon Kim. Fabrication and Characterization of Multi-Walled Carbon Nanotubes/Polymer Blend Membranes. *Journal of Membrane Science*, 284(1-2):406–415, 2006.

[200] C. A. Wilson, J. A. McCormick, A. S. Cavanagh, D. N. Goldstein, A. W. Weimer, and S. M. George. Tungsten Atomic Layer Deposition on Polymers. *Thin Solid Films*, 516(18):6175–6185, 2008.

[201] Ghalib A. Atiya, Andrew S. Grady, Douglas K. Russell, and Thomas A. Claxton. Vibrational Spectra of Monomeric Trimethylaluminium and Trimethylgallium. *Spectrochimica Acta Part A: Molecular Spectroscopy*, 47(3-4):467–476, 1991.

[202] B. G. Frederick, G. Apai, and T. N. Rhodin. Surface Phonons in Thin Aluminum Oxide Films: Thickness, Beam-Energy, and Symmetry-Mixing Effects. *Physical Review B*, 44(4):1880–1890, 1991.

[203] Kjeil-arne Sollia, Martin Ystenes, and Piotr Sobotab. FHR Studies of Titanium Tetrachloride- and Magnesium Dichloride-Complexes with Aromatic Esters Relevant to Ziegler-Natta Catalysts. *Proc. SPIE*, 1575:608–609, 1991.

[204] David J. Comstock and Jeffrey W. Elam. Mechanistic Study of Lithium Aluminum Oxide Atomic Layer Deposition. *The Journal of Physical Chemistry C*, 117(4):1677–1683, 2013.

[205] M. J. Frisch, G. W. Trucks, H. B. Schlegel, G. E. Scuseria, M. A. Robb, J. R. Cheeseman, G. Scalmani, V. Barone, B. Mennucci, G. A. Petersson, H. Nakatsuji, M. Caricato, X. Li, H. P. Hratchian, A. F. Izmaylov, J. Bloino, G. Zheng, J. L. Sonnenberg, M. Hada, M. Ehara, K. Toyota, R. Fukuda, J. Hasegawa, M. Ishida, T. Nakajima, Y. Honda, O. Kitao, H. Nakai, T. Vreven, J. A. Jr Montgomery, J. E. Peralta, F. Ogliaro, M. Bearpark, J. J. Heyd, E. Brothers, K. N. Kudin, V. N. Staroverov, R. Kobayashi, J. Normand, K. Raghavachari, A. Rendell, J. C. Burant, S. S. Iyengar, J. Tomasi, M. Cossi, N. Rega, N. J. Millam, M. Klene, J. E. Knox, J. B. Cross, V. Bakken, C. Adamo, J. Jaramillo, R. Gomperts, R. E. Stratmann, O. Yazyev, A. J. Austin, R. Cammi, C. Pomelli, J. W. Ochterski, R. L. Martin, K. Morokuma, V. G. Zakrzewski, G. A. Voth, P. Salvador, J. J. Dannenberg, S. Dapprich, A.D. Daniels, O. Farkas, J. B. Foresman, J. V. Ortiz, J. Cioslowski, and D. J. Fox. Gaussian 09, Revision A.02; Gaussian, Inc.: Wallingford, CT, 2009.

[206] Wade F. Ingram and Jesse S. Jur. Properties and Applications of Vapor Infiltration into Polymeric Substrates. *JOM*, 71(1):238–245, 2019.

[207] Marianna Kemell, Elina Färm, Mikko Ritala, and Markku Leskelä. Surface Modification of Thermoplastics by Atomic Layer Deposition of Al_2O_3 and TiO_2 Thin Films. *European Polymer Journal*, 44(11):3564–3570, 2008.

[208] Xinhua Liang, Steven M. George, Alan W. Weimer, Nai Hong Li, John H. Blackson, Joseph D. Harris, and Peng Li. Synthesis of a Novel Porous Polymer/Ceramic Composite Material by Low-Temperature Atomic Layer Deposition. *Chemistry of Materials*, 19(22):5388–5394, 2007.

[209] Yong Wang, Yong Qin, Andreas Berger, Eric Yau, Changcheng He, Lianbing Zhang, Ulrich Gösele, Mato Knez, and Martin Steinhart. Nanoscopic Morphologies in Block Copolymer Nanorods as Templates for Atomic-Layer Deposition of Semiconductors. *Advanced Materials*, 21(27):2763–2766, 2009.

[210] P. D.C. King and T. D. Veal. Conductivity in Transparent Oxide Semiconductors. *Journal of Physics Condensed Matter*, 23(33), 2011.

[211] Oliver Bierwagen. Indium Oxide - A Transparent, Wide-Band Gap Semiconductor for (Opto)electronic Applications. *Semiconductor Science and Technology*, 30(2), 2015.

[212] I. Noda, A.E. Dowrey, J.L. Haynes, and C. Marcott. *Physical Properties of Polymers Handbook*. Springer, 2007.

[213] Yoshiko Someya Hiraoka and Masao Mashita. Ab Initio Study on the Dimer Structures of Trimethylaluminum and Dimethylaluminumhydride. *Journal of Crystal Growth*, 145(1-4):473–477, 1994.

[214] Fan Yang, Jens Brede, Hayrensa Ablat, Mikel Abadia, Lianbing Zhang, Celia Rogero, Simon D. Elliott, and Mato Knez. Reversible and Irreversible Reactions of Trimethylaluminum with Common Organic Functional Groups as a Model for Molecular Layer Deposition and Vapor Phase Infiltration. *Advanced Materials Interfaces*, 4(18):1700237, 2017.

[215] Jeffrey W. Elam, David A. Baker, Alex B.F. Martinson, Michael J. Pellin, and Joseph T. Hupp. Atomic Layer Deposition of Indium Tin Oxide Thin Films Using Nonhalogenated Precursors. *Journal of Physical Chemistry C*, 112(6):1938–1945, 2008.

[216] Laura B. Hoch, Thomas E. Wood, Paul G. O'Brien, Kristine Liao, Laura M. Reyes, Charles A. Mims, and Geoffrey A. Ozin. The Rational Design of a Single-Component Photocatalyst for Gas-Phase CO_2 Reduction Using both UV and Visible Light. *Advanced Science*, 1(1):1–10, 2014.

[217] Christophe Girardeaux and Jean-Jacques Pireaux. Analysis of Poly(methyl methacrylate) (PMMA) by XPS. *Surface Science Spectra*, 4(2):134–137, 2002.

[218] Gabriel P. López, David G. Castner, and Buddy D. Ratner. XPS O 1s Binding Energies for Polymers Containing Hydroxyl, Ether, Ketone and Ester Groups. *Surface and Interface Analysis*, 17(5):267–272, 1991.

[219] Anil U. Mane, Amy J. Allen, Ravindra K. Kanjolia, and Jeffrey W. Elam. Indium Oxide Thin Films by Atomic Layer Deposition Using Trimethylindium and Ozone. *Journal of Physical Chemistry C*, 120(18):9874–9883, 2016.

[220] Joseph A. Libera, John N. Hryn, and Jeffrey W. Elam. Indium Oxide Atomic Layer Deposition Facilitated by the Synergy Between Oxygen and Water. *Chemistry of Materials*, 23(8):2150–2158, 2011.

[221] M.D. Groner, F.H. Fabreguette, J.W. Elam, and S. M. George. Low-Temperature Al_2O_3 Atomic Layer Deposition. *Chemistry of Materials*, 16:639–645, 2004.

[222] David A. Atwood, Alan H. Cowley, Paul R. Harris, Richard A. Jones, Stefan U. Koschmieder, Christine M. Nunn, Jerry L. Atwood, and Simon G. Bott. Cyclic Trimeric

Hydroxy, Amido, Phosphido, and Arsenido Derivatives of Aluminum and Gallium. X-ray Structures of [t-Bu2Ga(Aμ -OH)]3 and [t-Bu2Ga(A/*mu*-NH2)]3. *Organometallics*, 12(1):24–29, 1993.

[223] Mark R. Mason, Janna M. Smith, Simon G. Bott, and Andrew R. Barron. Hydrolysis of Tri-tert-butylaluminum: the First Structural Characterization of Alkylalumoxanes [(R2Al)2O]n and (RAlO)n. *Journal of the American Chemical Society*, 115(12):4971–4984, 1993.

[224] Eungnak Han, Karl O. Stuen, Young Hye La, Paul F. Nealey, and Padma Gopalan. Effect of Composition of Substrate-Modifying Random Copolymers on the Orientation of Symmetric and Asymmetric Diblock Copolymer Domains. *Macromolecules*, 41(23):9090–9097, 2008.

[225] R. Kumar. Indium Tin Oxide Films: State-of-the-Art In Synthesis and Properties. *Materials Technology*, 10(9-10):202–206, 2016.

[226] Keran Zhang, Furong Zhu, C. H.A. Huan, and A. T.S. Wee. Indium Tin Oxide Films Prepared by Radio Frequency Magnetron Sputtering Method at a Low Processing Temperature. *Thin Solid Films*, 376(1-2):255–263, 2000.

[227] D. B. Chrisey, H. Mattoussi, C. M. Gilmore, J. S. Horwitz, H. Kim, Z. H. Kafafi, A. Piqué, and H. Murata. Electrical, Optical, and Structural Properties of Indium-Tin-Oxide Thin Films for Organic Light-Emitting Devices. *Journal of Applied Physics*, 86(11):6451–6461, 2002.

[228] Ratnabali Banerjee, Debajyoti Das, Swati Ray, A. K. Batabyal, and A. K. Barua. Characterization of Tin Doped Indium Oxide Films Prepared by Electron Beam Evaporation. *Solar Energy Materials*, 13(1):11–23, 1986.

[229] S. R. Sarath Kumar and S. Kasiviswanathan. Role of Oxygen Vacancies in the High-Temperature Thermopower of Indium oxide and Indium Tin Oxide Films. *Semiconductor Science and Technology*, 24(2), 2009.

[230] W. J. Maeng, Dong won Choi, Jozeph Park, and Jin Seong Park. Atomic Layer Deposition of Highly Conductive Indium Oxide Using a Liquid Precursor and Water Oxidant. *Ceramics International*, 41(9):10782–10787, 2015.

[231] Hossein Salami, Alan Uy, Aarathi Vadapalli, Corinne Grob, Vivek Dwivedi, and Raymond A Adomaitis. Atomic Layer Deposition of Ultrathin Indium Oxide and Indium Tin Oxide Films Using a Trimethylindium, Tetrakis(dimethylamino)tin, and Ozone Precursor System. *Journal of Vacuum Science & Technology A*, 37:10905, 2019.

[232] Raphael Edem Agbenyeke, Eun Ae Jung, Bo Keun Park, Taek Mo Chung, Chang Gyoun Kim, and Jeong Hwan Han. Thermal Atomic Layer Deposition of In_2O_3 Thin Films Using Dimethyl(N-ethoxy-2,2-dimethylcarboxylicpropanamide)indium and H_2O. *Applied Surface Science*, 419:758–763, 2017.

[233] Volker Blum, Ralf Gehrke, Felix Hanke, Paula Havu, Ville Havu, Xinguo Ren, Karsten Reuter, and Matthias Scheffler. Ab Initio Molecular Simulations with Numeric Atom-Centered Orbitals. *Computer Physics Communications*, 180(11):2175–2196, 2009.

[234] Jmol: an open-source Java viewer for chemical structures in 3D. http://www.jmol.org/.

[235] Carlo Adamo and Vincenzo Barone. Toward Reliable Density Functional Methods without Adjustable Parameters: The PBE0 Model. *Journal of Chemical Physics*, 110(13):6158–6170, 1999.

[236] John P Perdew, Kieron Burke, and Matthias Ernzerhof. Generalized Gradient Approximation Made Simple. *Physical Review Letters*, 77(18):3865–3868, 1996.

[237] Geoffrey M. Geise, Ho Bum Park, Alyson C. Sagle, Benny D. Freeman, and James E. McGrath. Water permeability and Water/Salt Selectivity Tradeoff in Polymers for Desalination. *Journal of Membrane Science*, 369(1):130–138, 2011.

[238] Ho Bum Park, Jovan Kamcev, Lloyd M. Robeson, Menachem Elimelech, and Benny D. Freeman. Maximizing the right stuff: The trade-off between membrane permeability and selectivity. *Science*, 356(6343), 2017.

[239] Zeev Dagan, Sheldon Weinbaum, and Robert Pfeffer. An Infinite-Series Solution for the Creeping Motion Through an Orifice of Finite Length. *Journal of Fluid Mechanics*, 115:505–523, 1982.

[240] Zeting Zhang, Jian Gao, Weidong Zhang, and Zhongqi Ren. Experimental Study of the Effect of Membrane Porosity on Membrane Absorption Process. *Separation Science and Technology*, 41(14):3245–3263, 2006.

[241] Kyu-Jin Kim, Paul V. Stevens, and Anthony G. Fane. Porosity Dependence of Pore Entry Shape in Track-Etched Membranes by Image Analysis. *Journal of Membrane Science*, 93(1):79–90, 1994.

[242] A.G. Fane and C.J.D. Fell. A Review of Fouling and Fouling Control in Ultrafiltration. *Desalination*, 62:117–136, 1987.

[243] Jenyuk Lohwacharin and Kumiko Oguma and Satoshi Takizawa. Ultrafiltration of Natural Organic Matter and Black Carbon: Factors Influencing Aggregation and Membrane Fouling. *Water Research*, 43(12):3076–3085, 2009.

[244] Amit Mehta and Andrew L. Zydney. Permeability and Selectivity Analysis for Ultrafiltration Membranes. *Journal of Membrane Science*, 249(1):245–249, 2005.

[245] John D. Ferry. Ultrafilter membranes and ultrafiltration. *Chemical Reviews*, 18(3):373–455, 1936.

[246] L. J. Zeman and M. Wales. Polymer Solute Rejection By Ultrafiltration Membranes. In A.F. Turbak, editor, *Synthetic Membranes, Volume II*, pages 411–434, Washington DC, 1981. American Chemical Society.

[247] Peter M. Bungay and Howard Brenner. The Motion of a Closely-Fitting Sphere in a Fluid-Filled Tube. *International Journal of Multiphase Flow*, 1(1):25–56, 1973.

[248] Subir Bhattacharjee, Ashutosh Sharma, and Prashant K. Bhattacharya. Estimation and Influence of Long Range Solute. Membrane Interactions in Ultrafiltration. *Industrial & Engineering Chemistry Research*, 35(9):3108–3121, 1996.

[249] L. J. Zeman and Andrew L. Zydney. *Microfiltration and Ultrafiltration*. Marcel Dekker, New York, 1 edition, 1996.

[250] Seiichi Mochizuki and Andrew L. Zydney. Theoretical Analysis of Pore Size Distribution Effects on Membrane Transport. *Journal of Membrane Science*, 82(3):211–227, 1993.

[251] Andrew L. Zydney, Pierre Aimar, Martine Meireles, Joseph M. Pimbley, and Georges Belfort. Use of the Log-Normal Probability Density Function to Analyze Membrane Pore Size Distributions: Functional Forms and Discrepancies. *Journal of Membrane Science*, 91(3):293–298, 1994.

[252] Ruth E. Baltus. Characterization of the pore area distribution in porous membranes using transport measurements. *Journal of Membrane Science*, 123(2):165–184, 1997.

[253] S. Derjani-Bayeh and V.G.J. Rodgers. Sieving Variations due to the Choice in Pore Size Distribution Model. *Journal of Membrane Science*, 209(1):1–17, 2002.

[254] Skand Saksena and Andrew L. Zydney. Pore Size Distribution Effects on Electrokinetic Phenomena in Semipermeable Membranes. *Journal of Membrane Science*, 105(3):203–215, 1995.

[255] Jizhong Ren, Zhansheng Li, and Fook-Sin Wong. A New Method for the Prediction of Pore Size Distribution and MWCO of Ultrafiltration Membranes. *Journal of Membrane Science*, 279(1):558–569, 2006.

[256] S. Ranil Wickramasinghe, Shane E. Bower, Zhen Chen, Abhik Mukherjee, and Scott M. Husson. Relating the Pore Size Distribution of Ultrafiltration Membranes to Dextran Rejection. *Journal of Membrane Science*, 340(1):1–8, 2009.

[257] Enrique Antoń, José Ignacio Calvo, José R. Álvarez, Antonio Hernańdez, and Susana Luque. Fitting Approach to Liquid-Liquid Displacement Porosimetry Based on the Log-Normal Pore Size Distribution. *Journal of Membrane Science*, 470:219–228, 2014.

[258] Milagro Marroquin, Terri Bruce, John Pellegrino, S. Ranil Wickramasinghe, and Scott M. Husson. Characterization of Asymmetry in Microporous Membranes by Cross-Sectional Confocal Laser Scanning Microscopy. *Journal of Membrane Science*, 379(1):504–515, 2011.

[259] J.I. Calvo, A. Hernández, G. Caruana, and L. Martínez. Pore Size Distributions in Microporous Membranes: I. Surface Study of Track-Etched Filters by Image Analysis. *Journal of Colloid and Interface Science*, 175(1):138–150, 1995.

[260] Woo Lee and Sang-Joon Park. Porous Anodic Aluminum Oxide: Anodization and Templated Synthesis of Functional Nanostructures. *Chemical Reviews*, 114(15):7487–7556, 2014.

[261] Ilin Sadeghi, Papatya Kaner, and Ayse Asatekin. Controlling and Expanding the Selectivity of Filtration Membranes. *Chemistry of Materials*, 30(21):7328–7354, 2018.

[262] Majid Ebrahimi Warkiani, Ali Asgar S. Bhagat, Bee Luan Khoo, Jongyoon Han, Chwee Teck Lim, Hai Qing Gong, and Anthony Gordon Fane. Isoporous Micro/Nanoengineered Membranes. *ACS Nano*, 7(3):1882–1904, 2013.

[263] Byron D. Gates, Qiaobing Xu, Michael Stewart, Declan Ryan, C. Grant Willson, and George M. Whitesides. New Approaches to Nanofabrication: Molding, Printing, and Other Techniques. *Chemical Reviews*, 105(4):1171–1196, 2005.

[264] Yongqi Fu, Ngoi Kok Ann Bryan, and Loh Thian Fatt. Fabrication and Characterization of Nanopore Array. *Journal of Nanoscience and Nanotechnology*, 6(7):1954–1960, 2006.

[265] A. J. Storm, J. H. Chen, X. S. Ling, H. W. Zandbergen, and Cees Dekker. Fabrication of Solid-State Nanopores with Single-Nanometre Precision. *Nature Materials*, 2(8):537–540, 2003.

[266] Ivan Vlassiouk, Pavel Y. Apel, Sergey N. Dmitriev, Ken Healy, and Zuzanna S. Siwy. Versatile Ultrathin Nanoporous Silicon Nitride Membranes. *Proceedings of the National Academy of Sciences*, 106(50):21039–21044, 2009.

[267] L.J. Heyderman, B. Ketterer, D. Bachle, F. Glaus, B. Haas, H. Schift, K. Vogelsang, J. Gobrecht, L. Tiefenauer, O. Dubochet, P. Surbled, and T. Hessler. High Volume Fabrication of Customised Nanopore Membrane Chips. *Microelectronic Engineering*, 67-68:208–213, 2003.

[268] Lauri Sainiemi, Jukka Viheriälä, Tiina Sikanen, Janne Laukkanen, and Tapio Niemi. Nanoperforated Silicon Membranes Fabricated by UV-nanoimprint Lithography, Deep Reactive Ion Etching and Atomic Layer Deposition. *Journal of Micromechanics and Microengineering*, 20(7):077001, 2010.

[269] Bhargav P. Nabar, Zeynep Çelik-Butler, Brian H. Dennis, and Richard E. Billo. A Nanoporous Silicon Nitride Membrane Using a Two-Step Lift-off Pattern Transfer with Thermal Nanoimprint Lithography. *Journal of Micromechanics and Microengineering*, 22(4):045012, 2012.

[270] Keping Han, Wendong Xu, Ariel Ruiz, Paul Ruchhoeft, and Shankararaman Chellam. Fabrication and Characterization of polymeric Microfiltration Membranes Using Aperture Array Lithography. *Journal of Membrane Science*, 249(1):193–206, 2005.

[271] Jongyoon Han, Jianping Fu, and Reto B. Schoch. Molecular Sieving Using Nanofilters: Past, Present and Future. *Lab Chip*, 8:23–33, 2008.

[272] Pieter Stroeve and Nazar Ileri. Biotechnical and Other Applications of Nanoporous Membranes. *Trends in Biotechnology*, 29(6):259–266, 2011.

[273] William H. Fissell, Anna Dubnisheva, Abigail N. Eldridge, Aaron J. Fleischman, Andrew L. Zydney, and Shuvo Roy. High-Performance Silicon Nanopore Hemofiltration Membranes. *Journal of Membrane Science*, 326(1):58–63, 2009.

[274] S. Kuiper, R. Brink, W. Nijdam, G.J.M. Krijnen, and M.C. Elwenspoek. Ceramic Microsieves: Influence of Perforation Shape and Distribution on Flow Resistance and Membrane Strength. *Journal of Membrane Science*, 196(2):149–157, 2002.

[275] Aijuan Zhang, Hua Bai, and Lei Li. Breath Figure: A Nature-Inspired Preparation Method for Ordered Porous Films. *Chemical Reviews*, 115(18):9801–9868, 2015.

[276] Xuehua Ruan, Kaimin Zhang, Xiaobin Jiang, Xiujuan Zhang, Xiaoming Yan, Ning Zhang, and Gaohong He. Facile Fabrication of Reinforced Homoporous MF Membranes by In Situ Breath Figure and Thermal Adhesion Method on Substrates. *Journal of Membrane Science*, 554:291–299, 2018.

[277] Bing Yu, Hailin Cong, Zejing Li, Hua Yuan, Qiaohong Peng, Ming Chi, Shujing Yang, Ruixia Yang, S. Ranil Wickramasinghe, and Jianguo Tang. Fabrication of Highly Ordered Porous Membranes of Cellulose Triacetate on Ice Substrates Using Breath Figure Method. *Journal of Polymer Science Part B: Polymer Physics*, 53(8):552–558, 2015.

[278] Jaleh Mansouri, Evi Yapit, and Vicki Chen. Polysulfone Filtration Membranes with Isoporous Structures Prepared by a Combination of Dip-Coating and Breath Figure Approach. *Journal of Membrane Science*, 444:237–251, 2013.

[279] Seon Ju Yeo, Gwan H. Choi, and Pil J. Yoo. Multiscale-architectured Functional Membranes Utilizing Inverse Opal Structures. *Journal of Materials Chemistry A*, 5:17111–17134, 2017.

[280] Suzana Pereira Nunes. Block Copolymer Membranes for Aqueous Solution Applications. *Macromolecules*, 49(8):2905–2916, 2016.

[281] Elizabeth A. Jackson and Marc A. Hillmyer. Nanoporous Membranes Derived from Block Copolymers: From Drug Delivery to Water Filtration. *ACS Nano*, 4(7):3548–3553, 2010.

[282] Marc A. Hillmyer. Nanoporous Materials from Block Copolymer Precursors. *Advances in Polymer Science*, 190(1):137–181, 2005.

[283] Lloyd M. Robeson. Correlation of separation factor versus permeability for polymeric membranes. *Journal of Membrane Science*, 62(2):165–185, 1991.

[284] William A. Phillip, Marc A. Hillmyer, and E. L. Cussler. Cylinder Orientation Mechanism in Block Copolymer Thin Films Upon Solvent Evaporation. *Macromolecules*, 43(18):7763–7770, 2010.

[285] Elizabeth A. Jackson, Youngmin Lee, Madalyn R. Radlauer, and Marc A. Hillmyer. Well-Ordered Nanoporous ABA Copolymer Thin Films via Solvent Vapor Annealing, Homopolymer Blending, and Selective Etching of ABAC Tetrablock Terpolymers. *ACS Applied Materials & Interfaces*, 7(49):27331–27339, 2015.

[286] Leiming Guo and Yong Wang. Monolithic Membranes with Designable Pore Geometries and Sizes via Retarded Evaporation of Block Copolymer Supramolecules. *Macromolecules*, 48(23):8471–8479, 2015.

[287] Leiming Guo, Zhaogen Wang, and Yong Wang. Perpendicular Alignment and Selective Swelling-Induced Generation of Homopores of Polystyrene-*b*-poly(2-vinylpyridine)-*b*-poly(ethylene oxide) Triblock Terpolymer. *Macromolecules*, 51(16):6248–6256, 2018.

[288] Eungnak Han, Karl O. Stuen, Melvina Leolukman, Chi-Chun Liu, Paul F. Nealey, and Padma Gopalan. Perpendicular Orientation of Domains in Cylinder-Forming Block Copolymer Thick Films by Controlled Interfacial Interactions. *Macromolecules*, 42(13):4896–4901, 2009.

[289] Weiyin Gu, Sung Woo Hong, and Thomas P. Russell. Orienting Block Copolymer Microdomains with Block Copolymer Brushes. *ACS Nano*, 6(11):10250–10257, 2012.

[290] Gurpreet Singh, Saurabh Batra, Ren Zhang, Hongyi Yuan, Kevin G. Yager, Miko Cakmak, Brian Berry, and Alamgir Karim. Large-Scale Roll-to-Roll Fabrication of Vertically Oriented Block Copolymer Thin Films. *ACS Nano*, 7(6):5291–5299, 2013.

[291] Mei Ling Wu, Dong Wang, and Li Jun Wan. Directed Block Copolymer Self-Assembly Implemented via Surface-Embedded Electrets. *Nature Communications*, 7:1–7, 2016.

[292] Xunda Feng, Kohsuke Kawabata, Gilad Kaufman, Menachem Elimelech, and Chinedum O. Osuji. Highly Selective Vertically Aligned Nanopores in Sustainably Derived Polymer Membranes by Molecular Templating. *ACS Nano*, 11(4):3911–3921, 2017.

[293] Manesh Gopinadhan, Youngwoo Choo, Kohsuke Kawabata, Gilad Kaufman, Xunda Feng, Xiaojun Di, Yekaterina Rokhlenko, Lalit H. Mahajan, Dennis Ndaya, Rajeswari M. Kasi, and Chinedum O. Osuji. Controlling orientational order in block copolymers using low-intensity magnetic fields. *Proceedings of the National Academy of Sciences*, 114(45):E9437–E9444, 2017.

[294] Rachel M. Dorin, William A. Phillip, Hiroaki Sai, Jorg Werner, Menachem Elimelech, and Ulrich Wiesner. Designing block copolymer architectures for targeted membrane performance. *Polymer*, 55(1):347–353, 2014.

[295] Ana-Maria Popa, Philippe Niedermann, Harry Heinzelmann, Jeffrey A Hubbell, and Raphaël Pugin. Fabrication of Nanopore Arrays and Ultrathin Silicon Nitride Membranes by Block-Copolymer-Assisted Lithography. *Nanotechnology*, 20(48):485303, 2009.

[296] Tandra Ghoshal, Justin D Holmes, and Michael A. Morris. Development of Ordered, Porous (Sub-25 nm Dimensions) Surface Membrane Structures Using a Block Copolymer Approach. *Scientific Reports*, 8:7252, 2018.

[297] Eric E. Nuxoll, Marc A. Hillmyer, Ruifang Wang, C. Leighton, and Ronald A. Siegel. Composite Block Polymer-Microfabricated Silicon Nanoporous Membrane. *ACS Applied Materials & Interfaces*, 1(4):888–893, 2009.

[298] Klaus-Viktor Peinemann, Volker Abetz, and Peter F. W. Simon. Asymmetric Superstructure Formed in a Block Copolymer via Phase Separation. *Nature Materials*, 6(12):992–996, 2007.

[299] Sofia Rangou, Kristian Buhr, Volkan Filiz, Juliana Isabel Clodt, Brigitte Lademann, Janina Hahn, Adina Jung, and Volker Abetz. Self-Organized Isoporous Membranes with Tailored Pore Sizes. *Journal of Membrane Science*, 451:266–275, 2014.

[300] Juliana I. Clodt, Barbara Bajer, Kristian Buhr, Janina Hahn, Volkan Filiz, and Volker Abetz. Performance study of isoporous membranes with tailored pore sizes. *Journal of Membrane Science*, 495:334–340, 2015.

[301] Janina Hahn, Juliana I. Clodt, Clarissa Abetz, Volkan Filiz, and Volker Abetz. Thin Isoporous Block Copolymer Membranes: It Is All about the Process. *ACS Applied Materials & Interfaces*, 7(38):21130–21137, 2015.

[302] William A. Phillip, Brandon O'Neill, Marc Rodwogin, Marc A. Hillmyer, and E. L. Cussler. Self-Assembled Block Copolymer Thin Films as Water Filtration Membranes. *ACS Applied Materials & Interfaces*, 2(3):847–853, 2010.

[303] Yizhou Zhang, Jessica L. Sargent, Bryan W. Boudouris, and William A. Phillip. Nanoporous Membranes Generated from Self-Assembled Block Polymer Precursors: Quo Vadis? *Journal of Applied Polymer Science*, 132(21), 2015.

[304] Thomas Bucher, Volkan Filiz, Clarissa Abetz, and Volker Abetz. Formation of Thin, Isoporous Block Copolymer Membranes by an Upscalable Profile Roller Coating Process — A Promising Way to Save Block Copolymer. *Membranes*, 8(3), 2018.

[305] Rachel Mika Dorin, Hiroaki Sai, and Ulrich Wiesner. Hierarchically Porous Materials from Block Copolymers. *Chemistry of Materials*, 26(1):339–347, 2014.

[306] Mingjie Wei, Wei Sun, Xiansong Shi, Zhaogen Wang, and Yong Wang. Homoporous Membranes with Tailored Pores by Soaking Block Copolymer/Homopolymer Blends in Selective Solvents: Dissolution versus Swelling. *Macromolecules*, 49(1):215–223, 2016.

[307] Sarah E. Querelle, Elizabeth A. Jackson, Edward L. Cussler, and Marc A. Hillmyer. Ultrafiltration Membranes with a Thin Poly(styrene)-*b*-poly(isoprene) Selective Layer. *ACS Applied Materials & Interfaces*, 5(11):5044–5050, 2013.

[308] Elizabeth A. Jackson, Youngmin Lee, and Marc A. Hillmyer. ABAC Tetrablock Terpolymers for Tough Nanoporous Filtration Membranes. *Macromolecules*, 46(4):1484–1491, 2013.

[309] Yong Wang. Nondestructive Creation of Ordered Nanopores by Selective Swelling of Block Copolymers: Toward Homoporous Membranes. *Accounts of Chemical Research*, 49(7):1401–1408, 2016.

[310] Hyungju Ahn, Sungmin Park, Sang-Woo Kim, Pil J. Yoo, Du Yeol Ryu, and Thomas P. Russell. Nanoporous Block Copolymer Membranes for Ultrafiltration: A Simple Approach to Size Tunability. *ACS Nano*, 8(11):11745–11752, 2014.

[311] Zhaogen Wang, Leiming Guo, and Yong Wang. Isoporous Membranes with Gradient Porosity by Selective Swelling of UV-Crosslinked Block Copolymers. *Journal of Membrane Science*, 476:449–456, 2015.

[312] Wei Sun, Zhaogen Wang, Xueping Yao, Leiming Guo, Xiaoqiang Chen, and Yong Wang. Surface-Active Isoporous Membranes Nondestructively Derived from Perpendicularly Aligned Block Copolymers for Size-Selective Separation. *Journal of Membrane Science*, 466:229–237, 2014.

[313] Yong Wang and Fengbin Li. An Emerging Pore-Making Strategy: Confined Swelling-Induced Pore Generation in Block Copolymer Materials. *Advanced Materials*, 23(19):2134–2148, 2011.

[314] Jiali Wang, Md. Mushfequr Rahman, Clarissa Abetz, Sofia Rangou, Zhenzhen Zhang, and Volker Abetz. Novel Post-Treatment Approaches to Tailor the Pore Size of PS-*b*-PHEMA Isoporous Membranes. *Macromolecular Rapid Communications*, 39(18):1800435, 2018.

[315] Seth B. Darling. Perspective: Interfacial Materials at the Interface of Energy and Water. *Journal of Applied Physics*, 124(3):030901, 2018.

[316] Hui-Jun Zhou, Guan-Wen Yang, Yao-Yao Zhang, Zhi-Kang Xu, and Guang-Peng Wu. Bioinspired Block Copolymer for Mineralized Nanoporous Membrane. *ACS Nano*, 12(11):11471–11480, 2018.

[317] Qi Zhang, Yibei Gu, Yuk Mun Li, Peter A. Beaucage, Teresa Kao, and Ulrich Wiesner. Dynamically Responsive Multifunctional Asymmetric Triblock Terpolymer Membranes with Intrinsic Binding Sites for Covalent Molecule Attachment. *Chemistry of Materials*, 28(11):3870–3876, 2016.

[318] Yibei Gu and Ulrich Wiesner. Tailoring Pore Size of Graded Mesoporous Block Copolymer Membranes: Moving from Ultrafiltration toward Nanofiltration. *Macromolecules*, 48(17):6153–6159, 2015.

[319] Jinwoo Lee, M. Christopher Orilall, Scott C. Warren, Marleen Kamperman, Francis J. Disalvo, and Ulrich Wiesner. Direct Access to Thermally Stable and Highly Crystalline

Mesoporous Transition-Metal Oxides with Uniform Pores. *Nature Materials*, 7(3):222–228, 2008.

[320] Hao-Cheng Yang, Ruben Z. Waldman, Zhaowei Chen, and Seth B. Darling. Atomic layer deposition for membrane interface engineering. *Nanoscale*, 10:20505–20513, 2018.

[321] Matthieu Weber, Anne Julbe, Philippe Ayral, Andréand Miele, and Mikhael Bechelany. Atomic Layer Deposition for Membranes: Basics, Challenges, and Opportunities. *Chemistry of Materials*, 30(21):7368–7390, 2018.

[322] Sujin Ham, Changhak Shin, Eunhye Kim, Du Yeol Ryu, Unyong Jeong, Thomas P. Russell, and Craig J. Hawker. Microdomain Orientation of PS-*b*-PMMA by Controlled Interfacial Interactions. *Macromolecules*, 41(17):6431–6437, 2008.

[323] Eungnak Han, Karl O. Stuen, Young-Hye La, Paul F. Nealey, and Padma Gopalan. Effect of Composition of Substrate-Modifying Random Copolymers on the Orientation of Symmetric and Asymmetric Diblock Copolymer Domains. *Macromolecules*, 41(23):9090–9097, 2008.

[324] Lorenzo Guio, Claire Liu, Dean Boures, Patrick T. Getty, Ruben Waldman, Xiaoying Liu, and Seth B. Darling. Procedure for the Transfer of Polymer Films onto Porous Substrates with Minimized Defects. *Journal of Visualized Experiments*, (148):1–9, 2019.